
ULTRAFAST NONLINEAR SPECTROSCOPY
OF NANOSTRUCTURES

Von der Universität Bayreuth
zur Erlangung des Grades eines
Doktors der Naturwissenschaften (Dr. rer. nat.)
genehmigte Abhandlung

VON
JULIAN MAGNUS OBERMEIER
geb. in Waiblingen

1. Gutachter: Prof. Dr. Markus Lippitz
2. Gutachter: Prof. Dr. Georg Herink

Tag der Einreichung: 22.03.2022
Tag des Kolloquiums: 29.07.2022

ABSTRACT

Nanostructures like subwavelength metal nanoparticles or quantum dots build the bridge between the atomic length scale and the macroscopic one. Although they consist of thousands of atoms, they show properties only explainable by quantum mechanical approaches. Nowadays, those systems are widely used in commercially available technologies but are still object of scientific research, even down to the clarification of fundamental physical questions. The formation of strongly coupled systems, formed by two or more nanostructures, sources for entangled photons and the nonlinear response of nanosystems are topics of worldwide research in the field of nanooptics. Especially the later offers many open questions and often it is not clear, if restrictions like, e.g., symmetry restrictions from the macroscopic scale still hold in the nanoscopic universe. We address some of those open questions in this thesis experimentally as well as theoretically. The use of ultrafast pump-probe techniques allow us to reveal temporal dynamics on the femto second timescale, while spectroscopic measurements complete the picture. For theoretical modeling, we combine intuitive analytical models with numerical approaches like optimization algorithms and the Finite Element Method. Our research ranges from isolated gold nanoparticles over complex waveguide-like nanocircuits to layered semiconductor structures with embedded quantum dots.

The first two chapters lay a basis of physical framework for the later investigated topics. The field of plasmonics is embedded in the theory of electromagnetism and we give an insight in the field of nonlinear optics. Moreover, we introduce computational electrodynamics with a focus on the Finite Element Method and nanostructures that are of interest in the subsequent work.

The following two chapters focus on second-harmonic generation on the nanoscale. We demonstrate theoretically and experimentally, that the current understanding has to be expanded. In contrast to the past understanding, subwavelength particles made of a symmetric material do not necessarily have to possess a geometrical asymmetry to emit second-harmonic light. In fact, it is already sufficient if an optical or plasmonic mode of appropriate symmetry is present. We prove our hypothesis in a complex plasmonic nanocircuit, carefully exclude influences that could weaken our statement and, moreover, explore the nonlinear operation of the nanocircuit to its full extend. The later is described by an intuitive analytical model.

The next chapter marks the transition towards time resolved experimental techniques. We investigate the temporal dynamics of a low density, quantum dot based semiconductor saturable absorber mirror. We reveal time constants of the recovery process after saturation and determine characteristic constants of the saturation process itself, offering enough information for a future application as mode locking device in an ultrafast red emitting vertical-external-cavity surface emitting laser. Moreover, we also conduct

experiments with varying wavelength, that reveal the structure's behavior in spectral proximity to the desired operation wavelength.

The last chapter of the thesis focuses again on plasmonic nanostructures but lays focus on the temporal dynamics of quasi free, hot electrons and their role in nonlinear optical processes. Up to now, this relation, as well as the connection to the bandstructure of the material itself, remains rather unclear. We present our experimental approach, involving a multi-color pump-probe setup. We create hot electrons in the conduction band with a 400 nm pump pulse, probe the structure with a delayed infrared probe pulse and investigate the impact on the nonlinear signals. Namely, second-harmonic generation, third-harmonic generation and multi-photon luminescence. We observe partly differing changes in all three of them regarding the sign of the modulation as well as recovery and decay times. In the subsequent measurements, we sacrifice the spectral information for a better signal-to-noise ratio by a Lock-In detection scheme with a single photon counting device. Therefor, we focused on the dominating signal, given by changes in the photo luminescence. We investigate excitation power dependent changes in the pump-probe peak and present first steps towards a theoretical model involving a two-temperature model for the thermalization of the generated hot electrons. Moreover, we present a technique for ultrafast multi-color pulse characterization. We use difference-frequency generation in order to obtain cross-correlation frequency resolved optical gating traces from nonlinear micro crystals and also gold nanorods themselves in the sample plane of the experiment.

ZUSAMMENFASSUNG

Nanostrukturen wie beispielsweise Subwellenlängen-Metallnanopartikel oder Quantenpunkte stellen den Übergang zwischen der atomaren und der makroskopischen Längenskala dar. Obwohl sie aus Tausenden von Atomen bestehen, zeigen sie Eigenschaften, die nur durch quantenmechanische Ansätze erklärbar sind. Diese Systeme sind heutzutage in kommerziell verfügbaren Technologien weit verbreitet, aber dennoch auch Gegenstand wissenschaftlicher Forschung. Dies reicht hin bis zur Klärung grundlegender physikalischer Fragen. Die starke Kopplung zwischen zwei oder mehr Quantensystemen, Quellen für verschränkte Photonen und die nichtlineare Antwort von Nanosystemen sind aktuelle Themen auf dem Gebiet der Nanooptik. Insbesondere letzteres bietet viele offene Fragen und oft ist unklar, ob z.B. Symmetriestriktionen der makroskopischen Skala auch noch im nanoskopischen Universum gelten. In der vorliegenden Arbeit befassen wir uns sowohl experimentell, als auch theoretisch mit aktuellen Fragestellungen der Nanophotonik. Wir verwenden ultraschnelle Pump-Probe Techniken, um zeitliche Dynamiken auf der Femtosekunden-Zeitskala zu untersuchen und nutzen spektroskopische Methoden, um die sich ergebenden Bilder zu vervollständigen. Im Bereich der theoretischen Modellbildung kombinieren wir intuitive analytische Modelle mit numerischen Ansätzen wie Optimierungsalgorithmen und der Finite-Elemente-Methode. Unsere Forschung erstreckt sich von isolierten Gold-Nanopartikeln über komplexe Nanoschaltkreise bis hin zu Halbleiterschichtstrukturen mit eingebetteten Quantenpunkten.

Innerhalb der ersten zwei Kapitel erläutern wir die im Laufe der Arbeit benötigten, physikalischen Grundlagen. Wir gehen auf das Forschungsgebiet der Plasmonik innerhalb der Theorie des Elektromagnetismus ein und geben einen Einblick in Grundzüge der nichtlinearen Optik. Darüber hinaus erläutern wir die Finite-Elemente-Methode und legen dabei den Fokus auf Nanostrukturen, die für die nachfolgenden Kapitel von zentraler Bedeutung sind.

Die beiden folgenden Kapitel konzentrieren sich auf die Erzeugung der zweiten Harmonischen auf der Nanoskala. Wir zeigen sowohl theoretisch als auch experimentell, dass das bisherige Verständnis einer Erweiterung bedarf. Im Gegensatz zum bisherigen Stand der Forschung, müssen Subwellenlängenteilchen aus einem symmetrischen Material nicht notwendigerweise eine geometrische Asymmetrie besitzen, um eine Emission der zweiten Harmonischen aufzuweisen. Es reicht bereits aus, wenn eine optische oder plasmonische Mode passender Symmetrie zur Emission zur Verfügung steht. Wir beweisen unsere Hypothese in einem komplexen plasmonischen Nanoschaltkreis, schließen sorgfältig Einflüsse aus, die unsere Aussage widerlegen könnten und untersuchen darüber hinaus das vollständige nichtlineare Verhalten der Struktur. Letzteres lässt sich durch ein entwickeltes, intuitives analytisches Modell beschreiben.

Das nächste Kapitel stellt den Übergang von statischen zu zeitaufgelösten Experimenten dar. Wir untersuchen die zeitliche Dynamik eines sättigbaren Absorberspiegels auf Quantenpunktbasis mit niedriger Quantenpunktdichte. Wir bestimmen sowohl zeitliche Konstanten des Sättigungsprozesses, als auch die charakteristische Sättigungsfluenz des Systems. Letztere ist entscheidend für eine zukünftige Anwendung zum Modenkoppeln in einem ultraschnellen, rot emittierenden, oberflächenemittierenden Laser mit vertikaler externer Kavität. Zusätzlich untersuchen wir das wellenlängenabhängige Verhalten der Struktur um Informationen über den Sättigungsprozess in spektraler Nähe zur gewünschten Betriebswellenlänge zu erhalten.

Das letzte Kapitel des Haupttextes konzentriert sich erneut auf plasmonische Nanostrukturen, legt den Fokus jedoch auf die zeitliche Dynamik quasi freier, heißer Elektronen und ihren Einfluss auf nichtlineare optische Prozesse. Dieser Zusammenhang sowie der Einfluss der Bandstruktur des Materials selbst, ist bislang ungeklärt. Wir präsentieren unseren experimentellen Ansatz mit einem mehrfarbigen Pump-Probe-Aufbau. Wir erzeugen heiße Elektronen im Leitungsband mit einem 400 nm Pumpimpuls, untersuchen die Struktur mit einem verzögerten Probestimpuls im infraroten Spektralbereich und untersuchen die Auswirkung auf die emittierten, nichtlinearen Signale. Explizit auf die Erzeugung der zweiten Harmonischen, die Erzeugung der dritten Harmonischen und die Multiphotonenlumineszenz. In den Messungen zeigen sich bei allen dreien, teils unterschiedliche, Änderungen hinsichtlich des Vorzeichens der Modulation sowie der Abklingzeiten. In den nachfolgenden Messungen verzichten wir auf die spektrale Auflösung zugunsten eines besseren Signal-Rausch-Verhältnisses. Die Detektion erfolgt mit Hilfe eines Einzelphotonendetektors und anschließender Demodulation mit einem Lock-In Verstärker. Das Signal wird in diesen Messungen von der dominanten Photolumineszenz bestimmt. Wir untersuchen anregungsleistungsabhängige Änderungen im Pump-Probe-Peak und entwickeln erste Teile eines theoretischen Modells zur Beschreibung der beobachteten Effekte. Zur Beschreibung der Elektronenthalisierung verwenden wir ein Zweitemperaturmodell. Darüber hinaus präsentieren wir eine Technik zur ultraschnellen mehrfarbigen Pulscharakterisierung. Mittels Differenzfrequenzerzeugung tasten sich Pump und Probestimpuls gegenseitig ab und wir erhalten frequenz- und zeitaufgelöste Informationen über die Pulskombination. Für den Messprozess verwenden wir nichtlineare Mikrokristalle und demonstrieren die Technik darüber hinaus in einem einzelnen Gold Nanodraht.

PUBLICATIONS

articles in scientific journals

1. M. Grossmann, J. Obermeier, T. Schumacher, M. Lippitz, R. Bek, M. Jetter, and P. Michler, *Ultrafast reflectivity dynamics of a InP/AlGaInP QD SESAM for red-emitting mode-locked VECSELs*, **in preparation**
2. T.-Z. Chen, J. Obermeier, T. Schumacher, F.-C. Lin, J.-S. Huang, M. Lippitz, and C.-B. Huang, *Modal Symmetry Controlled Second-Harmonic Generation by Propagating Plasmons*, **Nano Letters** **19(9)**, 6424–6428 (2019)
3. M. Schnepf, Y. Brasse, F. Gößler, A. M. Steiner, J. Obermeier, M. Lippitz, A. Fery, and T. König, *'Single Particle Spectroscopy of Radiative Processes in Colloid-to-Film-Coupled Nanoantennas'*, **Zeitschrift für Physikalische Chemie** **232(9-11)**, 1593-1606 (2018)
4. J. Obermeier, T. Schumacher, and M. Lippitz, *'Nonlinear spectroscopy of plasmonic nanoparticles'*, **Advances in Physics: X** **3(1)**, 1454341 (2018)

contributions on international conferences

1. J. Obermeier, T.-Z. Chen, T. Schumacher, F.-C. Lin, J.-S. Huang, C.-B. Huang, and M. Lippitz, *Symmetry-forbidden second-harmonic generation in a fully centro-symmetric plasmonic nanocircuit*, **Talk**, DPG spring meeting 2018 - Berlin/Germany
2. J. Obermeier, T.-Z. Chen, T. Schumacher, F.-C. Lin, J.-S. Huang, C.-B. Huang, and M. Lippitz, *Second harmonic generation in fully symmetric gold nanostructures*, **Talk**, DPG spring meeting 2018 - Berlin/Germany
3. J. Obermeier, T.-Z. Chen, T. Schumacher, F.-C. Lin, J.-S. Huang, C.-B. Huang, and M. Lippitz, *Second harmonic generation in fully symmetric gold nanostructures*, **Talk**, OPON 2018 - Münster/Germany
4. J. Obermeier, and M. Lippitz, *Higher harmonics generation in tapered plasmonic waveguides*, **Poster**, DPG spring meeting 2017 - Dresden/Germany

Further talks on workshops and seminars

1. J. Obermeier, T. Schumacher, M. Lippitz, M. Grossmann, R. Bek, M. Jetter, and P. Michler, *Pump-probe spectroscopy of SESAMs*, seminar, october 2019 - Hirschegg, Kleinwalsertal/Austria
2. J. Obermeier, T.-Z. Chen, T. Schumacher, F.-C. Lin, J.-S. Huang, C.-B. Huang, and M. Lippitz, *Symmetry-forbidden second-harmonic generation in a fully centro-symmetric plasmonic nanocircuit*, workshop, september 2019 - Dresden/Germany
3. J. Obermeier, T.-Z. Chen, T. Schumacher, F.-C. Lin, J.-S. Huang, C.-B. Huang, and M. Lippitz, *Second harmonic generation in two wire transmission lines*, seminar, september 2017 - Hirschegg, Kleinwalsertal/Austria

CONTENTS

1	INTRODUCTION AND OUTLINE	1
2	THEORETICAL BACKGROUND	5
2.1	Light Matter Interaction	5
2.2	Drude-Lorentz Theory	6
2.3	Plasmonics	8
2.3.1	Fundamentals of Plasmonics	8
2.3.2	Plasmonics in complex systems	9
2.4	Nonlinear Optics	12
2.4.1	Second Order Nonlinear Effects	13
2.4.2	Third Order Nonlinear Effects	15
2.4.3	Symmetry Considerations and Conservation Laws	15
3	NUMERICAL METHODS	19
3.1	The Finite Element Method	19
3.2	Scattering and Absorption in isolated Nanoparticles	21
3.2.1	determination of cross-sections	23
3.2.2	field and charge distribution	24
3.3	Plasmonic Waveguides	27
4	SECOND-HARMONIC GENERATION IN PLASMONIC STRUCTURES	31
4.1	second-harmonic emission from nanoparticles	32
4.1.1	calculation of the nonlinear polarization	32
4.1.2	emission properties of specific nanostructures	34
4.2	second-harmonic generation in plasmonic waveguides	36
5	EXPERIMENTAL OBSERVATION OF SECOND-HARMONIC EMISSION IN SYMMETRIC NANOSTRUCTURES	41
5.1	Structure layout and experimental setup	41
5.2	second-harmonic generation in a TWTL	46
5.3	Modal Symmetry Controlled SHG	48
5.4	Influence of locally generated SHG	53
5.4.1	antenna generated SHG	53
5.4.2	mode detector SHG	56
5.5	nonlinear Propagation effects in a TWTL	58
5.6	Influence of ITO spacer-layer	62
5.7	Conclusion	66
6	TEMPORAL DYNAMICS OF QUANTUM LAYERED SYSTEMS	67
6.1	Introduction to SESAMs and time resolved measurements	67
6.2	Experimental Setup	70
6.3	Characteristics of the SESAM under investigation	72
6.4	Fluence dependent Saturation Dynamics	74
6.5	Wavelength dependent Dynamics	77
6.6	Conclusion	79
7	NONLINEAR PUMP-PROBE SPECTROSCOPY OF GOLD NANOWIRES	81

7.1	Theoretical Background	81	
7.1.1	band structure of gold	82	
7.1.2	plasmon assisted excitations	82	
7.1.3	the two-temperature model	85	
7.2	experimental details	86	
7.2.1	setup and structures	87	
7.2.2	alignment and stability	88	
7.3	linear and nonlinear emission properties of a nanowire		91
7.4	DFG supported pulse cross-correlation	95	
7.4.1	XFROG in lithium niobate micro-crystals	96	
7.4.2	XFROG in an isolated plasmonic wire	97	
7.5	pump-probe measurements on an isolated nanowire		99
7.6	data evaluation and near-resonance behavior	103	
7.7	Power dependent measurements	104	
7.7.1	power dependent change of rates	105	
7.7.2	power dependent change of amplitudes	107	
7.8	spectral behavior	109	
7.9	outlook and discussion	112	
8	CONCLUSION	115	
A	APPENDIX	119	
A.1	Linear and Nonlinear Absorption Processes	119	
A.2	Mode Profiles of a Two Wire Transmission Line	121	
A.3	Modulation of Optical Signals	124	
	BIBLIOGRAPHY	127	

INTRODUCTION AND OUTLINE

The field of nanophysics has emerged into an indispensable part of our technologically advanced society. The continuous downsizing of microelectronics gives constantly rise towards higher and higher computing powers as described by Moore's law [1]. Bringing light down to the few nano meter length scale, in the last years, was the next step in this ongoing process [2–5]. Nowadays, the smartphone in everyone's pocket has a higher performance than high-end computers from 2 decades ago and the current development in quantum computing promises a, rhetorically well suited, quantum leap to a whole new level [6–8]. Combined with photonic signal processing and circuitry, undreamed-of possibilities open up [9–13]. All these technological advances have their foundation in the research field of nanoelectronics and nanooptics. But as a matter of fact, those fields do not only push technological advances but also have the capability to investigate and clarify fundamental physical questions and pave the way towards a new physical understanding.

Nanoobjects like metal nanostructures or quantum dots build the bridge between the atomic or quantum scale and the macroscopic scale. Although those structures consist of thousands of atoms, they still show characteristics of single quantum systems. Similar to the bonding and anti-bonding states that are formed in an H_2^+ molecule, two nanosystems can hybridize and form a new system with new properties [14, 15], show strong coupling to other quantum systems [16–20] or emit single photons [21]. Therefore, they are perfectly suited as model systems but also to explore the fascinating properties of the structures themselves. Plasmonic nanostructures can be used in order to create sub-wavelength hot spots of light [22–24], act as antenna for smaller systems [25–27], for the creation of meta materials [28–30] or as photon sources that can provide a pair of entangled photons [31]. While the linear regime of those structures has been under intense investigation in the last decades and is well understood [32], the nonlinear regime still has many open questions to offer.

In this thesis we investigate the nonlinear response of different nanoscale systems theoretically and experimentally. Our main focus lies on gold nanostructures and ranges from a single particle to a complex plasmonic nanocircuit. Additionally, we investigate a semiconductor saturable absorber mirror featuring low density quantum dots as saturable system. For our experiments we mainly use spectroscopic methods as well as ultra fast pump-probe measurements. The theoretical calculations feature intuitive analytical models that are partly combined with finite element calculations.

First, we start by giving a physical framework to the investigated fields. We embrace the field of plasmonics within the body of electrodynamics and discuss plasmonic excitations bound to different geometrical interfaces. Starting from a flat metal-dielectric interface, we continue over waveguides to sub-wavelength particles. Finally, we lay our focus on nonlinear optics, present effects up to a third order nonlinearity and also note symmetry restrictions related to the discussed effects.

In chapter 3, we continue by giving an overview over numerical methods in the field of electrodynamics before we focus on the Finite Element Method. After a review of the method itself, we discuss the detailed application for plasmonic waveguides and particles. Here, we already introduce and discuss the properties of structures, used throughout the thesis. Beside of a plasmonic two-wire transmission line for waveguide applications, we study the optical properties of gold nanowires and the more complex split ring resonator. The study of the later two is picked up in chapter 4, where we dig deeper into second-harmonic generation in nanostructures. After a review of potential sources, stemming from the bulk material and the surface, we focus on the later and explain a model for the calculation of the second order nonlinear polarization. We return to symmetry restrictions in second order nonlinear processes and discuss them for nanoscale systems. Finally, we proceed by introducing a new idea and structure to extend the previous understanding of second-harmonic generation on the nanoscale. The project was first introduced to us by Prof. C.-B. Huang and investigated in a collaboration [33].

Chapter 5 fully centers attention on second-harmonic generation in a plasmonic two-wire transmission line. We take the numerical and theoretical considerations from the previous chapter and validate them experimentally. We show, that in contrast to the past understanding, no asymmetry in the material nor the geometrical shape has to be present in order to allow second-harmonic generation. In fact, an optical or plasmonic mode of appropriate symmetry is already a sufficient criterion. After proving this point by the use of the two eigenmodes of the two-wire transmission line, which offer different symmetries, we explore the nonlinear behavior of the nanocircuit to its full extend. By using a superposition of the two eigenmodes, we demonstrate a complex coupling behavior, that can be well understood by an intuitive, symmetry based theoretical model and can even be expanded beyond our experimental findings. Throughout the chapter, we also consider experimental influences that could weaken our statement on symmetry considerations in second-harmonic generation on the nanoscale but are able to fully exclude them and validate our point. Moreover, we introduce a model, that adds a nonlinear substrate to our structure and could potentially lead to an even more complex or more efficient nonlinear behavior of the nanocircuit. Additionally, we use the well known coupled amplitude equations for second-harmonic generation, include optical losses and apply them to our measurements.

With chapter 6, we move away from plasmonic systems and towards semiconductors. After introducing the physical framework, we investigate the temporal dynamics of a semiconductor saturable absorber mirror via ultrafast pump-probe measurements. The novelty of the structure is the saturable absorbing system. The structure, made by the group of Prof. Michler from Stuttgart, is based on low-density quantum dots and absorbing in the red spectral range. First, we introduce our setup for degenerate pump-

probe measurements and perform a characterization of the sample itself. Subsequently, we investigate the saturation dynamics of the absorber and reveal ultrafast recovery times. Finally, the structure is excited with different wavelengths in order to obtain information about the spectral behavior. We attribute changes in the recovery process to different components of the absorber.

In chapter 7 we revisit plasmonic structures but are interested in ultrafast phenomena. We want to resolve the question how the process of third-harmonic generation and multi-photon luminescence in subwavelength gold nanoparticles is connected to the band structure. In order to bring light into this relation, we perform ultrafast pump-probe experiments. We excite hot electrons in the conduction band of gold and measure the time-dependent influence on nonlinear optical processes. We start this chapter by taking a closer look at the band structure of gold, possible optical absorption mechanisms and decay channels for plasmonic excitations. This includes especially the generation of hot electrons in the conduction band and the subsequent thermalization that can be well described by a two temperature model. After that, we introduce our experimental setup, the detection mechanisms and the structures under investigation. We include special alignment steps and quantify spatial sample drifts in the setup. Before moving on to pump-probe measurements, we present the nanostructure's response upon excitation with only pump and only probe light. We focus on emission polarization and on linearly and nonlinearly generated photo luminescence. As first pump-probe measurements, we let our two beams sample each other in a nonlinear medium in order to determine the combined pulse length. This measurement was performed in a powder of a nonlinear optical crystal, as well as in a gold nanowire. With the knowledge of the exact temporal zero and the combined pulse length, we move on to spectrally resolved pump-probe measurements on an isolated gold nanowire and investigate the influence of hot electrons on higher-harmonics generation and multi-photon luminescence. Afterwards, we switch the detection mechanism and use Lock-In amplified traces, obtained from a single photon detector. This enables us to move to lower excitation powers and perform pump and probe power dependent measurements. We introduce a model to quantify changes in the pump-probe peak and discuss the observed connections. Moreover, we start to build a theoretical model, based on a two temperature model, in order to describe the observed effects. Finally, we look at power dependent spectra at different positions on the pump-probe peak for different excitation powers. The combined measurements give a very interesting overview over possible effects and pave the way towards new experiments.

THEORETICAL BACKGROUND

In this chapter we lay the basic physical framework for the subsequent chapters. We start by a brief summary of the required fundamental electromagnetic equations and the interaction of light with matter. The later includes the description of matter via an harmonic oscillator model. Afterwards, we focus on electromagnetic effects at metal-dielectric interfaces of varying geometries - first simple planar interfaces, then more complex shapes. Finally, we extend our description of light matter interaction from a linear to a nonlinear one and give a brief introduction into nonlinear optics.

2.1 LIGHT MATTER INTERACTION

The behavior of electromagnetic radiation and its interaction with matter is described by Maxwell's equations [34]

$$\nabla \cdot \mathbf{D} = \rho_{\text{ext}} \quad , \quad (1)$$

$$\nabla \cdot \mathbf{B} = 0 \quad , \quad (2)$$

$$\nabla \times \mathbf{E} = -\frac{\partial \mathbf{B}}{\partial t} \quad , \quad (3)$$

$$\nabla \times \mathbf{H} = \mathbf{j}_{\text{ext}} + \frac{\partial \mathbf{D}}{\partial t} \quad , \quad (4)$$

here shown in their macroscopic formulation. The complex vector fields \mathbf{E} and \mathbf{B} describe the electric and the magnetic field, \mathbf{D} and \mathbf{H} the displacement and magnetizing field. ρ_{ext} and \mathbf{j}_{ext} picture external, i.e. free, charge and current densities. In this formulation, the influence of bound charges and currents, i.e., influence of matter, is incorporated in the fields \mathbf{D} and \mathbf{H} . This set of partial differential equations is completed by two constitutional relations

$$\mathbf{D} = \epsilon_0 \mathbf{E} + \mathbf{P} \quad , \quad (5)$$

$$\mathbf{H} = \frac{1}{\mu_0} \mathbf{B} - \mathbf{M} \quad , \quad (6)$$

where \mathbf{P} and \mathbf{M} depict the polarization and magnetization field. The two universal constants ϵ_0 and μ_0 are called the permittivity and permeability of free space and are related to the vacuum speed of light $c_0 = \frac{1}{\sqrt{\epsilon_0 \mu_0}}$. \mathbf{P} and \mathbf{M} describe how matter responds to applied electric and magnetic fields and can be viewed as induced electric and magnetic dipole or, more general, multi pole moments per unit volume. Therefore, they represent macroscopic averaged quantities. Permanent moments of the matter are

also included. For our purposes it is convenient to restrict to non-magnetic materials which simplifies equation 6 to

$$\mathbf{H} = \frac{1}{\mu_0} \mathbf{B} . \quad (7)$$

Under the assumption of a linear, isotropic medium, the polarization \mathbf{P} can be written as

$$\mathbf{P} = \epsilon_0 \chi(\omega) \mathbf{E} = \epsilon_0 (\epsilon_r(\omega) - 1) \mathbf{E} . \quad (8)$$

where χ is the frequency dependent susceptibility and ϵ_r the frequency dependent relative permittivity.

2.2 DRUDE-LORENTZ THEORY

In order to describe the interaction of electromagnetic waves, in particular optical frequencies with matter, several approaches exist. The easiest and most intuitive ansatz is given by the Drude-Lorentz theory. The theory derives an expression for the linear, frequency dependent material response $\chi(\omega)$ (respectively $\epsilon_r(\omega)$) to applied electric fields. The concept is to look at a bound electron excited by a monochromatic electric field $\mathbf{E}(t) = \mathbf{E}_0 e^{-i\omega t}$. The temporal dynamic of the electrons position $\mathbf{x}(t)$ is described by the differential equation of a driven, damped harmonic oscillator [35, 36]

$$\frac{d^2}{dt^2} \mathbf{x} + \gamma \frac{d}{dt} \mathbf{x} + \omega_0^2 \mathbf{x} = -\frac{e}{m} \mathbf{E}(t) , \quad (9)$$

where ω_0 is the eigenfrequency of the undamped oscillator, γ the damping constant and m the mass of the electron. The solution to equation 9 is given by

$$\mathbf{x}(t) = -\frac{e}{m} \frac{1}{\omega_0^2 - \omega^2 - i\gamma\omega} \mathbf{E}(t) , \quad (10)$$

and the resulting dipole moment of the bound electron can be calculated as

$$\mathbf{p}(t) = -e\mathbf{x}(t) . \quad (11)$$

The macroscopic polarization is derived by a multiplication with the electron density n

$$\mathbf{P}(t) = \frac{ne^2}{m} \frac{1}{\omega_0^2 - \omega^2 - i\gamma\omega} \mathbf{E}(t) . \quad (12)$$

By comparing the result to equation 8, an expression for the frequency dependent relative permittivity is found

$$\epsilon_r(\omega) = 1 + \frac{\omega_p^2}{\omega_0^2 - \omega^2 - i\gamma\omega} , \quad (13)$$

with the commonly used plasma frequency $\omega_p = \sqrt{\frac{ne^2}{m\epsilon_0}}$. If we now limit the description to metallic materials, which have partially occupied conduction bands and therefore quasi free electrons, we can set $\omega_0 = 0$ and equation 13 simplifies to

$$\epsilon_r(\omega) = 1 - \frac{\omega_p^2}{\omega^2 + i\gamma\omega} . \quad (14)$$

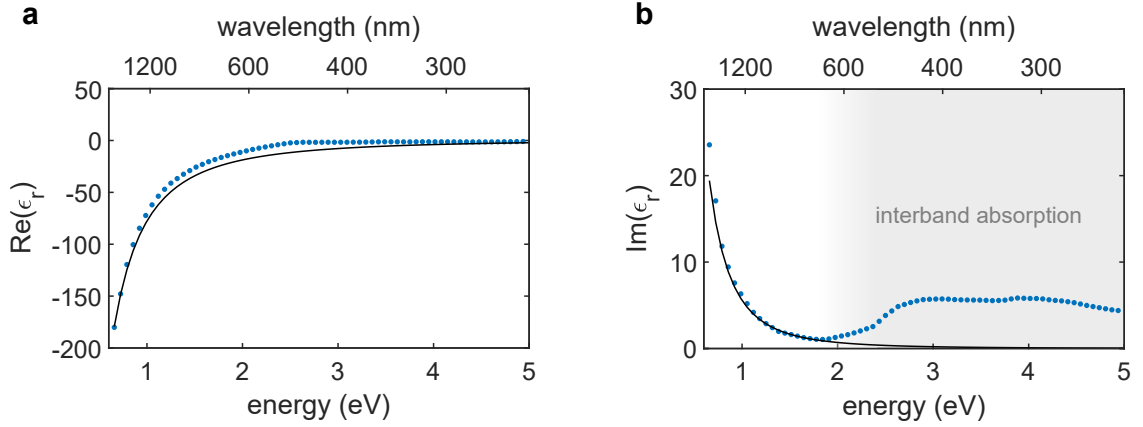


Figure 1: Real (a) and imaginary (b) part of the relative permittivity of gold. The blue dots represent the experimental data by Johnson and Christy and the solid black lines show the description by the Drude model. The gray shaded area in (b) marks the beginning of interband absorptions in gold.

In this work the most present material is gold. Consequently, we will compare the derived model to experimental data of gold. The comparison, split in the real and the imaginary part of the complex permittivity, is shown in figure 1. The blue points represent the measured data by Johnson and Christy [37] and the black lines the Drude model with the plasma frequency $\omega_p = 1.35 \cdot 10^{16}$ Hz and a damping of $\gamma = 1.08 \cdot 10^{14}$ Hz [38]. For energies below 1.8 eV, the experimental data is well described by the Drude model. Moving to higher energies interband transitions, that the model does not account for, cause deviations in the imaginary part. These transitions are the d-band absorptions of gold [39] and become considerably large at nominally 2.4 eV [40]. Yet, they still have an influence down to 1.8 eV.

In practice, it's common to use the interpolated data of Johnson and Christy in order to describe optical properties of gold. Nevertheless, the Drude model gives a simple analytical expression in which also distinct parameters can be varied or modulated if needed. Furthermore, also phenomenologically extended versions of the Drude model exist [41] or one can revert to fully calculated band structures by, e.g., many body perturbation theory [42] or relativistic band calculations [40]. Often those approaches are combined with density functional theory to hybrid approaches, which lead to results close to experimentally obtained data.

In the field of optics it is more convenient to describe materials by their complex refractive index \tilde{n} rather than their relative permittivity. The relation between both is given by

$$\tilde{n} = n + ik = \sqrt{\epsilon_r} \quad , \quad (15)$$

$$n = \sqrt{\frac{1}{2}(|\epsilon_r| + \text{Re}(\epsilon_r))} \quad , \quad (16)$$

$$k = \sqrt{\frac{1}{2}(|\epsilon_r| - \text{Re}(\epsilon_r))} \quad . \quad (17)$$

The real part n of the refractive index causes a frequency dependent phase velocity of light in a medium and the imaginary part k accounts for absorption.

2.3 PLASMONICS

In the scope of this work we mainly focus on metallic nanostructures. Therefore, it is necessary to discuss electromagnetic effects on the nanoscale, that explicitly involve the surface or interface of the structures.

2.3.1 Fundamentals of Plasmonics

For light-matter interaction in the specific case of the material being metallic, we can start with a simple consideration. We assume a finite volume of a positively charged lattice and a free electron gas. Now, a static electric field displaces the electron gas with respect to its equilibrium position and is turned off again. The electron gas will overshoot the initial equilibrium position and coherent oscillations start. In the case of an undamped motion, the oscillation frequency is the plasma frequency ω_p . The quasiparticle of this electron or plasma oscillation is called plasmon. By nature this collective charge oscillation has a longitudinal character and represents a horizontal line in the dispersion relation of the electron gas (see figure 2 (a)). For frequencies $\omega > \omega_p$ the oscillation has a transverse character and follows the generic dispersion relation

$$k^2 = \epsilon_r \frac{\omega^2}{c^2} . \quad (18)$$

Including the permittivity obtained from the Drude model (equation 14), we obtain the plasma or free electron gas dispersion for an undamped motion ($\gamma = 0$)

$$\omega = \sqrt{\omega_p^2 + k^2 c^2} . \quad (19)$$

For frequencies $\omega < \omega_p$ plasma oscillations become of particular interest. They have a longitudinal character and occur at metal-dielectric interfaces. The dipole-carrying electron oscillation in the metal couples to light and forms the so called surface plasmon polariton (SPP). As self consistent solutions of Maxwell's equations they represent traveling modes, that are bound and localized on a subwavelength scale to the metallic surface. The dispersion relation is commonly given in the implicit form

$$k_{\text{SPP}} = \frac{\omega}{c} \sqrt{\frac{\epsilon_{r,\text{metal}}(\omega) \epsilon_{r,\text{diel}}(\omega)}{\epsilon_{r,\text{metal}}(\omega) + \epsilon_{r,\text{diel}}(\omega)}} . \quad (20)$$

In figure 2 (a), the dispersion relation of a surface plasmon polariton at a gold-air interface is shown. In this case gold is approximated as a lossy Drude metal. For the geometric reason of a single interface, the SPP dispersion curve does not asymptotically approach the frequency ω_p but $\frac{\omega_p}{\sqrt{2}}$. Figure 2 (b) shows a propagating SPP at a gold-air interface. The electric field component along the surface normal is shown as well as the electric field lines (E_y, E_z). Perpendicular to the interface, the electric field decays on a short length scale - the so called skin depth. Due to material properties, the electric field

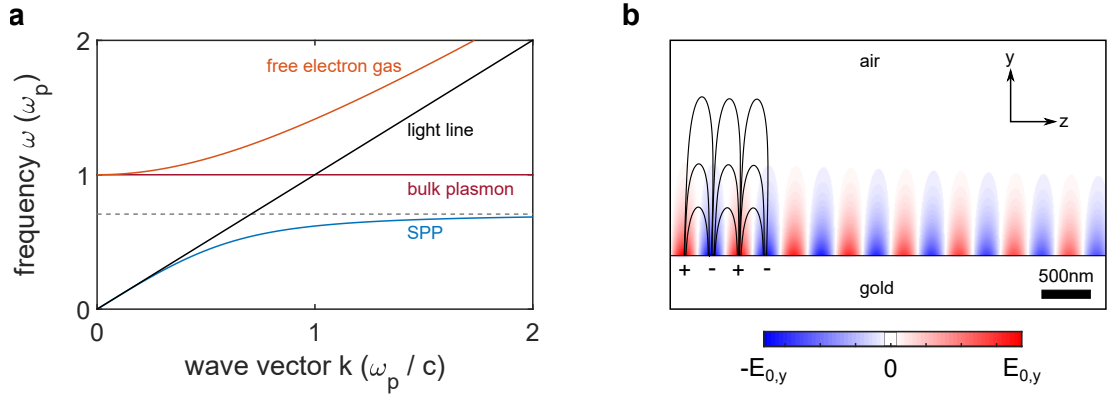


Figure 2: Characteristics of plasmons. (a) The dispersion relation of a free electron gas and surface plasmons for a lossy Drude metal. The axes are normalized to characteristic constants. (b) Surface plasmon polariton ($\lambda_{\text{SPP}} = 570 \text{ nm}$) at a gold-air interface. The electric field component E_y is color coded while the black streamlines show the tupel (E_y, E_z) . The charges at the interface are also indicated.

in the gold halfspace is not visible on a linear scale. In propagation direction the bound SPP gets exponentially damped, leading to a system specific propagation length

$$l_{\text{prop}} = \frac{1}{2|\text{Im}(k_{\text{SPP}})|} \quad (21)$$

solely depending on the imaginary part of the SPP's wave vector. Here, we defined the propagation length as the length after which the energy of the SPP mode has decreased to $1/e$. For gold-air interfaces, the values are typically in the range of several tens of microns in the visible to NIR spectral range. In general, the propagation length increases with increasing wavelength as we move further away from interband absorptions in gold.

In the dispersion relation of the SPP in figure 2 (a) the light line is indicated as black solid line. Since there is no intersection with the SPP dispersion, a direct excitation with light is not possible. Using prism couplers to bend the light line or grating couplers to shift the light line by specific values $k = \frac{2\pi}{l_{\text{grating}}}$ efficient excitation becomes possible [43–45]. Moreover, also edges of structures can be used for excitation, as they represent a special case of grating, or nanoparticles which offer a broad spectrum of k -vectors.

2.3.2 Plasmonics in complex systems

waveguides

As stated, plasmons exist at metal-dielectric interfaces of which a two-halfspace geometry with a planar interface is only the most simple example. The propagating SPPs can also be localized to more complex surfaces like, e.g., the surface of an infinitely long gold wire embedded in a dielectric surrounding. An example is shown in figure (3). We consider an infinitely long wire with a radius of 70 nm in the x - y plane and propagation

in z -direction (a). In the x - y plane the wire supports a plasmonic mode (b) similar to light-modes in optical waveguides. The electric field in the structure can be written as

$$\mathbf{E} = \mathbf{E}_0(x, y) e^{i(k_z z - \omega t)} , \quad (22)$$

$$k_z = \beta - i\delta \quad \text{with} \quad \delta > 0 . \quad (23)$$

The vector field $\mathbf{E}_0(x, y)$ describes the mode profile and the complex exponential function the time harmonic propagation in z -direction. The wave vector k_z is complex and is commonly split into two parts. The real part β accounts for dispersion, while the imaginary part δ induces losses due to absorption. The notation for plasmonic and optical waveguides coincide, yet, there are fundamental differences. While in optical waveguides the so called core of the waveguide has a higher refractive index than the surrounding medium, the plasmonic core, i.e., the gold wire, has a lower refractive index and high losses. The consequence is that in optical waveguides the modes travel in the core and are confined within the core. In plasmonic waveguides, on the other hand, the modes travel at the interface between core and surrounding and the electric fields on the outside are much higher than on the inside.

Another big difference is the spatial extend of the confined modes. While in optical waveguides the modes are in the same dimension as the lights wavelength, plasmonic modes can be confined far below the diffraction limit of light [46, 47]. If the radius of the wire decreases, the plasmonic modes become more and more localized while also the losses increase. Therefor, a sweet spot between losses and confinement has to be found [48]. If the radius of the wire increases, both waveguides show the same behavior. Higher order modes come into play if the geometrical extend of the structure is large enough [49, 50]. Throughout this thesis we only look at small dimension and therefor all single wire waveguides are considered to be single mode waveguides. One important parameter in waveguide theory is the so called effective mode index

$$n_{\text{eff}} = \frac{k_z}{k_0} = \frac{\beta}{k_0} - i \frac{\delta}{k_0} , \quad (24)$$

where k_0 is the vacuum wave vector of light. Consequently the mode index describes the deviation of the waveguide mode from a plane wave in vacuum.

particles

Aside of propagating SPPs, there is one other fundamental plasmonic excitation. The so called localized surface plasmon polariton (LSP) - commonly also referred to as particle plasmon. This plasmonic excitation is confined to metallic nanoparticles with sizes of several tens, up to several hundreds of nanometers. An important criterion for the particle size is that quantum effects can be neglected and a continuum description for the quasi free electrons is applicable. This regime is typically reached at a few nanometers [51].

If a nanoparticle is excited by monochromatic light, several effects come into play. Due to the small size of the particle compared to the wavelength of the light ($\lambda \gg d_{\text{particle}}$), the electric field over the particle volume can be considered constant for a fixed time

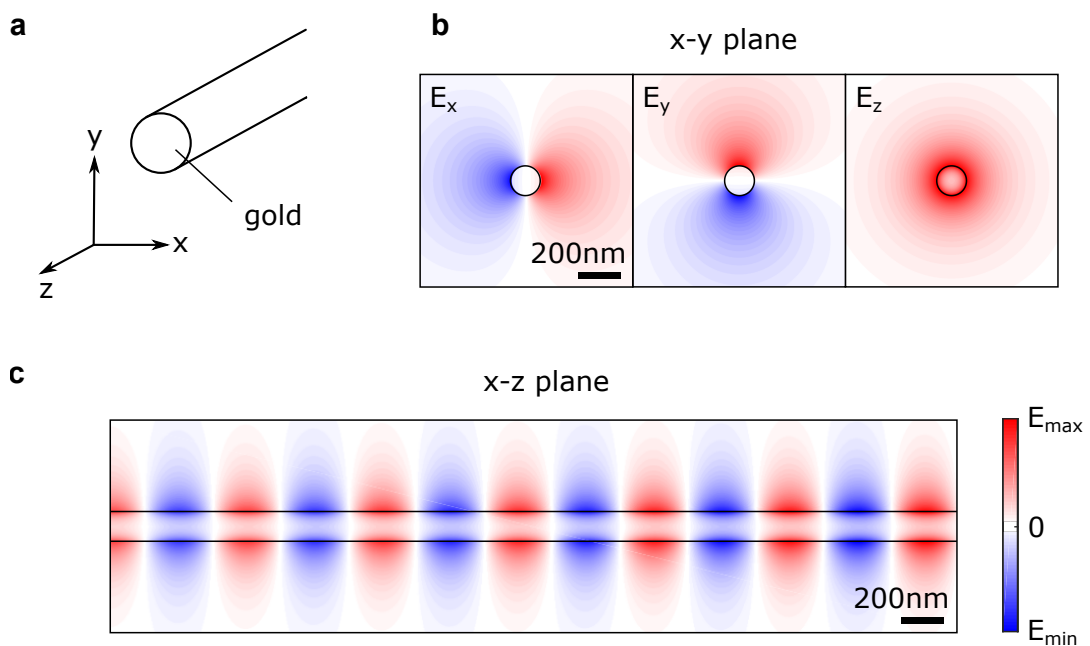


Figure 3: (a) Plasmonic waveguide with cylindrical cross-section (radius 70 nm). (b) The real part of the mode profile $E(x, y)$ is shown for all vector components $E_{x,y,z}$ (c) In propagation direction, the z-component of the electric field is strongly confined to the wire.

t_0 . The quasi free electrons will be accelerated. For times $t > t_0$ a restoring force by the lattice acts on the electron gas. Moreover, also the constant electric field of the exciting light will change its amplitude. Therefore, the system acts as driven harmonic oscillator. Due to the small extend of the nanoparticle, the excited plasmons will preferably build a standing wave like pattern within its geometry. Consequently, the shape and size of the particle strongly influences the resonance frequency of the particle [32, 52].

An example for a plasmonic nanoparticle, excited by monochromatic light, is shown in figure 4 (a). The gold rod experiences a constant electric field over its volume and a dipole-like charge distribution builds up. At the ends of the rod, this leads to highly localized electric fields as shown in figure 4 (c). Here, a x-y cut plane is drawn in the center of the particle and the absolute value of the electric field is plotted. The hotspots are confined to only a few tens of nanometers. The resonance spectrum of the rod in figure 4 (b) shows that despite the main resonance at 1250 nm also another smaller, blue shifted peak is present. This peak indicates a higher order mode. Similar to the quantum mechanical potential well also charge distributions with multiple nodes can build up within the particles geometry. The resulting electric field of the third order mode at 550 nm is shown in figure 4 (d). The resonance spectrum is calculated for the excitation of the gold rod with an incident plane wave. Therefore, even-order higher modes are not visible since they cannot couple to plane waves.

In general, calculations like shown in figure 4, are done using numerical methods like finite element methods or finite difference time domain algorithms. Only for a spherical nanoparticle in a homogeneous environment an analytical solution exists. Although it

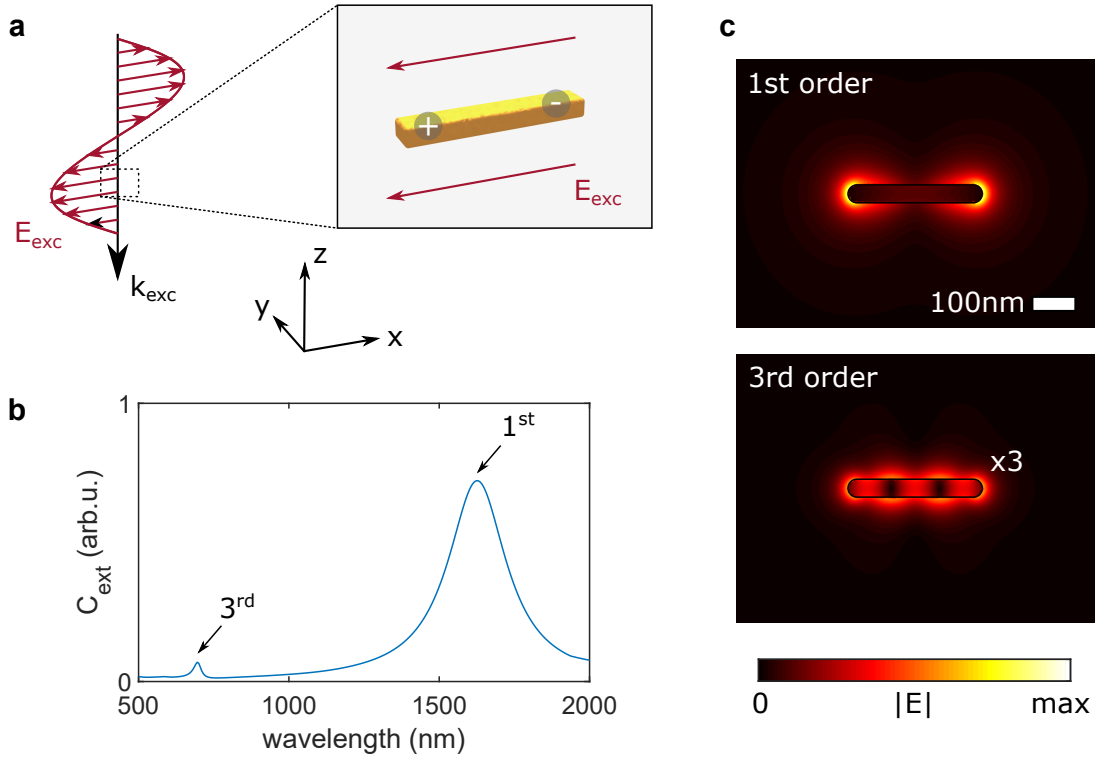


Figure 4: Example of a localized plasmon resonance in a gold nanorod. (a) The subwavelength particle is experiencing a constant electric field from the exciting light for a fixed time. Consequently, the quasi free charges are separated. (b) The calculated extinction cross-section for the structure. The first two far-field resonances - first and third order resonance - are visible. (c) The field distribution in the $x - y$ cross-section of the wire allows the characterization of the modes.

wasn't intended, LSP in metallic nanoparticles are included in the Mie Theory for scattering and absorption of small particles [53].

2.4 NONLINEAR OPTICS

In section 2.2, a description for electrons in an external electric field was given and the linear material response $\chi(\omega)$, respectively $\epsilon(\omega)$, was derived. In the case of strong electric fields, like for example generated by ultrashort laser pulses at their peaks, a purely linear description of the electron movement is not suitable anymore [54]. In equation 9 additional nonlinear restoring forces have to be added, in order to account for the anharmonicity of the electron potential given by the cores. Treating the resulting differential equation with perturbation theory yields additional nonlinear terms in the material's polarization. It can be expressed by a power series with respect to the applied electric field

$$\begin{aligned}
 \mathbf{P}(t) &= \epsilon_0 \chi^{(1)} \mathbf{E}(t) + \epsilon_0 \chi^{(2)} \mathbf{E}(t)^2 + \epsilon_0 \chi^{(3)} \mathbf{E}(t)^3 + \dots, \\
 &= \underbrace{\mathbf{P}^{(1)}(t)}_{\mathbf{P}_{\text{lin}}(t)} + \underbrace{\mathbf{P}^{(2)}(t) + \mathbf{P}^{(3)}(t) + \dots}_{\mathbf{P}_{\text{nonlin}}(t)}
 \end{aligned} \tag{25}$$

where the polarization is split into a linear part $\mathbf{P}_{\text{lin}}(t)$ and nonlinear part $\mathbf{P}_{\text{nonlin}}(t)$. The nonlinear susceptibilities $\chi^{(n)}$ are tensors of the rank $n + 1$. This tensorial character is neglected in the following description of nonlinear optical phenomena. In general, the nonlinear susceptibilities allow photon-photon interactions as well as nonlinear interactions between photons and matter. In the following we give a brief introduction to nonlinear optics which follows the notation of [55].

2.4.1 Second Order Nonlinear Effects

second-harmonic generation

The lowest order of the nonlinear susceptibility is $\chi^{(2)}$ and is discussed in more detail. We assume a strong monochromatic electric field in a nonlinear medium

$$\mathbf{E}(t) = \mathbf{E}_0 e^{-i\omega t} + \text{c.c.} \quad . \quad (26)$$

The resulting nonlinear polarization reads

$$\begin{aligned} \mathbf{P}^{(2)}(t) &= \epsilon_0 \chi^{(2)} \mathbf{E}(t)^2 \quad , \\ &= \underbrace{2\epsilon_0 \chi^{(2)} \mathbf{E}_0 \mathbf{E}_0^*}_{\text{optical rectification}} + \underbrace{\epsilon_0 \chi^{(2)} [\mathbf{E}_0^2 e^{-i2\omega t} + \text{c.c.}]}_{\text{second harmonic generation}} \quad , \end{aligned} \quad (27)$$

and consists of two parts, related to two nonlinear optical phenomena. The first part is called optical rectification (OR) and describes a DC polarization induced in the medium. The second part is called second-harmonic generation (SHG). It depicts a generated polarization that oscillates with the doubled input frequency. As the polarization represents a dipole density per unit volume, it is a source of light at the second-harmonic frequency. This is depicted in figure 5 (b). In a quantum mechanical picture, two incoming photons at the frequency ω are annihilated in the nonlinear medium and one photon at the doubled frequency 2ω is generated. Commonly, this process is sketched in an energy level diagram with virtual energy levels shown as dashed lines. The nonlinear interaction happens instantaneous and requires no populatable states.

sum- and difference-frequency generation

If the exciting electric field consists of multiple frequencies, also non-degenerate photon-photon interactions become possible

$$\mathbf{E}(t) = \mathbf{E}_1 e^{-i\omega_1 t} + \mathbf{E}_2 e^{-i\omega_2 t} + \text{c.c.} \quad . \quad (28)$$

The induced second order nonlinear polarization has multiple terms

$$\begin{aligned} \mathbf{P}^{(2)}(t) &= \epsilon_0 \chi^{(2)} [\mathbf{E}_1^2 e^{-i2\omega_1 t} + \mathbf{E}_2^2 e^{-i2\omega_2 t} + 2\mathbf{E}_1 \mathbf{E}_2 e^{-i(\omega_1 + \omega_2)} \\ &\quad + 2\mathbf{E}_1 \mathbf{E}_2^* e^{-i(\omega_1 - \omega_2)} + \text{c.c.}] + 2\epsilon_0 \chi^{(2)} [\mathbf{E}_1 \mathbf{E}_1^* + \mathbf{E}_2 \mathbf{E}_2^*] \quad , \end{aligned} \quad (29)$$

and by using an appropriate notation, these contributions can be separated by their frequencies ω_n

$$\mathbf{P}^{(2)}(t) = \sum_n \mathbf{P}^{(2)}(\omega_n) e^{-i\omega_n t} \quad . \quad (30)$$

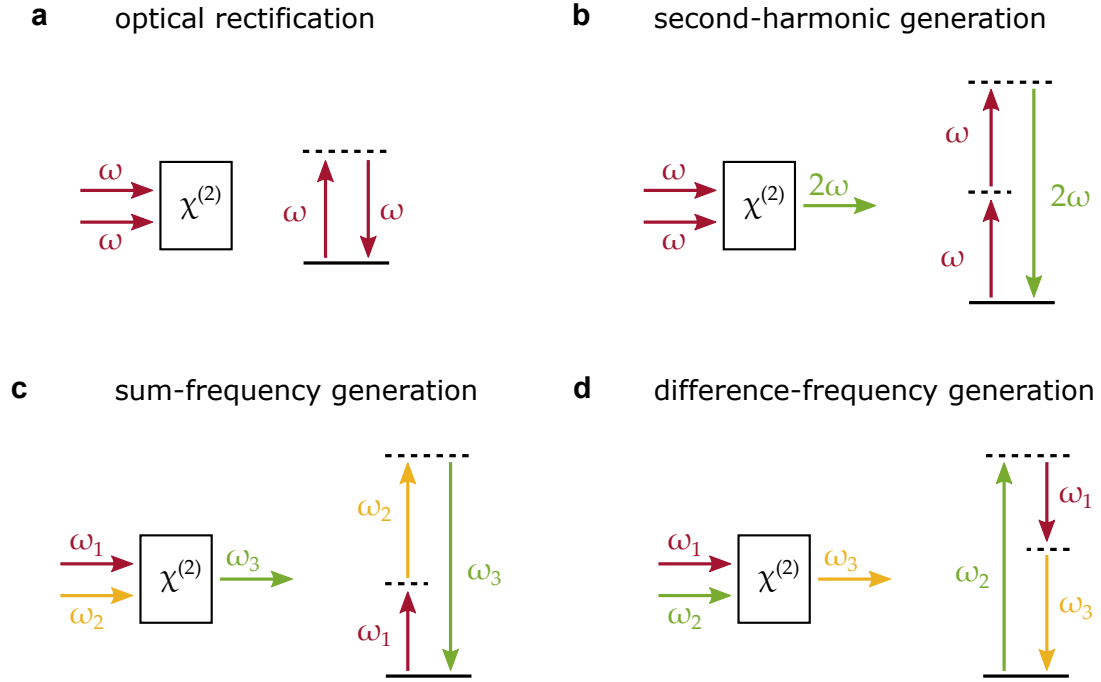


Figure 5: Second order nonlinear optical processes. (a) optical rectification, (b) second-harmonic generation, (c) sum-frequency generation and (d) difference-frequency generation. The left side of each panel depicts the in- and outgoing electric fields while the right side shows energy level diagrams. Solid lines mark real, populatable states while dashed lines indicate virtual states.

The index n runs over positive and negative frequencies. The resulting frequency dependent amplitudes $\mathbf{P}^{(2)}(\omega_n)$ are given by

$$\mathbf{P}^{(2)}(0) = 2\epsilon_0\chi^{(2)}[\mathbf{E}_1\mathbf{E}_1^* + \mathbf{E}_2\mathbf{E}_2^*] \quad (\text{OR}) \quad , \quad (31)$$

$$\mathbf{P}^{(2)}(2\omega_1) = \epsilon_0\chi^{(2)}\mathbf{E}_1^2 \quad (\text{SHG}) \quad , \quad (32)$$

$$\mathbf{P}^{(2)}(2\omega_2) = \epsilon_0\chi^{(2)}\mathbf{E}_2^2 \quad (\text{SHG}) \quad , \quad (33)$$

$$\mathbf{P}^{(2)}(\omega_1 + \omega_2) = 2\epsilon_0\chi^{(2)}\mathbf{E}_1\mathbf{E}_2 \quad (\text{SFG}) \quad , \quad (34)$$

$$\mathbf{P}^{(2)}(\omega_1 - \omega_2) = 2\epsilon_0\chi^{(2)}\mathbf{E}_1\mathbf{E}_2^* \quad (\text{DFG}) \quad . \quad (35)$$

The first contribution, at the frequency zero, is optical rectification by both excitation fields while the two following contributions are second-harmonic generation at each frequency. The last two contributions are new phenomena called sum- and difference-frequency generation (SFG, DFG). Here, the generated photons have the sum- or difference-frequency of the input photons. These two effects are sketched in figure 5 (c)-(d). In general, SFG is the non-degenerate case of SHG.

DFG, on the other hand, has a fundamental difference. Here, not two input photons are annihilated to create a new one. Although two input photons are present, only the higher frequency photon is annihilated and two photons are created. One at the difference frequency and one at the lower input frequency. Therefore, the lower frequency input field is amplified and gives this physical effect the additional name optical parametric amplification.

2.4.2 Third Order Nonlinear Effects

The next higher order of nonlinear effects are $\chi^{(3)}$ -nonlinearities. Again, we consider a monochromatic electric field

$$\mathbf{E}(t) = \mathbf{E}_0 e^{-i\omega t} + \text{c.c.} , \quad (36)$$

which leads to a third order nonlinear polarization of the form

$$\begin{aligned} \mathbf{P}^{(3)}(t) &= \epsilon_0 \chi^{(3)} \mathbf{E}(t)^3 , \\ &= \underbrace{\epsilon_0 \chi^{(3)} [\mathbf{E}_0^3 e^{-i3\omega t} + \text{c.c.}]}_{\text{third harmonic generation}} + \underbrace{3\epsilon_0 \chi^{(3)} [|\mathbf{E}_0| \mathbf{E}_0 e^{-i\omega t} + \text{c.c.}]}_{\text{nonlinear refractive index}} . \end{aligned} \quad (37)$$

In the nonlinear polarization two terms can be identified. First, we observe third-harmonic generation (THG). This effect is similar to SHG with the only difference that three input photons are annihilated in order to create a new one. Consequently, the output photon has the tripled frequency. Second, we see a term that oscillates with the frequency ω . It can be shown, that this term leads to a nonlinear, intensity dependent contribution to the refractive index

$$n = n_0 + n_2 \langle \mathbf{E}(t)^2 \rangle , \quad (38)$$

with the linear refractive index n_0 and the additional contribution n_2 . This small change in the refractive index is also referred to as second-order index of refraction. The angular brackets indicate a time average of the electric field $\langle \mathbf{E}(t)^2 \rangle = 2\mathbf{E}_0 \mathbf{E}_0^*$. With the refractive index being complex, this does not only lead to an intensity dependent dispersion by the real part of n_2 but also to an intensity dependent absorption by the imaginary part [56]. This new absorption mechanism is called two-photon absorption (TPA). If the energy of two photons is large enough, they can be simultaneously absorbed with a virtual state in between [57]. This allows the population of excited states as sketched in figure 6 (b). Although the process of two-photon absorption looks similar to SHG, it is in fact a $\chi^{(3)}$ process. A more detailed description of linear and nonlinear absorption is given in the appendix A.1.

2.4.3 Symmetry Considerations and Conservation Laws

For the conclusion of this chapter, we want to point out two important aspects we haven't treated yet, but which play a fundamental role in nonlinear optics. First, the symmetry of the nonlinear material itself can have a great influence on the nonlinear response and second, also fundamental conservation laws, like energy and momentum conservation, have to be fulfilled.

Symmetry

The susceptibility $\chi^{(n)}$ represents the response function of a material to an applied electric field. Therefore, it also reflects given symmetries of the material. There are complete tables of the shape of the susceptibility tensor for many different symmetry groups [58].

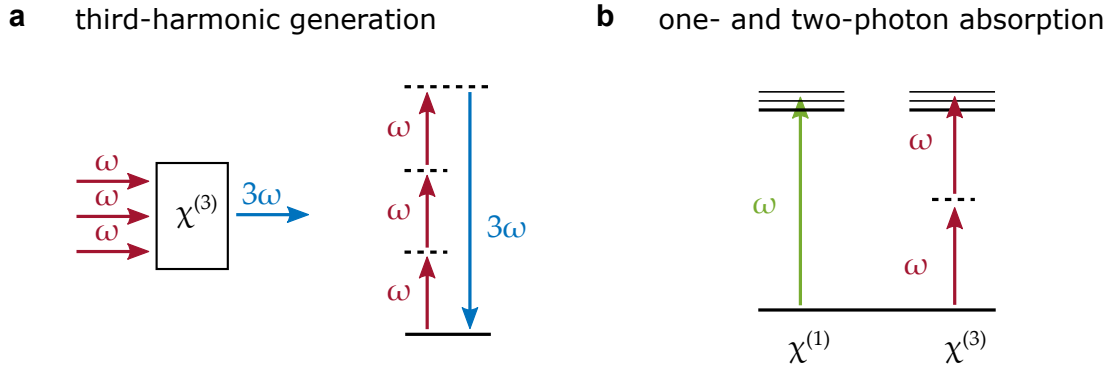


Figure 6: Third-order nonlinear effects. (a) Analogous to SHG, three photons can be annihilated in order to create one with triple frequency. (b) Like in linear optics, it is possible to perform optical transitions with two incoming photons. For two-photon absorption, the mid-state doesn't have to be a real state. Although only two photons are involved in the absorption process, it is in fact a third order nonlinear effect.

Here, we will only treat the case of inversion symmetry, as it has an important consequence for even-order nonlinear phenomena. In order to describe space inversion we use

$$\mathbf{r} \rightarrow -\mathbf{r} \quad , \quad (39)$$

$$\mathbf{E}(t) \rightarrow -\mathbf{E}(t) \quad , \quad (40)$$

$$\mathbf{P}(t) \rightarrow -\mathbf{P}(t) \quad . \quad (41)$$

Applying these replacements to equation 25 yields

$$-\mathbf{P}(t) = -\epsilon_0\chi^{(1)}\mathbf{E}(t) + \epsilon_0\chi^{(2)}\mathbf{E}(t)^2 - \epsilon_0\chi^{(3)}\mathbf{E}(t)^3 + \dots \quad , \quad (42)$$

Comparing this result to equation 25 requires $\chi^{(2n)} = 0$ for $n \in \mathbb{N}$. Consequently, all even-order nonlinear susceptibilities have to be zero in an inversion symmetric material and the related nonlinear optical processes are forbidden. This consequence only holds as long as one remains in a description of matter that restricts to electric dipoles. Already the inclusion of magnetic dipole transitions can allow nonlinear phenomena in an inversion symmetric material [59, 60]. This is a consequence of the magnetic field being an axial vector. In contrast to the electric field (equation 40), the magnetic field transforms as $\mathbf{B} \rightarrow +\mathbf{B}$ and consequently breaks the inversion symmetry.

Conservation Laws

For all observed nonlinear optical interactions, energy and momentum conservation have to be fulfilled. We express both in a general form

$$\hbar \sum_i \omega_i = 0 \quad , \quad (43)$$

$$\hbar \sum_i \mathbf{k}_i = 0 \quad . \quad (44)$$

During our derivation and description of nonlinear phenomena, energy conservation has always been fulfilled. Momentum conservation, on the other hand, hasn't been accounted for yet. If we use the dispersion relation of light, we can rewrite equation 44 and get the condition

$$\hbar \sum_i \frac{\omega_i n(\omega_i)}{c_0} = 0 \quad . \quad (45)$$

In order to fulfill equations 43 and 45 simultaneously, the index of refraction has to be the same for all involved frequencies, i.e., $n(\omega_i) = \text{const}$. This is hard to achieve because naturally the refractive index is wavelength dependent. This, combined with the fact that the material also has to offer a large nonlinearity, requires special workarounds. One can, for example, make use of birefringent materials where the refractive index of the extra-ordinary ray can be tuned via the angle incorporated with the optical axis [61]. In the last years also more complex concepts like quasi-phase matching became state of the art. Here, a material parameter is periodically varied in order to compensate a phase mismatch [62]. If phase matching cannot be fully achieved, an additional vector Δk is added to the momentum conservation

$$\hbar \sum_i \mathbf{k}_i + \Delta \mathbf{k} = 0 \quad , \quad (46)$$

and accounts for the phase mismatch. It leads to a drastically decreased overall efficiency of the nonlinear process. Moreover, a phase mismatch leads to an oscillation of energy between all involved fields during propagation in a nonlinear medium, that can be characterized by a coherence length [63]

$$l_{\text{coh}} = \frac{\pi}{\Delta k} \quad . \quad (47)$$

NUMERICAL METHODS

An important key in research is the modeling and simulation of experimentally observed effects, or vice versa designing experiments based on simulations. In general, analytical solutions cannot be obtained for complex systems or only under rigorous assumptions and idealizations. Therefore, numerical methods, which search an approximated solution, play an important role in modern physics. As nanoobjects build the bridge between the atomic and the macroscopic scale, the requirements on the numerical methods are not clear *ab initio*. For systems like quantum dots or nanocrystals, a quantum mechanical treatment is necessary, like also for small interparticle distances that allow electron tunneling effects. For structures ≥ 10 nm those effects can be neglected and a continuum description of the matter is applicable. This is the regime where our work is based in.

The task for a tool in computational electromagnetics (CEM) is to discretize Maxwell's equations on the geometry of a given problem and subsequently obtaining a numerical solution. There are three common methods [64]: the Finite-Difference-Time-Domain method (FDTD), the Method of Moments (MoM) and the Finite Element Method (FEM). Those methods differ in the way the systems geometry is discretized (meshed), the formulation that is chosen for Maxwell's equations (integral or differential), the domain the equations are solved in (time- or frequency domain) and last, the numerical effort. Depending on the individual needs, the most suited method can be chosen. In this chapter we focus on FEM, as it is most suited for our purposes, outline the basic principle of the method based on [65] and present models that are used throughout following chapters. This includes 2 dimensional models for waveguiding applications of infinitely extended plasmonic waveguides as well as 3 dimensional models that numerically calculate near and far field properties of resonant, subwavelength nanoparticles.

3.1 THE FINITE ELEMENT METHOD

In order to describe the basic principle of FEM we assume a domain Ω where the governing differential equation is given by

$$\mathcal{L}\phi = f, \quad (48)$$

where \mathcal{L} is a differential operator, ϕ the unknown quantity and f the excitation function - in CEM for example an exciting electric field. There are two common approaches to solve the problem numerically. The Ritz principle and the Galerkin-Method [66–68]. We present the later, which is a weighted residual method. Here, an approximated solution

$\tilde{\phi}$ is assumed that leads to a non-vanishing residuum r and equation 48 is reformulated as

$$r = \mathcal{L}\tilde{\phi} - f \neq 0 \quad . \quad (49)$$

The idea is to find an approximated solution that minimizes the residuum. Therefore, the key is to disassemble the domain Ω into e subdomains Ω^e , the so called finite elements

$$\Omega = \bigcup_{e=1}^M \Omega^e \quad . \quad (50)$$

The way the finite elements can be formed gives FEM two big advantages which make it very well suited for plasmonic applications. First, arbitrary shapes can be chosen for the elements, ranging in 3D from cubes over prisms to tetrahedral forms - even a combination of different elemental shapes is possible. This allows a close-to-reality representation of arbitrary curved surfaces which benefits interface effects like plasmonic excitations. Second, each element is independent in size and edge lengths. Therefore, big systems involving small details, e.g. rounded edges, can be meshed without loss of structural information while still keeping reasonable computation times.

Each finite element contains n nodes which are the corner points. Now, on each finite element e a weighted residual integral R_i^e , based on equation 49, is formulated

$$R_i^e = \int_{\Omega^e} w_i^e (\mathcal{L}\tilde{\phi}_i^e - f) d\Omega \quad \text{with } i = 1 \dots n \quad , \quad (51)$$

with the weighting function w_i^e . The approximated solution $\tilde{\phi}_j^e$ on the element is described as sum

$$\tilde{\phi}_j^e = \sum_{j=1}^n N_j^e \phi_j^e \quad , \quad (52)$$

where ϕ_j^e is the value of ϕ at the j -th node and N_j^e the interpolation function. N_j^e is also referred to as expansion or basis function and chosen as polynomial of first or higher order. Moreover, N_j^e are also only non-zero within the e -th element. Usually, the interpolation functions are also used as weighting functions in equation 50. Now, equations 51 and 52 are combined. By taking all finite elements into account, a global system of equations in matrix form is obtained. It has to be mentioned that the transition from the local finite elements to a global system is not trivial since neighboring elements share nodes with each other. The result is formulated as

$$[K]\{\phi\} = \{b\} \quad , \quad (53)$$

where $[\cdot]$ marks a matrix and $\{\cdot\}$ a vector. $\{b\}$ is related to the excitation function. In the sense of CEM, equation 53 describes a system that involves scattering or radiation. The matrix $[K]$ is the sparse matrix of the system. Due to the fact that the basis functions N_j^e are only non-zero within their corresponding element, the matrix is nearly of diagonal shape and only features few off-diagonal elements. If the system is free of sources or excitations, i.e. $\{b\}$ vanishes, equation 53 can be rewritten as

$$[A]\{\phi\} = \lambda[B]\{\phi\} \quad , \quad (54)$$

with $[K] = [A] + \lambda[B]$ which has the form of an eigenvalue equation with the eigenvalues λ . In CEM, this formulation corresponds to, e.g., waveguide modes or resonances in cavities.

Here, we will discuss examples for both cases - numerical models based on equation 53 and 54. In our case this corresponds to a 3D scattering model of plasmonic nanoparticles and a 2D mode analysis in plasmonic waveguides. As software we use the commercial FEM solver Comsol Multiphysics with the wave optics module. All calculations are based in the frequency domain. Therefore, first a time harmonic ansatz for the electric field is chosen

$$\mathbf{E}(\mathbf{r}, t) = \mathbf{E}(\mathbf{r})e^{i\omega t} . \quad (55)$$

The governing differential equation for both - 2D and 3D system - is in general given by the vector wave equation of the electric field. The equation can be derived from Maxwell's equations (equations 1-4). After including the time harmonic ansatz from equation 56, the wave equation reads

$$\nabla \times \mu_r(\mathbf{r}, \omega)^{-1} (\nabla \times \mathbf{E}(\mathbf{r}, \omega)) - \frac{\omega^2}{c_0^2} \left(\epsilon_r(\mathbf{r}, \omega) - i \frac{\sigma(\mathbf{r}, \omega)}{\omega \epsilon_0} \right) \mathbf{E}(\mathbf{r}, \omega) = 0 . \quad (56)$$

with the frequency and position dependent relative permeability μ_r , relative permittivity ϵ_r and conductivity σ . Due to the separation ansatz (equation 55), the wavelength dependency of the system can be obtained by consecutively solving equation 56.

3.2 SCATTERING AND ABSORPTION IN ISOLATED NANOPARTICLES

The biggest challenge for 3D scattering or radiation calculations of single nanoparticles are the boundary conditions. By nature the problems have open boundaries with an infinite free space as surrounding medium. Therefore, the way the domain is truncated is of great importance. Using hard boundaries like, e.g., Dirichlet or Neumann conditions can lead to backreflections of outgoing waves back into the model and cause artifacts. To circumvent this, it became common to border the domain with an artificial absorbing layer - the so called perfectly matched layer (PML) [69, 70].

In figure 7 (a) an example for a 3D scattering model is shown. The spherical domain, with a centered nanoparticle, is truncated by a PML shown in cyan. The inner radius is chosen as 700 nm and the PML thickness as 200 nm. The long axis of the nanostructure is 270 nm. The model and the nanostructure are designed for the NIR spectral region. The material properties of the nanostructure are taken from the interpolated data of Johnson and Christy [37] and the surrounding medium has a homogeneous refractive index. If the structure should be located on a substrate, e.g., glass, an effective medium approach can be used. Instead of adding the substrate to the geometry, a homogeneous environment is used with a modified refractive index - the so called effective refractive index n_{eff} . From experience $n_{\text{eff}} = 1.4$ is a good approximation for modelling a glass-air interface with a founded flat nanostructure. The PML is given the same refractive index. The yellow sphere in figure 7 (a) is a permeable layer that has no physical effect.

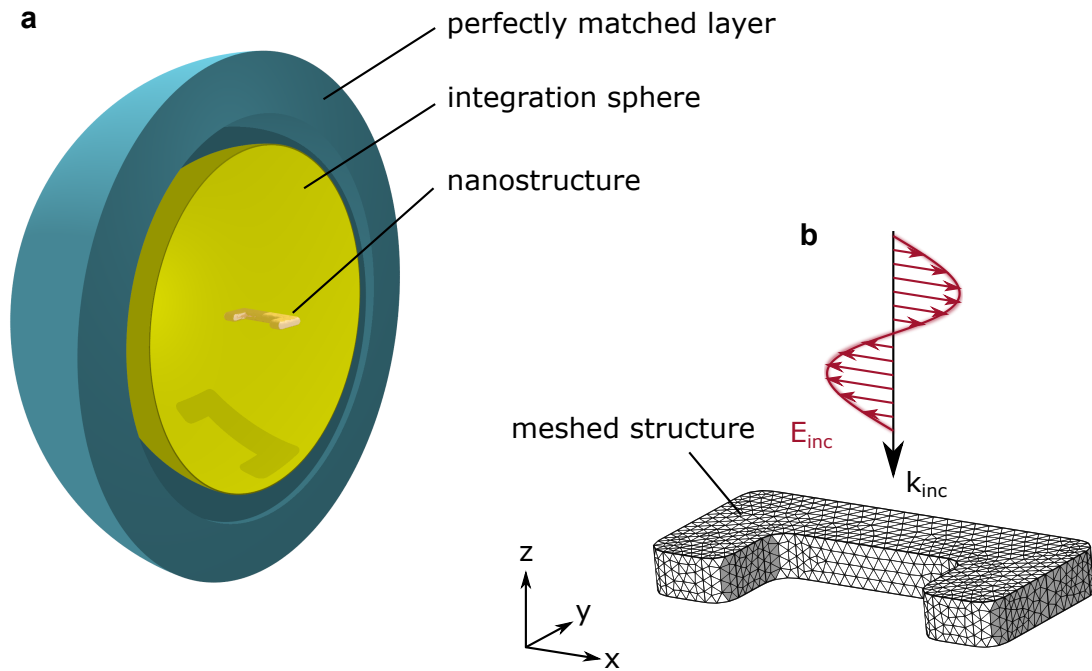


Figure 7: Example of a 3D FEM model. (a) In the center of the model the nanostructure under investigation is positioned. The whole model is truncated by the PML shown in cyan. The radius of the PML is chosen bigger than the wavelength of the exciting electromagnetic field. The yellow sphere has no physical influence and is only defined and used as integration sphere to determine scattering properties of the particle. (b) An example mesh of a nanostructure is shown. The tetrahedral mesh has an adaptive size that allows meshing of small details like, e.g., edge roundings. In the final FEM calculation the structure is excited by an electric field E_{inc} traveling in negative z -direction.

It serves as integration layer in order to determine far field scattering properties of the nanoparticle.

In figure 7 (b) an example for the nanostructures mesh is shown. It is clearly visible that the variable mesh provided by FEM, allows a detailed representation of the structure itself. While the nanoparticle has a fine mesh, it can be chosen coarser in the surrounding medium, where there is no more structural variation. The form adaptive mesh can also be seen within the particle. At corners with small radii of curvature, the mesh becomes finer while bigger elements are used for flat parts of the structure. Important to mention is, that there are also mesh restrictions for the PML. Neglecting these can lead to unphysical artifacts in the calculation. Radially outgoing, the PML should at least consist of 5 elements. Additional precautions like, e.g., a point symmetric mesh, with respect to the model center, can also lead to a more stable operation of the FEM solver. For the subsequent calculation, the total electric field \mathbf{E} is split into two parts - the incident electric field \mathbf{E}_{inc} , which represents, e.g., an exciting laser beam and the field \mathbf{E}_{scat} scattered by the nanoparticle

$$\mathbf{E}(\mathbf{r}, \omega) = \mathbf{E}_{scat}(\mathbf{r}, \omega) + \mathbf{E}_{inc}(\mathbf{r}, \omega) \quad . \quad (57)$$

As exciting electric field we use a monochromatic plane wave that travels in negative z -direction and is polarized in the $x - y$ plane. The assumption of an exciting plane

wave is reasonable, since the typical nanostructures are much smaller than the exciting wavelength. If the structures become bigger, the excitation should be switched to a Gaussian beam in case a direct comparison to an experiment has to be drawn. The monochromatic, plane wave excitation fields reads

$$\mathbf{E}_{\text{inc}}(\mathbf{r}, \omega) = \begin{pmatrix} E_{0,x} \\ E_{0,y} \\ 0 \end{pmatrix} e^{-i n_{\text{eff}} k_z z} . \quad (58)$$

3.2.1 determination of cross-sections

Characteristic values of the particle, that are determined by numerical simulations, are the wavelength dependent absorption and scattering cross-section. They image for example localized plasmon resonances (LSPR) which allows a distinct design of nanostructures for experiments. For the calculation of the cross-sections, the energy flux density $\mathbf{S}(\mathbf{r}, t)$, also called Poynting vector, is needed

$$\mathbf{S}(\mathbf{r}, t) = \mathbf{E}(\mathbf{r}, t) \times \mathbf{H}(\mathbf{r}, t) . \quad (59)$$

By including the chosen time harmonic ansatz for fields, we find for the time averaged energy flux density

$$\mathbf{S}(\mathbf{r}, \omega) = \langle \mathbf{S}(\mathbf{r}, t) \rangle = \int_0^T \mathbf{S}(\mathbf{r}, t) dt = \frac{1}{2} \text{Re} \{ \mathbf{E}(\mathbf{r}, \omega) \times \mathbf{H}^*(\mathbf{r}, \omega) \} , \quad (60)$$

which can now be defined for all involved fields - incident, scattered and total. For the excitation field the absolute value reads

$$\langle S_{\text{inc}} \rangle = \frac{1}{2} E_0^2 n_{\text{eff}} c_0 \epsilon_0 , \quad (61)$$

with the absolute value E_0 of the incident electric field. In order to obtain the scattering and absorption cross-sections we have to calculate the integral of the corresponding time averaged flux density through the integration sphere with respect to its local surface normal \mathbf{n}

$$C_{\text{abs}} = \frac{1}{\langle S_{\text{inc}} \rangle} \oint_{\text{surf}} \mathbf{S}(\mathbf{r}, \omega) \cdot \mathbf{n} dA , \quad (62)$$

$$C_{\text{scat}} = \frac{1}{\langle S_{\text{inc}} \rangle} \oint_{\text{surf}} \mathbf{S}_{\text{scat}}(\mathbf{r}, \omega) \cdot \mathbf{n} dA , \quad (63)$$

$$C_{\text{ext}} = C_{\text{abs}} + C_{\text{scat}} . \quad (64)$$

The extinction cross-section C_{ext} of the particle is then formulated as sum of absorption and scattering cross-section. For nanoparticles the extinction cross-section at the plasmon resonance can easily overcome the geometrical cross-section by orders of magnitude, while the individual contribution of scattering and absorption strongly depends on the particle's size. For sizes of few tens of nanometers or less, the absorption is the

dominant contribution [32]. With increasing particle size, scattering is not negligible anymore and finally dominates over the absorption. For example in case of a 20 nm gold sphere, the absorption is 100 times stronger than the scattering. If we consider an 80 nm sphere, the two cross-sections are already of equal strength [71].

In single particle experiments, mostly the extinction or the scattering cross-section is measured. Therefore, additional factors have to be considered. If the scattering contribution becomes significant, i.e., larger particles are considered, one has to keep in mind that forward and backward scattering are not equivalent. Consequently, it makes sense to split the integration sphere into two parts - for forward and backward direction. This is especially necessary if experiments, involving particles of arbitrary sizes on substrate interfaces, shall be theoretically explored. Here, the substrate poses a break in symmetry and strongly alters the scattering process or also the emission process of the particle [72, 73]. In these cases one also reaches a limit of the effective medium approach. While spectral positions of, e.g., plasmonic resonances and their connections to geometrical dimensions can be properly predicted, the altered scattering cannot be described. If, on the other hand, a substrate and split integration spheres are incorporated, it is also possible to match the simulation better to the experiment by taking the used objective into account. A reduced integration sphere, accounting for the numerical aperture, can be defined.

3.2.2 *field and charge distribution*

The FEM solver provides the full vectorial electric and magnetic fields within the whole model domain. Despite of the calculated cross-sections from the previous section, we also have access to field distributions on arbitrary chosen probe surfaces. This helps not only to understand the observed plasmonic resonances and classify them as first or higher order, but also allows the engineering of field distributions in more complex geometries. The applications range from rather simple hot spot engineering in dimer or bow-tie antenna configurations [74, 75] to more complex ones [76]. Moreover, the exact field distribution near plasmonic structures allows to investigate the coupling of emitters like, e.g., single molecules [77], quantum emitters [78], nanocrystals or quantum dots [79] and further gives rise to engineered plasmonic cavities in metal-insulator-metal cavities [80].

Here, we will discuss a split ring resonator (SRR) as example structure, as it will also be referred to in the subsequent chapters. The SRR has its origin in the microwave regime [81] and was used in order to create meta materials that are composed of sub-wavelength unit cells and allow the creation of media with unique optical properties [82]. Later, the idea was downsized to plasmonic structures in order to create optical meta materials [83]. Here, the SRR did not only gain popularity as component of meta materials but also the properties of the structure itself were, and still are part of present research. On one hand, the SRR can create a strong magnetic moment which makes it suitable as antenna for magnetic emitters [84], while, on the other hand, it also offers a broken symmetry, which makes it interesting for nonlinear plasmonics [85]. We will be

interested in the later.

In figure 8 results of a FEM simulation for a SRR are shown. The structure has a base length of 270 nm, an arm length of 120 nm and a height of 30 nm. The width was in both cases chosen as 60 nm and the radius for the edge rounding as 15 nm. In the model, a substrate was included via the effective medium approach with an effective refractive index of $n_{\text{eff}} = 1.4$. In figure 8 (a) and (b), the wavelength dependent extinction cross-sections for the SRR are shown for two different excitation polarizations - parallel and perpendicular to the base of the structure, as indicated by the inset in the plots. For parallel excitation we observe a fundamental, i.e., first order, resonance at about 1750 nm. This equals the resonance that produces a large magnetic moment [84]. For smaller wavelengths, we get higher order modes that are not discussed further. Under perpendicular excitation (figure 8 (b)), the observed resonances are, concerning the order of the resonance, blue shifted and noticeably weaker than for parallel excitation. The first order perpendicular resonance is located at 900 nm and a factor of 2.5 smaller in magnitude. Here, we are likewise also not discussing higher order modes. In figure 8 (c) and (d), the electric field distributions are shown for the parallel and perpendicular excited first order mode. The field distributions are shown in a cut plane, centered in z-direction in the middle of the structure (see figure 7). For visualization only the real part of the electric fields are plotted. The shape and sign of the fields allow to phenomenologically draw charges inside the SRR and identify them as lowest order plasmonic modes [86]. The modes under parallel (c) and perpendicular (d) excitation correspond to dipolar modes along the system's long and short axis.

In general, the electric fields near the structure are very strong, which is typical for plasmonic nanostructures. Further observation shows, that the strong electric fields especially exist in the arms of the SRR. The investigated design of the SRR, i.e., ratio of base to arm length, is optimized for applications in the field of nonlinear plasmonics - as we shall see later. If, on the other hand, the structure is intended to generate strong magnetic moments or highly localized hot spots, this ratio has to be chosen different. Longer arms and a shorter base lead to a smaller gap and, therefore, the desired effect [87]. Another approach is to use a partly closed gap, where the design resembles a quadratic ring with a small cut through one edge, as originally proposed [83].

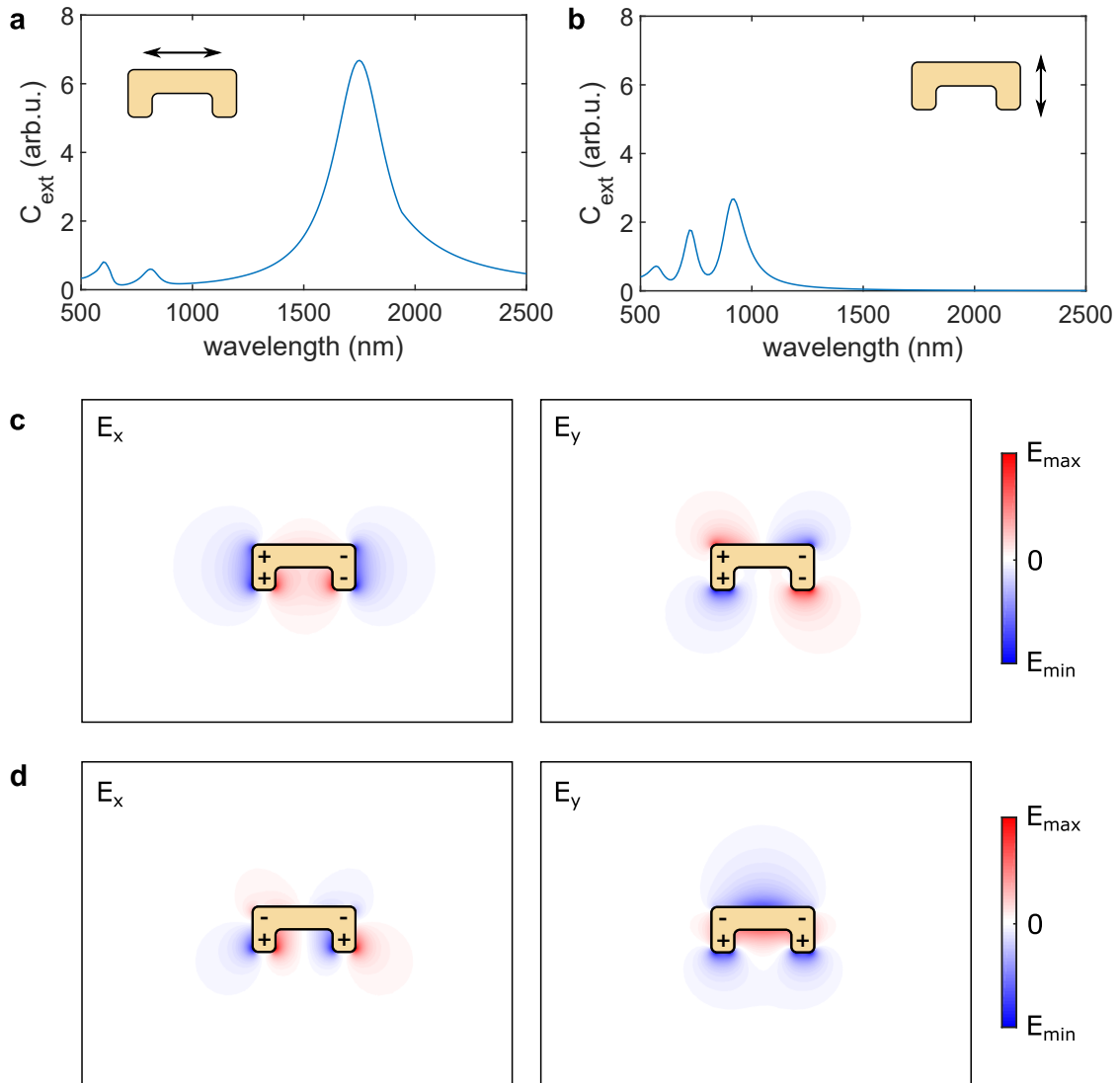


Figure 8: FEM simulations of a plasmonic SRR. The calculated, wavelength dependent extinction cross-sections for parallel (a) and perpendicular (b) excitation polarization show the fundamental, as well as higher order modes. In the inset, the corresponding excitation polarizations are indicated. The electric in-plane field distributions, at both fundamental resonances, are depicted in (c) for parallel and in (d) for perpendicular excitation. The left panels show the x-component of the electric field and the right ones the y-component. For visualization only the real part of the electric field is plotted.

3.3 PLASMONIC WAVEGUIDES

The second CEM field we are interested in, are plasmonic waveguides. As semiconductor based circuits are nowadays reaching their fundamental speed and bandwidth limits, plasmonic waveguide based circuits become of great interest. While maintaining localizations far below the diffraction limit of light [88], the obtained speed remains still near the speed of light. Various types of plasmonic waveguides have been exploited, ranging from gap waveguides [89, 90] to wire-like ones with different cross-sections [91, 92]. Also more complex applications have been under research, like waveguide ring-resonators [93] or nano-focusing geometries [47]. The plasmonic waveguide we are interested in, is the so called two-wire transmission line (TWTL). It consists of two parallel, coupled wires [94]. Under optimized geometry, this structure supports only two different plasmonic modes - a symmetric and an anti-symmetric one.

For the theoretical investigation of the TWTL we use 2D FEM simulations - under the assumption of an infinitely extended waveguide which geometrical cross-section does not change. After rewriting the systems governing equation 56 as

$$\begin{aligned} \nabla \times \nabla \times \mathbf{E}(\mathbf{r}, \omega) - \Lambda \mathbf{E}(\mathbf{r}, \omega) &= 0 \quad , \\ \text{with } \Lambda &= k_0^2 \left(\epsilon_r(\mathbf{r}, \omega) - i \frac{\sigma(\mathbf{r}, \omega)}{\omega \epsilon_0} \right) \quad , \end{aligned} \quad (65)$$

it can be clearly identified as eigenvalue equation with the eigenvalue Λ . For the given representation the assumption $\mu_r = 1$ was made. The model we used is defined according to figure 9. In panel (a) the, in z-direction infinitely extended, TWTL is shown and an x-y cut plane is indicated. Hence, it is convenient to express the electric field in the waveguide as

$$\mathbf{E}(\mathbf{r}, \omega) = \mathbf{E}(x, y, \omega) e^{-i n_{\text{eff}} k_0 z} \quad , \quad (66)$$

where n_{eff} denotes the effective mode index and $k_0 = \frac{\omega}{c_0}$ the vacuum wave vector for the desired frequency of light. The factor $\mathbf{E}(x, y, \omega)$ describes the profile of the localized mode and the second factor the propagation in z-direction. n_{eff} is in general complex and can be regarded as factor, that describes the deviation from the propagation of a plane wave in vacuum. The real part gives the refractive index of the mode while the imaginary part is linked to the propagation length. Figure 9 (b) shows the model that is defined in Comsol. The two wires have a width of 140 nm and a height of 60 nm. The gap was chosen as 100 nm and an edge rounding of 25 nm was assumed to circumvent unrealistic field excesses at the corners. The size of the quadratic surrounding in figure 9 (b) is not true to scale and was chosen as 9.1 μm . This huge difference in size is again only possible because of the scalable mesh elements provided by FEM. In the TWTL the mesh elements have sizes between 0.5 nm and 3 nm, while the elements in the surrounding are allowed to have sizes of up to 150 nm. For neighbouring elements a certain growth rate can be defined. Consequently, the mesh in the structure, at the interface as well as in the adjacent surrounding is very fine - which is also the region where the plasmonic mode is localized at. In a greater distance from the actual structure and the bound mode, the elements get larger. An example section of the mesh is shown in the inset of the figure. Since we are looking for bound modes in the rather small center of the model, the boundary condition at the outer model domain is simple - the

electric field shall be zero. One way to achieve this easily is to use the predefined perfect electric conductor (PEC) boundary condition

$$(\mathbf{n} \times \mathbf{E}(\mathbf{r}, \omega))|_{\text{boundary}} = 0, \quad (67)$$

where \mathbf{n} denotes the local normal vector of the boundary. Of course this does not necessarily require the electric field to be zero in all components but, combined with additional restrictions, only physical reasonable results are obtained. Here, unreasonable results would be waveguide modes engaging the complete surrounding medium, i.e., using the domain borders as resonator. To exclude such modes from the calculation one can, for example, specify a desired region for the effective mode index. The wanted modes have an index higher than the one of the surrounding medium, while environment engaging modes have a lower one. Moreover, also the imaginary part of the mode index can be used for sorting of modes. The plasmonic modes are bound to the gold surface which leads to increased damping, while the environmental modes are predominantly located in the surrounding (here $n_{\text{air}} = 1.0002$), which is assumed to be lossless.

The FEM mode analysis yields two different plasmonic modes in the vis-NIR spectral region. In figure 9 (c), the mode profiles are shown. In the absolute value of the electric field, the fundamental difference between the two modes is visible. The first one has a localized field in the gap and an anti-symmetric charge distribution, while the second one has localized fields at the outer edges of the TWTL, a field minimum between the two wires and a symmetric charge distribution. In literature, the anti-symmetric mode is also referred to as gap-mode [77, 78]. In figure 9 (d), characteristic values of the modes, besides the profile, are shown. Each mode has its own panel. In blue the real part of the effective mode index n_{eff} is shown and in orange the propagation length for different wavelengths. For both modes the spectral trend is the same. With increasing wavelength, the mode index decreases while longer propagation lengths are obtained. In the visible regime only short propagation lengths, even below $10 \mu\text{m}$, are obtained. This is due to the interband absorptions in gold, that are spectrally located at 520 nm and 650 nm (see chapter 2.2). Consequently, gold as material for the TWTL is only suited for applications in the NIR regime. For visible experiments it is strongly recommended to switch to silver as plasmonic material, as it offers long propagation length even down to 500 nm [78]. An important fact to mention, is the difference in propagation length between the two modes. In the NIR region, the symmetric mode offers propagation lengths that are about as twice as big as the ones for the anti-symmetric mode. Qualitatively this can be understood by taking a look at the mode profiles again. The field in the gap of the TWTL is stronger localized than the field at the outer edge. In plasmonics, it is typical that one experiences a trade off between localization and damping [48]. If higher localization is achieved, it comes with the cost of increased damping.

In the following chapters, we are only interested in the symmetry of the TWTL modes. Therefore, it is convenient to restrict to a homogeneous environment in the simulations. The addition of a substrate will not alter the symmetry of the modes but only affect the mode profile, magnitude of the mode index and total propagation length. However, all discussed trends will remain the same. For completeness, the mode profile for all electric field components E_x , E_y and E_z and also a comparison to a TWTL with added substrate, is given in the appendix A.2.

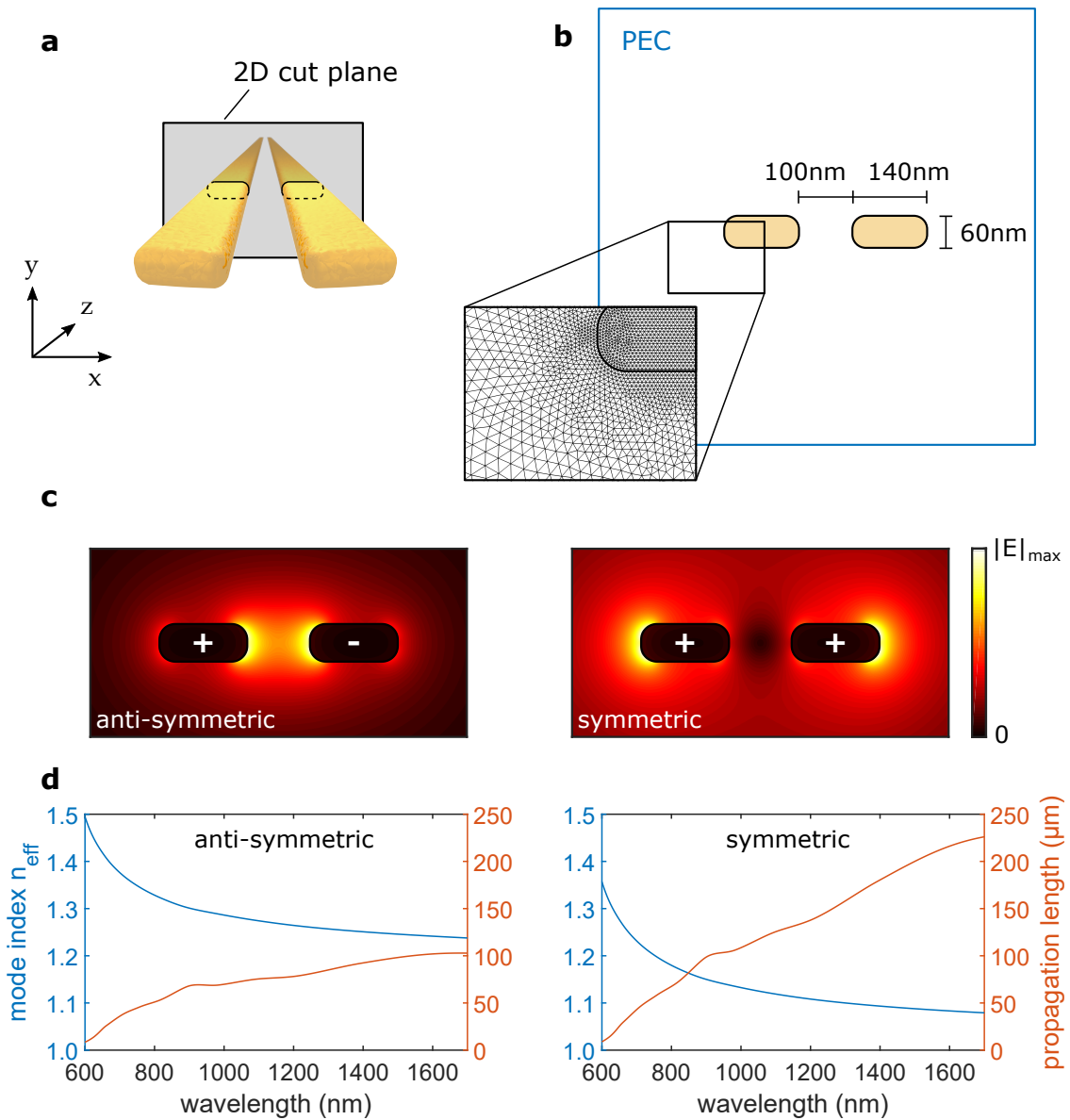


Figure 9: (a) 3D view of a TWTL. The used coordinate system as well as the 2D cut plane for numerical analysis of the waveguide are indicated. (b) Defined model for FEM simulations. The optical properties of gold are taken from Johnson and Christy and the surrounding medium was chosen as air (lossless). The model is bordered by a perfect electric conductor (PEC) and not drawn true to size. The inset shows an example for the used mesh. (c) Supported modes by the TWTL. In the vis-NIR regime two modes are obtained by the FEM mode analysis. The absolute value of the electric field is shown and charges are indicated. The two modes differ in real part of the complex mode index n_{eff} and the propagation length which is shown in (d).

SECOND-HARMONIC GENERATION IN PLASMONIC STRUCTURES

In standard literature about nonlinear optics [55], it is stated that second-harmonic generation (SHG) is forbidden in centro- or inversion symmetric materials. The corresponding derivation was given in chapter 2.4.3. As the most common plasmonic materials, like gold, silver or aluminum exhibit this symmetry, SHG or more general even-order harmonic generation shouldn't play a role. Nevertheless, SHG has been observed from, e.g., metallic films [95–97] and also been theoretically investigated [98–100]. The common derivation, that requires a vanishing even-order nonlinear susceptibility in inversion symmetric materials, is limited to a purely electric dipolar description as well as an infinitely extended homogeneous medium. If the multipole description of the material is expanded beyond electric dipoles \mathbf{p}_ω , i.e., magnetic dipoles \mathbf{m}_ω and electric quadrupoles $Q_{\omega,jk}$ as next higher order

$$\mathbf{p}_\omega = \int \mathbf{P}_\omega(\mathbf{r}) d\mathbf{r} \quad , \quad (68)$$

$$\mathbf{m}_\omega = -i\frac{\omega}{2} \int \mathbf{r} \times \mathbf{P}_\omega(\mathbf{r}) d\mathbf{r} \quad , \quad (69)$$

$$Q_{\omega,jk} = \int [3(r_j P_{\omega,k} + r_k P_{\omega,j}) - 2\delta_{jk} \mathbf{r} \cdot \mathbf{P}_\omega(\mathbf{r})] d\mathbf{r} \quad , \quad (70)$$

even-order nonlinear effects become allowed. Despite of higher order multipole corrections from bulk material, SHG is also allowed at the surface of inversion symmetric materials. In the surface layer, consisting of only a few atoms, this symmetry is obviously broken. Here, we have to take two aspects into account [100]. First, the structural discontinuity, which leads to local, i.e., dipole allowed SHG. Second, the discontinuity of fields, that causes a nonlocal, quadrupole-type contribution to the surface SHG. It has been shown, that both contributions can be represented effectively by a local, dipole allowed nonlinear susceptibility tensor $\chi_s^{(2)}$ [100].

Concluded, SHG from a finite metal structure can be described by a nonlinear surface $\mathbf{P}_s^{(2)}$ and a nonlinear bulk polarization $\mathbf{P}_b^{(2)}$ [101]

$$\mathbf{P}_s^{(2)}(\mathbf{r}) = \epsilon_0 \chi_s^{(2)} \mathbf{E}(\mathbf{r}) \mathbf{E}(\mathbf{r}) \delta(\mathbf{r} - \mathbf{r}_s) \quad , \quad (71)$$

$$\begin{aligned} \mathbf{P}_{b,i}^{(2)}(\mathbf{r}) = & \gamma \nabla_i [\mathbf{E}(\mathbf{r}) \cdot \mathbf{E}(\mathbf{r})] + \delta' [\mathbf{E}(\mathbf{r}) \cdot \nabla] E_i(\mathbf{r}) \\ & + \beta E_i(\mathbf{r}) [\nabla \cdot \mathbf{E}(\mathbf{r})] + \zeta E_i(\mathbf{r}) \nabla_i E_i(\mathbf{r}) \quad , \end{aligned} \quad (72)$$

where γ , δ' , β and ζ represent material parameters. Often, one or more terms in $\mathbf{P}_b^{(2)}$ can be set zero or are negligible [101, 102]. In general, it has been demonstrated, that for

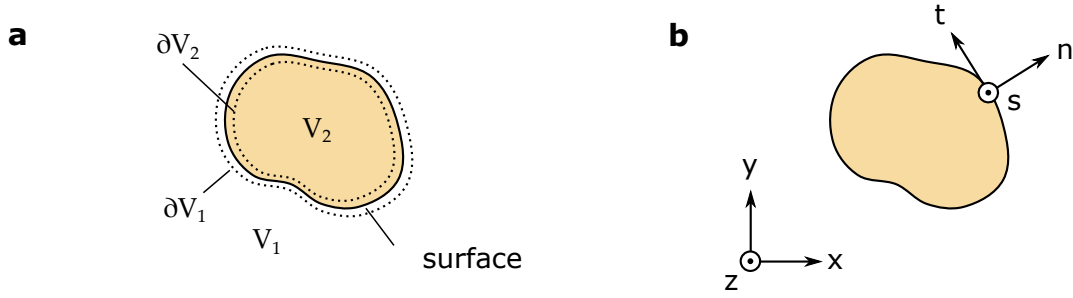


Figure 10: Definition of the geometry. (a) The plasmonic (indicated by golden face color) structure with volume V_2 is located in a homogeneous medium V_1 . The paths $\partial V_{1/2}$ run along the surface S in the corresponding volume ($V_{1/2}$) with an infinitesimal distance from S . (b) For the given model two coordinate systems are defined. (x, y, z) represents the global system, while (t, n, s) describes a local system to the surface S .

noble metals the surface nonlinearity dominates over the bulk nonlinearity by an order magnitude or more [102, 103]. Especially in plasmonics, where the small structures benefit the surface to volume ratio, it is sufficient to only consider the surface nonlinearity. Therefore, we restrict in the following to a surface nonlinearity solely in order to describe SHG by gold nanoparticles and structures.

4.1 SECOND-HARMONIC EMISSION FROM NANOPARTICLES

In order to calculate the SHG from plasmonic structures we assume an incident electric field $\mathbf{E}(\omega)$ on an arbitrarily shaped metallic volume V_2 (see figure 10). The surface S of the structure is assumed to be piece wise smooth. An important approximation for the calculation is the so called non-depleted pump approximation that states, once generated, the second-harmonic fields do not couple back to the fundamental fields. In consequence, the problem becomes linear at both involved frequencies, ω and 2ω , and can be solved stepwise. In the first step, the linear response of the system to the exciting electric field is determined. In our case this is achieved by FEM simulations presented in the previous chapter. In the second step, the second order nonlinear polarization $\mathbf{P}_S^{(2)}$ at the surface is calculated from the obtained linear field distribution. Finally, the second-harmonic emission of the nanostructure can be determined from $\mathbf{P}_S^{(2)}$ as it acts as source for the second-harmonic fields.

4.1.1 calculation of the nonlinear polarization

We assume that the linear response of the system has already been calculated and the full vectorial, complex electric field $\mathbf{E}(\mathbf{r}, \omega)$ is known. Now, the second order nonlinear polarization is calculated via

$$\mathbf{P}_i^{(2)}(2\omega) = \epsilon_0 \sum_{j,k} \chi_{ijk}^{(2)} E_j E_k \quad , \quad (73)$$

where the indices i, j, k run over the spatial directions. Moreover, the index S referring to the surface is dropped since we are restricting the calculation only to the surface. For the calculation it is crucial to take the tensorial character of $\chi_{ijk}^{(2)}$, a third-rank tensor containing 27 elements, into account. In a general global coordinate system (x, y, z) , this is a challenging task as an arbitrary shaped volume combined with an anisotropic tensor will lead to complex expressions. But if we move locally to the surface, we can assume local isotropy, i.e., a local $C_{\infty v}$ symmetry. This leads to only seven non-vanishing elements in the local nonlinear susceptibility of which only three are independent. Consequently, an evaluation of $\mathbf{P}^{(2)}(2\omega)$ in a local surface coordinate system is beneficial. In order to move from the global system to the local one $(x, y, z) \rightarrow (t, n, s)$ (see figure 10 (b)), we use the rotation matrix D consisting of the local $\{\hat{t}, \hat{n}, \hat{s}\}$ and global $\{\hat{x}, \hat{y}, \hat{z}\}$ unit vectors. This leads to local electric fields described by

$$\begin{aligned} \begin{pmatrix} E_t \\ E_n \\ E_s \end{pmatrix} &= D \begin{pmatrix} E_x \\ E_y \\ E_z \end{pmatrix} = \begin{pmatrix} \hat{t} \cdot \hat{x} & \hat{t} \cdot \hat{y} & \hat{t} \cdot \hat{z} \\ \hat{n} \cdot \hat{x} & \hat{n} \cdot \hat{y} & \hat{n} \cdot \hat{z} \\ \hat{s} \cdot \hat{x} & \hat{s} \cdot \hat{y} & \hat{s} \cdot \hat{z} \end{pmatrix} \begin{pmatrix} E_x \\ E_y \\ E_z \end{pmatrix} \\ &= \begin{pmatrix} t_x & t_y & t_z \\ n_x & n_y & n_z \\ s_x & s_y & s_z \end{pmatrix} \begin{pmatrix} E_x \\ E_y \\ E_z \end{pmatrix} . \end{aligned} \quad (74)$$

Using equation 73, the nonlinear polarization can now be calculated with $i, j, k \in \{t, n, s\}$. The non-vanishing components of the nonlinear susceptibility are [103]

$$\chi_1^{(2)} \equiv \chi_{nnn}^{(2)} , \quad (75)$$

$$\chi_2^{(2)} \equiv \chi_{nss}^{(2)} = \chi_{ntt}^{(2)} , \quad (76)$$

$$\chi_3^{(2)} \equiv \chi_{ssn}^{(2)} = \chi_{sns}^{(2)} = \chi_{ttn}^{(2)} = \chi_{tnt}^{(2)} , \quad (77)$$

and are known to have different relative magnitudes $\chi_1^{(2)} = 250 \chi_2^{(2)}$, $\chi_3^{(2)} = 3.6 \chi_2^{(2)}$ [102]. This shows that especially the $\chi_{nnn}^{(2)}$ component of the nonlinear susceptibility is the predominantly driving part for second order surface nonlinearities. Using the redefinitions from equations 75-77, this results in a local nonlinear polarization

$$P_t^{(2)} = 2\epsilon_0 \chi_3^{(2)} E_n E_t , \quad (78)$$

$$P_n^{(2)} = \epsilon_0 \chi_1^{(2)} E_n^2 + \epsilon_0 \chi_2^{(2)} [E_s^2 E_t^2] , \quad (79)$$

$$P_s^{(2)} = 2\epsilon_0 \chi_3^{(2)} E_n E_s . \quad (80)$$

An important question that arises is which electric fields are used at the interface and especially how fields at interfaces are defined by the FEM software. In particular the question is, if the surface is counted to the particles volume or to the surrounding medium. In Comsol the fields at interfaces are formulated as mean value of the field just inside and just outside of the particle. This corresponds to fields along the paths $\partial V_{1/2}$ (see figure 10 (b)). Sipe et al. [99] showed, that for the calculation of the nonlinear polarization the electric fields just inside the particle has to be used in equations 78-80. Using suitable operators in Comsol, it is possible to only extract the electric field along

the path ∂V_2 . After the calculation of the nonlinear polarization, a back transformation to the global coordinate system is performed via

$$\begin{pmatrix} P_x^{(2)} \\ P_y^{(2)} \\ P_z^{(2)} \end{pmatrix} = D^{-1} \begin{pmatrix} P_t^{(2)} \\ P_n^{(2)} \\ P_s^{(2)} \end{pmatrix} = \begin{pmatrix} t_x & n_x & s_x \\ t_y & n_y & s_y \\ t_z & n_z & s_z \end{pmatrix} \begin{pmatrix} P_t^{(2)} \\ P_n^{(2)} \\ P_s^{(2)} \end{pmatrix}. \quad (81)$$

$\mathbf{P}^{(2)}(2\omega)$ now represents a density of dipoles, acting as source for second-harmonic fields. If the total second-harmonic emission into the far field has to be determined, an easy way is given by nonlinear scattering theory [104, 105]. Using Lorentz reciprocity, the emission process breaks down to a mode overlap between $\mathbf{P}^{(2)}(2\omega)$ and second-harmonic fields $\mathbf{E}(2\omega)$ launched from a point source at the detectors position [106]. Important to mention is, that for radiation applications the calculated nonlinear polarization is placed just outside the structure [99] - in contrast to its preceding derivation, where the fundamental electric fields just inside the structure were used. However, for qualitative statements and a fundamental understanding of second-harmonic emission from nanostructures, calculations beyond equation 81 are not necessary. Since the spatial dimensions of the nanostructure are smaller than the wavelength of light $d \ll \lambda$, retardation effects between the second-harmonic dipoles $\mathbf{P}^{(2)}(2\omega)$ can be neglected. Consequently, opposing second-harmonic dipoles can cancel each other out and emission only occurs, if a non-zero net dipole moment remains. This is of course only true if a plane wave detection scheme, i.e., coupling to plane waves, is assumed.

4.1.2 emission properties of specific nanostructures

In the following we discuss calculated nonlinear polarizations for two specific nanostructures and state the current understanding of second-harmonic emission stemming from plasmonic nanoparticles. In figure 11 (a) the two structures under investigation are shown - a wire and a SRR. Both are excited with a monochromatic infrared electric field, oriented parallel to the long axis of the structures. Figure 11 (b) shows the calculated resulting second order nonlinear polarization $\mathbf{P}^{(2)}(2\omega)$ in the mid height of the structures. In the case of the wire, we directly see that $\mathbf{P}^{(2)}(2\omega)$ has a symmetric shape with respect to the particle's center. Depending on the current phase, the field is either completely pointing in or outwards the structure. If we look at the arrows as oscillating dipoles and neglect retardation effects, it's clear that dipoles from opposing surfaces will cancel each other out. Since the structure itself is symmetric, opposing dipoles are of equal strength. This leads to the conclusion that, although we have a nonlinear polarization at the particles surface, no second-harmonic emission is expected, since the nanostructure itself is still of symmetric geometrical shape. This statement was generalized for all subwavelength nanoparticles.

The SRR, on the other hand, is a representative of asymmetric nanostructures. As one directly observes, the nonlinear polarization in the arms of the SRR overcomes the one in the long axis of the structure. As consequence, a non-vanishing total dipole moment remains and second-harmonic emission into the far field is possible. The SRR itself is only one of the most easy asymmetric particle shapes. Structures, whose capability of

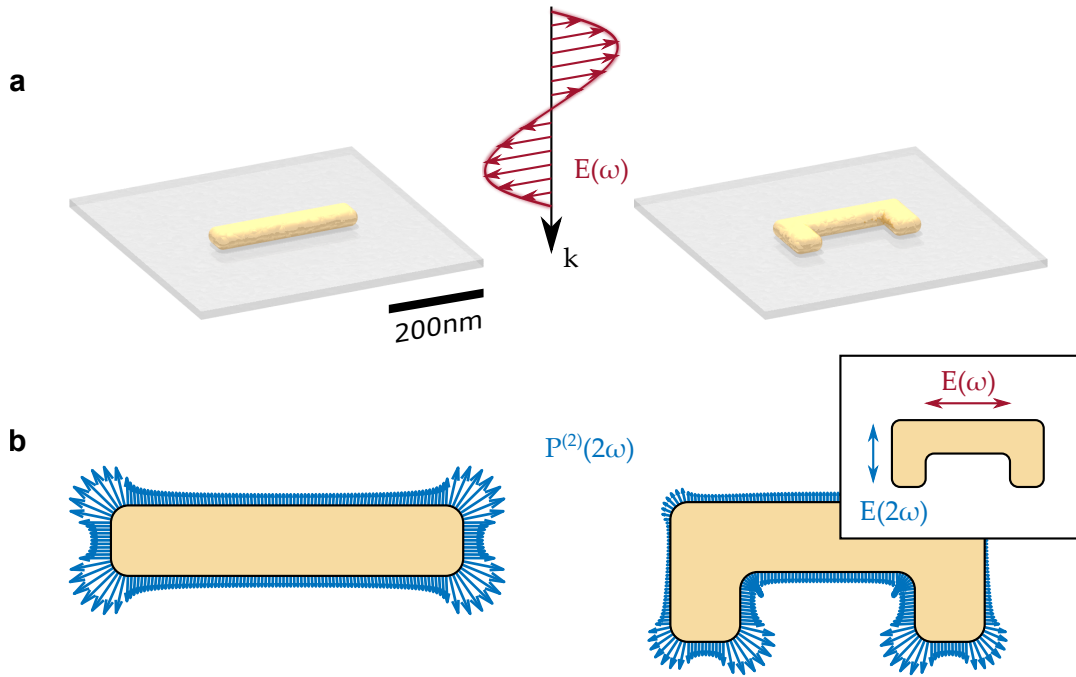


Figure 11: Second order nonlinear polarization for a plasmonic wire and a SRR. (a) Both structures are excited with plane waves of the frequency ω . The excitation is along the long axis of the structures. (b) The resulting nonlinear polarization $\mathbf{P}^{(2)}(2\omega)$ is indicated by blue arrows. The shown cut plane is centered in the middle of the structure. The inset in the right panel indicates the excitation polarization as well as the polarization under which second-harmonic emission will occur.

second-harmonic emission has also been studied in great detail, are L- or V-shaped structures, triangles as well as chiral G-shapes, which show second-harmonic circular dichroism. A collocation of asymmetric nanoparticles under investigation can be found in review papers [85, 107].

Another look at figure 11 (b) shows, that the generated nonlinear polarization is predominantly oriented vertically, i.e., along the arms of the SRR. This is additionally indicated by the inset in the figure, where $\mathbf{E}(2\omega)$ describes the polarization under which the second-harmonic light will be emitted. This behavior of the SRR has experimentally been verified by several groups [86, 106]. Consequently, a change of the SRRs arm length will have a strong influence on the second-harmonic emission. One way to think about it is, that an increasing arm length leads to a stronger asymmetry of the structure itself. This has been investigated by O'Brien et al. [106]. They found, that the second-harmonic emission into the far field increases with the arm length until a certain ratio between base and arm length. From there on, the second-harmonic emission starts to decrease again. If we think in terms of plasmonic resonances along the SRRs base and its arms, this can easily be explained (a detailed analysis of the modes was given in chapter 3.2.2). If the base length exceeds the arm length, the fundamental plasmon resonance parallel to the base will lie, e.g., in the near infrared spectral range while the resonance along the arms is blue shifted to the visible spectral range. This allows tailoring the SRR for

efficient second-harmonic emission. While the exciting infrared laser is located at the horizontal resonance, the vertical resonance can be matched to the resulting second-harmonic light. Therefore, the second-harmonic emission will be greatly enhanced.

4.2 SECOND-HARMONIC GENERATION IN PLASMONIC WAVEGUIDES

Keeping the results from the previous section in mind, the question arises, if a geometrical asymmetry is a necessary criterion for second-harmonic emission from nanostructures, or, if already the presence of a suitable optical or plasmonic mode is sufficient to allow second-harmonic emission in symmetric materials. The idea for this project and the first experimental observation of second-harmonic emission in symmetric nanostructures came from the group of Prof. C.-B. Huang and was subsequently investigated in a collaboration [33].

In order to demonstrate that optical modes of suitable symmetry are sufficient to allow SHG and neither a structural asymmetry nor a non-inversion symmetric material are required, we need a suitable structure. Despite of being symmetric, the structure should provide different modes. The key idea is to show, that second-harmonic emission is only possible into modes that provide a certain symmetry and, at the same time, not into other present modes. A structure well suited for this purpose is the TWTL (see chapter 3.3). It offers two modes of defined symmetry - anti-symmetric and symmetric. Moreover, those modes exist for both involved frequencies and the profile is broadband. This means it is in first approximation independent of the wavelength. The main difference between the two frequencies lies in the lower propagation length for the second-harmonic and does not affect symmetry based argumentations.

The scheme, we use to prove Prof. C.-B. Huang's hypothesis, is sketched in figure 12. (a) shows a rendered image of the TWTL with an indicated cut plane for (b). There, the basic concept for calculations is presented. The fields are now represented by arrows with omitted head, in order to maintain clarity. The lines always start at the sketched surrounding of the TWTL and the magnitude is given by the length. The relative phase at different points is coded in the direction of the field, relative to the surface normal - outwards or inwards pointing. The wavelength of the fields is indicated by color. The fundamental wavelength (1560 nm) is shown in red and the second-harmonic (780 nm) in blue. The fundamental electric field distribution $E(\omega)$ of both modes is obtained from FEM calculations (row 1) and used to determine the resulting second order nonlinear polarization (row 2). Those $P^{(2)}(2\omega)$ are the source for second-harmonic fields. In order to determine if and into which modes emission is possible, we need to consider the available modes at 2ω that are provided by the TWTL. Those modes are again obtained via FEM simulations and shown in row 3. How coupling between the two $P^{(2)}(2\omega)$ and the two $E(2\omega)$ modes occurs, is indicated by arrows. As one directly observes, both generated nonlinear polarizations are of symmetric character, although, they originate from different fundamental symmetries. Consequently, it is quite obvious that second-harmonic emission will only be possible into a second-harmonic mode that offers a symmetric field distribution $E(2\omega)$.

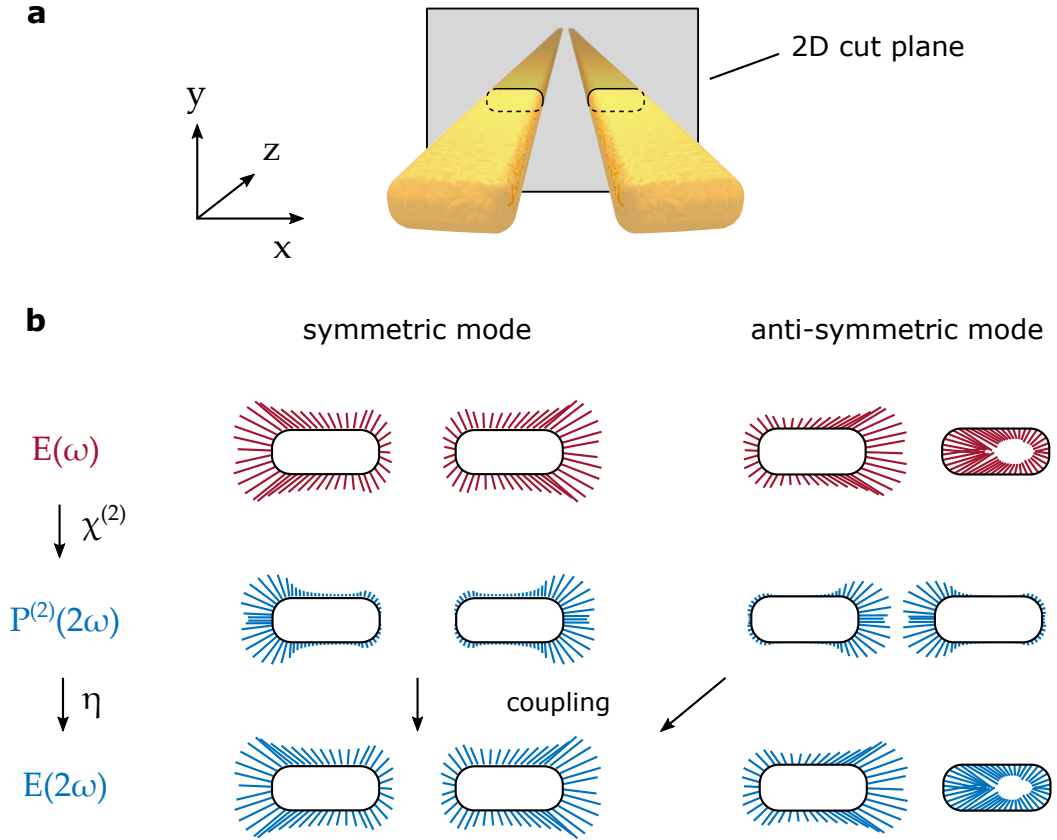


Figure 12: Schematic for SHG in a fully symmetric nanostructure. (a) The TWTL is shown and a 2D cutplane for further analysis is indicated. (b) Illustration of the calculation steps. The wavelength of the fields is indicated by red (1560 nm) and blue (780 nm) and the fields are shown at the contour of the TWTL. The orientation is given by the direction of the arrows, with respect to the local surface normal. From the fundamental fields in the upper row, the nonlinear polarization is calculated (mid row). The outgoing arrows indicate that both obtained nonlinear polarization modes are of symmetric character, which only allows coupling to a symmetric second-harmonic mode (lowest row). Published in Ref. [33], used and adapted with permission. Copyright 2019 American Chemical Society.

In order to describe coupling process in a more quantitative approach, we make use of standard mode matching theory. Whenever two optical modes need to be matched, an overlap integral between source and target mode can be defined as [108]

$$\eta = \frac{|\int \mathbf{E}_{\text{source}} \mathbf{E}_{\text{target}}^* dA|^2}{\int |\mathbf{E}_{\text{source}}|^2 dA \int |\mathbf{E}_{\text{target}}|^2 dA} . \quad (82)$$

In our case, the source mode is provided by the generated nonlinear polarization and the target mode is the waveguide mode at the second-harmonic frequency. Since we restrict solely to a surface nonlinearity, the surface integral reduces to a line integral along the 2D surface ∂A of the TWTL. This results in the overlap integral

$$\eta = \left| \int_{\partial A} \mathbf{P}^{(2)}(2\omega) \mathbf{E}(2\omega)^* ds \right|^2 . \quad (83)$$

Now both, source and target mode, can be either of symmetric or anti-symmetric character, which leads to four different combinations. In order to have an easy representation, we do not look at the resulting values η of the overlap integral but at the integrand $\mathbf{P}^{(2)}(2\omega)\mathbf{E}(2\omega)^*$ itself. As it is still a complex value, we use the absolute value and phase for representation. All four combinations of possible modes are shown in figure 13. The columns represent the two source modes, i.e., the nonlinear polarization $\mathbf{P}^{(2)}(2\omega)$ and the rows are the TWTL's possible target modes $\mathbf{E}(2\omega)$ at the second-harmonic frequency. The cross-section of the waveguide is in the x-y plane and in z-direction, the normalized absolute value of the overlap integrand is shown. The squares in the x-y plane are 100×100 nm. The phase of the integrand is color coded and runs continuously from $-\frac{\pi}{2}$ (blue) over 0 (white) to $\frac{\pi}{2}$ (red). It appears, that only phases of $-\frac{\pi}{2}$ or $\frac{\pi}{2}$ are observed and depending on the combination of source and target modes, the relative phase between the two branches of the TWTL is either 0 (symmetric target mode) or exactly π (anti-symmetric target mode). If the TWTL branches have the same phase, the 1D surface integral from equation 83 will give a non-zero result. Consequently, emission into the symmetric mode at 2ω is possible for both source modes. For a phase difference of π , on the other hand, the contributions of the two branches will cancel each other out during the integration process as a consequence of the axial symmetry of the TWTL at $x = 0$. Therefore, emission into the anti-symmetric target mode is not allowed. This full vectorial mode matching calculation further proves our argumentation presented in figure 12 (b). The overlap is only non-zero for coupling to a symmetric second-harmonic mode. In figure 13, we sketched the overlap integral's integrands with normalized values. This was done due to better visibility and does not affect symmetry based argumentations. Due to the spatially differing mode profiles it is clear, that the coupling to a symmetric second-harmonic mode is more efficient if the nonlinear polarization stems from a symmetric fundamental mode.

In summary, we have shown theoretically that nanostructures do not necessarily have to provide an asymmetric geometrical shape in order to allow second-harmonic emission. An optical or plasmonic mode of matching symmetry is already sufficient. The key to prove this statement was to move away from resonant nanoparticles, that are in the far field limited to one emission mode - plane waves - to plasmonic waveguides. Here, two possible target modes with fundamentally different symmetry properties are present and coupling occurs only to one of them.

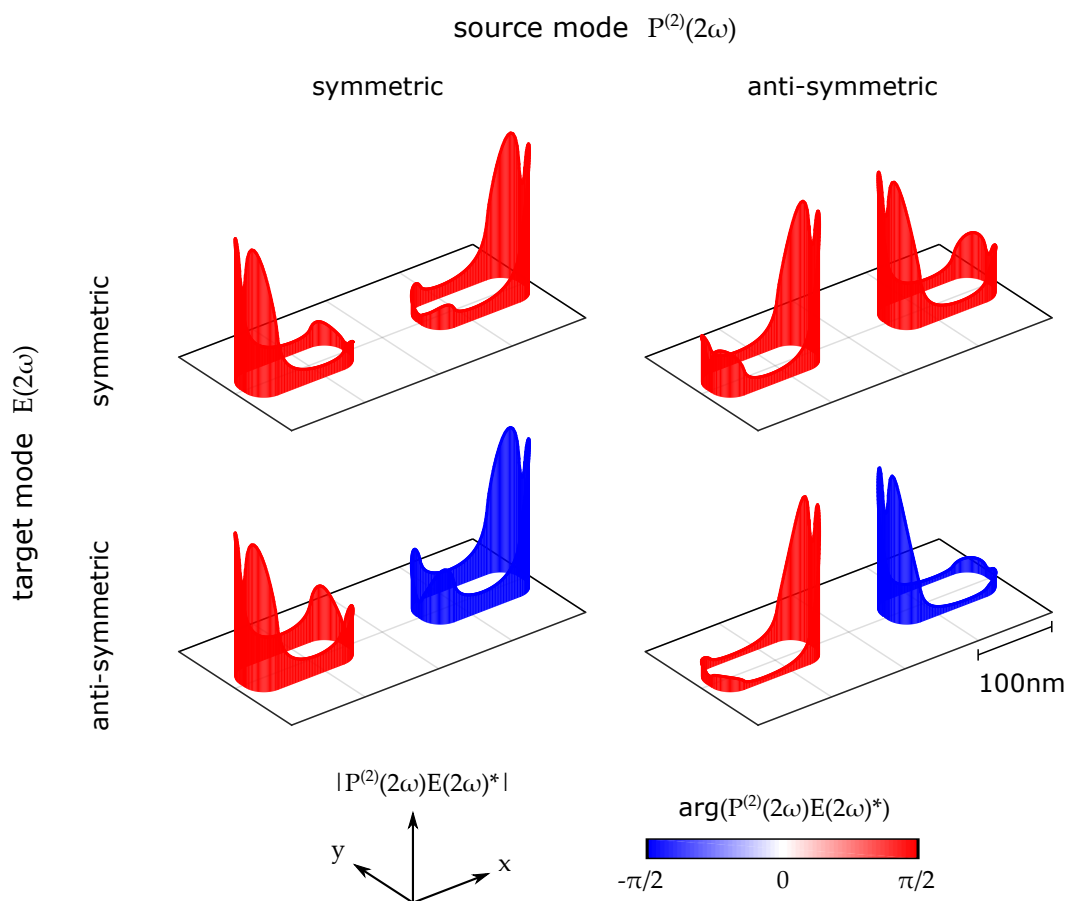


Figure 13: The four possible combinations of overlap integrals resulting from two source and two possible target modes. The cross-section of the TWTL is in the x - y plane - the dimensions are indicated by a scale bar. The normalized absolute value $|P^{(2)}(2\omega)E(2\omega)^*|$ is shown in z -direction and the phase $\arg(P^{(2)}(2\omega)E(2\omega)^*)$ is color coded. If the two branches of the TWTL have the same phase, the total coupling integral will be non-zero. A phase difference of π will lead to a vanishing coupling integral. Consequently, the nonlinear polarization can only couple to a target mode with symmetric character. Published in Ref. [33], used and adapted with permission. Copyright 2019 American Chemical Society.

EXPERIMENTAL OBSERVATION OF SECOND-HARMONIC EMISSION IN SYMMETRIC NANOSTRUCTURES

In the previous chapter we have presented a theoretical model that states, that in contrast to previous understanding, SHG in symmetric nanostructures is possible within the electric dipole approximation. To complete our argumentation, we now demonstrate that the model is in agreement with experimental findings and is also capable of describing further observed effects. The project, including theoretical and experimental work, was done and published in a collaboration with the groups of Prof. C.-B. Huang and Prof. J.-S. Huang [33]. The focus of our work was on theoretical modeling as well as data analysis and data processing.

In this chapter we start by introducing the nanostructure under investigation. We discuss how an infinite TWTL can be experimentally realized and present mechanisms, that allow the distinct excitation and measurement of the two eigenmodes of the system. Additionally, we provide a short insight into the fabrication process as well as the experimental setup. In a first experiment we excite the system's eigenmodes and demonstrate, that the second-harmonic emission is only observed from a symmetric waveguide mode and not from an anti-symmetric one. Afterwards, we move away from the excitation of pure fundamental modes and use a mode superposition. The results open up a completely new coupling behavior where the previously discussed cases are only special cases of a more generalized behavior. We demonstrate that this generalized mechanism can also be described by basic mode matching theory and symmetry arguments. Moreover, the model and experiments with mode superpositions allow us to completely rule out or quantify local SHG contributions which are not stemming from inside the TWTL. Therefor, we can experimentally show, that the SHG takes place within a symmetric plasmonic waveguide. We conclude the chapter by an intuitive model that adds a third spatial direction (the propagation direction) to our theoretical modeling and, furthermore, discuss the influence of complex and nonlinear substrates on the coupling procedure. Parts of this chapter are published in Ref. [33]. Figures are used and adapted with permission. Copyright 2019 American Chemical Society.

5.1 STRUCTURE LAYOUT AND EXPERIMENTAL SETUP

For the theoretical modeling of SHG in a plasmonic waveguide we assumed an infinitely extended TWTL. In experiments this can be realized by using a reasonably long TWTL, i.e., several microns. Additional requirements are, that the two eigenmodes of the system can be excited and, moreover, also detected separately. Therefor, the TWTL has to

be completed by two additional elements. An antenna, that allows controlled mode excitation and a detector segment, that is able to distinguish between the different launched modes. To achieve this, we adapted the design introduced by Geisler et al. [94] in a slightly modified way. Our structure, as well as the basic working principle, is presented in figure 14. Panel (a) shows a rendered image of the experiment where the structure is located on a substrate. A focused laser pulse at the fundamental frequency ω excites the modes at the antenna. During propagation through the TWTL part of the structure, SHG occurs. The TWTL is then terminated by a mode detector that allows distinguishing between the eigenmodes of the TWTL. Here, the emission at the second-harmonic frequency 2ω is radiated into the far field and can be measured.

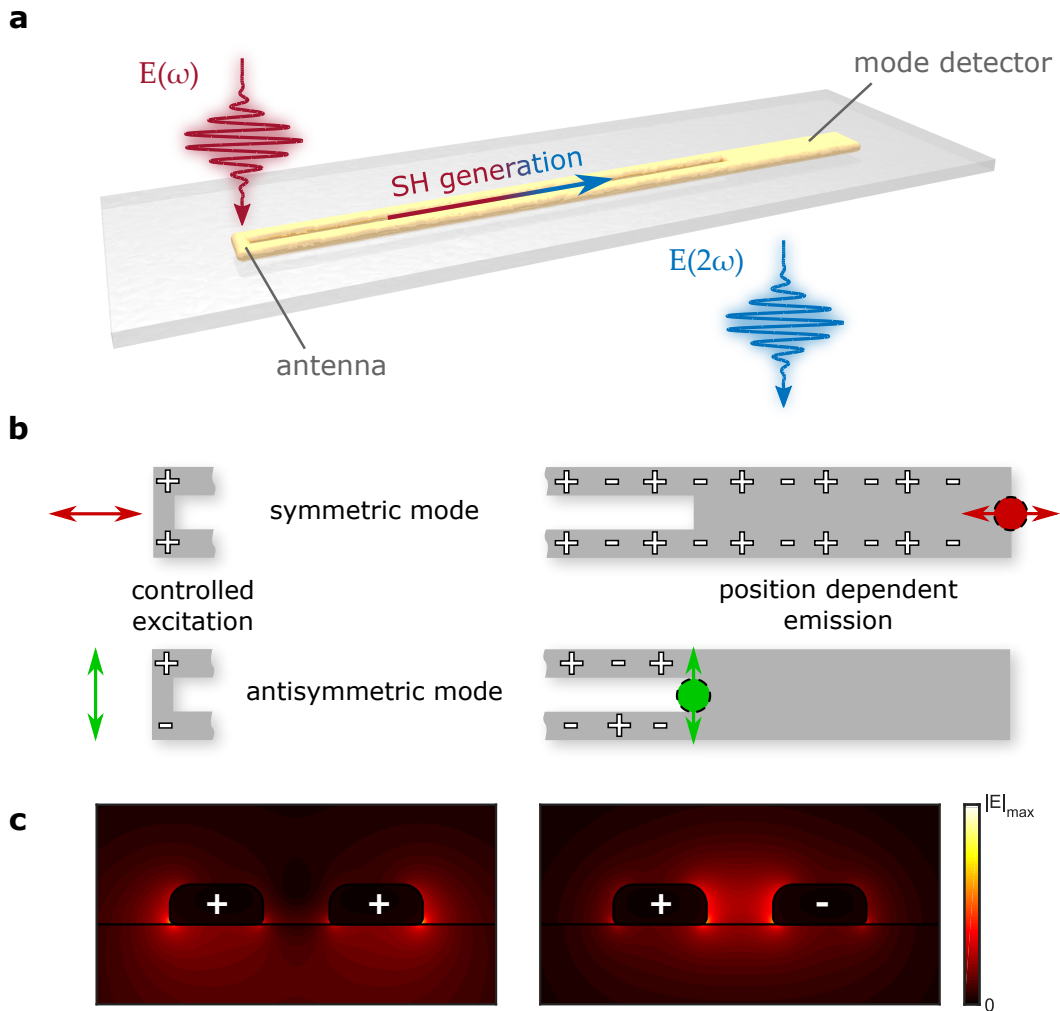


Figure 14: Working principle of the experimental structure. (a) Schematic sketch of the experiment. The TWTL is located on a glass substrate. At the antenna, the two eigenmodes of the system can be excited and propagate through the waveguide. The second-harmonic signal, generated during the propagation, is then emitted from the mode detector. The working principle of the antenna (b) relies on the creation of charge distributions, that resemble those of the two eigenmodes (shown in (c)). Symmetric and anti-symmetric charge distributions can simply be achieved by using an appropriate excitation polarization (indicated by red and green arrows). In detection, the two modes can be separated via their mode profiles. At the mode detector, the TWTL transitions to a slab waveguide and the anti-symmetric mode is scattered into the far field. The symmetric mode travels until the end of the mode detector and is emitted from there. In emission, the polarization of both modes is conserved as indicated by arrows.

antenna

A crucial part of the waveguide design is the antenna for excitation of the modes. It has to offer the possibility to excite both eigenmodes distinctively and, moreover, as efficient as possible. A design well suited is a simple shortcut between the two transmission lines. In figure 14 (b) the resulting excitation mechanism for both modes is sketched. If the anti-symmetric eigenmode is to be excited, we have to create a dipolar charge distribution in the antenna. This is achieved by using an excitation polarization parallel to the antenna's shortcut. The induced charges will now extend into the TWTL and, hence, create the anti-symmetric mode. In this case, the antenna can be regarded as a SRR with infinitely extended arms which still offers a dipolar resonance in the base (see also chapter 3.2.2). If, on the other hand, the symmetric eigenmode is to be launched, also a corresponding charge distribution has to be prepared in the antenna. Here, an excitation polarization perpendicular to the antenna is used and the shortcut acts as scattering edge. The excitation efficiency could be enhanced in this case by using a scattering grating rather than a simple edge. But in order to use the grating efficiently, the excitation spot has to be chosen larger which would on the counter part mean less efficient excitation for the anti-symmetric mode. Consequently, it is state of the art to use simple scattering edges in research involving antenna excited TWTLs [79, 109, 110].

mode detector

In order to distinguish between the two eigenmodes in detection, Geisler et al. [94] made use of the strongly differing mode profiles. In figure 14 (c) the profiles of a TWTL on a glass substrate are shown. The results are again obtained from FEM simulations, the absolute value of the electric field is plotted and charges are indicated. Like in the case of a homogeneous environment (see chapter 3.3), the symmetric mode is predominantly located at the outer edge of the TWTL, while the anti-symmetric mode travels in the gap of the waveguide. The key idea of the mode detector is to terminate, i.e., fill the gap at some point and, therefor, partly reflect the gap mode but also partly scatter it via the edge into the far field. This is sketched in figure 14 (b). After the termination of the gap, the anti-symmetric mode is no longer present. In contrast to that, the symmetric mode is still able to propagate further and in first approximation not influenced by the terminated gap. After a few microns, the slab waveguide is also terminated which, again, leads to partly reflected and emitted light. Consequently, it is possible to map the two different waveguide modes to two different spatial positions and, if the Rayleigh criterion is met, detect them separately in the far field. An interesting point of the detection scheme is, that the excitation polarization used to excite the modes is conserved. This has been demonstrated in experiments [110] and opens up the possibility of using polarizers in the detection path in order to further increase the signal to noise ratio. Especially for our case it is important to mention that the mode detector, like the TWTL, supports broadband spectral operation. Therefor, it works for all frequencies involved in our experiments.

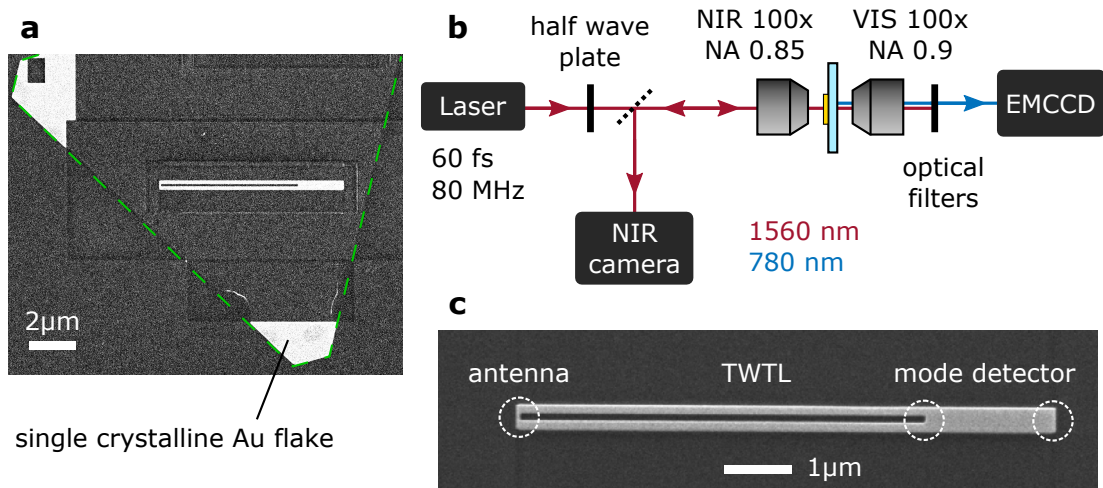


Figure 15: Experimental details. In (a) and (c) SEM images of the nanocircuit are shown. In (a), the former gold flake can still be seen (indicated by dashed green line). Panel (b) shows a sketch of the home-built setup. For excitation and detection, high NA objectives and imaging cameras are used. The fundamental signal is collected in reflection, while the second-harmonic one is imaged in transmission.

fabrication and setup

The spatial dimensions of the waveguide, involving antenna geometry and mode detector, were designed and optimized by Tz-Yu Chen using FDTD simulations. In the cross-section, the transmission lines have a width of 140 nm, a height of 60 nm and are separated by a gap of 100 nm. Our FEM geometry is matched to these dimensions. The width of the shortcut antenna has been chosen as 80 nm, in order to ensure most efficient mode excitation. The length of the TWTL is set to several microns in order to simulate an infinitely extended structure and avoid Fabry-Perot resonances between the antenna and the mode detector, whose length is set to 2 μm . For the fabrication of complex nanostructures and -circuits there are two common methods. Electron beam lithography (EBL) and focused ion beam milling (FIB). Both are top-down fabrication approaches and allow the design of arbitrary shapes. In EBL, a focused electron beam writes the structure into a photo resist which is later developed and the exposed areas are finally filled with gold in an evaporation process with a consecutive lift off. In FIB, the fabrication process starts with a thin gold film and the structure is cut out of it using a focused ion beam. The typically reached resolution is for both methods in the order of few tens of nanometers or even higher [111]. Nevertheless, FIB has one distinct advantage over EBL - one does not necessarily has to use evaporated gold but can revert to chemically grown single crystalline gold flakes. Those gold flakes provide an up to one single atom smooth surface, what allows structures of highest surface quality. A comparison of single and polycrystalline structures is given by [112].

As our waveguides, in their full extend, easily reach lengths near 10 μm , we have to ensure highest surface quality. In this way we maintain reasonable propagation lengths for our waveguide modes. Although the theoretically predicted values are generally quite high, even the same order of predicted magnitude is, up to date, hardly met in

any reported experiment. Consequently, we use FIB as fabrication process to ensure highest quality of our structures. In our case, the gold flakes are chemically grown and a flake of matching height is transferred onto a glass substrate that is coated with a 40 nm conducting indium tin oxide (ITO) film. A conducting subsoil is typically used to circumvent charging problems linked to the milling ion beam [113]. An example for a produced waveguide is shown in figure 15 (a). Parts of the initial gold flake can be still observed and the former circumference is indicated by a dashed green line. The final TWTL lies in the middle of the SEM picture. In the area where the gold flake has been milled off, rectangular shapes in the substrate can be observed. Those arise from the stepwise milling process. The sample preparation was realized by Fan-Cheng Lin and Jer-Shing Huang [33]. Figure 15 (c) shows a detailed SEM image of the finished structure. The high quality of the surface and the edges is clearly visible.

For the experimental investigation of the TWTL, a home built dual-confocal transmission microscope is used. A schematic representation of the setup is shown in figure 15 (b). For excitation of the fundamental waveguide modes a passively mode-locked fiber laser (Menlo Systems T-Light), operating at 1560 nm, is used. The transform limited pulses have a temporal width of 60 fs and are emitted with a 80 MHz repetition rate. The maximum averaged power is 100 mW. A half wave plate after the laser gives full control over the angle of the linearly polarized output. Therefor, distinct excitation of the two TWTL eigenmodes is possible independent of the samples orientation. For excitation, the laser is focused onto the antenna using a 100 fold long working distance NIR objective (Olympus LCPLN100XIR) with $NA = 0.85$ from the substrate side of the sample. In reflection, the waveguide's operation at the fundamental frequency can be imaged using a NIR camera (Xenics Xeva-1.7-320). The second-harmonic light, on the other hand, is collected from the air side of the structure, using a 100 fold, $NA = 0.9$ VIS objective (Olympus MPLFLN100X). For detection, an electron-multiplied charge-coupled device (EMCCD, Andor iXon 897U-CSO-EXF) is used. Additional optical filters, a short-pass (Thorlabs FESH0900) and a bandpass filter (Thorlabs FL780-10), ensure that neither fundamental light, nor THG or multi-photon luminescence distort the second-harmonic signal. Moreover, a polarizer is added to the detection path in order to separate the emitted modes better and increase the SNR.

5.2 SECOND-HARMONIC GENERATION IN A TWTL

The experiment itself consists of two parts. First, we have to verify that our produced structure is working correctly, i.e., excitation, waveguiding and detection works. To do this, we use the reflection part of our microscope and monitor the TWTL's operation at the fundamental frequency. We excite both eigenmodes of the TWTL separately and demonstrate that emission is obtained from the predicted position of the mode detector. In the second step, we use the transmission part of the setup and prove that the second-harmonic emission always stems from one position of the mode detector, no matter which fundamental eigenmode we excite. The recorded images of both, the visible and NIR camera, are shown in figure 16. In the left column, the fundamental emission is shown. For noise reduction the images were filtered by a 3×3 median filter. To correct the images for read-out artifacts, caused by the NIR camera, a background subtraction

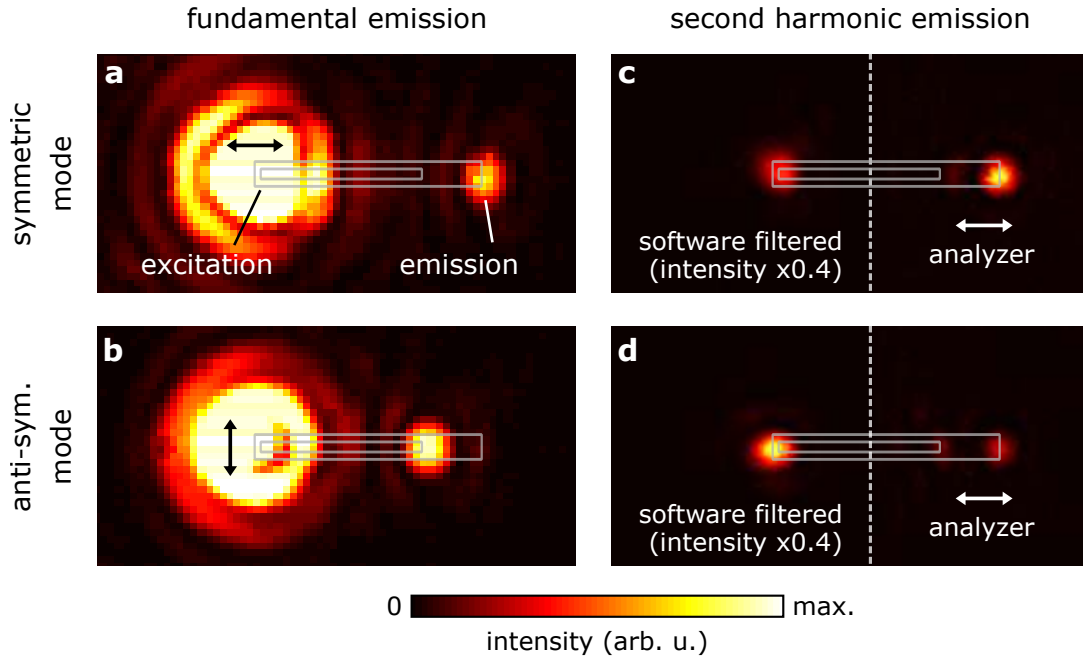


Figure 16: Experimental observation of SHG in a symmetric nanostructure. The panels (a) and (b) show camera images at the fundamental frequency for both launched eigenmodes of the TWTL. The excitation polarization is indicated by black arrows next to the antenna. The emission of the modes stems from the respective mode detector ends. In the second-harmonic images ((c) and (d)), we observe that the emission at the mode detector stems from a symmetric waveguide mode for both fundamental eigenmodes. The antenna part of the images was software filtered as indicated by the insets. An additional polarization analyzer increases the SNR.

based on a line correction was performed. In the right column, images at the second-harmonic frequency, the same median filter was applied. The background subtraction was done using the mean value of a dark area. For an easy understanding of the images the surrounding of the waveguide structures is indicated by gray lines.

If the antenna is excited by fundamental light polarized perpendicular to it (figure 16 (a)), we excite the symmetric eigenmode of the TWTL. The excitation polarization is indicated by a black arrow near the antenna. In consequence, a bright emission spot at the right end of the mode detector appears and indicates fundamental emission from a symmetric waveguide mode. If, on the other hand, we excite with a $\pi/2$ rotated polarization (see figure 16 (b)), the anti-symmetric mode is excited and emitted from the left, i.e., inner end of the mode detector. This proves that our structure works as designed and that we are able to distinguish the TWTL's eigenmodes by the position of emission at the mode detector. In the second-harmonic images (figure 16 (c)-(d)), an additional polarizer was used in the detection path in order to focus on the desired emission polarization at the mode detector. A detailed discussion of general polarization properties is given at a later point. In the images we first observe strong, local second-harmonic scattering at the antenna which is damped by a software based ND filter. At the mode detector, we see exactly what our theory predicts. No matter which fundamental eigenmode we launch,

the second-harmonic emission will always stem from a symmetric waveguide mode, i.e., the right side of the mode detector. In the case of an anti-symmetric fundamental mode, the emission at the mode detector is not as strong as for the symmetric fundamental case. This can be attributed to a reduced spatial mode overlap with the necessarily symmetric second-harmonic mode. At this point it is not clear if we can fully rule out SHG at the antenna, locally at the mode detector or related to the underlying ITO layer. Those exclusions are treated in own sections in the following. We want to point out, that the presence of the glass substrate does not alter our argumentation from chapter 4.2. The exact mode profile is slightly changed (see appendix A.2) but fundamental properties, like the charge symmetry as well as the localization of the modes to the gap or the outer parts of the TWTL, remain the same.

5.3 MODAL SYMMETRY CONTROLLED SHG

The question that arises at this point is whether coupling can only occur to the symmetric second-harmonic waveguide mode, or, if it's also possible to achieve coupling to the anti-symmetric mode. Until now, we only focused on launching pure fundamental eigenmodes of the system which, of course, corresponds only to two special cases of a more general behaviour. If we use an arbitrary excitation polarization at the TWTL's antenna, we will not launch pure eigenmodes, but instead we excite a superposition

$$\begin{aligned} \mathbf{E}_{\text{tot}} &= \cos \theta \mathbf{E}_s + \sin \theta r e^{i\phi} \mathbf{E}_{\text{as}} \quad , \\ &= c_s \mathbf{E}_s + c_{\text{as}} r e^{i\phi} \mathbf{E}_{\text{as}} \quad , \end{aligned} \quad (84)$$

of the symmetric (\mathbf{E}_s) and anti-symmetric mode (\mathbf{E}_{as}). The amplitude factors $\sin \theta$ and $\cos \theta$ are given by the fundamental excitation polarization under the angle θ , while the complex term $r e^{i\phi}$ accounts for a different strength of the modes as well as a phase difference ϕ that is caused by the excitation process at the antenna. The key is, that in SHG the fundamental field enters nonlinear and therefor we will obtain not only quadratic terms of the two summands, but also a mixed term. For a better understanding we will now omit the tensorial character of $\chi^{(2)}$ and use only the nnn component for further analysis and model building. This can be assumed free of doubt, because it is by far the dominant tensor component (see chapter 4.1.1). Consequently, the second order nonlinear polarization is now calculated as

$$\mathbf{P}_n^{(2)} = \epsilon_0 \chi_{nnn}^{(2)} \mathbf{E}_n^2 \quad . \quad (85)$$

The general expression for the excited modes from equation 84 leads to a general nonlinear polarization that can be sorted into symmetric and anti-symmetric contributions

$$\mathbf{P}_n^{(2)} \propto \underbrace{c_s^2 \mathbf{E}_s^2 + c_{\text{as}}^2 r^2 e^{2i\phi} \mathbf{E}_{\text{as}}^2}_{\text{symmetric}} + \underbrace{2c_s c_{\text{as}} r e^{i\phi} \mathbf{E}_s \mathbf{E}_{\text{as}}}_{\text{anti-symmetric}} \quad . \quad (86)$$

The first two summands correspond to the two special cases we already discussed theoretically as well as experimentally. The eigenmodes in their pure forms lead to symmetric field distributions which are only able to couple to the symmetric second-harmonic

waveguide mode. In order to predict the coupling for a general mixed mode, we take another look at the overlap integral and split the nonlinear polarization into its symmetric and anti-symmetric part

$$\eta = \left| \int_{\partial\Lambda} (\mathbf{P}_s^{(2)}(2\omega) + \mathbf{P}_{as}^{(2)}(2\omega)) \mathbf{E}_{s/as}(2\omega)^* ds \right|^2 . \quad (87)$$

As second-harmonic target modes we allow both, symmetric and anti-symmetric, modes $\mathbf{E}_{s/as}(2\omega)$. The resulting concept breaks down to simple symmetry arguments. If the function under the integral is symmetric, a non-zero value is obtained and if the integrand is anti-symmetric, the total integral vanishes. Consequently, our previous model from chapter 4.2 is now generalized as the product of two anti-symmetric fields will lead to a symmetric integrand and, therefore, a finite value of the overlap integral. Coupling to the anti-symmetric second-harmonic mode is possible, if the nonlinear polarization possesses an anti-symmetric contribution. In order to demonstrate this effect in the experiment, we use the half-wave plate in front of the laser and rotate the linearly polarized light by specific angles which can be transferred to a change in the amplitude via the angle θ . The relative phase between both modes remains unchanged and is given by the antenna as an intrinsic property. The results are shown in figure 17. The panels (a) and (b) show the emission at both ends of the mode detector in a polar representation for different fundamental excitation angles $\theta \in [0, \pi]$. The measured data is given by black dots and the solid colored lines are model fits. For data analysis, the recorded images are preprocessed like in section 5.2. To determine the emission strength, regions of interest were defined at the corresponding mode detector positions and the maximum value was taken within.

The fundamental emission for different excitation polarizations (figure 17 (a)) can be described by a model directly derived from equation 84. We observe a $\sin^2 \theta$ behavior for emission from the anti-symmetric mode and a $\cos^2 \theta$ behaviour for the symmetric one. The fitting model also includes a parameter to account for a finite offset. The offset can have two different sources. Parts of it we can attribute to structural imperfections and therefore non-ideal operation and another part can be linked to the symmetric waveguide mode. The operation of the mode detector is based on the fact, that the gap vanishes which does not influence the symmetric mode traveling at the outer edges of the TWTL. But yet, the field of the symmetric mode in the gap is only weak and not zero. If we compare the model to the measured data, we see a very good agreement and consequently argue that there is no need for an offset that is more complex than a constant function.

The emission behavior at the second-harmonic frequency (figure 17 (b)) is more complicated than the fundamental one. For the coupling to the symmetric mode (outer end of the mode detector), we observe maximum efficiencies for $\theta = 0$ and $\theta = \pi/2$ excitation, which correspond to the already discussed cases. Nevertheless, we observe two interesting things. We see that coupling from a symmetric $\mathbf{P}_s^{(2)}$ is a factor of about 2 more efficient than coupling from an anti-symmetric $\mathbf{P}_{as}^{(2)}$ one, which we attribute to the reduced spatial mode overlap of the fields. This experimentally observed factor cannot be directly compared to relative efficiencies predicted by the theoretical model in chapter 4.2, since the pure mode coupling efficiency is also accompanied by excitation efficiencies at the antenna. Therefore, we do not draw comparison between values. The

second feature we observe is that we do not have a monotonous transition between the two values, but that there is a minimum in between at about 45 deg. If we look at the second-harmonic emission from the inner end of the mode detector, i.e., from an anti-symmetric waveguide mode, we observe minima for the pure fundamental eigenmodes but a maximum in between. This maximum is also located at about 45 deg. The model we used to describe the measured data is based on equation 87. We assume the emitted second-harmonic light $I_{s/as}(2\omega)$ to be proportional to corresponding coupling efficiencies and add scaling factors $\alpha_{s/as}$. This leads to the expressions

$$\begin{aligned}
I_s(2\omega) &= \alpha_s \left| \int_{\partial A} \epsilon_0 \chi_{nnn}^{(2)} (\cos \theta \mathbf{E}_s(\omega) + \sin \theta r e^{i\phi} \mathbf{E}_{as}(\omega))^2 \mathbf{E}_s(2\omega)^* ds \right|^2 \\
&= \alpha_s \left| \cos^2 \theta \underbrace{\int_{\partial A} \epsilon_0 \chi_{nnn}^{(2)} \mathbf{E}_s^2(\omega) \mathbf{E}_s(2\omega)^* ds}_{=A} \right. \\
&\quad + \sin^2 \theta r^2 e^{2i\phi} \underbrace{\int_{\partial A} \epsilon_0 \chi_{nnn}^{(2)} \mathbf{E}_{as}^2(\omega) \mathbf{E}_s(2\omega)^* ds}_{=B} \\
&\quad \left. + 2 \cos \theta \sin \theta r e^{2i\phi} \underbrace{\int_{\partial A} \epsilon_0 \chi_{nnn}^{(2)} \mathbf{E}_s(\omega) \mathbf{E}_{as}(\omega) \mathbf{E}_s(2\omega)^* ds}_{=0} \right|^2 \\
&= \alpha_s |A \cos^2 \theta + B \sin^2 \theta r^2 e^{2i\phi}|^2 \quad , \tag{88}
\end{aligned}$$

$$\begin{aligned}
I_{as}(2\omega) &= \alpha_{as} \left| \int_{\partial A} \epsilon_0 \chi_{nnn}^{(2)} (\cos \theta \mathbf{E}_s(\omega) + \sin \theta r e^{i\phi} \mathbf{E}_{as}(\omega))^2 \mathbf{E}_{as}(2\omega)^* ds \right|^2 \\
&= \alpha_{as} \left| \cos^2 \theta \underbrace{\int_{\partial A} \epsilon_0 \chi_{nnn}^{(2)} \mathbf{E}_s^2(\omega) \mathbf{E}_{as}(2\omega)^* ds}_{=0} \right. \\
&\quad + \sin^2 \theta r^2 e^{2i\phi} \underbrace{\int_{\partial A} \epsilon_0 \chi_{nnn}^{(2)} \mathbf{E}_{as}^2(\omega) \mathbf{E}_{as}(2\omega)^* ds}_{=0} \\
&\quad \left. + 2 \cos \theta \sin \theta r e^{2i\phi} \underbrace{\int_{\partial A} \epsilon_0 \chi_{nnn}^{(2)} \mathbf{E}_s(\omega) \mathbf{E}_{as}(\omega) \mathbf{E}_{as}(2\omega)^* ds}_{=C} \right|^2 \\
&= \alpha_{as} |2C \cos \theta \sin \theta r e^{i\phi}|^2 \quad , \tag{89}
\end{aligned}$$

where some integrals can be directly set zero, since the integrand is an anti-symmetric function. The other integrals are constant for our purposes and we assign them the parameters A, B and C. For the final fitting functions, we evaluate the expressions from equations 88-89, absorb the values A, B and C into the fitting parameters r and ϕ and obtain the following expressions

$$I_s(2\omega) = \alpha_s (\cos^4 \theta + r^4 \sin^4 \theta + 2r^2 \cos 2\phi \cos^2 \theta \sin^2 \theta) \quad , \tag{90}$$

$$I_{as}(2\omega) = \alpha_{as} 4r^2 \cos^2 \theta \sin^2 \theta + \beta_{as} \quad , \tag{91}$$

where β_{as} is an artificially added offset. The model itself would require a vanishing coupling to the anti-symmetric mode for excitations at $\theta = 0$ deg and 90 deg. In the experiment this cannot be obtained due to structural imperfections, a non-ideal operation of the mode detector and locally scattered SHG. As we observe in figure 17 (b),

our model is perfectly capable of describing the second-harmonic emission for different fundamental excitation polarizations. Moreover, we obtain values for the fitting parameters $r = 0.83$ and $\phi = 73.3$ deg. Those parameters describe unknown quantities like excitation efficiencies, exact values of overlap integrals and also second-harmonic phase matching properties which are constant in the experiment.

The fitted values allow us to extrapolate the behavior of mode coupling beyond different strengths in amplitude. Using equations 90 and 91, we can predict the nonlinear operation of the TWTL also for relative phase differences between the two fundamental modes. The resulting 2D coupling maps are shown in figure 17 (c). On the x-axis, the fundamental excitation angle at the antenna is plotted while the y-axis marks a phase difference. The coupling efficiency η is color coded. Dashed white lines in both plots, symmetric and anti-symmetric target modes, indicate where the fits from figure 17 (b) are located within the images. We see that the nonlinear emission into the anti-symmetric second-harmonic mode is not affected by a phase difference. Zero, i.e., minimum emission is always at 0 deg and 90 deg amplitude difference and the maximum near 45 deg. The emission into the symmetric mode, on the other hand, is strongly influenced by the relative phase. For phase differences near $\phi = 0$ and $\phi = \pi$, a change in excitation angle will only lead to a monotonous transition between two coupling values. But around $\phi = \pi/2$ an additional minimum arises between those two values. By engineering the relative phase between the two eigenmodes, it is therefore possible to achieve zero emission into the symmetric target mode.

In summary, we have not only shown that SHG is possible in symmetric structures consisting of a symmetric material by simply offering plasmonic modes of appropriate symmetry, but also presented a completely new degree of freedom for nanocircuitry. The nonlinear operation strongly depends on amplitude and phase of the two eigenmodes and allows completely new schemes of operation.

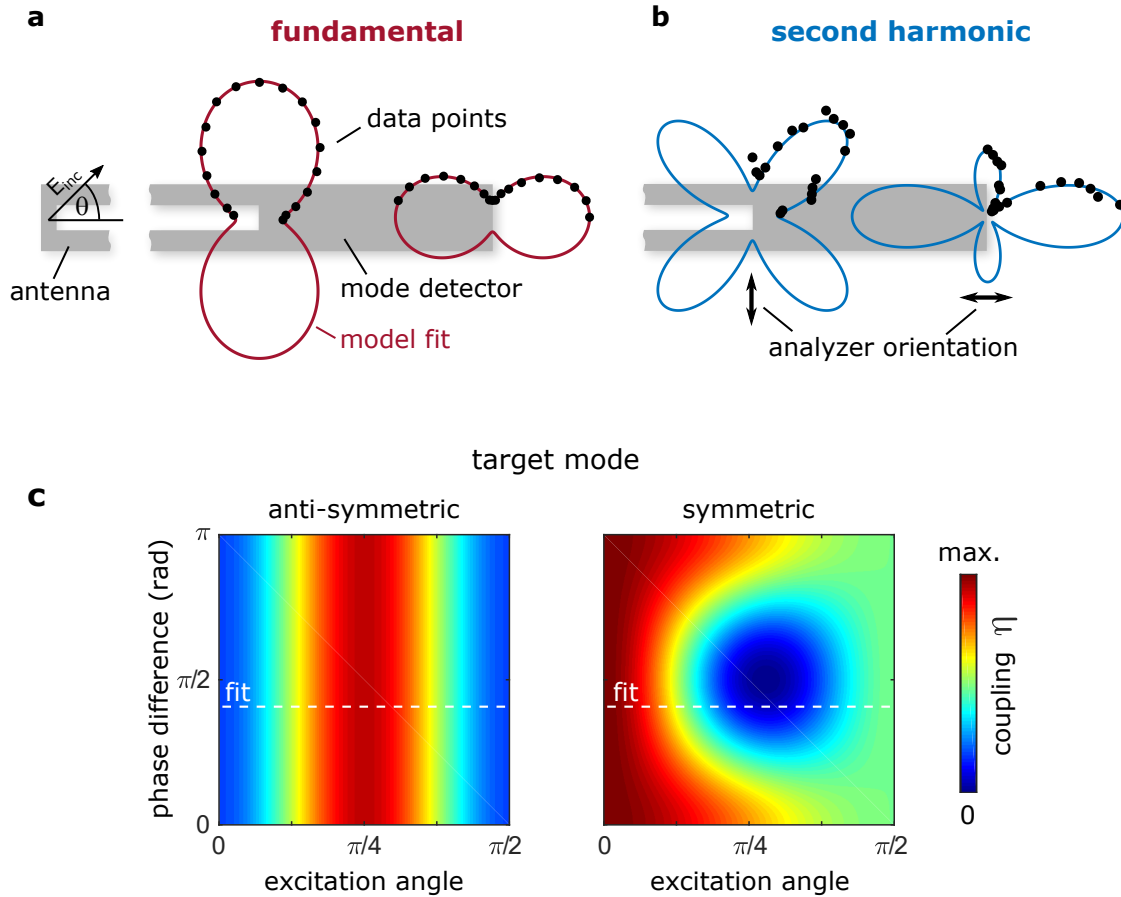


Figure 17: Generalized SH coupling properties of the nanocircuit. A fundamental mode superposition is obtained by a controlled excitation polarization of the laser under the angle θ w.r.t. the antenna. At the fundamental frequency (a), the two contributions of the mode superposition are mapped onto the corresponding mode detector ends. The black dots mark the measured emission under the excitation polarization θ and the solid lines represent model fits. At the second-harmonic frequency (b), the coupling behavior becomes more complex but is nicely described by our symmetry based model. By fitting the model to the data, we can recover enough information to predict the coupling behavior for changes in the relative phase ϕ of the superposition (c). The coupling to the anti-symmetric and symmetric target mode can be displayed in 2D color plots. Dashed white lines indicate the model curves plotted in (b).

5.4 INFLUENCE OF LOCALLY GENERATED SHG

One important point that hasn't been treated so far, is the influence of locally generated second-harmonic emission. In order to verify our findings from the previous sections free of any doubt, we have to carefully exclude this influence from our measurements and models. In general, there are two possibilities how local SHG could influence our findings. The first point of interest is the antenna used for excitation of the modes. As we observe in figure 16 (c)-(d), a strong signal of scattered second-harmonic light is visible at the antenna's location. This light could also partly couple into the TWTL and alter the experiment. The second point of interest is the mode detector. At both ends of the mode detector strong fundamental fields can be present - depending on the currently excited mode or mode superposition. During the outcoupling process of fundamental modes also second-harmonic scattering can occur and affect the light stemming from second-harmonic TWTL modes. We will treat both points of interest separately and show - that all of our observed effects stem from nonlinear interaction within the TWTL and are not influenced by local SHG.

5.4.1 antenna generated SHG

The antenna as excitation part of the structure is of course of asymmetrical shape and therefor second-harmonic emission into the far field is possible and observed. The question is, if also a reasonable amount of light could couple into the TWTL and cause the second-harmonic emission at the mode detector. In order to clarify this, we compared the scattered second-harmonic light from the antenna to an experimental model system. The antenna itself can be considered as a SRR with infinitely extended arms. Therefor, we use a SRR of similar geometry with long arms, i.e. 400 nm, as a reference system. This ensures that we are far away from strong, low order plasmon resonances in the arms at the second-harmonic frequency. Consequently, the process of SHG is not further boosted in comparison to the TWTL's antenna geometry. The measurements, resulting from this comparison, are shown in figure 18. It consists of two parts, corresponding to the fundamental (shown in red) and second-harmonic (blue) emission. The rows mark two perpendicular analyzer orientations while the columns at both frequencies are dedicated to the SRR and the antenna. For both structures, a true to size sketch is shown and the lasers excitation polarization is indicated as angle θ . The black dots in the polar plots mark the measured fundamental and second-harmonic emission, while the colored dashed lines serve as guides to the eye. They are obtained from periodically continued smoothing splines and offer an easier view on the excitation angle dependent emission.

If we look at the fundamental emission of the two structures, we observe a strong similarity in the patterns for both analyzer orientations. Moreover, the emission polarization also closely follows the excitation polarization. This leads to the conclusion that the off-resonant SRR is a well suited model system for the scattering properties of the TWTL's antenna. The second-harmonic emission pattern are more complex but also in good agreement. For vertically polarized detection, we observe minima at $\theta = 0$ deg and 90 deg with a maximum at about 45 deg in between. In the case of horizontal detection, we observe an elliptical shaped emission with differing aspect ratios. While the

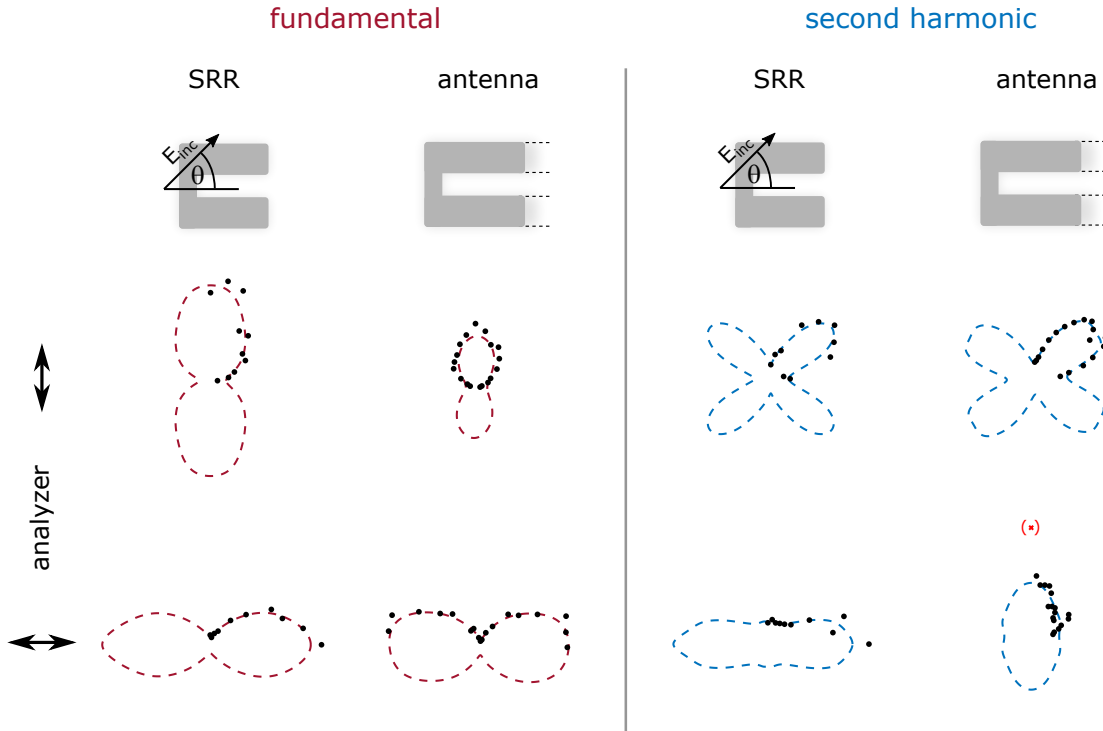


Figure 18: Excitation angle resolved fundamental (left, red) and second-harmonic (right, blue) emission of the antenna compared to a SRR. In each panel, the structure under investigation - antenna or SRR - is indicated. The two rows mark two different analyzer positions in front of the cameras. The measured signals are shown as black dots while the colored dashed lines serve as guides to the eye. Data points, excluded from the analysis, are displayed in red.

antenna's emission is predominantly oriented in vertical direction, the one of the SRR is horizontal. We attribute this feature to the finite length of the arms of the SRR. The off-resonant design makes it suitable as reference structure but especially in the horizontal polarization direction the shape still alters the scattering properties slightly.

In order to discuss potential correlations between local SHG at the antenna and the SHG emitted from the mode detector, we compare the excitation angle dependency of the emitted light from both positions. The comparison is shown in figure 19 (b), (c) for the two analyzer positions. The corresponding spatial positions on the structure are indicated in (a) and distances are given. Especially for the vertical analyzer position (b), the resemblance of the polar plots is very strong, thus, justifying the question if the measured signals at the mode detector could purely stem from local SHG at the antenna that couples to the TWTL. In order to rule this out we make two steps. First, we use the signals emitted from the mode detector and estimate how much scattered second-harmonic light would have to be emitted into the TWTL. We compare this value to the second-harmonic light scattered into the far field at the antenna and show that we would need an unphysically high ratio of coupling to scattering. In the second step, we argue that the antenna can be modeled as SRR with additional loss channel. If this loss

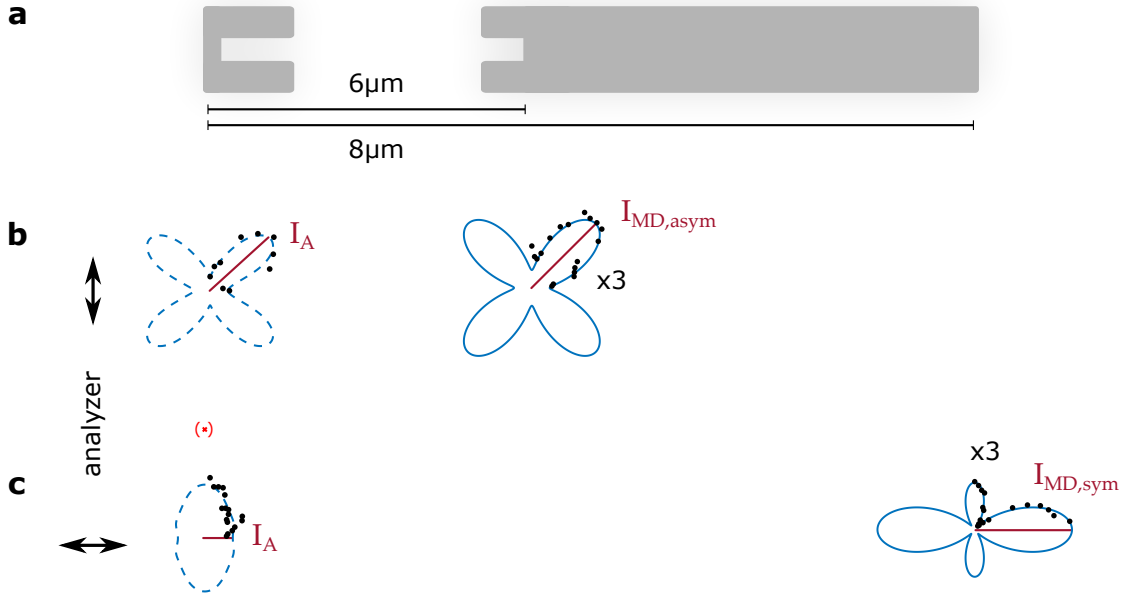


Figure 19: Excitation angle resolved second-harmonic emission from different positions of the nanocircuit. In (a) the positions are indicated. The emission pattern under the two analyzer positions are shown in (b) and (c). Black dots mark the measured data points, while solid lines represent model fits and dashed ones guides to the eye. For both analyzer directions the emission at the mode detector is scaled up by a factor of 3. The intensities I_A and $I_{MD,sym/asym}$ are defined in red for later analysis.

channel is really as big as calculated, it is not likely that the far field scattering pattern between antenna and SRR are still in good agreement.

analyzer	I_A	$I_{MD,asym}$	$I_{MD,sym}$	L_{prop} [μm]	$I_{TWTL}(0)$
↑	$6.0 \cdot 10^3$	$2.4 \cdot 10^3$	–	2.3	$3.5 \cdot 10^4$
↔	$2.2 \cdot 10^3$	–	$2.6 \cdot 10^3$	2.8	$4.7 \cdot 10^4$

Table 1: Measured and calculated intensities at different positions of the nanocircuit. The columns I_A and $I_{MD,sym/asym}$ are determined from measurements (see also figure 19). The last column $I_{TWTL}(0)$ represents the theoretical second-harmonic signal at the beginning of the TWTL and is calculated from the measured emission at the mode detector and theoretically obtained values for the propagation lengths l_{prop} .

For the estimation of potential antenna SHG, coupled to the waveguide, we use the second-harmonic signals from both ends of the mode detector. The chosen values and names of the variables are indicated in figure 19 (b) and (c) in red. The corresponding counts are given in table 1. While the plasmonic modes propagate along the TWTL, they experience damping which is described by the propagation length L_{prop} . For our estimation we use the relation

$$I_{TWTL}(l) = I_{TWTL}(0) e^{-\frac{l}{L_{prop}}} , \quad (92)$$

where $I_{TWTL}(l)$ describes the second-harmonic intensity at a certain length l of the waveguide. For $l = 0$ this value represents the total amount of second-harmonic light

coupled to the waveguide. To simplify the estimation, we assume an outcoupling efficiency of 100% and thus set $I_{\text{TWTL}}(l = \text{end}) = I_{\text{MD}}$. For the propagation of the anti-symmetric mode, we use a TWTL length of $6 \mu\text{m}$ and for the symmetric mode we neglect the transition in the waveguide's shape at the mode detector and use $8 \mu\text{m}$. The propagation lengths for the two modes are obtained from FEM simulations that take a lossless glass substrate as well as the 40 nm ITO layer into account. The refractive indices for ITO are taken from [114]. The calculated propagation lengths are given in table 1. If we compare the estimated intensities that would have to couple to the TWTL ($I_{\text{TWTL}}(0)$) with the ones scattered into the far field (I_{A}), we see that the coupling needs to be higher by a factor of 6 and 22 than the scattering. This ratio seems already quite unrealistic and we have to point out, that these ratios represent theoretical and highly idealized values. In reality, we will not have an outcoupling efficiency of 100% - already a value of 50% is an optimistic assumption. This will already double the coupling to scattering ratio. An adjusted propagation length will have an even bigger influence as it enters exponentially in the calculation. The value we chose for the calculation represents the theoretically reachable value and those values are hardly met in experiments. If we assume that we can reach 70% of the predicted value, the coupling to scattering factor at the antenna already increases to 36 and 150. Even if this factor would be reached in the experiment, the coupling to the TWTL poses an extremely efficient loss channel for the antenna. As we have shown, we can use a SRR to experimentally model the excitation angle dependent scattering from the antenna with the only difference of the TWTL being an additional loss channel. Under the circumstances of such tremendous additional losses we argue, that it is highly unlikely that the far field scattering pattern of both structures still agree very well. As consequence, we rule out that local SHG at the antenna couples efficiently to the waveguide and causes a noticeable contribution to the second-harmonic emission from the mode detector.

5.4.2 mode detector SHG

The second part in the experiment, where we could expect local SHG to alter our findings, is directly at the mode detector. Depending on the launched fundamental mode superposition, we obtain fairly high fundamental fields at either one or both ends. During the outcoupling process of the fundamental modes also local second-harmonic scattering can occur. We argue, that this is indeed possible and observed in the experiment, but only poses a minor contribution to our measured signals.

In this case the verification can again be done using excitation polarization resolved emission - now from the mode detector. The key point is, that we will not only investigate the emission under the predicted polarization but also the one rotated by 90 deg . We look at both mode detector ends under both analyzer directions. The results obtained for fundamental as well as second-harmonic emission are shown in figure 20. Again, solid lines represent model fits and dashed ones are guides to the eye. In the fundamental emission we observe the already discussed $\sin^2 \theta$ and $\cos^2 \theta$ behavior. They occur for a vertical analyzer position at the inner end of the mode detector and for a horizontal detection at the outer end. On the corresponding other ends we also observe fundamental emission, which is about a factor of 10 weaker but follows the angular behavior of the brighter end. Consequently, we attribute this emission to mode-splitting

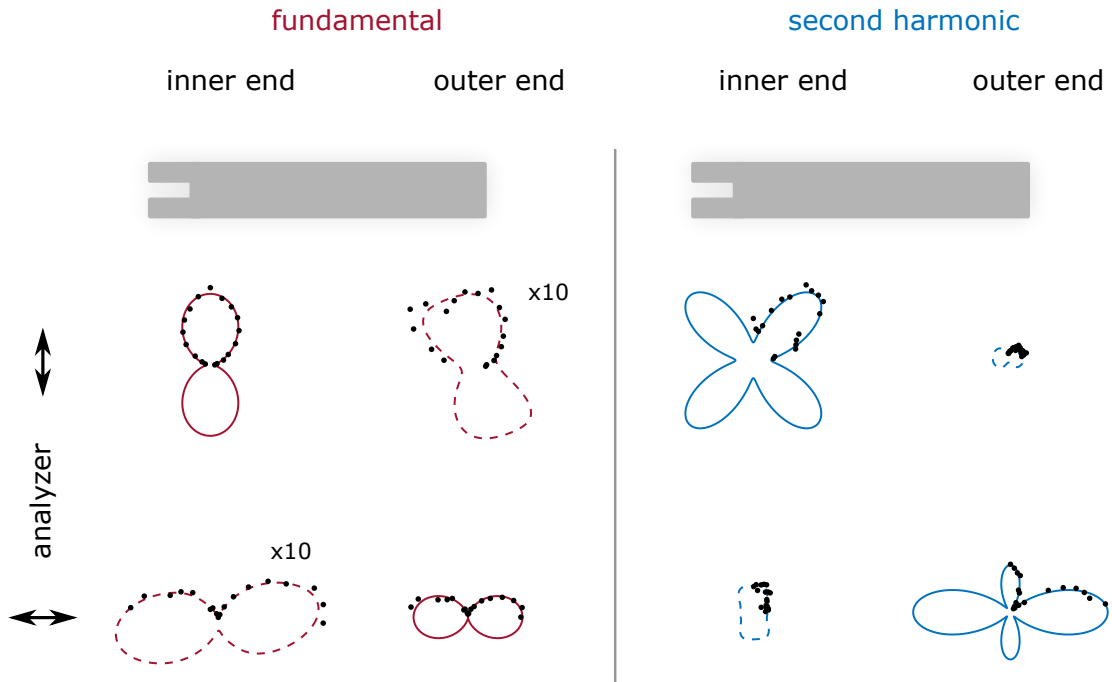


Figure 20: Excitation polarization resolved fundamental (left, red) and second-harmonic (right, blue) emission at the mode detector under two analyzer positions. The spatial origin of the individual signals is indicated by the schematic drawings of the mode detector. Again, black dots represent data points, dashed lines guides to the eye and solid lines model fits. Within the left and right panel all intensities are comparable in magnitude. Scaled amplitudes are indicated by the corresponding factor nearby.

quality of the structure. This can be caused by structural imperfections but also theoretically a perfect splitting is not possible. The two modes - anti-symmetric and symmetric - predominantly exist in the gap or on the outer edges of the waveguide but yet, the fields do not vanish at the other position. Therefore, always a certain portion of the mode will be emitted from the not desired mode detector end.

For the second-harmonic emission we also have the already discussed cases on the diagonal of the polar plot matrix. But in contrast to the fundamental case, the emission from the other mode detector ends (dashed lines) does not resemble the bright emission described by our model (solid lines). Therefore, it cannot be attributed to a limited mode splitting quality. We explain this emission by local SHG, caused by strong fundamental fields. Due to the locally curved surface of the TWTL, we argue that the second-harmonic light is strongly depolarized, scattered into the far field and follows the fundamental intensity at the corresponding mode detector positions. Both assumptions are backed up by the measurements. At the inner position of the mode detector, the fundamental pattern is oriented vertically (upper left, fundamental panel). If we look at the not expected second-harmonic emission from the inner end (lower left, second-harmonic panel), we notice that the pattern exactly follows the fundamental intensity. In general, this second-harmonic contribution is always present - also in the upper left panel. But there, it is just an additional offset for the strong, waveguide generated second-harmonic emission. Due to the depolarized nature of the scattering

process, this emission is also visible under the 90 deg rotated analyzer direction (lower left, second-harmonic panel). Therefore, it is not accompanied by strong waveguide SHG and we are able to relate the pattern to the strong fundamental intensity. The same chain of arguments can be applied to the second-harmonic emission from the outer mode detector end under vertical analyzer detection (upper right, second-harmonic panel). Here, the pattern is oriented horizontally and, therefore, follows the fundamental intensity at this position (lower right, fundamental panel). Again, the emission is visible because of the depolarized second-harmonic scattering.

Moreover, the pattern prove in a second way that local SHG at the mode detector only is a minor contribution to the overall process and that we, indeed, observe SHG generated during propagation in the TWTL. For a dominant local SHG at the mode detector, the second-harmonic emission would have to follow the fundamental intensity, which is obviously not the case for the diagonal pattern. Only our model, based on SHG during propagation, is capable of describing the observed effects. We can also rule out that an interference between the two fundamental modes can cause the observed pattern as for example at the outer end of the mode detector only one fundamental mode is left. We conclude, that local SHG at the mode detector is possible and also observed but only plays a minor and partly neglectable role in our experiments.

5.5 NONLINEAR PROPAGATION EFFECTS IN A TWTL

Up to this point, we only treated SHG in the TWTL in a 2 dimensional approach. The model for the coupling process of the second order nonlinear polarization to waveguide modes at the second-harmonic frequency takes place in a 2D cross-section of the waveguide and is purely based on symmetry arguments. Unknown parameters like, e.g., a phase mismatch between the traveling modes, was absorbed into fitting parameters and there was no necessity for a detailed investigation. The fact that we were able to exclude local SHG sources at the incoupling antenna and the mode detector as main source for the observed effects, we can extend our theoretical modeling to 3 dimensions and focus on SHG originating from the waveguide. Here, the mathematical formalism of the waveguide modes gives us certain advantages. The modes are described by a profile in the cross-section and the propagating part is given by a plane wave, differing from a free space mode by the effective mode index. This allows us to use a slightly modified plane wave ansatz like it is demonstrated in all standard text books on nonlinear optics. In order to treat propagating nonlinear phenomena, the Helmholtz equation in the following form is used

$$\nabla^2 \mathbf{E}(\mathbf{r}, t) - \frac{1}{c^2} \frac{\partial^2}{\partial t^2} \mathbf{E}(\mathbf{r}, t) = \frac{1}{\epsilon_0 c^2} \frac{\partial^2}{\partial t^2} \mathbf{P}(\mathbf{r}, t) \quad , \quad (93)$$

where the general polarization, including linear and nonlinear terms, acts as source for new electric fields. To adapt the equation for our needs, we use a time harmonic ansatz and only consider the propagation direction z . The electric fields at the frequency ω_n are written as $\mathbf{E}(\omega_n) = E_z(\omega_n)$. Moreover, we only consider second order nonlinear phenomena. This simplifies equation 93 to

$$\nabla^2 E(\omega_n) + k^2(\omega_n) E(\omega_n) = -\mu_0 \omega_n^2 P^{(2)}(\omega_n) \quad . \quad (94)$$

As we focus on SHG, we only need to consider two frequencies $\omega_n \in \{\omega, 2\omega\}$ and obtain a set of two coupled differential equations

$$\frac{d^2}{dz^2}E(\omega) + k^2(\omega)E(\omega) = -2\mu_0\epsilon_0\omega^2\chi^{(2)}E(2\omega)E^*(\omega) \quad , \quad (95)$$

$$\frac{d^2}{dz^2}E(2\omega) + k^2(2\omega)E(2\omega) = -4\mu_0\epsilon_0\omega^2\chi^{(2)}E(\omega)^2 \quad . \quad (96)$$

The second equation describes the process of SHG, while the first one describes the reverse down-conversion process from one photon at 2ω to two photons at the fundamental frequency. In order to solve these equations, we extract the propagating harmonic parts and write the electric fields as

$$E_\omega(z) = n_\omega^{-\frac{1}{2}}A_\omega(z)e^{-ik_\omega z} \quad , \quad (97)$$

$$E_{2\omega}(z) = n_{2\omega}^{-\frac{1}{2}}A_{2\omega}(z)e^{-ik_{2\omega}z} \quad , \quad (98)$$

with amplitudes $A_{\omega/2\omega}$ solely depending on the propagation direction z . At this point it is important to note that in our case the refractive indices $n_{\omega/2\omega}$ as well as the wave vectors $k_{\omega/2\omega}$ are complex valued. Due to this fact, the subsequent calculation differs from standard textbooks which frequently assume those values to be real. Inserting the ansatz 97 and 98 into equations 95 and 96 leads to

$$\frac{d^2}{dz^2}A_\omega + c_1\frac{d}{dz}A_\omega = c_2A_{2\omega}A_\omega^*e^{-i(k_{2\omega}-2\text{Re}\{k_\omega\})z} \quad , \quad (99)$$

$$\frac{d^2}{dz^2}A_{2\omega} + c_3\frac{d}{dz}A_{2\omega} = c_4A_\omega^2e^{-i(2k_\omega-k_{2\omega})z} \quad , \quad (100)$$

with the coefficients

$$c_1 = -2ik_\omega \quad , \quad (101)$$

$$c_2 = -2\mu_0\epsilon_0\omega^2\chi^{(2)}n_{2\omega}^{-\frac{1}{2}}(n_\omega^{-\frac{1}{2}})^*n_\omega^{\frac{1}{2}} \quad , \quad (102)$$

$$c_3 = -2ik_{2\omega} \quad , \quad (103)$$

$$c_4 = -4\mu_0\epsilon_0\omega^2\chi^{(2)}n_\omega^{-1}(n_{2\omega}^{\frac{1}{2}}) \quad . \quad (104)$$

Finally, we use the slowly varying envelope approximation (SVEA), which simplifies our coupled differential equation system to

$$\frac{d}{dz}A_\omega = \frac{c_2}{c_1}A_{2\omega}A_\omega^*e^{-i(k_{2\omega}-2\text{Re}\{k_\omega\})z} \quad , \quad (105)$$

$$\frac{d}{dz}A_{2\omega} = \frac{c_4}{c_3}A_\omega^2e^{-i(2k_\omega-k_{2\omega})z} \quad . \quad (106)$$

One important thing we observe in the equations are the damped oscillating terms, incorporated by complex exponential functions. On one hand, they lead to damping in the lossy material and, on the other hand, they lead to an oscillating behavior of energy between the fundamental and the second-harmonic wave, if there is a phase mismatch between the wave vectors. The length corresponding to this phase mismatch is the coherence length (see chapter 2.4.3). For our waveguide, this length can be assumed to lie in the range of a few microns and should, therefore, be measurable.

In order to adapt those equations completely to our structure, we have to take SHG at the antenna as well as local SHG at the mode detector into account. Although antenna SHG will not reach the mode detector, as we argued in the previous chapter, we will include it as it may play a role on short length scales. Local SHG at the mode detector was also found to play a minor to negligible role, but will also be included for the purpose of generality. Finally, this leads to an electric field that reads

$$E_{\text{total}}(2\omega, z) = E_{\text{TWTL}}(2\omega, z, \alpha_0, \phi_0) + \underbrace{E_{\text{MD}}(2\omega, z)}_{\propto E(\omega, z)^2}, \quad (107)$$

where E_{TWTL} is the electric field obtained from the coupled differential equations. The starting conditions α_0, ϕ_0 account for antenna SHG in the equations. E_{MD} accounts for local SHG at the end of the structure and is proportional to the squared fundamental field strength. If we look at the coupling from the anti-symmetric fundamental mode to the symmetric second-harmonic mode, this last term can be neglected, because there is no fundamental power reaching the end of the mode detector in first approximation. Finally, the intensity at the second-harmonic frequency is calculated as squared absolute value of the electric field.

In order to investigate the phase mismatch between fundamental and second-harmonic waveguide mode, we use structures of different length, i.e., different lengths of the TWTL. Here, the challenge is to account for potentially different antenna excitation efficiencies on different structures. One way to treat this problem is to investigate several structures for each length and perform a statistical analysis. We decided for a different, more efficient approach and produced waveguides that feature an additional reference arm. An SEM picture of such an H-shaped structure is shown in figure 21 (a). The upper part of the nanocircuit is the structure under investigation, where the length of the TWTL is tuned from 2.5 to 6 μm . The lower part is the reference arm with a fixed length of 3 μm for all structures. In both arms, the TWTL is terminated with a mode detector in order to distinguish between modes. One important thing we want to mention is, that the antenna is now of a more symmetric shape. Therefore, one could expect less SHG to be scattered into the far field. Counterintuitively, we observed stronger SHG from the H-shaped antenna and attribute this to an increased scattering at surface roughnesses. Although the antenna is of symmetric shape, the geometrical cross-section filled with gold has increased. This leads to an increased scattering from structural imperfections and edges. In the near field, this change in antenna symmetry has no effect since SHG is not symmetry forbidden on this length scale. The only thing we want to point out is, that of course the launched power of the fundamental modes is split into both arms and, moreover, the relative phase that the antenna gives to the modes might change in comparison to the single sided nanocircuit.

The idea for the experiment is to measure structures with different lengths, scale the emission to the reference arm and finally fit the developed model (equations 105 - 106) to the obtained data. Therefore, the system of coupled differential equations is implemented in an optimization algorithm and solved consecutively with varying parameters, until an optimum is found. Here, it is important to fix as many open parameters as possible, in order to avoid an overparameterized problem. In our system, the unknown parameters are the wave vectors $k_{\omega/2\omega}$ and the refractive indices $n_{\omega/2\omega}$. Fortunately, those values are connected via the known vacuum wave vector $k_{0,\omega/2\omega}$. Due to the complex nature

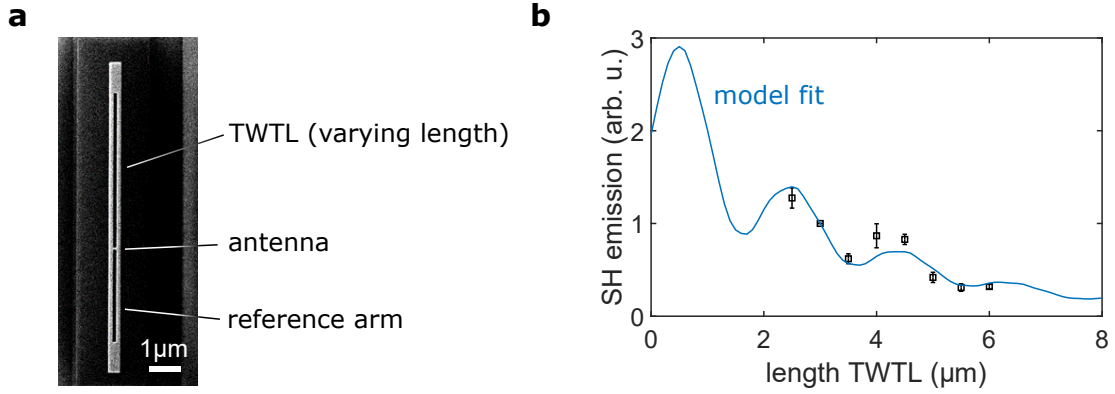


Figure 21: Experimental data on nonlinear propagation effects in the TWTL. The H-shaped structure (a) consists of two connected nanocircuits. The upper arm has a TWTL with varying length and the length of the lower arm, the reference arm, is fixed. Both arms are terminated with a mode detector. Varying the upper arm's length yields length dependent second-harmonic emission (b) (black dots), that can be well described by our model (solid blue line).

of those parameters, we have four unknown quantities - regarding real and imaginary parts as separate values. A further determination of parameters could be done using values obtained from theoretical simulations, but this poses two problems. First, we already mentioned that theoretical propagation lengths (linked to the imaginary part of the wave vectors) are commonly much higher than in experiments. Second, the simulations would also require to involve the ITO spacer layer beneath the nanocircuit with preferably accurate optical properties. As an alloy, those properties strongly depend on the fabrication process [115] and the potentially followed treatment like, e.g., tempering. Consequently, reported optical properties differ [114–117] and often only values for the visible spectral range are reported. Especially in the near to mid infrared range, the complex refractive index of ITO varies strongly with changes in the fabrication process. From our point of view, it would be necessary to fully characterize the complex refractive index of our ITO layer, using spectral ellipsometry, if all mode indices have to be fixed to certain values.

Nevertheless, we decided to fix certain values of the mode indices. As the reported optical constants for ITO in the visible spectral region seem to be the most reliable, we use the data of König et al. [114] for the 40 nm ITO spacer layer and obtain an effective mode index of $\text{Re}(n_{\text{eff}}(2\omega)) = 1.77$ from Comsol simulations. The real part of the fundamental mode index is kept as open parameter as it will influence the coherence length in the model. The imaginary part, on the other hand, can be determined in experiments. By measuring structures of different lengths at the fundamental frequency, the propagation length of the structure was determined to be $l_{\text{prop}}(\omega) = 6.5 \mu\text{m}$ for the anti-symmetric waveguide mode. Additional efforts to measure the propagation length at the second-harmonic frequency, using our laser with doubled frequency for excitation, were not successful. Even for a TWTL length of $2.5 \mu\text{m}$, no emission from the mode detector was observed for the symmetric waveguide mode. Therefore, we decided to fix the propagation length to $l_{\text{prop}}(2\omega) = 1.5 \mu\text{m}$. The additional two parameters, that are left open, are the starting conditions (a_0, ϕ_0) we provide to the equation system. As

mentioned previously, we investigate the coupling from a fundamental anti-symmetric mode to a second-harmonic symmetric one and local SHG at the mode detector is thus negligible. The measured data as well as the fitted model from equation 107 is shown in figure 21 (b). Already in the experimental data an oscillating behavior of the emitted second-harmonic intensity can be observed. Moreover, this behavior is nicely described by our developed model. The fitted real part of the fundamental mode index is determined as $\text{Re}\{n_{\text{eff}}\} \approx 1.4$, which lies in the region of refractive indices reported for ITO films in the infrared spectral region [117].

Yet, we want to point out that the model could still be optimized and incorporate additional details. For example, we neglected the distance the second-harmonic mode has to travel along the mode detector as well as the transition from the TWTL to the slap-like shape. The first assumption can be made in the case of anti-symmetric-to-symmetric coupling, as only the second-harmonic mode travels this distance. If the fundamental mode and, thereby, local SHG at the mode detector cannot be neglected, this additional length in the structure has to be taken into account. Moreover, additional measurements, including more data points, would benefit the fitting procedure of the model and allow a more stable optimization. Despite these circumstances, the model represents an easy and intuitive approach that, combined with our previous findings, further proves that we observe SHG from the TWTL part of our nanocircuit.

5.6 INFLUENCE OF ITO SPACER-LAYER

The final potential influence on our measurements, that we want to discuss, stems from the ITO film beneath the nanocircuit. Despite the complex and partly unknown exact linear optical properties, also nonlinear properties can play a role. It is long known that ITO itself possesses a non-vanishing second order nonlinearity [118, 119]. In general, the surface nonlinearity of gold overwhelms the bulk nonlinearity of ITO [120]. However, under certain circumstances, the nonlinearity of ITO can become quite strong. The region in which this happens is called the epsilon-near-zero (ENZ) region. As the name states, the electric permittivity, to be exact the real part, is close to zero. This class of materials has recently been under investigation and unexpected high nonlinear efficiencies have been reported [121, 122]. We do not want to discuss the circumstances in detail and refer the interested reader to a recently published review on this topic [123]. In all studies, that involve high conversion efficiencies from ITO, the films were explicitly tailored to operate in the ENZ region. In order to achieve ENZ behavior in a certain spectral range, fabrication and post-fabrication steps (e.g. temperatures or additional tempering steps) have to be carefully modified. Outside these designed wavelength intervals, nonlinear efficiencies drop drastically by orders of magnitude. Since our ITO films were not explicitly designed as ENZ material, we argue that it is highly unlikely that, by accident, we achieved drastically enhanced nonlinear properties. Nevertheless, we want to investigate the potential influence of a nonlinear substrate theoretically and check if a tailored ENZ substrate might, in fact, give rise to an increased or modified nonlinear operation of the nanocircuit.

For the theoretical investigation of the ITO influence we make use of mode overlap integrals from chapter 4.2. In contrast to the previously used formulation from equation 83, which was formulated for surfaces, we use the general expression from equation 82. This applies if a bulk nonlinearity of the material is assumed. As mentioned previously, the optical properties of ITO can strongly differ depending on the exact fabrication and post-fabrication procedure. Therefore, we will not use an ITO layer per se, but rather a glass substrate and assign it the nonlinear properties of ITO. Since we are not interested in absolute coupling values or mode indices but only in coupling symmetries, this assumption can be made without loss of generality. The used mode profiles can be found in appendix A.2. In order to calculate the resulting second order nonlinear polarization, we use the information about the nonlinear susceptibility of ITO from [122]. The only non-vanishing tensor elements are

$$\chi_{yyyy}^{(2)} \neq 0 , \quad (108)$$

$$\chi_{zzz}^{(2)} = \chi_{zyz}^{(2)} = \chi_{xxy}^{(2)} = \chi_{xyx}^{(2)} \neq 0 , \quad (109)$$

$$\chi_{yyz}^{(2)} = \chi_{yxx}^{(2)} \approx 0 , \quad (110)$$

where the last two contributions are negligible. Between the two remaining contributions, the yyy -component was determined to be larger by a factor of 3.6. We want to point out, that in reference [122] the coordinate system was chosen differently. We adapted the parameters to our coordinate system and therefore the indices x, y, z are not directly comparable. Finally, we obtain the nonlinear polarization as

$$P_x^{(2)} \propto 2\chi_{xxy}^{(2)} E_x E_y , \quad (111)$$

$$P_y^{(2)} \propto \chi_{yyy}^{(2)} E_y E_y , \quad (112)$$

$$P_z^{(2)} \propto 2\chi_{zzz}^{(2)} E_z E_z . \quad (113)$$

The calculation is applied to the whole substrate underneath the TWTL. Performing a mode overlap calculation to the nonlinear substrate yields the results displayed in figure 22. The columns mark the nonlinear polarization $P^{(2)}(2\omega)$ as source mode and the rows the target modes $E(2\omega)$. In the plots, the cross-section of the TWTL is in the x - y plane and the circumference of the waveguide, as well as the cut to the substrate, is indicated by solid black lines. The absolute value of the coupling integrand is displayed as a surface with the corresponding strength in z -direction. Again, we use a color code to indicate the relative phase of the coupling integrand. If we look at the results, we see that the coupling behavior is similar to the one obtained for the gold surface nonlinearity. For both nonlinear polarizations - resulting from a symmetric and an anti-symmetric fundamental mode - we only obtain coupling to the symmetric second-harmonic mode. An emission into the anti-symmetric mode is not achieved due to a cancellation, originating from the phase difference of π between the two single wires. Consequently, a nonlinear substrate, that exhibits nonlinear properties like ITO, leads to the same coupling mechanism like the gold wires.

Although SHG from a nonlinear ITO substrate exhibits the same symmetry rules as SHG from a gold surface nonlinearity, we attribute the observed second-harmonic emission in our experiments to the later. As mentioned, both nonlinearities are only comparable, if the ITO is specifically designed to work in the ENZ region - which is not

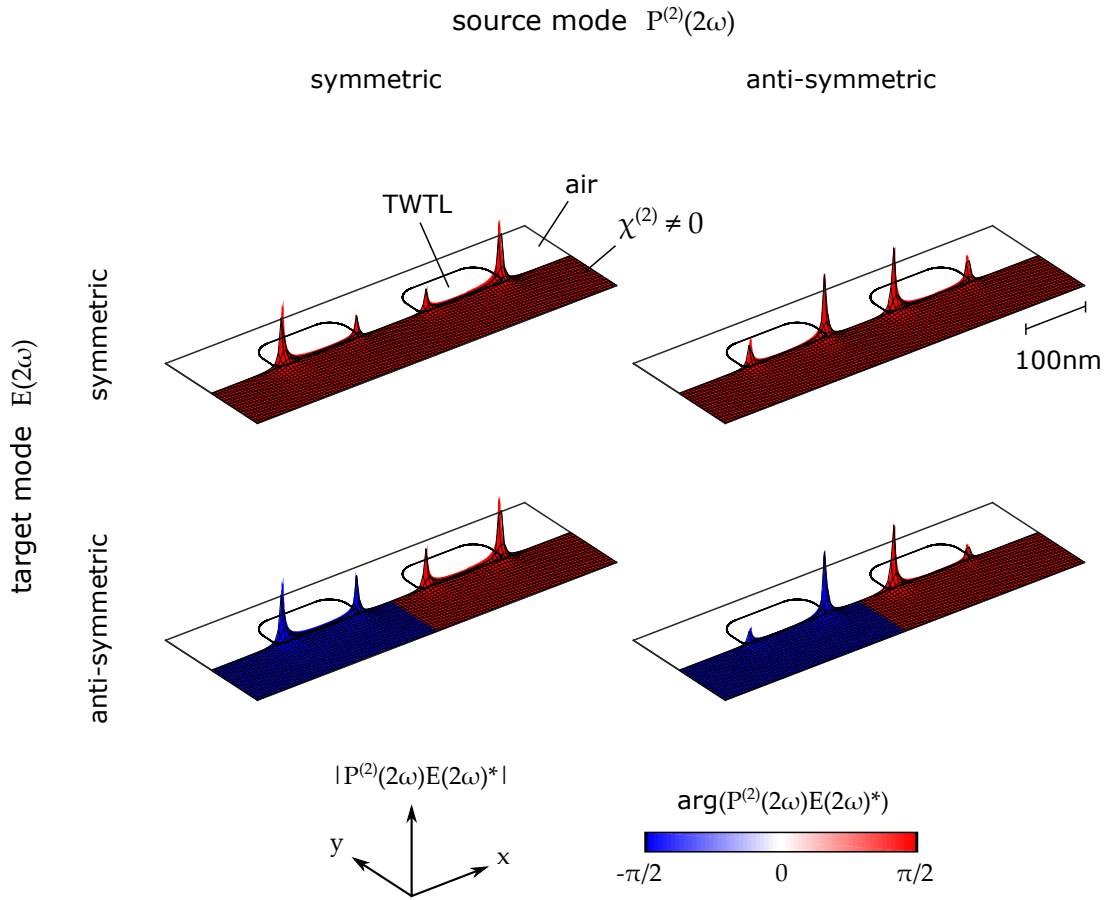


Figure 22: The four possible combinations of overlap integral integrands for a second order nonlinear substrate. The cross-section of the TWTL is in the x - y plane and the normalized absolute value of the integrand is in z -direction. The phase of the complex valued integrand is color coded. For the substrate, a non-vanishing second order non-linearity $\chi^{(2)} \neq 0$ is assumed. The interface as well as the TWTL is indicated in the cross-section.

the case in our experiments. For us, a potential influence of ITO poses therefor a unique possibility. If engineered to the ENZ region, we might be able to boost the efficiency of our nanocircuit's nonlinear operation further. Furthermore, this demonstrates the future possibilities of our findings. With simple mode overlap calculations, we can start to modify the coupling mechanism in the TWTL by a nonlinear substrate.

Nevertheless, we want to demonstrate experimentally that our findings originate from a gold surface nonlinearity, free of any doubt. For this purpose the most suited approach is to investigate a sample without ITO layer. As mentioned earlier, this layer was necessary for the FIB milling process (see chapter 5.1). Consequently, we switched to a different fabrication process that does not involve an ITO layer but only has a glass substrate underneath the nanocircuit. Although we lose the benefit of highest surface quality of single crystalline gold flakes, we decided to use EBL with rf-gold-sputtering. Structures with equivalent geometrical properties were fabricated and investigated. For a prove

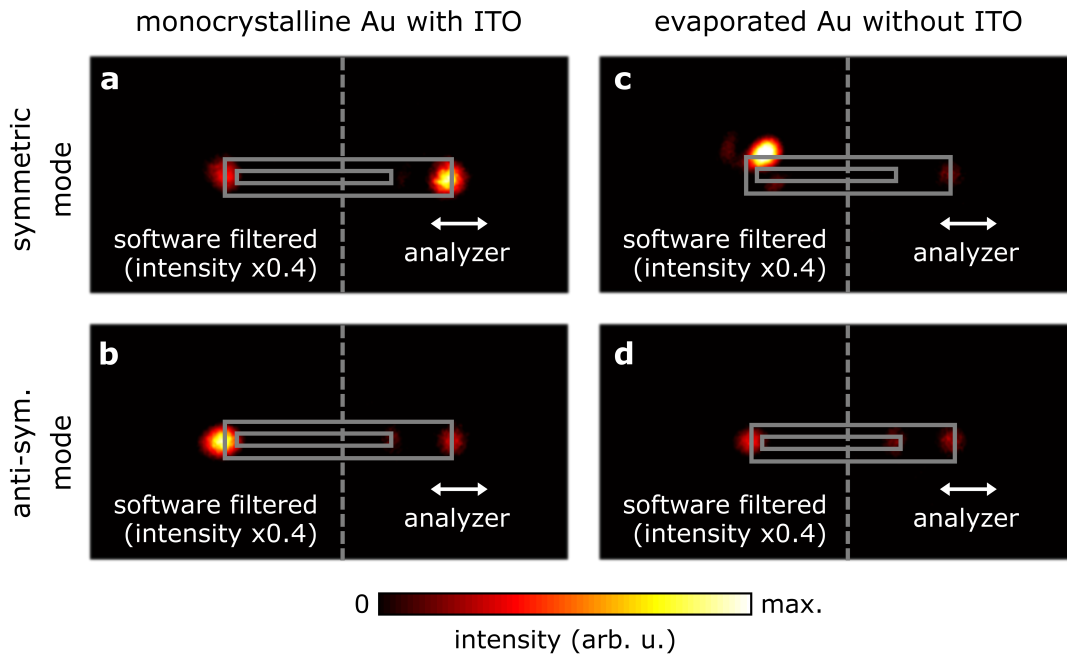


Figure 23: Comparison of the second-harmonic emission properties of two different sample types. In panels (a) and (b) the nanocircuit, involving antenna, TWTL and mode detector, is located on an ITO substrate. The fabrication was done via FIB milling on a single crystalline gold flake. This results in the highest possible surface quality. In (c) and (d) the same structure was produced via EBL and rf-sputtering. The resulting coarser surface as well as the change in substrate layer, leads to a decreased emission from the mode detector. Despite this fact, both sample show the same emission properties.

of concept, we repeated the measurements from figure 16 (c),(d) on those samples, i.e., demonstrated that pure symmetric and anti-symmetric fundamental modes only couple to a symmetric second-harmonic waveguide mode. The results are shown in figure 23. All panels show images of the waveguide at the second-harmonic frequency. At the incoupling part of the structure, a software based filter was applied in order to reduce the strong second-harmonic scattering. The rows mark the two different pure fundamental modes, while the columns distinguish between the two different samples - FIB and EBL production. Panels (a) and (b) were already discussed in section 5.2. In (c) and (d) we observe the same behavior. For a pure fundamental mode, the second-harmonic emission always stems from the right end of the mode detector, e.g., the symmetric waveguide mode. In general, the emitted number of photons from the mode detector in (c) and (d) are roughly three times weaker. We attribute this to a drastically increased surface roughness of the EBL sample due to the rf-sputtering process of the gold. Moreover, also the changed refractive index beneath the structure can have an influence. As designed and desired, the EBL substrate is only consisting of glass which of course offers a different refractive index. This can affect the effective indices of the modes as well as the outcoupling properties of the mode detector.

5.7 CONCLUSION

In summary, we have demonstrated experimentally that SHG in nanostructures, made of inversion symmetric materials, does not necessarily require a structural asymmetry. By the use of a plasmonic TWTL we were able to show that second-harmonic light is emitted, if an optical or plasmonic mode of suitable symmetry is present. The SHG from both fundamental eigenmodes of the system is only emitted into one second-harmonic waveguide mode. Additionally, we expanded the theory of this second-harmonic coupling mechanism to arbitrary fundamental mode superpositions and verified the model for different amplitude ratios. By the use of the experimentally obtained data, we were also able to exclude local SHG effects from our measurements and verify that the observed second-harmonic emission stems from the TWTL. Numerically we predicted a coupling behavior, involving also phase differences between fundamental modes, that offers a more complex scheme and therefor opens up new possibilities in the future. Moreover, we introduced a nonlinear propagation model based on lossy coupled amplitude equations, that intuitively adds a third, spatial dimension to our previous calculations. Finally, we explored a 2D coupling model that adds a nonlinear substrate and might give rise to an even more complex and variable coupling behavior as well as an increased nonlinear efficiency.

The research in the field of nonlinear optics and plasmonics requires high electric fields, in order to gain a substantially high nonlinear polarization. One way to achieve this, is of course the high and subwavelength localization of electric fields like, e.g., provided by plasmonic hotspots [124]. A more general approach is the use of short and ultra short laser pulses. Here, the peak amplitude of the electric field can easily overcome the continuous wave amplitude by several orders of magnitude for comparable time averaged powers. In general one can assume, the shorter the pulses, the higher the peak amplitude. Therefore, the generation of ultra short pulses is of great interest. The first techniques for short pulse generation involved active Q-switching, i.e., an active modulation of intra cavity losses in the laser [125]. Consequently, the obtained laser pulses are short but not ultra short. The discovery of passive Kerr-Lens modelocking in Titanium Sappire (Ti:Sa) oscillators changed the game and allowed an easy and stable generation of sub-picosecond laser pulses [126]. Parallel to that, other passive mode locking techniques, involving saturable materials, evolved. They can be used for short and ultra short pulse generation [127]. Nowadays, those saturable absorbers are used for mode locking of, e.g., vertical-external-cavity surface emitting lasers (VECSEL) [128] or to ensure stable or self starting mode locking in ultra short laser cavities [129].

In this chapter we focus on the investigation of a semiconductor saturable absorber mirror (SESAM), which is used to achieve pulsed operation in a VESCEL. The laser itself was already under investigation [130] but the ultra fast temporal dynamics of the newly designed SESAM, involving quantum dots (QDs), were not revealed until now. First, we provide an overview of SESAM fundamentals as well as over time resolved measurement techniques. This is followed by an explicit discussion of the QD-SESAM under investigation, including its unique possibilities, and finally we present measurements that reveal the temporal dynamics of the structure.

6.1 INTRODUCTION TO SESAMS AND TIME RESOLVED MEASUREMENTS

Especially for the measurement of ultrafast dynamics, real time techniques are not suitable anymore. Effects on the pico- and sub-picosecond time scale are too fast for the speed of electronics. This includes the measurement process as well as the subsequent data acquisition and data processing steps. Therefore, one has to make use of a different technique that is not based on real time monitoring, but transfers the time component to another quantity. This is done in pump-probe measurements. The basic principle is sketched in figure 24 (a) in an energy level diagram. A strong pump laser pulse with

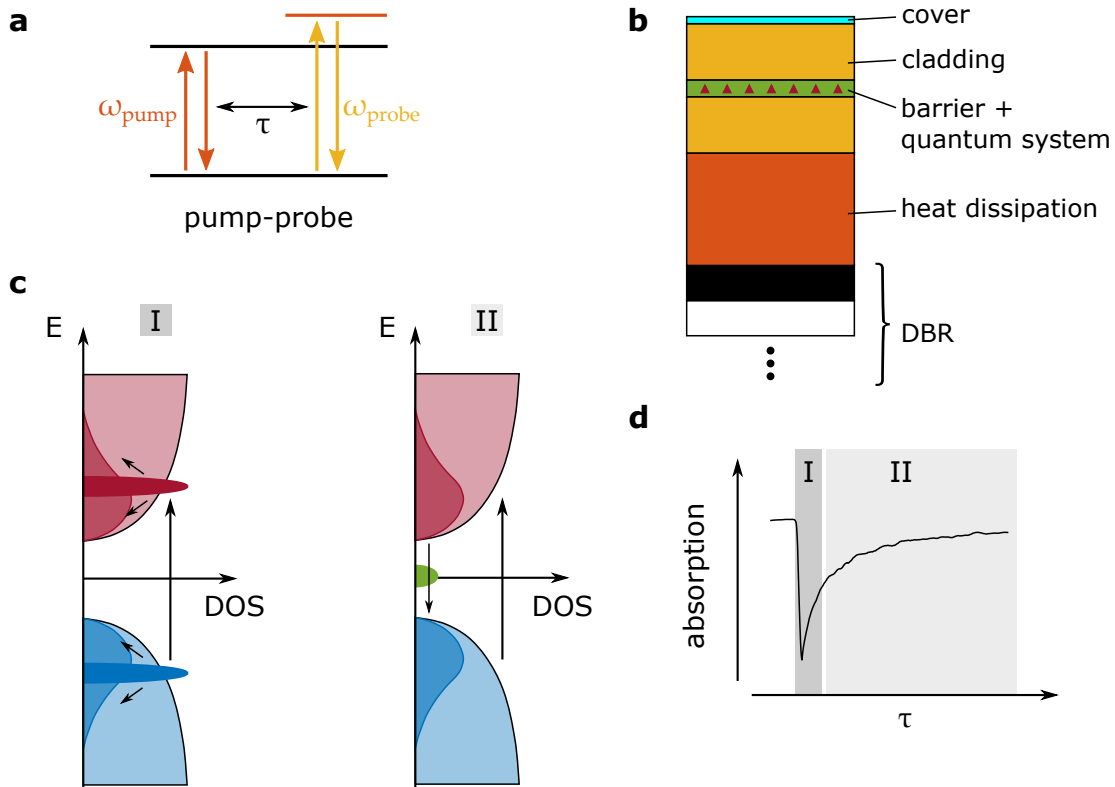


Figure 24: Principle of pump-probe measurements on SESAMs. (a) The pump-probe measurements can be represented in an energy level diagram. The pump pulse prepares the system in a perturbed state (orange energy level), that is monitored by a probe pulse after the time τ . (b) A SESAM consists of different layers of semiconductor material. The distributed Bragg reflector at the bottom leads to a high reflectivity and the active region, represented by the quantum system, can be saturated by high optical powers. (c) The saturation process is sketched in a DOS-energy diagram. After the saturation, the excited state relaxes via fast interband processes (regime I). On a longer time scale, radiative recombination takes place (regime II) and the system fully relaxes back to its initial state - sketch idea adapted from [127]. The relaxation times can be influenced by the creation of trap states in the material (green). (d) The corresponding absorption dynamic to (c) is shown in a typical time trace.

the frequency ω_{pump} perturbs the system under investigation and after a defined time τ , a probe pulse with frequency ω_{probe} monitors the change via a change in, e.g., reflectivity, transmittance or absorption. In general, the pump-probe process can be seen as a photon-photon interaction process which does not depend on the pump phase. Consequently, it can also be written as an effective $\chi^{(3)}$ process

$$\mathbf{P}^{(3)}(\omega_{\text{probe}}) = \epsilon_0 \chi^{(3)} |\mathbf{E}(\omega_{\text{pump}})|^2 \mathbf{E}(\omega_{\text{probe}}) . \quad (114)$$

In measurements it is common to realize the temporal distance between pump and probe pulse via a relative change in the optical path length. Usually, this is achieved by a delay stage that changes the length of the pump or probe path before the recombination on the sample. Thus, the temporal resolution is limited by the pulse length of the two pulses as well as the resolution of the delay stage. In general, the first one is the

limiting factor.

In figure 24 (b) the basic composition of a SESAM is shown. The structure is located on a substrate and, from bottom to top, the first unit is a distributed Bragg reflector (DBR). The periodically alternating semiconductor layers are tailored to achieve a spectral window of high reflectivity in the region of the desired operation wavelength. Due to high optical powers, the next layer is a heat spreading layer that circumvents thermal damage to the system. In the next system of layers, the absorbance of the structure takes place. In the center a quantum system is located. It can be either one or several quantum wells (QW) or also quantum dots. These quantum systems will be saturated by incoming light and in consequence change the absorbance and, therefore, the reflectivity of the entire structure. Around the quantum system additional barrier and cladding layers are used - also consisting of semiconductor materials. They compensate strain induced by the quantum system and ensure an increased charge carrier confinement [131, 132]. At the top, the SESAM is terminated by a cover layer that prevents oxidation and other pollution of the semiconductor surface.

In figure 24 (c) and (d) the working principle of a SESAM is sketched. A more detailed description can be found in ref. [127]. (c) shows the energy dependent density of states. In blue, the valence band of the quantum system is shown and in red the conduction band. Vertical arrows indicate optical transitions. The drawing is shown for a QW SESAM. If an intense optical pulse hits the sample, a standing wave pattern builds up due to the DBR. In the QW, electrons are excited to the upper state until it is completely filled and further absorption is not possible. This is sketched in the left panel of (c). The corresponding regime (I) in the temporal evolution of the system is shown in (d). When the excited state gets saturated, no further absorption from the ground state is possible and the total absorption of the SESAM drops. The saturated excited state relaxes on a time scale of several hundreds of femto seconds via non radiative processes, followed by partly radiative recombination on a time scale of pico to nano seconds (regime II). Therefore, SESAMs are well described by a bi-exponential decay or recovery curve. The two time constants can be influenced by the choice of the semiconductor material and especially the quantum system in the active region. Additionally, a tailoring of the long time constant can be easily achieved by the intentional creation of trap states in the band gap (shown in figure 24 (c) in green). The modulation of the absorption makes the SESAM so well suited for applications in lasers. As part of the cavity, the SESAM is able to passively modulate the intra-cavity losses - the drop in absorption leads to an increased gain. Consequently, the pulses, traveling in the laser cavity, generate a low-loss window for themselves and stabilize the pulsed operation. Moreover, this technique can be used for self started mode locking.

The characteristic time constants of a SESAM are commonly investigated via pump-probe measurements [131]. The pump pulse is given a high power in order to saturate the absorber and the subsequent low power probe pulse monitors the time dependent change in the system via the perturbed reflection. With this, not only the dynamic evolution of the system can be revealed but, moreover, also parameters like, e.g., the pump power can be varied in order to gather further information about the saturation process.

6.2 EXPERIMENTAL SETUP

For the experimental investigation of a SESAM's saturation dynamics it is necessary to use the same wavelength for pump and probe. The result is a so called degenerate pump-probe experiment. The setup we used, is a home built reflection microscope and shown in figure 25 (a). As laser source serves a commercial optical parametric oscillator (OPO) from APE Berlin. In the visible configuration it provides wavelengths between 550 nm and 750 nm with a spectrally dependent power of up to several hundreds of milli watts and a pulse duration of about 200 fs. The OPO itself is pumped by a Ti:Sa oscillator (Coherent Mira HP, 150 fs, 808 nm, 76 MHz, 4.5 W) using a pump power of 2 W. After the OPO, the laser beam is split into pump and probe part and both are given orthogonal polarizations. In the pump path, a delay stage (Owis Limes 150) as well as an optical chopper (Thorlabs MC2000B-EC with MC2F47) for modulation are included. The delay stage has a travel of 15 cm, which allows an accessible delay range of up to nearly one nano second. Afterwards, both beams are spatially filtered by pinholes, reunited in a polarizing beam splitter and focused onto the sample using a 35 mm focal length achromatic lens. Via a 50 : 50 beam splitter, the reflected signal from the sample is partly guided to the detection devices. Here, the remaining pump light is removed using a polarizer. An additional Soleil-Babinet compensator in front counterbalances a potential phase, added to the pump beam's polarization by optical elements in the path. After the compensator, the pump polarization can be assumed free of elliptical contributions and is highly efficient suppressed by a Glan-Thompson polarizer. For the detection of the probe light, a photo diode (femto OE100), combined with a Lock-In detector (Stanford Research Systems SR830), is used. In order to suppress fluctuations in the probe beam, we use balanced detection, i.e., we detect the difference of the detection diode and a reference diode in the probe path. The Lock-In detector demodulates on the reference signal given by the optical chopper in the pump path at a frequency of $f_{\text{pump}} = 700$ Hz.

In general acousto-optical modulators (AOMs) are preferred over optical choppers as they allow much higher modulation frequencies. In this experiment we decided for a chopper based on two arguments. First, we want to have as much accessible pump power as possible. In an AOM the light wave is refracted at a phonon wave and only the first refraction order is modulated and used for the later experiment. Nowadays, there are highly optimized AOMs but yet, one still loses power. Second, we want to keep our setup as flexible as possible, which includes wavelength tuning with the OPO. Again, the refraction in the AOM poses a problem, as the angle of the first refraction order is wavelength dependent. In consequence, a change in the operation wavelength would require a complete realignment of the setup. In similar experiments [131], often a double modulation scheme, including additional probe modulation, is used. In these cases, the Lock-In is referencing on the sum- or difference-frequency signal. We decided against this technique because we observed a parasitic signal at the detection frequency, when we used one chopper head with a dual frequency chopper blade for modulation. Details can be found in the appendix A.3.

One parameter we intend to vary in our experiments is the pump fluence. This quantity is directly related to the pump power as well as the spot size on the sample. Therefore, it is important to measure the later in the sample plane with our used 35 mm achromatic

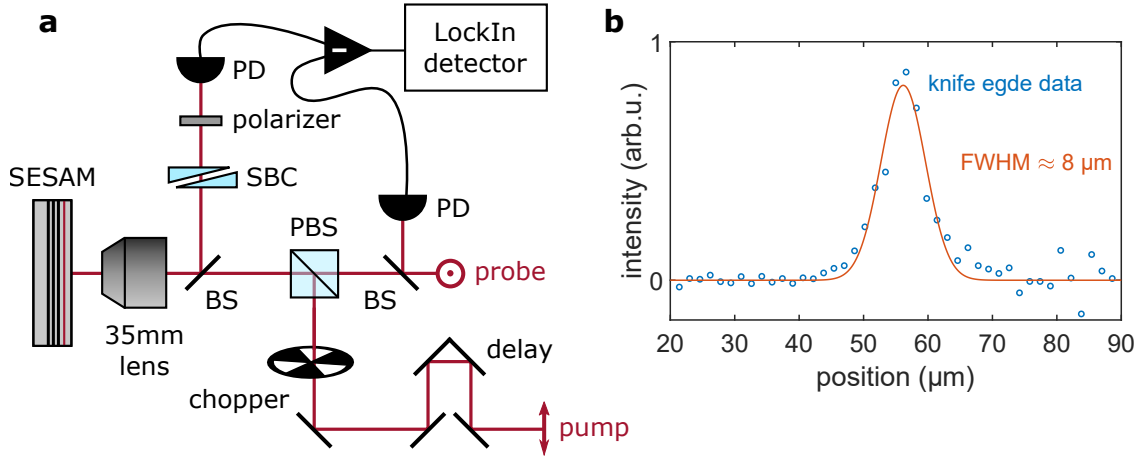


Figure 25: Characteristics of the degenerate pump-probe setup. **(a)** The setup is a home-built reflection microscope. The pump and probe beam have orthogonal polarizations in order to suppress remaining pump light in the detection. In order to achieve high suppression, a combination consisting of a Glan-Thompson polarizer and a Soleil-Babinet compensator (SBC) is used. The two beams are reunited in a polarizing beam splitter (PBS) and focused on the sample by a 35 mm achromatic lens. A beam splitter (BS) guides the reflected light to the detection unit. There, a balanced detection scheme, based on two photo diodes (PD), is used combined with a Lock-In amplifier, that demodulates on the chopper frequency in the pump path. **(b)** The spot size, resulting from a knife edge measurement with a single crystalline gold flake, is well described by a gaussian shape. We obtain a FWHM of 8 μm .

lens. The approach we used is based on the knife edge method. We replaced the SESAM sample with a substrate with monocrystalline gold flakes. Bigger flakes easily reach diameters of 30 – 50 μm , heights of about 100 nm and have extremely sharp edges [133]. This makes them perfectly suitable as blade for the knife edge method. The only difference to the conventional method is, that we are not blocking the beam partly but simply change the reflection coefficient from glass to gold. The result is well described by an error-function. The numerical derivation of the measured data points is shown in figure 25 (b) in blue. The orange curve is a gaussian fit to the obtained data points. We obtained a full width half maximum (FWHM) of 8 μm . In order to calculate the fluence F from measured laser powers, we use the relations

$$F = \frac{\langle P_{\text{Laser}} \rangle}{A_{\text{spot}} f_{\text{rep}}} , \quad (115)$$

$$A_{\text{spot}} = \pi \sigma_{\text{spot}}^2 , \quad (116)$$

where $\langle P_{\text{Laser}} \rangle$ denotes the time averaged laser power, A_{spot} the spot area and f_{rep} the repetition rate of the laser. We assumed the laser spot to be symmetric and used the standard deviation σ_{spot} of the gaussian fit to calculate the spot area.

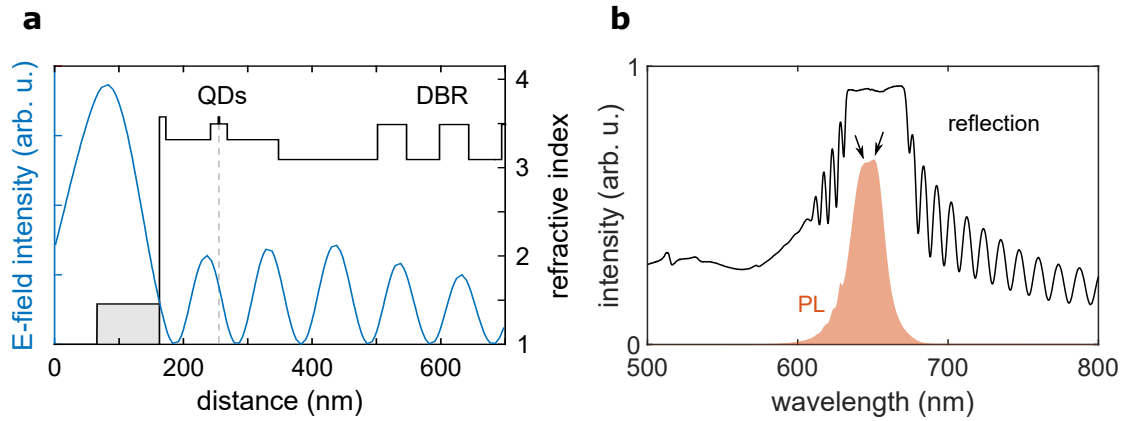


Figure 26: Characteristics of the SESAM. (a) The refractive indices of the top layers in the structure are shown (black). The QDs and the DBR are indicated. The grey shaded area marks the SiO₂ layer on top. In blue, the electric field intensity within the layered structure is plotted. The field is obtained via the transfer matrix formalism (adapted from [130] and used with permission). (b) Measured reflection spectrum of the SESAM. The reflected intensity is normalized to the reflection of a standard silver mirror. In orange, the PL spectrum of the structure, upon excitation with 530 nm light, is shown. Within the high reflection window of the DBR two peaks can be identified (marked by black arrows).

6.3 CHARACTERISTICS OF THE SESAM UNDER INVESTIGATION

The structure under investigation is a SESAM based on QD technology and fabricated by the group of Prof. Michler in Stuttgart. The important parameters of a SESAM are the operation wavelength, the modulation depth of the saturable absorption and also the recovery time of the quantum system. Here, QD based technology gives certain advantages over QW based systems. For QDs, the absorption wavelength can be tuned easier than for a QW. The SESAM we report on is operating in the ultrafast red spectral range. Another advantage the QDs offer, is the additional degree of freedom given by the growth density of the layer. It strongly influences the modulation depth of the structure and allows precise engineering of the SESAM for individual needs. Moreover, also the recovery time can be influenced by the creation of trap states around the QDs.

In our case the SESAM consists of InP QDs, grown via the Stranski-Krastanov mechanism. The dots are embedded in the center of a 24 nm Al_{0.1}GaInP barrier. The advantage of the InP QDs is the very broad accessible wavelength range, depending on specific growth parameters [134, 135]. All semiconductor layers are fabricated via metalorganic vapor phase epitaxy (MOVPE). The barrier is surrounded by Al_{0.55}GaInP cladding layers (top 76.5 nm, bottom 87.0 nm). On top, the structure is terminated by a 10 nm GaInP anti-oxidation layer and a SiO₂ coating. Beneath the active SESAM region we have a 157.5 nm AlAs heat spreading layer, followed by the DBR (55 × 54.4 nm AlAs / 46.0 nm Al_{0.45}GaAs). The entire SESAM is grown on a GaAs substrate. The composition of the structure is shown in table 2 and further fabrication details can be found in ref. [130, 136]. The top part of the SESAM is sketched with the respective refractive indices in figure 26 (a) in black. The active region as well as the heat spreading

layer and the beginning of the DBR is visible. In blue, the resulting electric field in the structure is shown. By using the transfer matrix formalism, the field distribution in a layered structure can be calculated easily. Within the structure, a standing wave pattern can form between the glass-semiconductor interface and the DBR. Commonly, this cavity is designed to be anti-resonant or near-anti-resonant [137] like in our case. This enables a broader wavelength operation and more important, a small chromatic dispersion. For pulsed operation a broad spectral window is important, as the spectral width of pulses increases inversely proportional to the pulse duration (at the Fourier limit). In our case, the additional SiO_2 layer flattens the group delay dispersion even further [130].

material	thickness [nm]	layer description
SiO_2	97	GDD flattening
GaInP	10	anti-oxidation
$\text{Al}_{0.55}\text{GaInP}$	76.5	cladding
$\text{Al}_{0.1}\text{GaInP}$	12	barrier
InP		QDs
$\text{Al}_{0.1}\text{GaInP}$	12	barrier
$\text{Al}_{0.55}\text{GaInP}$	87	cladding
AlAs	157.5	heat spreading
$\text{Al}_{0.45}\text{GaAs}$	46	first DBR layer
AlAs	54.4	DBR $55\times$
$\text{Al}_{0.45}\text{GaAs}$	46	
AlAs	54.4	last DBR layer
GaAs	30	buffer
GaAs	$350 \cdot 10^3$	substrate

Table 2: Layers of the SESAM under investigation.

In figure 26 (b) a pre-characterization of the SESAM is shown. The black reflection spectrum is measured with a halogen lamp included in the reflection microscope and referenced to the reflection spectrum of a standard silver mirror. One can nicely see the high reflective window formed by the DBR ranging from 633 nm to 670 nm. Outside of the window oscillations, typical for Bragg stacks, are observed. The red shaded area shows the photo luminescence (PL) spectrum of the SESAM. For the acquisition, the OPO's wavelength was tuned to 530 nm and two 550 nm longpass filters were added to the detection. Additionally, a polarization filter was used to suppress the excitation light further. In general, QDs can emit under distinct polarizations but due to the random orientation in the sample, we mostly suppress the excitation light and only a statistical average of the QD's emission. A close look at the PL shows two details. First, for lower wavelengths (below 630 nm), the emitted PL is modulated by the DBR. We observe an oscillating shape. Second, two higher energetic peaks arise at 645 nm and 651 nm (marked by arrows). The later, we attribute to emission stemming from the quantum dots, as it is the wavelength we use for later absorption and saturation of the QDs. The higher

energetic peak we link to the wetting layer. Additional influences by the $\text{Al}_{0.1}\text{GaInP}$ could also be possible. Yet, the contribution by the wetting layer is more likely since this PL peak has been observed in very similar structures and was explained by radiative emission from the wetting layer [138].

MicroPL measurements in Stuttgart revealed that the QD density is $n = 1.5 \cdot 10^7 \frac{1}{\text{cm}^2}$ for the sample under investigation and not $n = 10^{10} \frac{1}{\text{cm}^2}$ as expected. The reduced density of QDs leads to only about 8 dots in average in the FWHM focus of the laser. This is in contrast to other experiments where usually densities of $n = 4 - 5 \cdot 10^{10} \frac{1}{\text{cm}^2}$ are reported [139–141]. Here, we are in fact performing pump-probe measurements on a low-density QD SESAM. In our experiment the $x - y$ position on the sample was optimized in order to maximize the overall pump-probe signal and for the experiments the same spot on the sample was chosen in order to ensure comparability of measurements.

6.4 FLUENCE DEPENDENT SATURATION DYNAMICS

In the first pump-probe measurements of the SESAM, we are interested in two parameters. First, we want to investigate the decay times of the saturation process and second, the fluence dependent modulation depth of the QDs. Both parameters will heavily influence the application of the SESAM in lasers. The decay times represent the temporal low-loss window in the cavity and, therefore, impact the reachable pulse lengths while the fluence dependent modulation depth will refer to the intra cavity power. For stable operation, we have to ensure that the QDs are saturated but, on the other hand, the present fluences should not exceed this point too far as counter acting processes can come into play.

We performed pump-probe measurements on the SESAM at the desired operation wavelength of 651 nm. In figure 27 (a) the obtained pump-probe traces are shown for different pump fluences. In the left panel of (a) detailed scans in a 35 ps time interval are shown, while the right panel covers a bigger range of over 300 ps. In both cases the relative change $\Delta R/R$ in reflectivity of the sample is shown. The used pump fluence is color coded and ranges from $10 \frac{\mu\text{J}}{\text{cm}^2}$ to $300 \frac{\mu\text{J}}{\text{cm}^2}$. The probe fluence was kept constant at $100 \frac{\mu\text{J}}{\text{cm}^2}$. In all traces we observe a rapid change in reflectivity that decays on a fast time scale of about 500 fs (left panel), followed by a slow decay of more than several hundreds of pico seconds (right panel). At about 10 ps delay we observe a small artifact that we attribute to an optical reflection in the pump or probe beam path. The corresponding path length is 3 mm in total which could be linked to multi-reflections in a plate beam splitter for example. As this artifact only depicts a cosmetic issue and not a physical one, we do not discuss it further. The modulation of the reflectivity shows two interesting aspects. For low to moderate pump powers, the modulation around zero delay gets higher which can be attributed to saturated absorption in the QD layer. For high pump powers, on the other hand, the modulation decreases again and we observe a drop in reflectivity to negative values for several pico seconds. This effect is known in SESAMs and often referred to as inverse saturable absorption (ISA) [142]. The main reason for this process is described via TPA and potential subsequent free-carrier absorption (FCA) [143–145] (see also chapter 2.4.2). At reasonably high pump powers, third order nonlinear effects

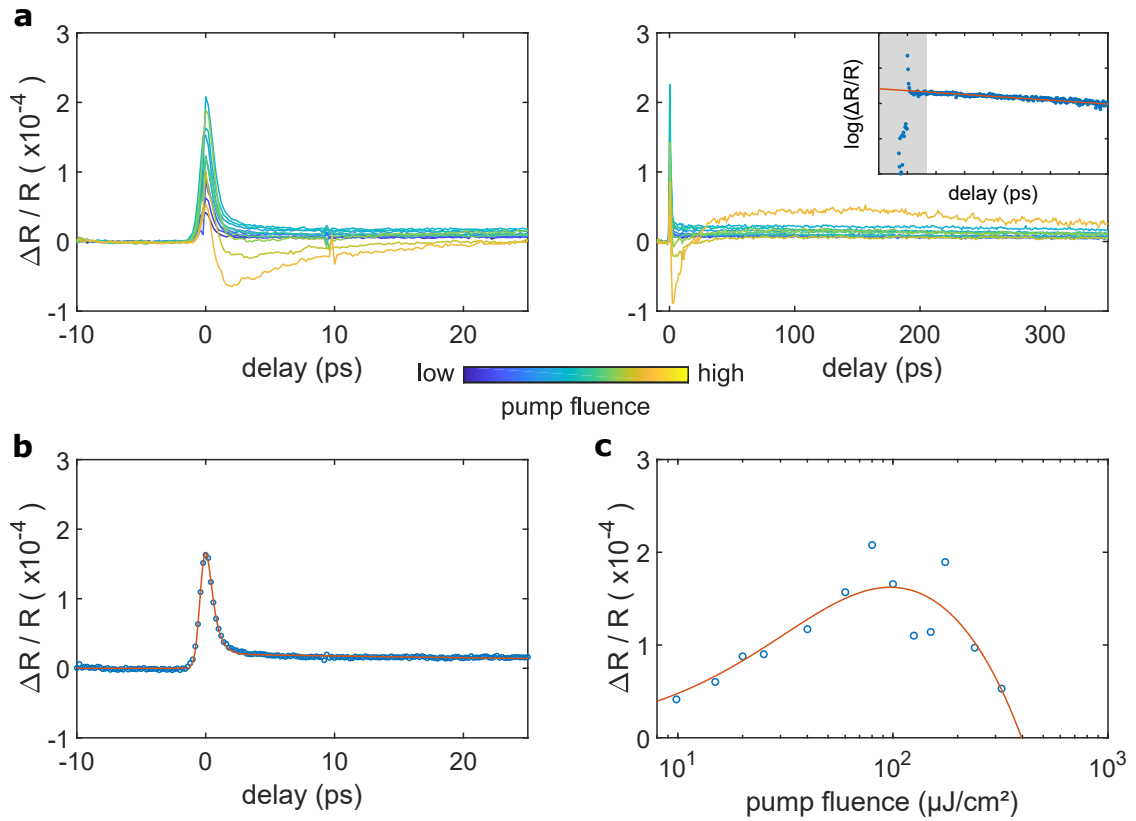


Figure 27: Pump fluence dependent pump-probe measurements. (a) Pump-probe traces for different pump fluences are shown. The fluence is color coded. In the left panel a detailed scan around the zero delay position is shown, while the right panel features longer delays. We observe an increasing modulation for increasing pump fluences at zero delay, that drops for high fluences due to ISA. The inset in the right panel shows an example for the determination of the slow decay time. Fast times are excluded and a linear function is fitted to semi-logarithmic data. (b) The detailed pump-probe scans (blue data points) are well described by a model (orange), consisting of a double exponential decay convoluted with a Gaussian pulse accounting for the temporal length of the pump and probe pulse. (c) By using the model from (b), the modulation depth at zero delay for different pump fluences can be extracted (blue data points). The orange curve is a model described in the text.

become a dominant contribution and can offer an additional, not saturated, absorption channel in the system. Therefore, further absorption of the laser is possible and the relative reflectivity of the SESAM can even drop below zero, if the TPA channel is efficient.

For a quantitative analysis of the modulation depth as well as the decay times, we perform fits to the pump-probe traces. Figure 27 (c) shows an example trace (blue dots) with a fitted model (orange). The shown measurement is for the pump fluence $F = 100 \frac{\mu\text{J}}{\text{cm}^2}$. As stated earlier, most SESAMs are well described by two decay times - a long (hundreds of pico seconds to nano seconds) and a short one (few pico seconds or less). Therefore, our fitting model consists of a double exponential decay. As the data points already indicate, the fast decay time is in the order of several hundreds of femto seconds and consequently in the same order of magnitude as our laser pulses. This is also indicated by the visible, finite rise time of the signal for negative delays. In order to

separate those contributions to the signal systematically, we take the laser pulse lengths into account in the model. The equations for the fitting procedure read

$$d(\tau) = a_1 e^{-\frac{\tau}{\tau_1}} + a_2 e^{-\frac{\tau}{\tau_2}} \quad , \quad (117)$$

$$g(\tau) = e^{-\frac{\tau^2}{2\tau_3}} \quad , \quad (118)$$

$$f(\tau) = g(\tau) * d(\tau) \quad . \quad (119)$$

For the final fitting function $f(\tau)$, the double exponential decay $d(\tau)$ is convoluted with a Gaussian function $g(\tau)$. The parameters a_i mark amplitudes while τ_i denotes time constants - decay times and the pulse duration. We decided to use a single Gaussian function as an effective approach, that keeps the number of open parameters low. In a close to experiment model one could also model the pump and probe pulse separately. In figure 27 (c) we see that the model describes the decay of the reflectivity, as well as the finite rise time, nicely. We also have to note that the model is capable of describing traces with visible ISA influence. From the traces we can extract a fast decay time of

$$\tau_1 = (519 \pm 148) \text{ fs} \quad .$$

This value is obtained as mean value of all extracted decay times excluding those with visible ISA. The standard deviation is used as error. The model, fitted to the detailed pump-probe traces from the left panel of figure 27 (a), already indicates that the second decay time is in the order of a few nano seconds. Therefore, the limited delay interval of those traces is not well suited to determine the long decay constant. Consequently, we use the traces from the right panel. As the other time constants - fast decay time and pulse length - are much faster, we can exclude small delay times and use a linear fitting function to the logarithm of the relative reflectivity. This is shown in the inset of the right panel. The data points are shown in blue and the resulting fit is in orange. The gray shaded area marks data points excluded from the fitting procedure. For the slow decay time we obtain

$$\tau_2 = (2.0 \pm 1.1) \text{ ns} \quad .$$

The large error indicates that even the delay range of over 300 ps is not enough to resolve the decay nicely. The fast decay time can be attributed to a thermalization of charge carriers in the QDs. Potentially, this can include thermal carrier escape to the wetting layer, which has been reported in similar structures [146]. In general, our determined fast decay time is in good agreement with previously reported times in QD based SESAMs [147, 148] and further strengthens the role of QD based systems for ultrafast, sub-picosecond laser operation. The slow decay time we extracted, can be linked to ground state recombination. In similar structures this has been done for time constants of several hundreds of pico seconds [149–151]. In general, additional processes like thermal escape of carriers [152], Auger recombination [153] and trapping in defect or interface states [154] could also have an impact on the measured long decay time. As we are mainly interested in the short decay time, possible influences on the longer one are not further discussed.

One additional parameter we obtained from the fits, based on equation 119, is the modulation depth. For a final use of the SESAM in laser applications this is an important parameter. The intra cavity laser powers should efficiently saturate the QDs but, at

the same time, not be too high that ISA counter acts on the modulation. In figure 27 (c) the reached modulation depth for different pump fluences is shown. We observe an increasing modulation up to about $100 \frac{\mu\text{J}}{\text{cm}^2}$ and afterwards ISA effects come into play and the overall modulation decreases again. In a theoretical model this fluence dependent change in reflectivity $R(F)$ can be described by [143]

$$R(F) = R_{\text{ns}} \ln \left[1 + \frac{R_{\text{lin}}}{R_{\text{ns}}} \left(e^{\frac{F}{F_{\text{sat}}}} - 1 \right) \right] \frac{F_{\text{sat}}}{F} e^{-\frac{F}{F_2}} . \quad (120)$$

The parameters R_{lin} and R_{ns} describe the linear, non-saturated reflectivity and the maximum reachable reflectivity, if ISA is neglected. In consequence, the value $\Delta R_{\text{ns}} = 1 - R_{\text{ns}}$ accounts for non-saturable losses in the absorber. The difference of the two reflectivities $\Delta R' = R_{\text{ns}} - R_{\text{lin}}$ is the highest, theoretically reachable modulation depth and defines the saturation fluence F_{sat} . It is defined as the fluence when the reflectivity has increased by $\frac{1}{e} \Delta R$ compared to the unsaturated case. Typically, SESAMs are designed to work at $3 \cdot F_{\text{sat}}$ in mode locking applications [155]. We want to point out that the value $\Delta R'$ does not correspond to the measured value ΔR shown in the figures. The last parameter F_2 is called coefficient of ISA and describes the fluence at which the change reflectivity has decreased again to $\frac{1}{e} \Delta R$ after its maximum, due to ISA processes. If the modulation depths are below 10 %, equation 120 can be simplified to [142]

$$R(F) = R_{\text{ns}} \left[1 - \Delta R' \frac{F_{\text{sat}}}{F} \left(1 - e^{-\frac{F}{F_{\text{sat}}}} \right) \right] e^{-\frac{F}{F_2}} . \quad (121)$$

Under further assumptions [142] we reach a final expression, that can be used as fitting function to the measured data points

$$R(F) - R_{\text{lin}} = \Delta R' - \Delta R' \frac{F_{\text{sat}}}{F} \left(1 - e^{-\frac{F}{F_{\text{sat}}}} \right) - \frac{F}{F_2} . \quad (122)$$

For the fitting procedure an additional scaling factor is added to the right side of the equation. In our experiment we determined the relative change in reflectivity, which equals an additional division of equation 122 by R_{lin} . The fit from equation is shown in figure 27 (c) as orange line and describes the trend of the data points very well. Finally, the saturation fluence can be extracted in absolute values as $25 \frac{\mu\text{J}}{\text{cm}^2}$. Again, we want to point out the big advantage of QD based SESAMs. If this saturation fluence is not in the desired fluence interval, it can simply be changed by a modification of the QD density. For this, only one step in the fabrication process has to be adjusted. In QW based systems, a modification of the saturation fluence requires more work. A change can be accomplished by the use of multiple QWs [132] but this adds additional layers to the system and might even force a re-design of the whole structure in order to keep the anti-resonant design.

6.5 WAVELENGTH DEPENDENT DYNAMICS

The last experiment we performed on the QD SESAM are wavelength dependent measurements. The general behavior of the structure nearby the operation wavelength of 651 nm is important in order to gain information about possible physical effects that could be disadvantageous for an optimized operation. As our laser source for pump

and probe is an OPO, the wavelength change can be done easily and without major changes in the experimental setup. In figure 28 pump-probe traces for 5 different wavelengths, in about 10 nm steps, are shown. The left panel shows traces on a long delay interval, while the right panel covers the near-zero delay position in a finer discretization. The individual wavelength is color coded. The $\Delta R/R$ values in the right panel show slightly higher values, which can be linked to the different discretization. The left panel was measured in 1 ps delay steps, while the right one was taken with 200 fs. Therefore, the sharp response of the QDs is better mapped in the right panel.

At an excitation wavelength of 634 nm, we see an exponentially decaying change in reflectivity that shows no fast time constant. This indicates, that the InP QDs do not contribute to the signal. At the next higher wavelength of 640 nm the modulation, described by the long time constant, has increased in strength and a sharp peak with a fast decay constant starts to become visible. Yet, the amplitudes are of similar strength. For 651 nm this changes and the QD contribution - the fast time constant - becomes dominant. A further increase of the pump-probe wavelength to 660 nm does not significantly change the ratio between the slow and fast contribution but leads to an overall decrease of the signal. We attribute this to a decreased absorption strength of the QDs. Finally, at 670 nm, the modulation of the reflectivity has dropped to zero and only a small spike at zero delay is observed. This peak could either originate from interference effects or potentially be explained as coherent spike [156]. The vanishing signal can be linked to two effects. On one hand, the absorption efficiency in the QDs drops and, on the other hand, the high reflectivity window, given by the DBR, ends. Therefore, also the electric field enhancement at the position of the QDs decreases, which further disadvantages the overall number of absorbed photons. A closer look at the slow decay constants at the operation wavelength and below reveals another interesting feature. The pump-probe traces for 634 nm and 640 nm suggest, that the dominant slow contribution is faster decaying than the measured $\tau_2 = (2.0 \pm 1.1)$ ns for the operation wavelength. Monoexponential decay fits, that exclude the data points of the first few pico seconds, lead to time constants of $\tau_2(634 \text{ nm}) = 0.45$ ns and $\tau_2(640 \text{ nm}) = 0.63$ ns. Consequently, there is also an indication for a trend that τ_2 increases until the value of the QDs is reached. Similar to the PL discussed in section 6.3, we suspect that the blue shifted change in behavior does not stem from the QDs themselves but from other layers in the structure. This suspicion is backed up by the fact, that the fast decay constant, related to the QDs, just starts to emerge with increasing wavelength. In contrast to the PL, we do not directly attribute the blue shifted absorption process to the wetting layer but to the barrier instead. An empirically obtained equation allows the estimation of the barrier band gap energy with the fraction x of aluminum as [157]

$$E_{\text{gap}}(x) = (1.90 + x \cdot 0.48) \text{ eV} \quad . \quad (123)$$

in our case this yields $E_{\text{gap}} = 1.948$ eV which equals approximately 636 nm. Among the group of used alloys, this represents the lowest energetic band gap [158, 159]. The fact that the modulation is strongest observed red shifted at 640 nm could originate from different influences. First, the high reflective DBR window just starts at 633 nm which could indicate a slightly less efficient absorption. Second, the empirical nature of equation 123 of course allows minor deviations and third, a change in temperature also impacts the energy of the band gap as previous studies on similar structures have

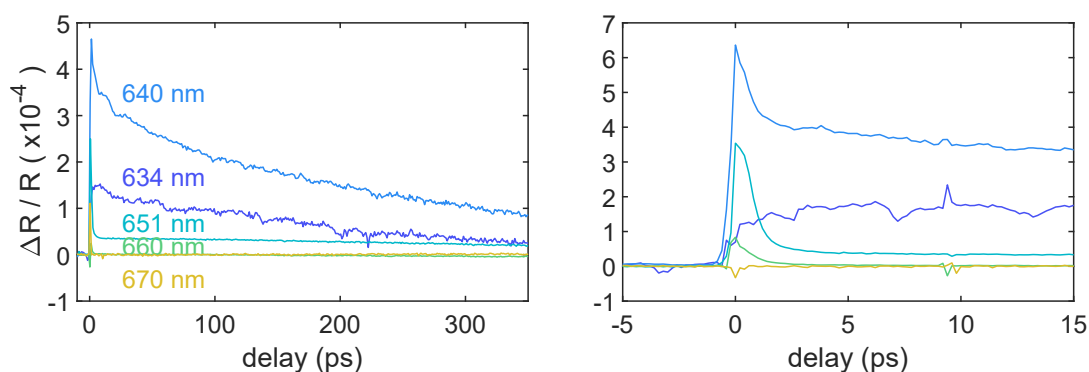


Figure 28: Wavelength dependent saturation dynamics of the SESAM. The left panel covers a long delay range, while the right panel is focused on the near-zero delay interval. With increasing wavelength, the QD related fast decay time becomes dominant and the contribution of the slower time constant decreases. We attribute the later to absorption processes in the barrier-layer.

demonstrated [138]. The present high optical fluences are partly transferred to heat and cause an increased sample temperature.

6.6 CONCLUSION

In this chapter we were able to reveal the dynamics of a red emitting, InP QD based SESAM with low QD density and determined two dominant decay times. A fast one in the range of 500 fs and a slower one of 2 ns. The fast decay time has the potential to create an ultrafast sub-picosecond VECSEL in the red spectral region. Moreover, an additional tailoring of the QDs emission can allow different operation wavelengths. Here, the broadly tuneable emission of the InP dots is highly beneficial. If the operation wavelength is shifted to higher energies, also a modification of the barrier might become necessary, as we observed a non-negligible absorption modulation probably linked to the barrier for a blue shift of 10 nm.

NONLINEAR PUMP-PROBE SPECTROSCOPY OF GOLD NANOWIRES

In current times, the field of nonlinear plasmonics is under intense investigation. Higher-harmonics generation [160], frequency mixing in general [161] and continuum generation are experimentally investigated in particle ensembles [162], on a single particle level [163], in mixed material structures [75, 164] and in propagating structures [165]. The large optical nonlinearity of nanostructured gold leads to high conversion efficiencies, up to an order of magnitude higher than in the bulk material [102, 103]. Combined with the subwavelength scale of the effects, the downsizing of nonlinear optics is paving the way towards optical and quantum signal processing, optical circuits and integrated optics [166]. However, the exact origin of the microscopic nonlinearity and other fundamental questions are not solved yet. Recently, the origin of THG could be allocated as a volume effect [167] and previously in this work, we were able to extend the understanding of symmetry restrictions in SHG. In other experiments it was, e.g. shown, that the d-band absorption of gold can effectively boost the THG efficiency [168]. Yet, one of the fundamental remaining questions is the connection between the electronic band structure, the occupation function and nonlinear processes. It has not been clarified which role quasi free electrons in the sp-band and bound ones in the d-band play. Our approach to solve this question is to modify electronic properties of nanostructures, i.e., the temperature of the electrons in the conduction band and measure the influence on nonlinear optical processes. This leads to a multi-color pump-probe experiment in which not the change at the fundamental probe frequency is monitored but the change in nonlinear optical processes. A similar experiment has recently been done on the 2D material graphene [169] and gave new insight in the electronic properties of the material itself.

In this chapter we present our experimental setup, including potential laser focus or sample drifts, pulse durations and the alignment procedure. Furthermore, we discuss the plasmonic nanostructures under investigation and show their linear and nonlinear response. Finally, we present obtained pump-probe data and discuss potential models to describe the observed effects.

7.1 THEORETICAL BACKGROUND

For a better understanding of the experiment, we start by giving an additional theoretical background. We start by a closer look into the band structure of gold, explain

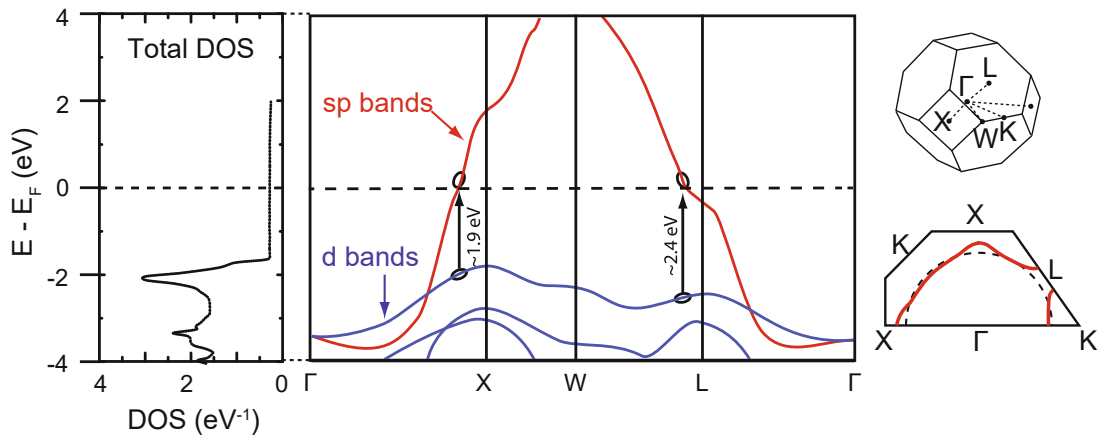


Figure 29: Band structure of gold. In the mid panel the calculated bandstructure is shown. The sp-bands are drawn in red and the d-bands in blue. The energy is shown with respect to the Fermi energy E_F . Possible optical transition near the X and L symmetry points are indicated by arrows. In the left panel the resulting DOS is plotted. The right panel shows the Fermi surface of gold. Figure adapted with permission from [171] (left and mid panel originally from [173], right panel from [174]).

temporal dynamics of hot electrons and give an intuitive model, the so called two temperature model (TTM), for the theoretical description.

7.1.1 band structure of gold

In section 2.2, we already discussed some features of the band structure that explained absorption bands in the optical data of gold. Now, we will take a closer look at the exact band structure. In figure 29 the calculated band structure is shown in the mid panel. The lower energetic d-bands are shown in blue, while the higher energetic sp-bands are drawn in red. The energies on the y-axis are plotted with respect to the Fermi energy E_F (indicated by a dashed line). On the x-axis, the symmetry points of the first Brillouin zone are shown and defined in more detail in the right panel of the figure. The left panel shows the resulting density of states (DOS), obtained from the calculated band structure. Within the band structure we observe two points of high symmetry, which allow direct, optically excited interband transitions in the visible spectral range [170] - at the X-point with an energy of 1.9 eV and at the L-point with 2.4 eV [39, 171]. In general, the absorption near the X-point is much weaker due to a smaller absorption cross-section [172].

7.1.2 plasmon assisted excitations

If we look at plasmon assisted excitations in gold nanostructures there are two possible routes to follow. Depending on the particle size, the plasmon can decay radiatively or non-radiatively [32]. The ratio is described by the ratio of the scattering and absorption cross-section. The dephasing and decay of the plasmon happens on a time scale of only a few femto seconds. If the plasmon is absorbed, one or multiple electron-hole pairs are

generated within the band structure. Here, again two relaxation mechanisms are possible - a radiative and a non-radiative one. Both are discussed in the following. We note that all of the discussed decay processes are also possible via direct optical excitation. The plasmon assistance simply boosts the excitation and partly modifies the subsequent relaxation processes.

radiative decay processes

If the energy transferred by the plasmon is above the interband threshold, PL from gold is observed. It has been attributed to a radiative recombination of the generated charge carriers [175, 176]. Interestingly, the emitted PL in nanostructures was found to be strongly influenced by the LSPR of the structure [177] and is also capable of enhancing the PL orders of magnitude [32, 178]. Beside of interband transitions also intraband transitions are possible. In principle those radiative transitions are momentum forbidden but are observed in experiments [179] and explained via weakened rules in nanosystems [170]. For PL, stemming from intraband transitions, the exact mechanism is still under debate. While it is often attributed to a radiative recombination of electrons and holes in the sp-band, there are also approaches that model it as electronic Raman scattering [180, 181]. Of course, optical transitions in gold nanostructures cannot only be excited by a single photon but also by multiple photons in a nonlinear optical regime. Multi-photon PL has already been demonstrated [182].

non-radiative decay processes

If we look at possible decay channels for excited electrons in metal nanostructures, the radiative recombination only displays a minor, and in total numbers negligible fraction. Due to the high electron density, the majority of the relaxation processes is taking place non-radiatively via scattering processes [32]. In order to describe the processes and address them to different time scales, we look at the temporal evolution of excited electrons in metals which is sketched in figure 30. In all panels the DOS is shown related to the energy. The solid colored lines represent bands (blue: sp-band, orange: d-band). For the sp-band, we chose a parabolic shape which corresponds to a free electron gas [183], while the d-band is simply approximated as a Gaussian function. In order to show the occupation of the states, the DOS is multiplied by the Fermi-Dirac distribution $f(E, T)$ for a certain temperature and pictured as color-shaded area. The distribution reads

$$f(E, T) = \frac{1}{e^{\frac{E-\mu}{k_B T}} + 1}, \quad (124)$$

with E being the energy, T the temperature of the electron gas and the Boltzmann constant $k_B = 8.617 \text{ eVK}^{-1}$. μ denotes the chemical potential and is for a temperature of 0 K equal to the Fermi energy E_F . For a better understanding of the upcoming processes, we show discretized occupation values in a stem-like plot in the corresponding colors. Initially the system has an equilibrium temperature T_0 , that is for example given by the surrounding room temperature. Here, the d-band is fully occupied and the sp-band is partially filled as described by the Fermi-Dirac statistic. After optical excitation, electrons above the Fermi level are generated. They can either originate from intraband or

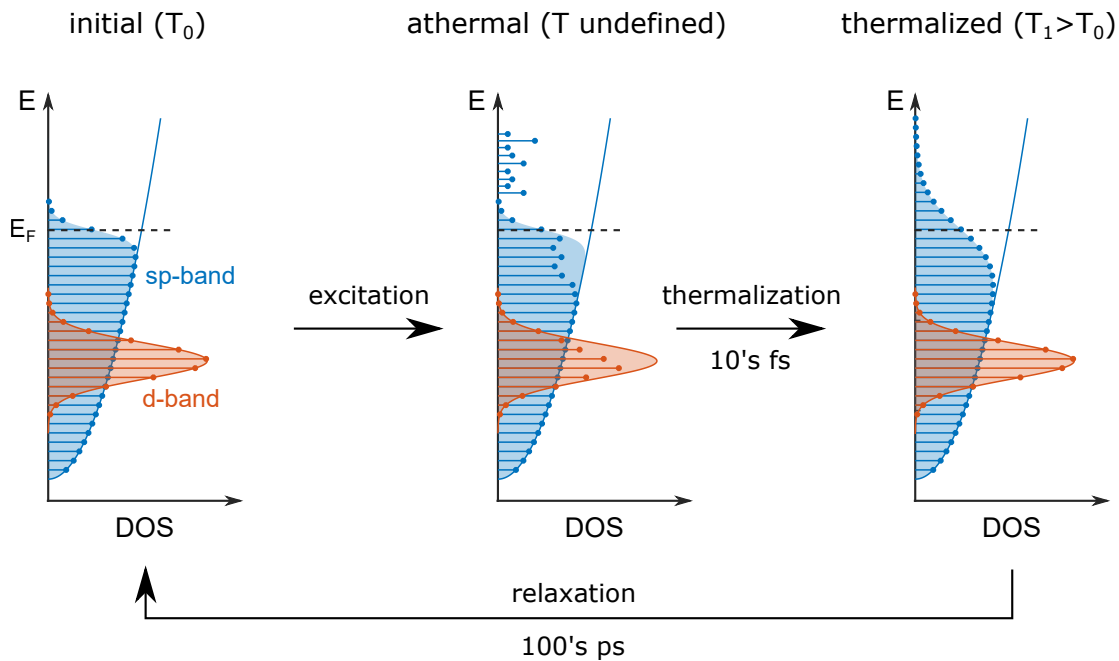


Figure 30: Sketch of the temporal dynamics of excited electrons in metallic structures. The d-band is shown in orange and the sp-band in blue. The population of the states is given by the Fermi-Dirac distribution, pictured by shaded areas. Additionally, a discretized population of the states is shown as a stem plot. The idea for the figure is taken from ref. [184] and the used temperatures as well as the stem plot values in the athermal panel are chosen arbitrarily for representation purposes. Initially, the population of the bands can be described by a Fermi-Dirac distribution with the temperature T_0 . After optical excitation an athermal electron distribution is created, that relaxes via electron-electron scattering on a fast time scale and subsequently via electron-phonon scattering on a slower scale. Finally, the heat is transferred to the surrounding and the initial temperature is reached.

interband transitions into the sp-band. The stem plot indicates that the occupation below the Fermi energy has been reduced and states above, in the sp-band, have been populated. We directly observe that the resulting occupation cannot be described by a Fermi distribution and therefore no macroscopic temperature can be assigned to the electron gas. This state is called an athermal occupation. After a few tens of femto seconds, the athermal electron distribution has relaxed via electron-electron scattering (including Auger processes, for the electrons originating from interband absorption, which fill up the d-band again) to a thermal distribution. This state can again be described by a Fermi distribution with an increased temperature ($T_1 > T_0$). In the scope of this work we will denote this state as state of hot electrons. From here on, the interaction between electrons and phonons becomes dominant and the electron gas relaxes via scattering processes - the heat is transferred to the lattice on a time scale of only a few pico seconds. Finally, the heat is transferred to the surrounding medium and after several hundreds of pico seconds, the initial electron distribution is reached. As noted before, those non-radiative decay processes are the dominating relaxation processes for excited electrons in metals. Only about $10^{-5} - 10^{-3}$ are radiative [32].

The different time scales of the mentioned processes have been under intense theoretical [184] and experimental investigation [185–189]. Experimentally, the short time interval of the athermal electron distribution is hard to access. The required laser pulses have to be in the range of only a few femto seconds. To our knowledge, this regime hasn't be accessed yet in experiments and the work up to now is purely theoretical. The longer time scales, on the other hand, are very well covered by experiments. Especially in the region of a hot lattice and the subsequent cooling effects, like acoustic oscillations due to the rapid increase in the lattice temperature, have been investigated [26].

7.1.3 the two-temperature model

If the athermal part of the electron dynamics can be neglected, e.g., because of pulse durations of several hundreds of femto seconds in the experiment, a quite intuitive model can be applied for the description - the so called two-temperature model (TTM). The basic mechanism is, that the energy of an exciting laser beam is partly absorbed by the electrons and, later on, the heat is transferred to the lattice. In order to describe this mathematically for subwavelength nanoparticles, a set of two coupled differential equations can be formulated [190]

$$C_e(T_e) \frac{\partial T_e}{\partial t} = -G(T_e - T_l) + S \quad , \quad (125)$$

$$C_l \frac{\partial T_l}{\partial t} = G(T_e - T_l) \quad , \quad (126)$$

with the electron and lattice temperatures $T_{e/l}$ and the electron-phonon coupling parameter $G = 2.2 \cdot 10^{16} \frac{W}{m^3K}$ [191]. The parameters $C_{e/l}$ denote the heat capacity of the electron gas and the lattice and are given by $C_e(T_e) = \gamma T_e$ with $\gamma = 71 \frac{J}{m^3K^2}$ [192] and $C_l = 2.45 \cdot 10^6 \frac{J}{m^3K}$ [183]. The parameter S accounts for the excitation of the laser and is described by

$$S = \frac{1}{V_p} \cdot \frac{P_{avg}}{f_{rep}} \cdot \frac{\sigma_{abs}}{\sigma_s^2 \pi} \cdot \frac{1}{\sqrt{2\pi}\sigma_t} e^{-\frac{(t-t_0)^2}{2\sigma_t^2}} \quad , \quad (127)$$

with the particle volume V_p . The division in the first factor is necessary because we use specific heat capacities in the equations 125-126. The second factor calculates the energy of a single laser pulse from the time averaged power P_{avg} and the repetition rate f_{rep} . The third factor determines how much of the energy is absorbed via the ratio of the absorption cross-section of the particle and the spot area of the laser. The later is calculated via the spatial standard deviation σ_s of the laser beam. The last factor simply describes a temporal Gaussian pulse of the length σ_t , at the time t_0 . The system of coupled differential equations models heat transfer from the laser pulse to the electrons and subsequently to the lattice. If only time spans up to several tens of pico seconds are considered, this is sufficient and the cooling of the lattice, via heat transfer to the substrate, can be neglected. It only becomes relevant at scales of hundreds of pico seconds. In this case also the spatial heat diffusion in the substrate should be added. A formulation, including those effects, can be found in [190].

An example for a numerical solution of equations 125-126 is shown in figure 31 (a). It models the excitation of a plasmonic wire ($\sigma_{abs} = 20 \cdot 10^4 nm^2$, $V_p = (60 \times 40 \times 270) nm^3$)

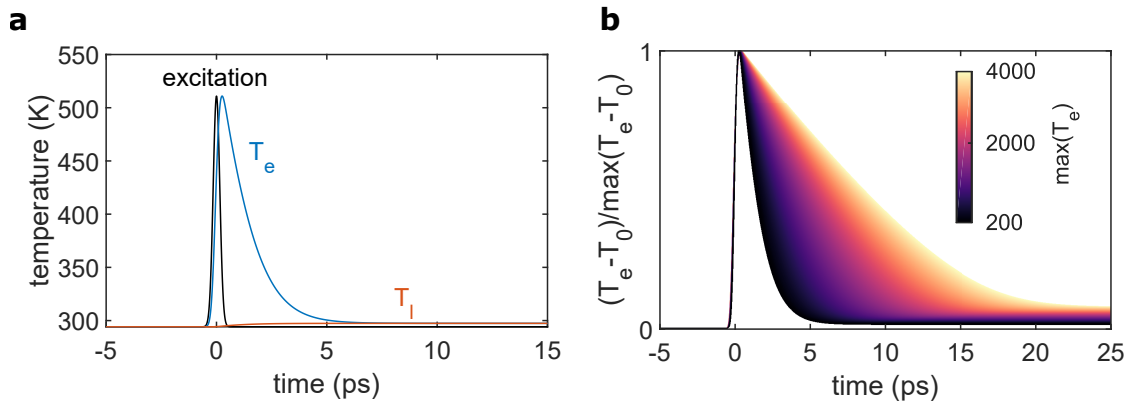


Figure 31: Numerical solution of the two-temperature model. (a) A plasmonic wire is excited at its IR plasmon resonance with a short laser pulse (black). The energy is partly transferred to the free electron gas as heat and the temperature rises (blue). The electrons thermalize via electron-phonon scattering and the lattice heats up (orange). (b) The decay times vary for different increases in the electron gases temperature. A set of decay curves, for varying maximum temperatures, is shown. The temperatures are color coded (see inset).

at the resonance, excited with a focused IR laser pulse ($\sigma_s = 900 \text{ nm}$, $\sigma_t = 150 \text{ fs}$). The laser pulse is drawn in black with an arbitrary scaled amplitude. Already during the interaction with the nanoparticle, the electron gas is heated up (solid blue line) from the initial room temperature to about 500 K. After about 2 ps, the temperature of the electron gas has decreased to $1/e$ via heat transfer to the lattice (solid orange line). At approximately 10 ps the electrons and the lattice have reached a new equilibrium temperature. Important to notice is, that the relaxation time depends on the initially reached maximum temperature of the electron gas. In figure 31 (b) the decay of hot electrons is shown for different increases in temperature. The temperatures in the plot are color coded. Although in literature the decay times are mostly named as 2 ps, times over 10 ps are easily reached for temperatures around $T_{e,\max} = 4000 \text{ K}$.

7.2 EXPERIMENTAL DETAILS

The idea for the experiment is to disturb a plasmonic system with a high energetic pump pulse, that triggers (partly plasmon assisted) interband transitions in gold nanostructures and subsequently creates a hot electron gas via Auger recombination. After a defined time, an IR probe pulse excites the structure near its plasmon resonance and HHG as well as MPPL is observed. The process is sketched in an energy level diagram in figure 32 (a). Depending on the delay time between the two pulses, we look at changes in the nonlinear optical, plasmon assisted processes. In the following we present our experimental setup and the structures under investigation.

7.2.1 setup and structures

The setup consists of a home-built transmission microscope and is sketched in figure 32 (b). As laser source for both, pump and probe, serves a Ti:Sa oscillator (Coherent Mira HP, 150 fs, 808 nm, 76 MHz, 4.5 W). The output is split into two parts. The first one is entering an OPO (APE Berlin, OPO PP Auto FAN) and infrared light, in the wavelength range 1050 nm to 1500 nm, is generated. This radiation is used as probe light. The second part of the Ti:Sa output is guided to a commercial SHG box (APE Berlin, HarmoniXX) and frequency doubled. The resulting light at 404 nm is used as pump light. Both, pump and probe, are guided to the microscope and are additionally modulated by optical choppers (Thorlabs MC2000B-EC with MC1F10HP / MC2F5360) at different frequencies. We use two separate chopper heads in order to avoid parasitic signals at multiples of the motor frequency (see appendix A.3). The ratio of the two modulation frequencies was set to 53/60 and the chosen frequencies lie in the range of 5 – 7 kHz. The chopper drivers obtain their reference signals from a dual channel frequency generator (Agilent 33500B), whose channels are frequency locked. In order to create a temporal delay between pump and probe pulse, a delay stage (Owis Limes 150) is placed into the pump path. Finally, the pump is focused with a high NA oil immersion objective (Olympus UPlanSApo 60x NA1.35) onto the sample. The sample is mounted on a x-y-z piezo stage and allows fully automated spatial scans of the sample and is synchronized with the detection units for data acquisition. From the other side of the sample, the probe is focused with an IR lens (NA0.6). The linearly generated PL of the pump and the nonlinear signal by the probe, is collected by the high NA objective and guided with a dichroic mirror (AHF HC BS 409) to the detection unit. For additional suppression of the remaining pump light, we use a long pass filter (AHF 405 LP Edge Basic). The detection unit consists of an APD (PicoQuant PDM Series) that is combined with a home-built, software based Lock-In amplifier and a spectrometer (Princeton Instruments Isoplan SCT320 with Pixis 400 eXcelon). The APD is fully synchronized with the piezo stage and enables confocal scans of the sample through the laser foci. The Lock-In amplifier consists of four dual-channel Lock-Ins and can demodulate at all involved frequencies - pump and probe frequency, as well as sum- and difference-frequency. The spectrometer is not synchronized with the rest of the setup.

As plasmonic example system we chose EBL fabricated gold wires with a fundamental resonance near the probe wavelength. In figure 33 characteristics of an example sample are shown. Before the fabrication process, we tailor the plasmon resonances via FEM simulations (figure 33 (a)). Since there can be discrepancies between simulation and fabricated structure, we always produce a set of wires with varying lengths. The lengths are designed to yield LSPR positions in an interval of about 500 nm. Consequently, we will always have a structure with a LSPR near our fixed probe wavelength, even if there is a fabrication based systematic offset in the wire length. On a final EBL sample we have multiple fields of structures (each $30 \times 30 \mu\text{m}$), which can have different properties. An example sketch of one field is shown in figure 33 (d). The basic structure is a pair of wires, separated far enough to avoid plasmon hybridization. On the horizontal axis of the field, the length of the wires systematically increases, while on the vertical axis the wire pairs are simply duplicated. In part (b) of the figure, a confocal scan of the sample through the probe focus is shown. Here, we see the advantage of all wire

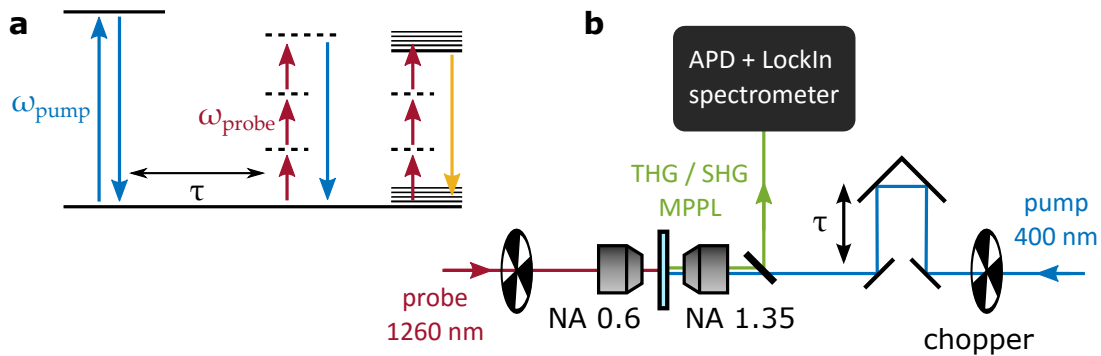


Figure 32: Schematic idea of the experiment. (a) The energy level diagram sketches the physical process under investigation. A high energetic pump pulse disturbs the electron gas in a plasmonic particle and a delayed probe pulse monitors the change via HHG and MPPL. (b) Simplified sketch of the experimental setup. The sample is mounted in a home-built transmission microscope with pump and probe beam entering from opposite sides. The signal is collected by a high NA objective and measured with a combination of APD and Lock-In amplifier and a spectrometer. Both beams are modulated by optical choppers.

lengths combined in one field - we directly observe which wire lengths have their LSPR closest to probe wavelength. Downwards the columns we can see the reproducibility of the wires. As we mostly observe signals of equal strength, we assume that there are no major variations in size or shape. The color coded nonlinear emission shown in the scan consists of THG, MPPL and also SHG. In our experiments we attribute the last to surface roughness and structural imperfections of the wires. Figure 33 (c) backs up this theory. Although the wires look very good in the SEM image, small imperfections and roughness can be seen at the surface.

7.2.2 alignment and stability

In the alignment of the setup there are two crucial overlaps of the two beams. First, the temporal overlap of the pulses and second, the spatial overlap including all three dimensions. The temporal overlap can be done in two steps. For the rough alignment, we ensure that the optical path length of both beams is the same after they are split behind the Ti:Sa oscillator. The exact overlap can be found by the APD in combination with a time correlated single photon counting (TCSPC) module (PicoQuant HydraHarp 400). For this, an additional trigger diode is placed into the pump beam path. Now, we excite the nanowire separately with pump and probe and perform a TCSPC measurement. Conventionally, TCSPC is used to measure PL lifetimes but here, all processes like HHG, MPPL and PL are happening on a time scale much faster than the typical instrument response. Therefore, we only measure the instrument response and by changing the position of the delay stage, we can overlap the response of the pump temporally with the one of the probe. An example of this technique is shown in figure 34 (a). The TCSPC trace upon pump excitation is drawn in blue and the corresponding trace upon IR excitation in red. Although the steep rise of the curves agrees temporally (around

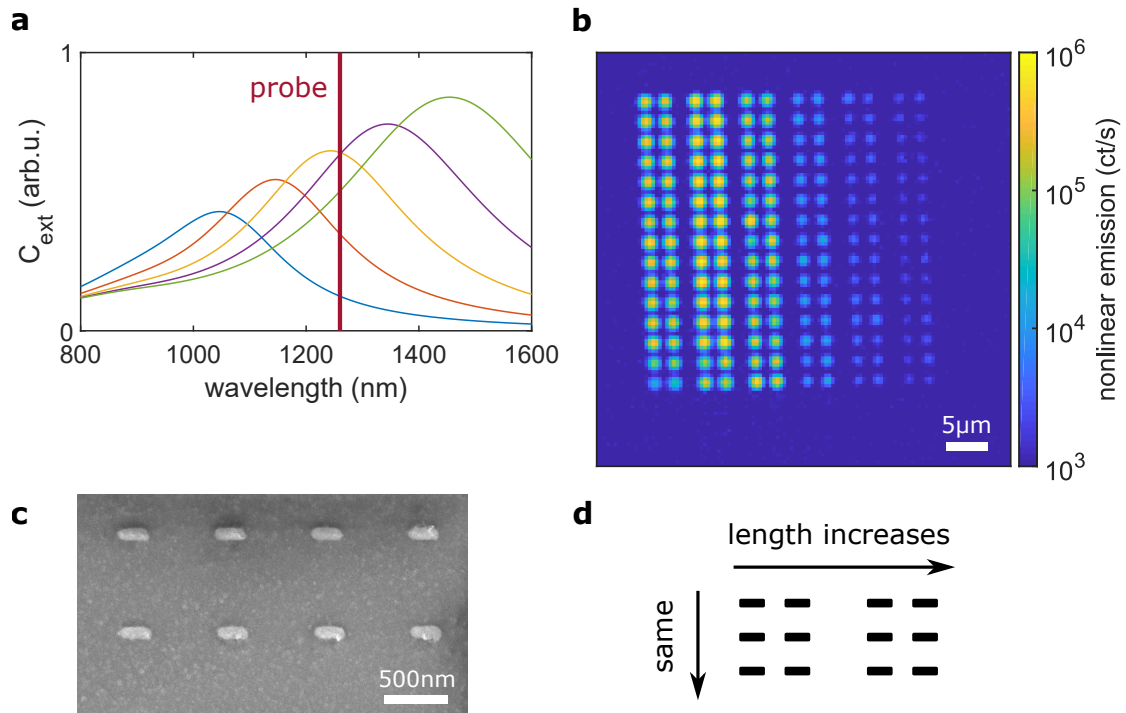


Figure 33: The structure under investigation are plasmonic wires of different lengths. (a) By using FEM simulations, the geometrical dimensions of the wires are designed. The five different curves show fundamental plasmon resonances along the long wire direction. The length increases from blue to green in 30 nm steps. The spectral position of the probe is indicated by a vertical red line. (b) Confocal scans of a wire field produced by EBL. The composition of the field is sketched in (d). As signal serves the nonlinear emission (THG, SHG, MPPL) of the probe. (c) A detailed SEM image of the wires shows small structural imperfections. Yet, they do not have a strong impact on the LSPR and the comparability of nominally same wires is given (b).

0.8 ns), the following shape of both differs. We attribute this to the spectrally dependent response function of the used APD. In the blue spectral range, the response is longer and more symmetrical, while in the green and red region it becomes shorter and has the typical asymmetric shape. With IR excitation we have SHG and MPPL but also THG, which is located around 420 nm. Therefore, we observe the a temporally long (150 ps) and symmetric response function. The pump excitation, on the other hand, leads to linear PL which is predominantly located in the red to green spectral region and therefore exhibits a short response of about 60 ps. We note that the pump induced TCSPC trace also shows minor contributions of additional lifetimes which we attribute to background signal from the substrate. In general, the TCSPC method is well suited to find the temporal overlap of the two pulses with an accuracy of only a few pico seconds by overlapping the steep rising flanks.

The spatial overlap of pump and probe is done with fully automated scans of the sample through the laser foci. We separate the lateral and the focal alignment from each other. With z-scans, the focus of the high NA objective is found and the focus of the

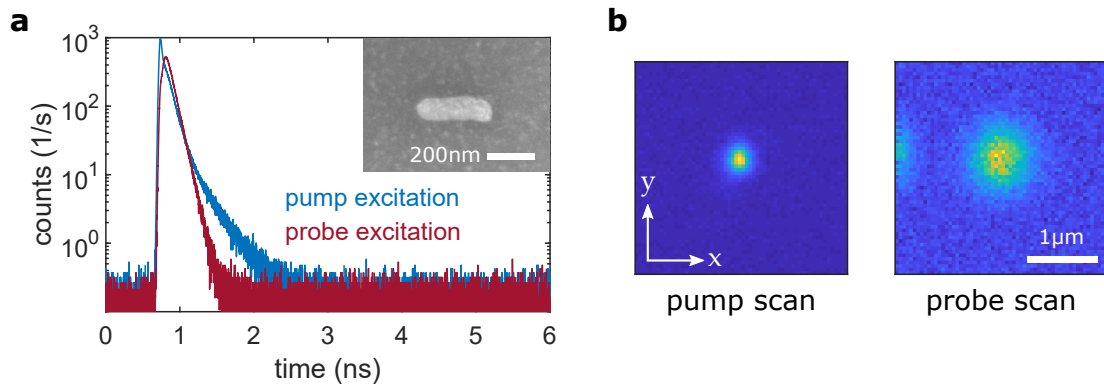


Figure 34: Alignment methods of the pump-probe setup. (a) TCSPC traces of the nanorod's signal upon pump (blue line) and probe (red line) excitation. The inset shows an SEM image of an example nanorod. (b) x-y scans of the structure. Pump and probe are both switched on and the signals are separated via Lock-In demodulation at the corresponding chopper modulation frequencies. To avoid physical interaction between both pulses, they are separated temporally.

IR objective is matched to it. For the lateral overlap, detailed spatial scans of a single nanostructure are performed with both beams. An example is shown in figure 34 (b). A corresponding example structure is shown as inset in (a). The two spatial scans can be done at the same time, which is a benefit of the double modulation. The Lock-In amplifier simultaneously demodulates at both, the pump and the probe, modulation frequencies. Both beams hit the sample but are temporally well separated via the delay. If the two recorded images do not overlap spatially, the position of the pump beam is changed via the last optical element in its path. Thereby, we maintain the alignment of the detection path for the nonlinear signal generated by the probe.

The fact that we can record pump and probe images at the same time also allows us to investigate and quantify drifts in the setup. We perform scans, like shown in figure 34 (b), for 100 times, project each image on the x and y axis, perform Gaussian fits and obtain the position of the particle in each beam. By calculating center-center distances of the obtained positions and a center coordinate, drifts between the two beams as well as an overall drift become visible. The result of this evaluation is shown in figure 35. In (a), the definition of the coordinates is given and in (b) the temporal drift of the center-center distance d_{cc} . Within 60 min d_{cc} drifts between 0 and 300 nm. The drift seems to occur on a periodic scale of about 10 min with a changing amplitude. The source of the oscillating drift was not investigated further because, compared to the size of the probe focus, the measured values are negligible. The x-y scans of the sample also allow us to estimate the pump and probe spot sizes as $\text{FWHM}_{\text{pump}} = 290 \text{ nm}$ and $\text{FWHM}_{\text{probe}} = 2.1 \mu\text{m}$. In figure 35 (d) the focal sizes of both beams are drawn as Gaussian functions in 2D with a center-center distance of 300 nm. This distance is also indicated as dashed line in (b). In contrast to this drift, the one of the center coordinate, shown in (c), is not negligible. In total, intervals of 200 nm are measured on both lateral axes. As our structures have dimensions of about $(300 \text{ nm} \times 60 \text{ nm})$, this drift can lead to a drastically reduced signal. Depending on the drift direction, the tightly focused pump might only excite the wire

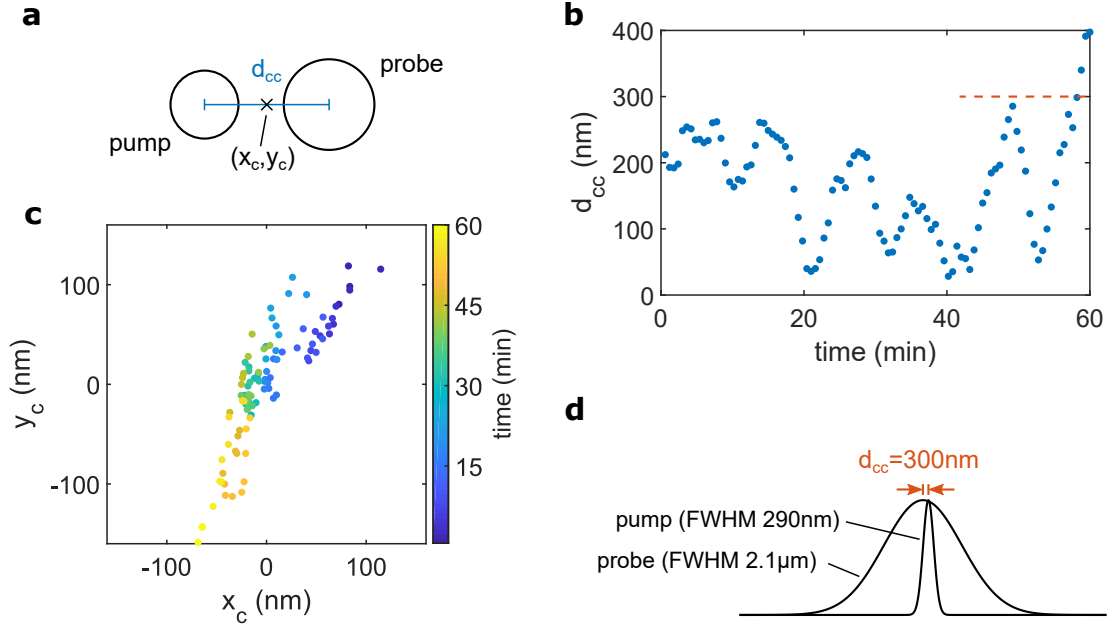


Figure 35: Drift measurements of the setup. Pump and probe images of a single rod are obtained at their respective modulation frequencies at the same time. After obtaining the spatial centers via Gaussian fits, the drift is quantified with the center-center distance d_{cc} and the center coordinate (x_c, y_c) defined in (a). The resulting drifts are plotted in (b) and (c) as drifts over time. (d) A true to scale sketch shows that the influence of a 300 nm center-center drift is negligible due to the large spot size of the probe beam.

with half the possible power after 30 min to 45 min. The consequence for our measurements is, that they should not take longer than 5 – 10 min without minor alignment corrections.

7.3 LINEAR AND NONLINEAR EMISSION PROPERTIES OF A NANOWIRE

Before discussing results of pump-probe measurements, we take a look at signals obtained upon pump and probe only excitation. In figure 36, the nonlinear emission from a single nanowire is shown spectrally resolved (a) and also polarization emission resolved (b). In the spectrum of the nanostructure, we can clearly identify three contributions, HHG, namely SHG and THG, and also MPPL. The later two are expected to arise because both do not underlie symmetry restrictions. SHG, on the other hand, is in principle dipole forbidden as our structures are of symmetric shape and the local density of optical states (LDOS) only features plane waves for our far field detection scheme. We link the observed SHG to two effects. The fabrication method based imperfect symmetry of the wire (see inset in figure 35 (a)), including surface roughness in the evaporated gold film and also the break in symmetry, introduced by the substrate underneath the nanostructure. We consider the first contribution to be the dominant one. In the shown spectrum, the different contributions to the nonlinear signals are indicated by differently shaded areas. By linearly interpolating the MPPL at the positions of HHG peaks, we are

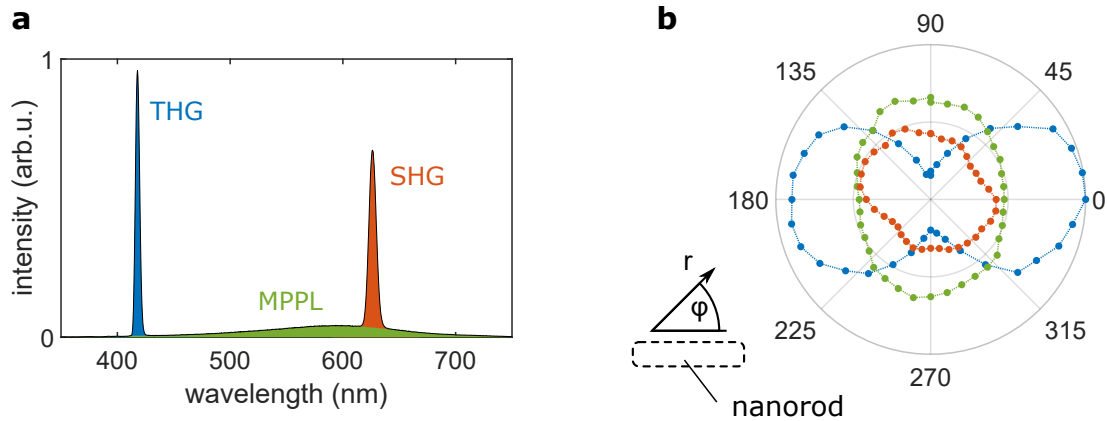


Figure 36: Characteristics of probe induced emission. (a) The spectrum upon IR excitation shows three major contributions. Beside of HHG (SHG, THG) we observe MPPL. The different contributions are indicated as colored areas and can be separated for isolated investigation. (b) The emission polarization resolved SHG, THG and MPPL of a nanorod show an interesting feature. The different resonances along the long and short wire direction cause perpendicular predominant emission directions for THG and MPPL, while SHG is comparatively unoriented.

able to separate all three and quantify their contribution to the total signal. This allows, for instance, a separated investigation of the emission polarization which is shown in figure 36 (b). Here, the angular emission was determined by an additional polarizer in the detection path. The THG shows a dipolar emission pattern with a maximum along the long wire direction. This is expected as THG is a coherent nonlinear process and the polarization clearly follows the fundamental one, which is along the resonant long wire axis. For MPPL, the pattern has a different shape that might at first look counterintuitively. It is elliptically shaped with a predominant direction along the short wire axis. A key to understand this is, that MPPL is not a coherent process and therefore properties of the fundamental excitation light are not kept. The emission is solely determined by the LDOS, to which we also count plasmonic modes. As already mentioned, the PL in nanostructures is strongly influenced by LPSRs. Along the long wire direction obviously higher order plasmon modes exist, which enhance MPPL but also along the short direction high energetic plasmon modes exist. For nanowires it has already been demonstrated that MPPL can be influenced by the wire's short resonance [182]. The emission polarization of the SHG is, compared to THG and MPPL, rather unoriented. A slightly preferred orientation can be seen under $\phi = -45$ deg but we attribute this to scattering properties of the individual particle. Since the second-harmonic scattering properties of the particle are not our main focus in this experiment we do not investigate this further.

In the second preliminary step we take a closer look at the linear and nonlinear PL, emitted from our structures. We investigate both processes separately and the result is shown in figure 37. In (a) and (b), the pump and probe induced PL/MPPL is shown for different excitation powers as normalized emission. The representation on the x-axis is now switched from wavelength to energy, in order to draw easier connections to the band structure of gold. The first feature we observe for both PLs, is an increase of the high energetic flank of the spectrum with an increasing excitation power. We link this

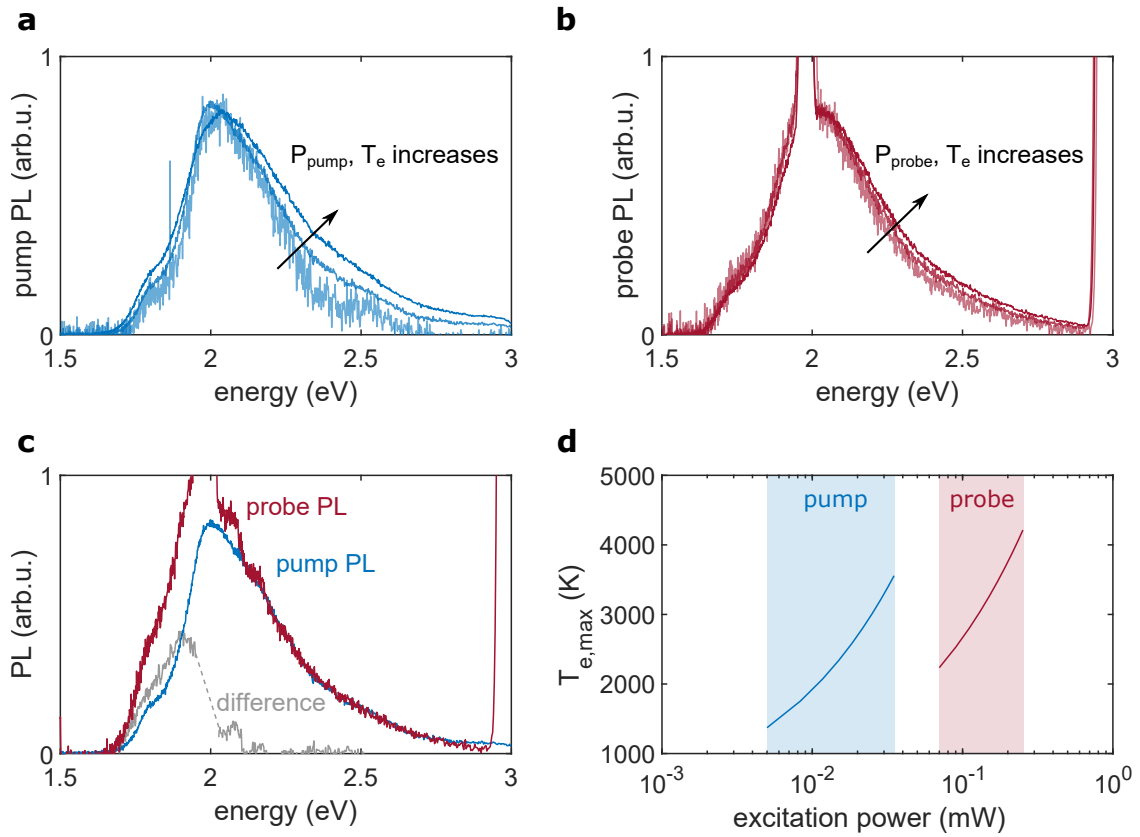


Figure 37: Characterization of the linear and nonlinear PL. For pump (a) and probe (b) excitation, the blue flank of the PL spectrum broadens for higher powers. The drawn arrows indicate the direction of increasing excitation power. As the two used power intervals lead to initial electron temperatures of the same order of magnitude (d), a direct comparison of the PL spectra can be drawn (c). For similar temperatures, the blue flank of PL and MPPL perfectly agrees and only a deviation in the lower energetic flank is observed. The low energetic difference is plotted in gray.

to an increased electron temperature that allows the electronic occupation of higher energetic states, from which radiative recombination takes place. The fact that the peak emission is located slightly above 2 eV might indicate that not only interband recombination is observed but also intraband recombination. Yet, this is only speculation. In figure 37 (c), a direct comparison between pump and probe induced PL is shown. The two signals are scaled in intensity in order to investigate the agreement of the high energetic flank. As we see, starting from around 2.1 eV, the two curves nearly perfectly overlap with each other. We take this as a hint, that the electron distributions in the sp-band have reached comparable temperatures. To verify this suspicion, we calculated the maximum reached temperatures via the TTM for both excitation powers. For the estimation, the measured spot sizes (see chapter 7.2.2), the used excitation powers and wavelength dependent absorption cross-sections, obtained from FEM simulations, were used. The relation between excitation powers and reached maximal electron temperatures is shown in figure 37 (d). The solid lines mark the calculated correlation, while the shades areas further highlight the used power intervals. We directly see that pump and probe powers lead to electron temperatures in the same order of magnitude which

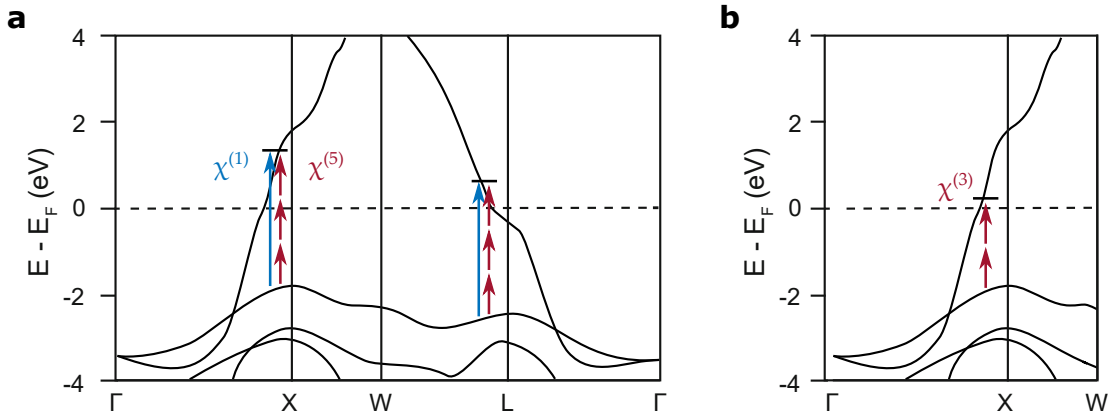


Figure 38: Linear and nonlinear absorption in the band structure of gold. (a) One pump photon (blue) or three probe photons (red) can excite optical transitions at the X- and the L-symmetry point. The excitations correspond to $\chi^{(1)}$ and $\chi^{(5)}$ processes. (b) At the X point also two-photon absorption by the infrared probe is possible, which corresponds to a $\chi^{(3)}$ process. Figure adapted with permission from [171] (originally from [173]).

makes our assumption in (c) reasonable. In a direct comparison the obtained temperatures differ a bit ($T_{e,\text{probe}} = 4000$ K and $T_{e,\text{pump}} = 3000$ K), but if the use of theoretically obtained absorption cross-sections is taken into account, this deviation can easily be explained. An additional feature can be observed in figure 37 (c). Although the high energetic flank of PL and MPPL agrees very well, a larger deviation between both is observed at the lower energetic flank. The MPPL seems to show an additional contribution that gets even more obvious if the difference between both curves is calculated (shown in gray). The difference strongly resembles an additional emission peak, originating either from a different energy band or an additional absorption channel. The fact that its maximum is located at 1.9 eV, which is exactly the energy of optical transitions at the X-symmetry point in the band structure, further strengthens this presumption. Yet, of course the question remains why this transition could be excited by the probe and not by the pump or why the probe should have an additional absorption channel here. This makes sense, if we take a closer look at the excitation mechanisms shown in figure 38 (a) and (b). The strong transition at the L-point can either be excited by one pump photon at 404 nm or three probe photons (see figure 38 (a)). Both processes result in energies, that allow transitions above the Fermi edge, near the symmetry point. At the X-point, we get a similar picture. Either one pump photon or three probe photons can excite the transition. Consequently, the pump and probe photons lead to PL at both symmetry points as a result of $\chi^{(1)}$ absorption (pump) and $\chi^{(5)}$ absorption (probe). Up to here, the PL stemming from pump and probe excitation should be very similar. Yet, we observe a difference that can be explained by figure 38 (b). For the probe photons an additional $\chi^{(3)}$ absorption channel exists at the X-point which corresponds to two-photon absorption. The resulting energy of 1.97 eV of two photons is nearly a perfect match to excite electrons slightly above the Fermi level. Consequently, it makes sense, that the probe excited PL features an additional contribution around 1.97 eV compared to the pump PL. In gold, the absorption at the L-point is far more efficient than at the X-point (see section 7.1.1) and might raise the question why we even see this additional PL peak. We argue that this difference in absorption strength might be counter balanced

by the difference in magnitude of $\chi^{(3)}$ and $\chi^{(5)}$. In general the relation $\chi^{(3)} \gg \chi^{(5)}$. Up to now, this is just an assumption that hasn't been verified free of any doubt.

7.4 DFG SUPPORTED PULSE CROSS-CORRELATION

If a partly unknown temporal response of a system is measured, it is crucial to have enough information about the pulses used for the excitation. The pulse duration has to be known, in order to distinguish between features simply related to the duration of the excitation pulses and the ones, that actually contain information about the system itself. Moreover, it is beneficial to know the temporal position of the pulse overlap as exactly as possible, in order to determine if the systems response is lacking or delayed in time. Our alignment procedure, up to now, only offers an accuracy of a few pico seconds. In the following section we will demonstrate a technique that allows the characterization of both parameters.

If we assume linearly polarized light and omit the spatial coordinates, a light pulse can be represented by the scalar electric field

$$E(t) = \frac{1}{2} \sqrt{I(t)} e^{i(\omega_0 t - \Phi(t))} + \text{c.c.} \quad , \quad (128)$$

with the temporal intensity $I(t)$ and the temporal phase $\Phi(t)$. In the field of ultrafast laser pulses it is common to omit the complex conjugate term in equation 128 and work with complex field amplitudes. This is called the analytic signal representation and simplifies the math noticeably [193]. If additionally the fast varying carrier frequency wave at ω_0 is removed, the electric field and its representation in Fourier space are given by

$$E(t) = \frac{1}{2} \sqrt{I(t)} e^{-i\Phi(t)} \quad , \quad (129)$$

$$\begin{aligned} E(\omega) &= \int_{-\infty}^{+\infty} E(t) e^{-i\omega t} dt \\ &= \sqrt{S(\omega)} e^{-i\phi(\omega)} \quad , \end{aligned} \quad (130)$$

where $S(\omega)$ is called the spectrum and $\phi(\omega)$ the spectral phase. It is common to represent the spectral (and also the temporal phase) as a Taylor series

$$\begin{aligned} \phi(\omega) &= \sum_{n=0}^{\infty} \frac{1}{n!} \left. \frac{d^n \phi}{d\omega^n} \right|_{\omega=\omega_0} (\omega - \omega_0)^n \\ &= \sum_{n=0}^{\infty} \frac{1}{n!} \phi^{(n)} (\omega - \omega_0)^n \quad . \end{aligned} \quad (131)$$

For well behaving pulses, like e.g., generated by most commercial lasers, only the first few terms have to be taken into account. The 0-th order term simply describes a relative phase between carrier and envelope of the pulse, while the 1-st order causes a shift in time. Up to this order, the shape of the pulses is not influenced and we speak of transform limited pulses. Starting from the 2-nd order, the so called linear chirp, the

shape of the pulses changes. A positive linear chirp ($\chi^{(2)} > 0$) causes the red components of the pulse to arrive earlier and a negative one the blue components to arrive earlier. Moreover, the pulse is stretched in time and energy conservation requires the peak intensity to decrease. Directly after the output, most lasers are chirp compensated and often nearly transform limited. Nevertheless, propagation through optical media will add an additional phase to the pulses and can cause them to be chirped. Depending on the frequency and material, this can be quite drastic. For example achromatic lenses, that often consist partly of heavy flint glass, can cause femto second pulses in the blue spectral region to be drastically stretched in time. Consequently, it is beneficial to obtain information about the pulse length and quality as close to the sample as possible. An easy way to measure pulse lengths, is the so called intensity auto-correlation [194]. Here, the pulse under investigation enters a Michelson interferometer and after recombination of the two split pulses, they enter a nonlinear crystal where SHG takes place. Due to the nonlinear scaling of the SHG intensity with the fundamental power, the length of the pulse is mapped as an autocorrelation

$$I_{AC}(\tau) \propto \int |E(t)E(t-\tau)|^2 dt \quad , \quad (132)$$

where τ represents the delay introduced by the interferometer. Small setups, giving rise to the intensity autocorrelation, are easily built and are commercially available. Nevertheless, this characterization procedure is not suited in our case. We want to determine the length of both pulses in the sample plane simultaneously and explicitly include the used objectives. Moreover, a measurement technique based on SHG is impractical for our 400 nm pump pulses as a complete set of UV-C optics, including detectors, would be required.

7.4.1 XFROG in lithium niobate micro-crystals

The easiest way to obtain the combined pulse lengths in the sample plane and a measurable signal in the visible spectral range, is to use DFG as mapping process (see chapter 2.4.1). If our IR pulse at 1260 nm is mixed with the 400 nm pump pulse, we obtain a difference frequency signal located around 600 nm. The necessary element, to induce a temporal delay between both pulses, is already given by the pump-probe setup's delay stage. If we further use the spectrometer for detection, we can not only separate the DFG signal from other background signals but we also can create cross-correlation frequency resolved optical gating traces (XFROG) [195, 196] which are described by

$$I_{XFROG}^{DFG}(\omega, \tau) \propto \left| \int E_{probe}(t)E_{pump}^*(t-\tau)e^{-i\omega t} dt \right|^2 \quad . \quad (133)$$

XFROG and FROG traces have the advantage over intensity autocorrelations, that they offer more information about the used pulses. With special algorithms, even a full retrieval of the pulses spectral phase is possible [193] and the amount of different chirp orders can be quantified.

The last ingredient for this technique is a nonlinear optical material. We decided to use LiNbO₃ crystal powder. The crystal itself is known to possess a large optical non-linearity [197]. The usage of crystal powder on a glass substrate gives us two additional

benefits over a large crystal. First, we can easily insert the material in our setup and second, the crystals have only sizes of a few microns and below. Therefore, phase matching has not to be considered for the nonlinear mixing process. For the sample preparation, we use commercially available crystal powder. 30 mg of powder are dissolved in 1 mL ethanol and put in an ultra sonic bath for 10 min. Afterwards, a small amount is extracted, surface-near, out of the preparation bottle and dropcasted onto a clean glass substrate. After evaporation of the remaining ethanol, the sample is finished. In figure 39 (a) a wide field image of the sample in the setup is shown. We clearly observe particle accumulations due to the dropcasting and subsequent evaporation process and also less dense particles in between. In our experience, both locations are suited for the XFROG measurements. In figure 39 (c) an example spectrum at the zero delay position is shown. We clearly observe the second-harmonic signal of the probe beam at 620 nm and a broad background, generated by the pump light. At approximately 595 nm, a strong DFG peak is visible, that only occurs if both beams hit the sample with zero delay. If we use the temporally resolved spectra, focus on the region of the DFG peak and interpolate the background by a linear function, we can extract the XFROG trace that is shown in (b). We see, that the cross-correlation of the two pulses indicates a chirp. For negative delays, the mixed DFG peak is located at 596 nm and experiences a blue shift to 593 nm for positive delays. Without further investigation, we assume that this chirp is mainly caused by a chirp of the pump pulse. Due to the spectral location at 404 nm, we are generally near absorption peaks in glass. It is known that in proximity to absorption peaks optical glasses cause non-negligible contributions to the spectral phase and, therefore, lead to higher order chirps. Especially optical components that feature heavy flint glass add tremendous amounts of linear chirp. We replaced all achromatic lenses, consisting of heavy flint glass, by spherical singlets but yet, the used high NA objective is an unknown quantity. Moreover, also pre-existing chirp might play a role. In contrast to the pump wavelength, the probe wavelength is not so critical, concerning higher order chirp from standard optical materials. Therefore, we assume the pump to be the source of the chirp, observed in the XFROG trace. For our purposes, a full retrieval of the spectral phase from the trace is not necessary. Yet, we want to point out that by an additional characterization of the probe pulse near the sample, the optical and spectral properties of the pump pulse can be retrieved even easier. For an evaluation of the traces we restrict to binning the trace on the delay axis and fit a temporal Gaussian function (see figure 39 (d)). As a result we get a cross-correlation FWHM of 420 fs.

7.4.2 XFROG in an isolated plasmonic wire

In section 7.3 we already observed noticeable second-harmonic emission from an isolated nanowire and attributed it to structural imperfections and surface roughness. Consequently, a non-negligible second order nonlinear polarization is present, that should in principle also allow DFG and, therefore, the possibility of obtaining XFROG traces from a single gold wire. In figure 40 (a), an example spectrum of a single wire upon pump and probe illumination at the zero delay position is shown. In the spectrum, we directly observe the strong second- and third-harmonic peaks, generated by the IR probe. The broad background, filling the entire visible spectral range, consists of three parts. We have signal stemming from the wire itself - pump excited PL and probe excited MPPL

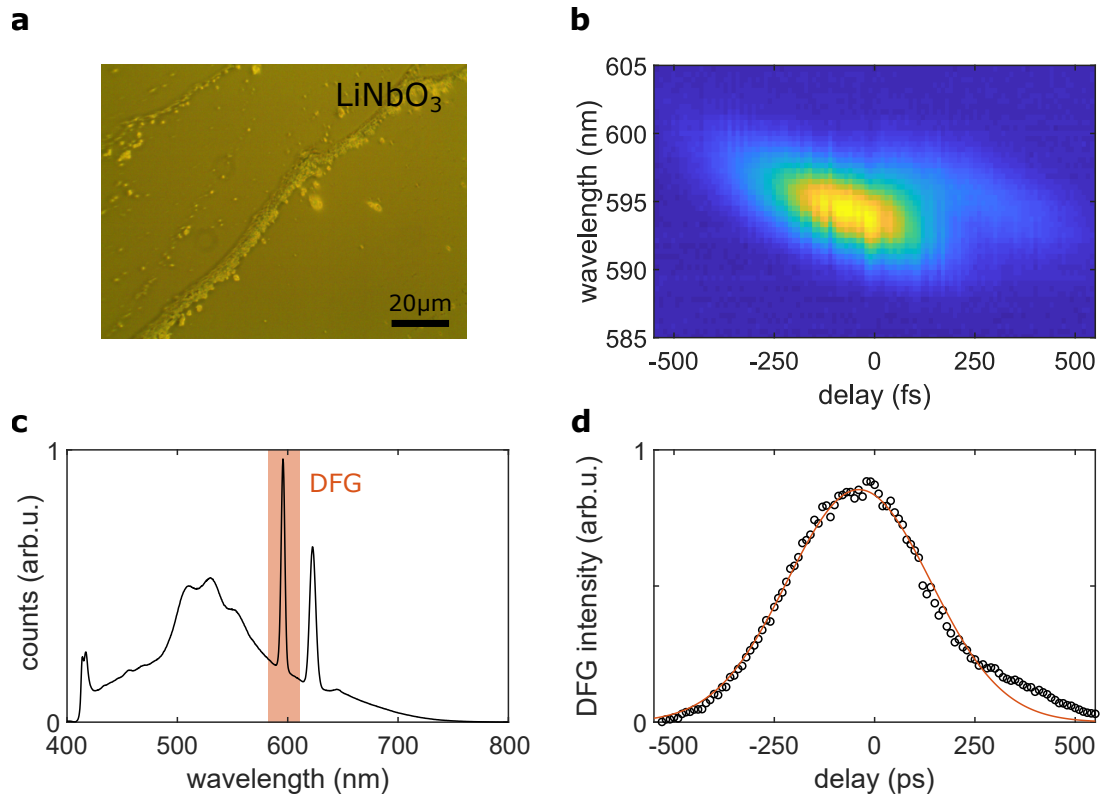


Figure 39: XFROG measurements in LiNbO_3 microparticles. (a) A wide field image of the sample shows the crystals. They accumulate in certain areas, caused by the evaporation of the solvent and in between single particles are found (b) By scanning the delay between pump and probe, an XFROG trace can be recorded with the spectrometer. The recorded intensity per wavelength and delay position is color-coded. An example spectrum at the zero delay position is shown in (c). Here, no background subtraction and flattening of the spectrum around the DFG peak was performed. (d) By binning the XFROG trace to the delay axis we get the cross-correlation pulse length.

- but also pump induced background from the glass substrate. Within the broad background, a small DFG peak near 600 nm is visible. In contrast to the LiNbO_3 sample discussed in the previous section, the amplitude is relatively low. Nevertheless, we can perform spectrally resolved delay scans and extract XFROG traces by isolating the spectral DFG region and interpolating the background. The resulting trace is shown in figure 40 (b). Similar to the trace obtained from the LiNbO_3 micro-crystals, we observe a chirp that causes red wavelengths to arrive earlier. The spectral shift in the wire occurs in the same spectral interval and length. Naturally, the question arises whether the XFROG trace from the particle could feature contributions of the wire itself or its LSPR. We omit this discussion and argue that DFG is only allowed by structural imperfections and local scattering at surfaces, which could lead to additional unknown influences. Yet, to our knowledge, this is the first time that XFROG traces have been obtained from a single, isolated plasmonic wire. For two color pump-probe experiments in single nanostructures this is an interesting technique, as it allows the characterization of the used pulses

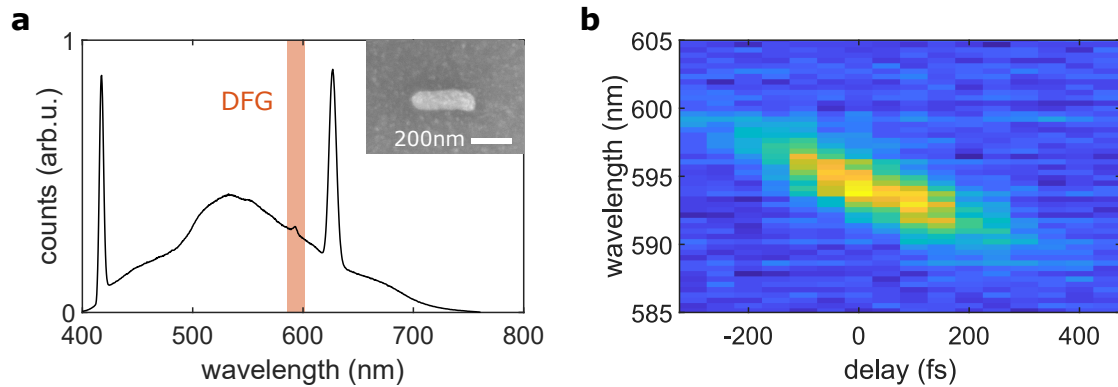


Figure 40: XFROG measurements from a single gold nanorod. (a) Spectrum of a wire upon simultaneous pump and probe excitation at zero delay. Beside the HHG peaks and a spectrally broad background, a peak at the DFG wavelength is observed (indicated by orange area). (b) By measuring delay-time resolved spectra, an XFROG trace can be extracted from the data. Ignoring the chirp and binning the trace to the delay axis yields a Gaussian pulse with $\text{FWHM} = 370$ fs.

in the same structures that are used for the actual experiment.

However, one still underlies certain restrictions. The used pump and probe powers have to be chosen carefully in order to avoid lattice temperatures that come close to the melting point of gold. From experience, the XFROG measurements worked best in larger wires. The spectral position of the LSPR can be kept constant, in first approximation, if the aspect ratio of the geometrical cross-section is kept constant.

7.5 PUMP-PROBE MEASUREMENTS ON AN ISOLATED NANOWIRE

For the acquisition of pump-probe traces, we have two possibilities in our detection unit. First, we can manually tune the delay and measure spectra at defined temporal positions. This technique was used for the XFROG based pulse characterization in the previous section. Second, we can abstain from the spectral resolution and use fully automated delay scans, that use the APD as detection unit. Regarding the signal-to-noise ratio (SNR) and also the signal-to-background ratio, the later has unmistakable advances. The obtained APD signal can be demodulated via a Lock-In at all involved frequencies and yield background-free traces at the sum- and difference-frequency of the two optical choppers. In figure 41 (a) and (c) example traces of the same structure are shown for the two different techniques. In the following, we will discuss the advantages of both methods and give a first insight in the data.

In figure 41 (a), a spectrally resolved pump-probe trace is shown. In contrast to the previous section, we are now using the spectral coordinate on the x-axis and the temporal one on the y-axis. We can clearly observe the HHG peaks at 420 nm and 630 nm and also gold luminescence, broadly located in the green to red spectral region. During the data processing, we removed dark counts from each temporal spectrum and subtracted

a spectrum of the wires response to the pump light only. Therefore, our background signal is simply given by the probe's response. A similar approach can be done for the probe but we decided against it, as slight fluctuations in the probe wavelength cause a dispersive signal at the position of the HHG peaks and makes the data harder to interpret. Of course, a probe background subtraction also leads to the same results that are discussed in the following. The obtained counts in the plot are color-coded. Around zero delay, we observe spectral changes in the pump-probe signal. While the luminescence increases, the HHG peaks show a sudden decrease. To emphasize these spectral features in more detail, we show the spectra of 0.4 ps and -5.6 ps in figure 41 (b) in red, respectively blue. Both changes are clearly visible. For further visualization, we separate the spectra into three parts. The higher-harmonics signals and the PL. In order to crop the broad PL we use spectral intervals of 150 – 200 nm centered around the HHG peaks, exclude the peaks themselves and use a 9th order Fourier series to fit the remaining data points. The choice of the fitting function has no physical base but was found to be the best method to smoothly interpolate the PL at the HHG positions. For a physical separation model, the PL process is too complicated as it would go far beyond a Gaussian or Lorentzian line shape. Consequently, even a theoretical model would likely possess many degrees of freedom, leading to an overparameterized fitting function and therefore again a questionable physical significance. A different approach, using a linear interpolation based on several data points to the left and right of the peaks, is also possible, leads basically to the same results but features a visible discontinuity in the PL and consequently systematic evaluation errors cannot be fully excluded.

The delay traces for the three signal contributions, THG, SHG and PL, are shown in figure 41 (d)-(f). The summed signals are drawn in scatter plots and connected via dashed lines as guides to the eye. The temporal zero, determined by an XFROG trace, is indicated by a gray line. Now, we clearly observe that the higher-harmonics emission experiences a signal drop at the overlap of pump and probe pulse, while the PL increases. From the data, we directly see that the relaxation, respectively recovery times of the different contributions seem to differ. For a first analysis we fitted monoexponential functions and retrieved time constants, shown in the plots. For negative delays, the THG seems to experience an increase in the signal strength that nearly instantly drops below the initial value at zero delay (figure 41 (d)). The recovery of the signal takes place within 120 ps. The fitted value has to be taken with care because of the large error of the fit (3700 ps). Although the error is larger than the actual fitted value we still give the order of magnitude of the obtained recovery time some significance because the large error is partly a result of the narrow delay span used for the fit. We assign the THG a long recovery time in the order of a few hundreds of pico seconds for the following discussion. In the SHG trace (figure 41 (e)), no significant signal increase is observed for negative delays. At zero delay, a signal drop is observed, that recovers with a faster time constant than for the THG. Here, we can in fact get a robust value of (1.9 ± 0.4) ps from the fit and the signal recovery is nicely visible in about 10 data points. The PL (figure 41 (f)) shows an increasing signal for negative delays, similar to the THG, that decreases for positive delays on a time scale of a few pico seconds. The general observed behavior is, that HHG becomes more inefficient, if the nanoparticle is pumped by blue light but that the process of PL gets stronger. Moreover, PL and SHG are affected on a fairly different time scale than THG. Although the fitted recovery time of the THG has a large error,

we definitely see no hint for a recovery time in the range of 2 – 5 ps as in the PL and SHG trace. This could indicate that the underlying physical effect of the modulation is different. For instance could a short decay time be connected to the temperature of the electron gas, while a longer one correlates with the lattice temperature. The last fact we want to point out is, that the total signal is dominated by PL, as it is about one order of magnitude bigger. Furthermore, also the modulation depth is by far the strongest. Therefore, we can expect the APD signal to be dominated by the PL. We want to point out, that the method of spectrally resolved pump-probe data acquisition is fairly inefficient. The measurement time of a single trace is about 6 – 10 min, where already setup drifts can come into play. Combined with unmodulated detection, this leads to a poor probability of acquiring meaningful traces. From experience about 60 – 70% of the traces have to be discarded and due to the significantly lower modulation depth only very few of the remaining traces show a variation in the higher-harmonics signals. Consequently, a spectrally resolved detection without additional demodulation is not suited for parameter studies. Especially excitation power dependent studies would have to be omitted because of the nonlinearly decreasing signal amplitude for lower excitation powers.

Under these circumstances we decided to use the APD as main detector and demodulate the obtained traces at sum- and difference-frequency of the two optical choppers. Afterwards, both traces are combined and we obtain results like shown in figure 41 (c). As mentioned, this trace is now dominated by a change of the PL. The shown measurement was performed instantly after the spectrally resolved measurement, shown in the other panels of the figure. No changes were made to the setup in between. The trace was rescaled and moved to a zero offset on the y-axis. This is justified because we do not use the trace for a quantitative analysis, but only for qualitative purposes. If we compare panel (c) to (f), which basically show the same physics, we notice the drastically increased quality of the signal. The signal itself now reveals a symmetric shape for positive and negative delays. In gray, the combined pulse length, obtained from XFROG measurements, is shown. We notice that the nanowire features a response for positive and negative delays. The reason for that can be simply explained by the measurements and calculations we performed until now. The signal is dominated by PL, which can be excited by the pump and the probe (see section 7.3). Moreover, the used excitation powers lead to electron gas temperatures in the same order of magnitude. Consequently, the symmetric shape is caused by the fact, that pump and probe are able to change their roles in the experiment. Alternatively, we could also speak of a double-pump PL-probe experiment.

We want to point out, that an isolated analysis of the HHG signals is not possible by combining the APD detection scheme with spectral filters like band passes. Beneath the HHG peaks, always PL is present. Therefore, we would always obtain a combination of decreasing HHG intensity and increasing PL. In the worst case, the two different contributions might cancel each other out. We always need full spectra, that allow a continuous extrapolation of the PL at the HHG peaks, in order to separate the contributions free of doubt.

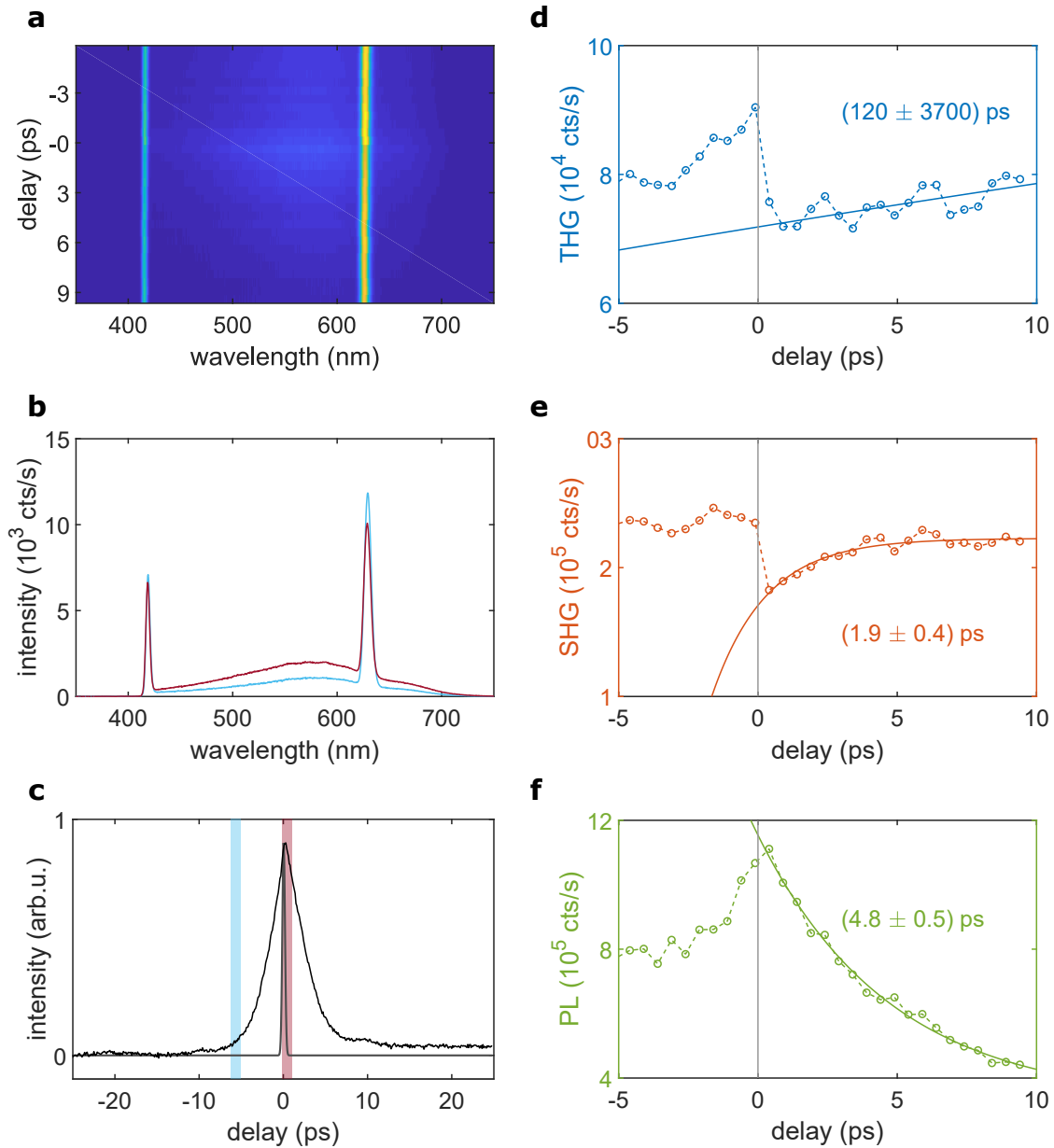


Figure 41: Pump-probe measurements on an isolated plasmonic wire. (a) In the spectrally resolved trace, the HHG peaks as well as the PL are clearly visible. The counts per second are color-coded. Two spectra (b) at different delay positions (red 0.4 ps, blue -5.6 ps) show clearly that the PL increases at the pulse overlap, while the HHG peaks decrease. In (d)-(f) we separated the contributions and show isolated traces as dots with dashed lines as guides to the eye. The gray lines highlight the zero delay position. Exponential functions were fitted (solid lines), in order to estimate decay or recovery times. The obtained time constants are given in the individual plots. In (c), a pump-probe trace with the same setup configuration is shown but we used an APD and Lock-In demodulation. The color-shaded areas correspond to the temporal position of the spectra in (b).

7.6 DATA EVALUATION AND NEAR-RESONANCE BEHAVIOR

One question to answer, is the influence of the fundamental LSPR on the pump-probe signal, i.e., is it better to be on the resonance or is a spectral location in the flank beneficial. If the signal is connected to a heat induced shift of the fundamental plasmon resonance, the pump-probe signal should be strongest, if we excite in the flank of the resonance, where the derivation of the LSPR is highest. Moreover, a change in the sign of the modulation would be expected. To clarify this question, we investigated the signal of wires of different lengths. Thereby, we are not spectrally tuning the laser over the resonance but tune the LSPR itself over the fixed probe wavelength. For the experiment, we used a sample with wires of lengths between 250 nm and 350 nm.

In figure 42 (a), the pump-probe trace of the shortest investigated wire is shown. The black line represents the combined data, obtained from sum- and difference-frequency demodulation of the APD signal. At zero delay we observe the characteristic, symmetrically shaped peak and the offset of the signal for positive and negative delays differs. This difference could be linked to changes in the system that decay on long time scales, e.g., changing lattice temperatures. Yet, we do not want to clarify this particular question and focus on the fast decaying pump-probe peak instead. In order to quantify the peaks, we first remove the offset via an error function, that creates a smooth transition between the two offset levels. The resulting offset is drawn as solid yellow line. Afterwards, the peak itself is modeled as a double sided exponential decay, convoluted with a Gaussian function, accounting for the finite pulse length of the pump and probe pulses. The model $f(\tau)$ reads

$$\begin{aligned}
 f(\tau) &= c(\tau) + \int d(t)g(t-\tau)dt \quad . \quad (134) \\
 d(t) &= \begin{cases} ae^{-k_r t} & \text{for } t \geq 0 \\ ae^{k_l t} & \text{for } t < 0 \end{cases} \quad , \\
 c(\tau) &= c_l + \frac{1}{2}(c_r - c_l) \left[1 + \operatorname{erf}\left(\frac{\tau}{\tau_c}\right) \right] \quad ,
 \end{aligned}$$

where $c(\tau)$ denotes the offset, $d(t)$ the double sided exponential decay and $g(t)$ the temporal Gaussian function which is given the width obtained from the XFROG data (see section 7.4.2). The exponential decay is described by an amplitude a and the two decay rates $k_{l/r}$, referring to the left ($\tau < 0$) and right ($\tau > 0$) decay. The offset function is given by the mean value of the first few (c_l) and the last few (c_r) data points of the trace. The error function's time constant τ_c was empirically chosen as 0.07 ps. With this fitting model, all of the obtained traces can be described. Depending on the pump and probe powers, a modulation is not only visible at the double modulation frequency ν_{double} but can also be visible at the two fundamental frequencies, as well as in the raw APD trace. Moreover, the traces at the fundamental frequency contain important information in their offsets. At the pump frequency, we see the linear PL counts in the parameter $c_l(\nu_{\text{pump}})$ and $c_l(\nu_{\text{probe}})$ at the probe frequency quantifies the nonlinear emission of the structure, featuring HHG and MPPL. From the raw APD trace, the number of totally emitted photons can be extracted as $c_l(\nu = 0)$.

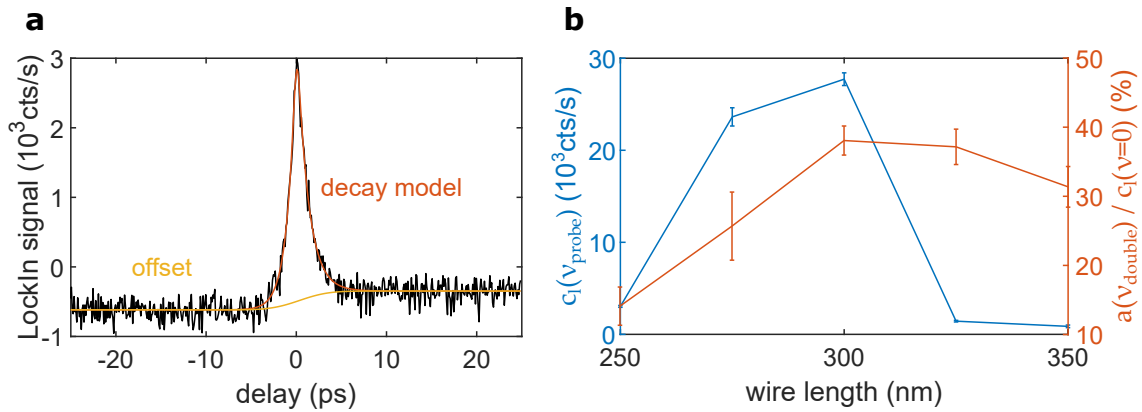


Figure 42: Evaluation of pump-probe traces and modulation depth near a LSPR. (a) For the evaluation of the pump-probe peaks we use the combined signal of sum- and difference-frequency demodulation (data shown in black). The underlying offset is described by an error function and pictured in yellow. The final decay model (orange) consists of a double sided exponential decay, convoluted with a temporal Gaussian function, accounting for the finite excitation pulse length. (b) We measured the relative modulation depth of the pump-probe peak for nanowires of different lengths (orange). In order to picture the spectral position of the LSPR, the Lock-In offset at the probe modulation frequency is also shown (blue). We see that the maximum modulation depth coincides with the LSPR.

In order to determine the modulation depth for the wires of different length, we use the fitting parameter $a(\nu_{\text{double}})$ and divide it by the left offset counts of the APD trace ($c_1(\nu = 0)$), which represents the total number of photons emitted, if the two pulses are separated by several pico seconds. We obtain a relative modulation depth that is shown in figure 42 (b, right y-axis). For the five different investigated lengths, the relative modulation is strongest for 300 nm. In order to correlate the modulation to the LSPR, we also plot the left offset of the Lock-In trace at the probe frequency ($c_1(\nu_{\text{probe}})$), which represents the total nonlinear emission. This quantity is strongest at the fundamental plasmon resonance of the wire. Due to the few measurement points, the resonance is not pictured in detail, but we can see that also the 300 nm wire is closest to the resonance. Consequently, a strong LSPR leads to a high modulation depth. From figure 42 (b) we see, that our pump-probe signal is not or only weakly connected to a spectral shift of the LSPR. Else, the relative modulation depth would have to show a dispersive shape with a transition from a negative modulation depth for short wires to a positive one for longer wires. Moreover, we should observe a zero crossing at the peak of the LSPR. Consequently, the only connection to the fundamental LSPR is, that the increased fundamental field at the resonance leads to an increased linear and nonlinear absorption and, therefor, higher electron and lattice temperatures.

7.7 POWER DEPENDENT MEASUREMENTS

One of the most important, if not the most important measurement for nonlinear optical processes, are excitation power dependent experiments. Characteristics like, e.g., the pulse area or the fluence are changed and important information can be gathered.

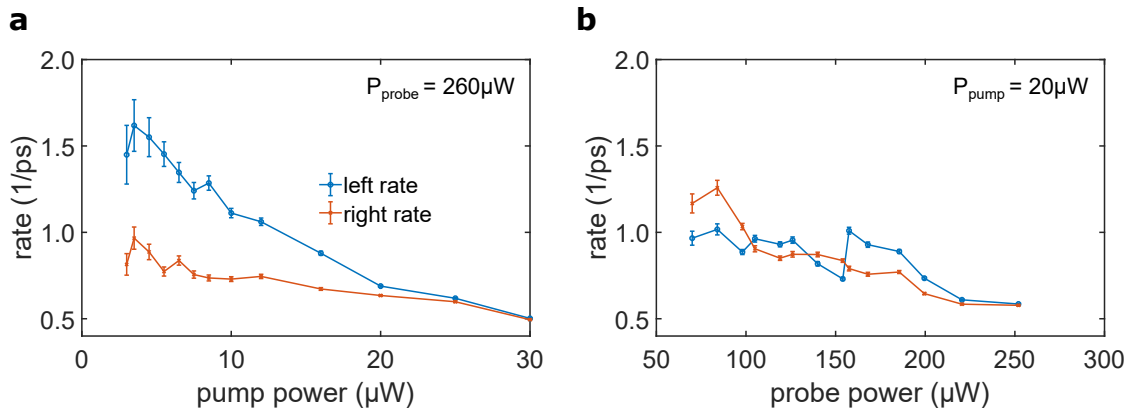


Figure 43: Power dependent changes in the decay rates of the pump-probe peak. (a) For varied pump powers both, the left and right rate, decrease with increasing powers. The same behavior holds for varying probe powers (b). For the highest measured powers, all rates approach a similar value around $k = 0.5 \text{ ps}^{-1}$. The difference between both measurements, (a) and (b), is the rate that changes more significant. While for increasing pump powers the left rate covers a larger rate interval, the opposite holds for increasing probe powers. Here, the right rate changes more significant.

The scaling of the nonlinear emission w.r.t. the excitation power can show the number of photons, involved in the nonlinear process or reveal counter-acting or competing processes as well as saturation dynamics (see, e.g., chapter 6). Therefore, we performed measurements, where one of both, pump or probe power, is varied while the other one remains fixed. We recorded APD traces and used the 8 channel Lock-In amplifier for demodulation. Finally, the data is evaluated like discussed in section 7.6.

7.7.1 power dependent change of rates

The first result of the parameter study, that we want to discuss, are the decay rates left and right of the pump-probe peak. Here, we evaluated the combined signal of the sum- and difference-frequency. In figure 43 the results from the fitting procedure (see equation 134) are shown. On the x-axis the pump (a) and probe (b) powers are given and on the y-axis the rates $k_{l/r}$. The indicated error bars are provided by the fitting algorithm. Overall, we see a trend that high excitation powers lead to low rates, while lower powers cause the rates to increase. In general, the left and right rates of the signals differ, but interestingly they seem to approach equal values for maximum powers P_{max} in both studies. Not only are the left and right rates approaching same values in both measurements but also study comprehensive the rates approach a similar value of $k_{l/r}(P_{\text{max}}) \approx 0.5$. The direct comparison between varied pump and probe powers also reveals another interesting detail. For changing pump powers, the left rate increases stronger than the right one, but for varied probe powers this dependency repeats. The right rate shows a stronger increase for decreasing powers. Yet, the left and right rate stick far closer together than for changing pump powers.

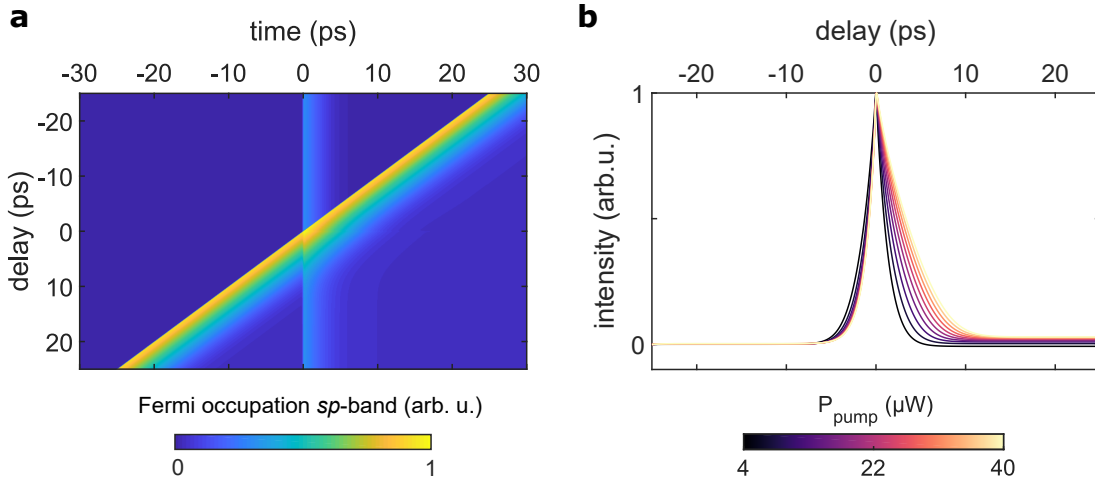


Figure 44: Results of the heuristic rate change model. The change of rates is connected to the electron temperature via a change in the sp-band's Fermi occupation. This value can be computed with a two-pulse TTM (a). In the false color plot the probe pulse remains constant at zero delay, while the pump pulses temporal position is changed. From (a), pump-probe traces (b) are created via a multiplication with the function $n(\dots)$ and subsequent integration over time.

If we change the picture from rates to decay times $\tau_{l/r} = k_{l/r}^{-1}$, we obviously get longer time constants for increasing excitation powers. This strongly resembles the results obtained by our TTM for single pulse excitation in section 7.1.3. For increasing powers, we observed higher electron temperatures that subsequently decayed on longer time scales. Therefore, the idea of linking the pump-probe peak itself or its physical origin to the electron temperature seems like a valid approach. We modified our TTM in order to allow for double-pulse excitation and calculate the 3d data set $T_{e,l}(t, \tau)$. In order to link the calculated temperatures to the pump-probe signal $I_{PP}(\tau)$, we used a simple heuristic approach

$$I_{PP}(\tau) \propto \iint [f(T_e, \tau, t, E) - f(T_i, \tau, t, E)] \rho_{DOS}(E) dE \times n(I_{pump}, I_{probe}, T_e, T_l, C_{abs}, \tau, t, \dots) dt, \quad (135)$$

where $f(T, \tau, t)$ represents the Fermi distribution, ρ_{DOS} the density of states of the sp-band and the function $n(\dots)$ is a function characteristic of the emission. It is linked to parameters like the electron and lattice temperatures, the excitation intensities as well as absorption cross-sections and of course the time. The product of the Fermi-Dirac distribution and the density of states, with subsequent integration over the energy E , describes the number of electrons in the sp-band of the gold structure. By subtracting a Fermi distribution with the system's initial temperature T_i , we only determine the newly generated electrons - by pump as well as probe pulse. In the model, we simply describe the sp-band's DOS with a square root function $\rho_{DOS} \propto \sqrt{E}$, which is known to describe the DOS of a free electron gas [35]. In figure 44 (a), the first integral is plotted with respect to the time and delay. The probe pulse is kept constant at the time $t = 0$, while the pump pulse is scanned through time. In the color code, the change in the Fermi occupation of the sp-band is shown. After the pump and probe pulse excite the

structure, we observe a fastly increased Fermi occupation, that decays on a longer time scale. In the region, where the two pulse lines cross in the (t, τ) -space, we observe an interaction of the pulses that leads to a slightly increased occupation, that decays on a longer time scale. In order to calculate pump-probe traces, using our model from equation 135, we need to find an expression for the unknown function $n(\dots)$. As a first try, we simply used normalized emission windows at the temporal position of the pulses. We omit the power scaling as we are interested in reproducing the changing rates in the system. The expression for the emission windows reads

$$n = \left[\frac{I_{\text{pump}}(t, \tau)}{\int I_{\text{pump}}(t, \tau) dt} + \frac{I_{\text{probe}}(t, \tau)}{\int I_{\text{probe}}(t, \tau) dt} \right] * e^{-\frac{t}{\tau_{\text{PL}}}} \Theta(t) \quad , \quad (136)$$

where we convoluted the normalized Gaussian pulses additionally with an exponential decay to account for a short time τ_{PL} of PL emission. To obtain a one sided decay, that is zero on the other side, the exponential function is multiplied by a Heaviside function $\Theta(t)$ [198]. In figure 44 (b), normalized example traces, calculated by the model, are shown. The pump powers, used for excitation, are color coded and range from $4\mu\text{W}$ to $40\mu\text{W}$. On the right flank of the signal, we observe a strong increase in the decay time constants, while the variation on the negative flank is less dominant. For positive delays, the modeled behavior is in its trend in agreement with the measurement. In the negative flank, on the other hand, the time constants decrease with increasing pump power which is the opposite of the observed behavior. For changing probe powers, the model leads to similar results and in consequence we abstain from a detailed presentation of the results. We conclude, that the model is capable of describing the rate behavior in the positive delay flank of the signal but it fails for negative delays. We attribute this to a too simple expression for the function $n(\dots)$. Two parameters, that could potentially solve this problem and lead to a more close-to-reality model, are the absorption cross-sections used during the calculation. Until now, they are kept constant but they are known to change with the electron and lattice temperatures. Another correlation, that has to be considered, are influences of the pump and probe power, that might go beyond electron heating. The function $n(\dots)$ could include terms, scaling with the excitation powers. Possible influences of both are discussed in the next section.

7.7.2 power dependent change of amplitudes

From the power dependent measurements, we used to determine the rates of the pump-probe peak, we can of course also extract the amplitude $a(\nu_{\text{double}})$. The fitting algorithm, presented in section 7.6, automatically provides us this value. Before discussing the obtained values, we take a closer look at the pump-probe traces at the fundamental modulation frequencies $\nu_{\text{pump/probe}}$. Aside of the pump-probe peak, the Lock-In signals at those frequencies are basically containing information about the two different light pulses, solely interacting with the structure. The values, we are now referring to, are the offsets $c_1(\nu_{\text{pump/probe}})$. From general theory about linear and nonlinear optics, we would expect the emission upon pump excitation to scale linearly with the power and the probe emission to scale nonlinearly. In figure 45 (a) and (b), the discussed values are presented for varied pump and probe excitation power (orange curves). The data points are shown with error bars and are connected via dashed lines, serving as guide

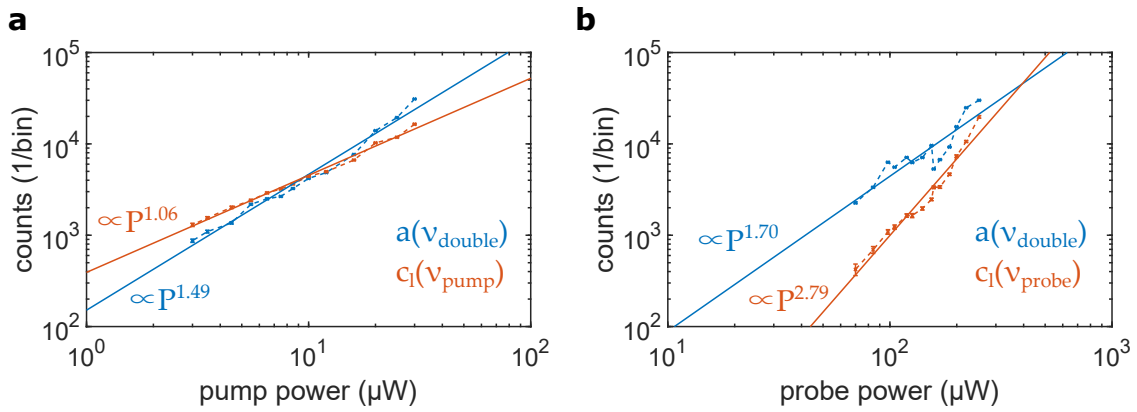


Figure 45: Power dependent change in the amplitude $a(\nu_{\text{double}})$ and Lock-In offsets $c_1(\nu_{\text{pump/probe}})$. The data points are represented with error bars and connected via dashed lines. The solid lines, in the corresponding colors, mark fitted power functions. The unit on the y-axis refers to a temporal bin with $\text{bin} = 0.1$ s. (a) The offset at the pump modulation frequency describes the systems response upon pump only excitation. We observe the expected linear power dependency, as the excited process is linear PL. For changing probe powers, we also obtain an expected nonlinear power dependency with an exponent of $n = 2.79$ at the probe modulation frequency (b). An unexpected dependency is measured at the pump-probe amplitude $a(\nu_{\text{double}})$. Here, we observe a superlinear behavior, that scales with a similar exponent $P_{\text{pump}}^{1.49}$ and $P_{\text{probe}}^{1.70}$.

to the eye. The solid lines represent fits with the function $I(P) = aP^n$. I denotes the measured counts for the individual excitation powers P , while a and n represent the fitting parameters. For the pump power tuning we get a value of $n = 1.06$, which nearly perfectly describes a linear scaling. This result is expected, since we are basically measuring linear PL. In the case of probe power tuning, the fitting procedure provides $n = 2.79$, which also lies in the expected region. Since the APD as detector is summing over all possible processes (SHG, THG and MPPL) an exponent between 2 and 3 is expected. In our measurements, the three-photon processes (THG, 3PPL) dominate, which leads to an exponent closer to three. This scaling was also confirmed on different gold nanostructures upon probe only illumination in the same setup, with the same configuration.

If we look at the power dependent signal amplitude $a(\nu_{\text{double}})$, we see that the measured data points are well described by a power function in both cases. For pump power tuning, we get an exponent of $n = 1.49$ and for the probe power $n = 1.70$. Within the measurement uncertainty one could even speak of the same value. But this has to be verified in repeated experiments, including a statistical analysis. The interesting fact is, that the signal scales higher than the linear PL but obviously less significant than the nonlinear signal upon probe only excitation. If the same scaling for both excitation powers can be confirmed by further experiments, this would give important information for the modeling of the function $n(\dots)$.

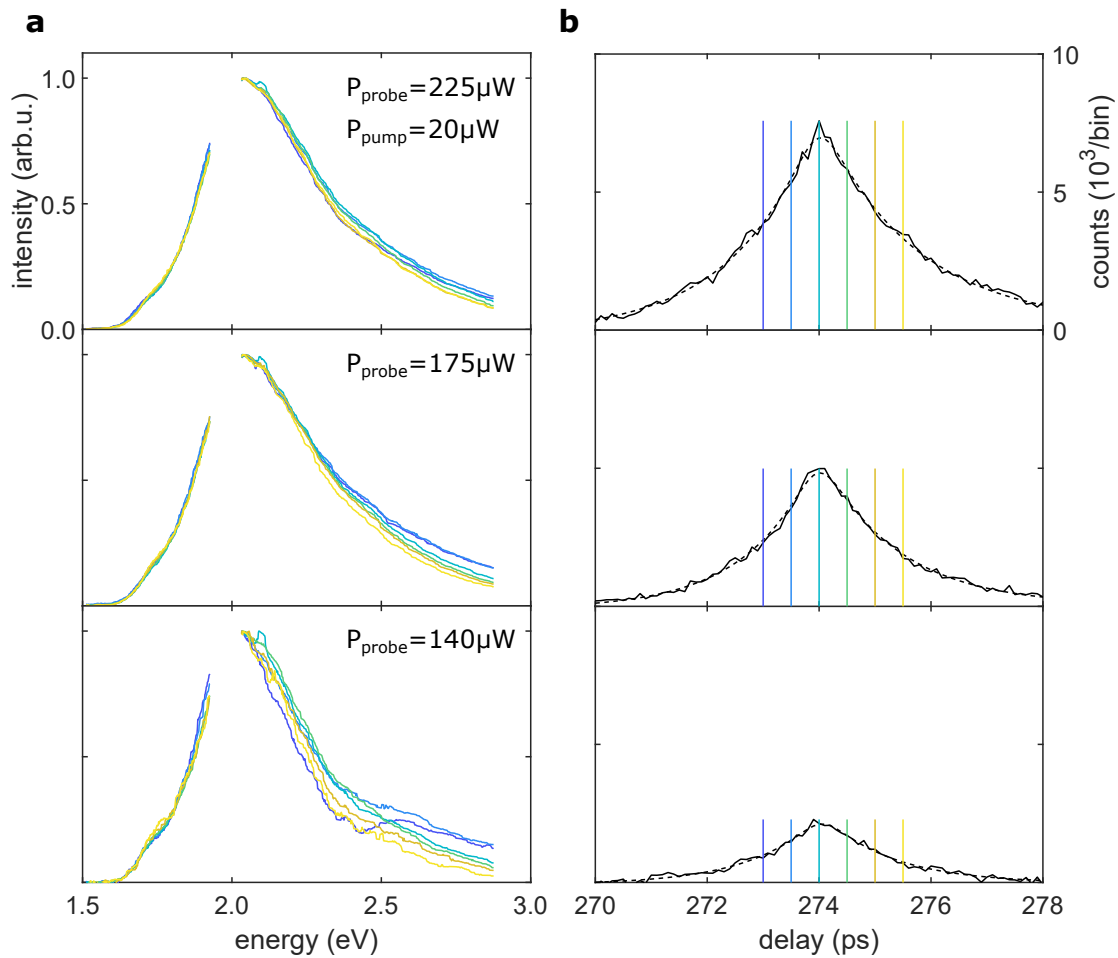


Figure 46: Pump-probe spectra around the zero delay position for varying probe powers. (a) The spectra are temporally separated by 500 fs. The temporal positions are indicated in the pump-probe traces in (b) via corresponding colors. The HHG peaks of the spectra are removed and the remaining signal is normalized to its maximum value. In (b), the data points are depicted as solid lines and the model fit is shown as dashed line. The panels of (a) and (b) show measurements with constant pump powers and decreasing probe powers (from top to bottom).

7.8 SPECTRAL BEHAVIOR

Another experiment, that can reveal further information about our pump-probe signal, are spectrally resolved, power dependent measurements. As we already discussed in section 7.5, the acquisition of spectrally resolved pump-probe traces is challenging by means of an efficient data recording process. Moreover, for lower excitation powers, we have to increase the measurement time which brings us to temporal regions where drifts of the sample are far from negligible. In consequence, we decided to take a qualitative look at pump-probe spectra, located around the zero delay position. We chose 6 positions around the pump-probe peak, separated by 500 fs steps and recorded spectra. In contrast to the previously obtained spectrally resolved traces, we have a lower temporal resolution and also a smaller time interval covered, but we gain the advantage of longer integration times. Especially for low excitation powers, this allows the acquisition of

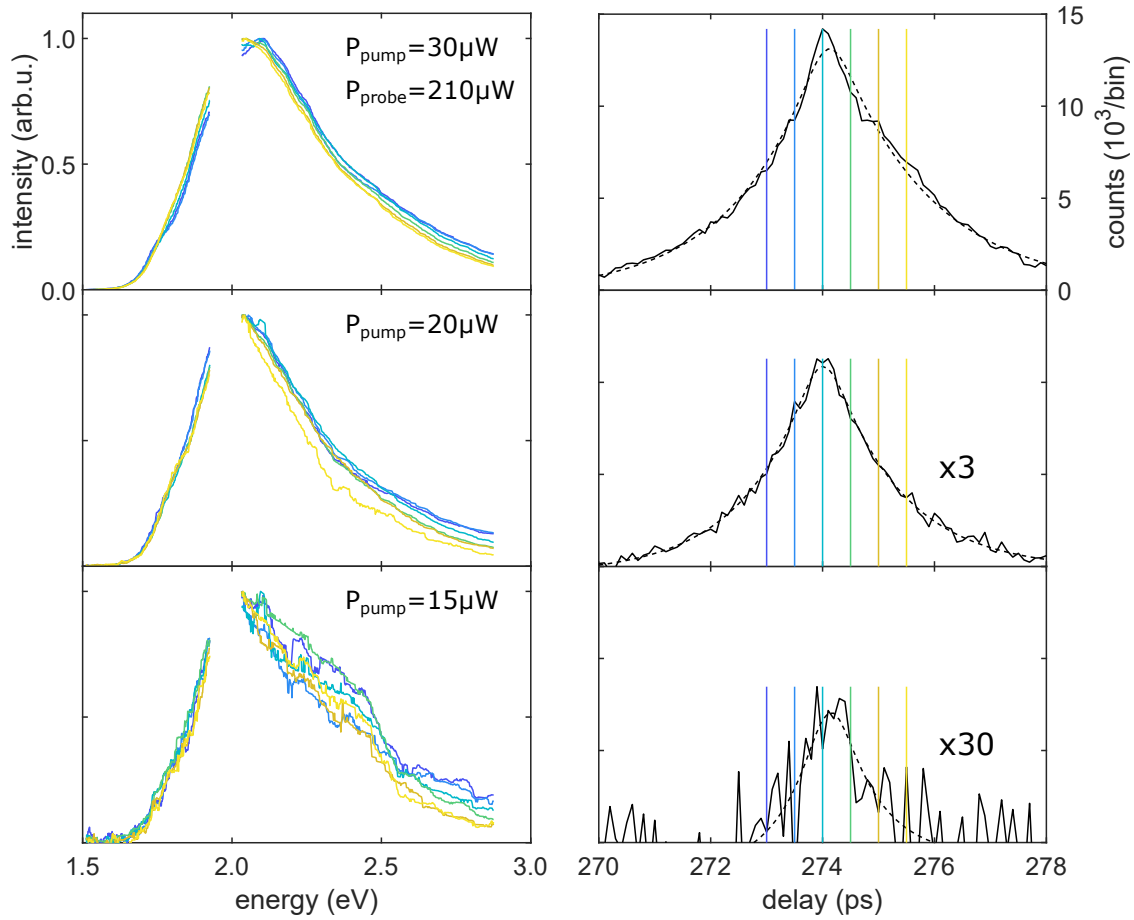


Figure 47: Pump-probe spectra for changing pump powers at different temporal positions. (a) The 500 fs separated, normalized spectra are shown in different colors, that correspond to the vertical lines shown in (b). In (b), the pump-probe traces at the combined double modulation frequency are shown as solid black lines, while the dashed lines represent model fits. The different panels of (a) and (b) show the data for decreasing pump powers in descending order from the top.

reliable data. In figure 47 and 46 obtained data for different pump and probe powers is shown. In the left panels we see the 6 different spectra and in the right panels the corresponding Lock-In traces at the combined double modulation frequencies. The solid black lines connect the data points and the dashed ones represents the model fit (see equation 134). Colored vertical lines in the right panels correspond to the line colors of the spectra and mark the temporal positions. The spectra in the left panel are background corrected and additionally a spectrum, obtained about 15 ps before the temporal zero, is subtracted. We removed the higher-harmonics peaks from the data and normalized the resulting spectra to their maximum values.

For a constant pump power and decreasing probe power (figure 46), we clearly observe that the blue flank of the pump-probe signal decreases while we scan over the zero delay position. This behavior is present for all investigated probe powers and seems to become more dominant if the power is reduced. The potentially most interesting spec-

trum is observed for the lowest probe power at the smallest delay position (left panel, lowest row, dark blue). Here, we seem to observe a drop in the spectrum short below 2.5 eV, that has recovered 500 fs later. This could be an indication that our pump-probe signal consists of different contributions. Starting at 2.4 eV an interband recombination contribution is likely to be observed and the lower energetic peak could be caused by intraband recombination or scattering. Moreover, a 2PPL process at 1.9 eV has to be considered (see section 7.3). Of course, this behavior has to be verified by further experiments, in order to rule out a measurement artifact. In the red flank of the spectra we also observe minor variations while scanning over the pump-probe peak, but in contrast to the blue flanks behavior this is less prominent and not discussed in detail.

In figure 47 the corresponding measurement, involving pump power tuning, is shown. The arrangement of the figure is equivalent to figure 46. The obtained data shows similarities to the probe power tuning experiment. We also observe a decreasing blue flank in the spectra, when we scan over the temporal zero. Moreover, this feature also becomes more dominant for lower excitation powers. Interestingly, we also observe a change of the spectral shape for the lowest powers compared to higher pump powers. In contrast to low probe powers, the blue flank of the spectrum (around 2.5 eV) seems to decrease stronger than the lower energetic part between 2.0 eV and 2.5 eV. One additional aspect is observed for the highest pump power. Here, we do not only observe variations in the blue (and red) flank of the spectrum, but we seem to measure a red shift of the peak.

A potentially interesting model, that describes spectrally resolved PL from isolated gold nanowires, is given in a publication by Cai et al. [179]. A quantum mechanical based approach, using the following equation is given

$$I_{\text{PL}}(\omega) = \sum_{E_i - E_j = \omega} \Gamma_{i \rightarrow j}(\omega) P_i (1 - P_j) \rho_{\text{EDOS}}(E_i) \rho_{\text{EDOS}}(E_j) \rho_{\text{PDOS}}(\omega) \quad . \quad (137)$$

The emitted spectrum of the structure is given by optical transitions between the energy levels E_i and E_j with the transition rates $\Gamma_{i \rightarrow j}$, determined by Fermi's golden rule. For the transition matrix elements, an easy expression can be obtained by simply approximating the nanostructure as a cylindrical well and the use of radial electronic wave functions within the independent electron approximation. The publication yields the expression $\propto e^{-\alpha(\sqrt{E_i} + \sqrt{E_j})}$ for the transition matrix element. The parameter α is artificially set to unity. The occupation probabilities of the states i, j are given by $P_{i,j}$. Here, the current electron temperature enters via the Fermi distribution. Also optical transitions, starting or ending on the respective state, have to be taken into account. To complete the model, the electronic density of states ρ_{EDOS} at the two energies is needed. In the publication, a rectangular function for the d-band and a square root function for the sp-band were sufficient. Besides the EDOS, also a photonic density of states ρ_{PDOS} is incorporated in the model and accounts for the plasmon resonance of the structure. Our first application of the model was not successful, as we could not recreate the observed spectrally varying features in the blue flank of the signal. Again, we used our two-pulse TTM in order to determine a Fermi distribution with respect to the time t and the delay τ . We used the resulting distribution in order to calculate the occupation prob-

abilities $P_{i,j}$ and artificially lowered the d-bands occupation in order to allow radiative recombination. The transition rate $\Gamma_{i \rightarrow j}$ was calculated as

$$\Gamma_{i \rightarrow j} = \frac{2\pi}{\hbar} e^{-(\sqrt{E_i} + \sqrt{E_j})} \rho_{\text{EDOS}}(E_j) \quad , \quad (138)$$

according to Fermi's golden rule and the publication. The calculated spectra seemed to be completely dominated by the PDOS, approximated as a Lorentzian function. Since we were not able to achieve significant spectral changes, we do not show results or discuss the model further. Yet, we still want to mention this model, as it seems to be well suited for our application. Probably further thinking has to be done, concerning temperature dependent changes in the PDOS and also modified transition rates in the excitation procedure, that are equivalent to a temperature dependent absorption cross-section. Additionally, an inclusion of optical transitions in the excitation process could change the game as we, until now, only used the Fermi occupation.

7.9 OUTLOOK AND DISCUSSION

Within this chapter we have discussed the band structure of gold, including the possible optical transitions as well as heating and subsequent cooling mechanisms for the quasi free electrons. After discussing the linear and nonlinear response of our nanowires upon pump and probe only excitation, we moved to spectrally resolved pump-probe traces. Although the traces have a low signal-to-noise ratio, we still could identify important changes. The main contribution to the overall signal is caused by a change in the PL. Minor contributions are given by changes in the THG and SHG. Due to the SNR we decided for measurements involving an APD for detection, a double modulation technique of pump and probe and subsequent Lock-In detection at all involved frequencies. The signal, that was found to be dominated by PL, is broadened to both sides of the pulse overlap. The temporal width and location of the later, we were able to identify via XFROG measurements in LiNbO₃ micro-crystals and also isolated gold nanostructures. Excitation power dependent measurements for both, the pump and the probe, revealed that the decay constants left and right to the zero delay position behave differently. A heuristic model, linking the rates to a change in the electron temperature, was partly successful as only the behavior of the right flank can be qualitatively described. For further modeling we believe the best approach is to take also temperature dependent changes in the absorption cross-section into account. This might be the key to model changes in the negative flank of the pump-probe signal. Further measurements provided power dependent spectra at 6 different positions around the temporal zero. Here, an interesting fact was observed. While scanning over the pulse overlap position, the blue flank of the spectrum seems to decrease. This effect becomes more dominant for decreasing powers - pump as well as probe powers.

Our findings indicate that our pump-probe signal is linked to an increased electron temperature but for a full understanding of the physical origin detailed, spectrally resolved measurements are indispensable. To get an acceptable SNR, that also allows reasonable measurement times, we believe that the acquisition of spectra should also be done with a fast readout technique combined with Lock-In demodulation. Especially

for low excitation powers, this could give the final hints for model building. Additional changes in the setup, like e.g. scanable mirrors in front of the microscope, could lead to an easier experimental access to the spatial overlap of pump and probe. A reproducible realignment procedure could additionally help to prevent drift problems and resulting capped measurement times. Here, scan mirrors offer a distinct advantage over manually tuned elements, as a manual realignment process can be time intensive and other long term drifts in the setup might come into play.

CONCLUSION

Nanostructures made of metals or semiconductor material represent the transition from the atomic scale to the macroscopic scale. Despite their size of several nanometers to a few hundreds of nanometers, they still show quantum mechanical effects and do not only lead to groundbreaking technological advances but are also subject of current fundamental research. In this thesis we investigated a nonlinearly operating nanocircuit and were thereby able to extend the current understanding of second-harmonic generation on the nanoscale. Moreover, we revealed the saturation dynamics of a semiconductor absorber mirror based on low density quantum dots before moving on to electron dynamics in gold nanorods and their influence on nonlinear optical processes.

In the beginning of the thesis, we gave the physical framework for understanding the subsequent topics (chapter 2). We introduced the field of plasmonics and discussed the bound, dipole carrying excitations at different metal-dielectric interfaces. Additionally, we summed up nonlinear optical effects up to the third order. Afterwards, we laid the focus on computational electrodynamics (chapter 3) and presented finite element models for different plasmonic nanostructures. We discussed nanowires and split-ring resonators as representatives of resonant nanostructures and a two-wire transmission line as a waveguide-like one.

Chapter 4 marked the beginning of our research in the field of second-harmonic generation in gold nanostructures. The project was brought to us by Prof. C.-B. Huang and investigated in a collaboration [33]. We demonstrated the past understanding of second-harmonic generation in sub-wavelength nanoparticles by calculating the nonlinear polarization in a simple gold nanowire and a split-ring resonator. We clearly saw, that this source for second-harmonic generation will only lead to emission into free space optical modes, if the structure possesses a geometrical asymmetry. As this is a consequence of the free space modes being plane waves, we decided to investigate a structure that is in fact symmetric but offers different modes of different symmetries for the emission. The structure of choice was a two-wire transmission line, consisting of two infinitely extended gold nanowires. It offers a symmetric fundamental mode, as well as an anti-symmetric one. This holds for all involved frequencies - fundamental and second-harmonic. By using mode overlap integrals, we demonstrated that the generated second order nonlinear polarization at the surface of the wires can emit into the symmetric waveguide mode but not into the anti-symmetric one. Chapter 5 moves this work from a theoretical basis to an experimental one. The measurements were performed by the group of Prof. C.-B. Huang and we were in charge of data evaluation as well as model building. In the collaboration, we were able to verify our model for

second-harmonic generation in a two-wire transmission line from the previous chapter. Moreover, we generalized the nonlinear coupling behavior and used fundamental mode superpositions instead of modes of purely symmetric or anti-symmetric character. In experiments, we varied the amplitude ratio of the two contributions and created an intuitive model, that is capable of fully reproducing the observed coupling behavior. Not only was this step successful, but allowed us also to extrapolate the coupling characteristics of the nanocircuit and include phase differences into the superposition of modes. An even more complex and variable mechanism was found. The measurements on fundamental mode superpositions did not only show us a generalized behavior, but also allowed us to exclude several influences of potential local sources for second-harmonic emission and strengthened our statement on second-harmonic generation in symmetric nanostructures.

Up to this point, our model and calculation was only based in the cross-section of the two-wire transmission line. By a modification of the well known coupled amplitude equations from standard textbooks, we built an intuitive model, that describes the propagation along the waveguide. Fitting this set of coupled differential equations to measurements on varying waveguide lengths, gave us a hint, that we might be able to observe back conversion from the generated second-harmonic modes to the fundamental ones. Yet, to verify this assumption free on any doubt, further measurements have to be conducted. The work in this chapter was concluded by moving our interest towards a nonlinear substrate beneath the nanocircuit. We were able to exclude an influence of the ITO layer beneath our structures and also demonstrated, that a tailored nonlinear substrate could in fact either boost the efficiency of our circuit or even offer a more complex operation. This poses an opportunity for the creation of nonlinearly operating elements for optical circuitry.

With chapter 6, we moved away from plasmonic nanostructures and towards nanostructured semiconductor systems. We investigated a semiconductor saturable absorber mirror by ultrafast pump-probe measurements. The structure under investigation will be used for mode locking in an ultrafast red emitting vertical-external-cavity surface emitting laser. The sample was produced by the group of Prof. Michler from Stuttgart and was based on quantum dots as saturable absorber. After explaining the physical background of saturable absorbers and the structure under investigation, we introduced our setup for degenerate pump-probe measurements. In the measurements, we revealed two recovery times after the initial saturation process of the quantum dots. A biexponential function, convoluted with a Gaussian function, accounting for a finite pump and probe pulse length, provided the two time constants - 520 fs and 2 ns. By performing pump fluence dependent measurements, we were able to determine the saturation fluence of the structure as $25 \frac{\mu\text{J}}{\text{cm}^2}$. Here, we want to point out, that our sample featured a quantum dot density orders of magnitude lower than reported for comparable structures. Consequently, we have the possibility to further influence the saturation fluence in the future. Moreover, it is to our knowledge the first time, that the saturation dynamics of a saturable absorber are investigated in a quantum dot based absorber in this spectral range. Finally, wavelength dependent measurements revealed the spectral dependency of the saturation process. We observed changes in the composition of the two recovery

constants and attributed them to different properties of the system.

In chapter 7, we revisited plasmonic nanostructures but instead of waveguides our focus was on resonant gold nanowires. In the current research on nonlinear plasmonics it is still unknown what role the bandstructure and the exact occupation play. To resolve this question, we decided to conduct multi-color pump-probe experiments. In the beginning of the chapter, we took a close look at the bandstructure of gold, possible optical excitation mechanisms, the fate of excited plasmons and especially the role of hot electrons in the conduction band. After excitation to high energetic states in the conduction band, the electrons thermalize and this process can be nicely described by a two temperature model. Our approach was, to excite hot electrons with a blue pump pulse, use a time delayed infrared probe pulse and monitor the changes in the nonlinear emission. After explaining our setup in detail and the plasmonic structures under investigation, we proceeded with spectrally resolved pump-probe measurements. By a separation of the higher-harmonics signals and the linear and nonlinear photo luminescence, excited by the pump and probe beam, we were able to draw first conclusions. First, the signal was dominated an order of magnitude by changes in the photo luminescence and second, we got hints on decay and recovery times of the signal. Interestingly, the luminescence increase at the temporal overlap of the two pulses, while the higher-harmonics signals decrease. Moreover, we got a first indication, that the recovery of the third-harmonic signal might be on a drastically longer timescale than the recovery of the second-harmonic signal. Yet, this was only a first hint and has to be verified by future experiments. The last fact to note was the shape of the luminescence pump-probe peak. While the higher-harmonics peaks have their changes for positive pulse delays, the luminescence peak is broadened to both sides. We argued that both, pump and probe pulse, are able to generate hot electrons in the conduction band, while also both are able to excite photo luminescence - linearly or nonlinearly. Consequently, a peak broadened to positive and negative delays is even expected. Due to the poor signal-to-noise ratio of the spectrally resolved traces, we were forced to switch to a Lock-In based detection scheme involving a single photon counter. Of course, this means a loss of spectral information and that the signal will be dominated by changes in the linear and nonlinear photo luminescence but allowed us to conduct excitation power dependent measurements, that involve low optical powers. Here, we were able to picture the influence of varying pump and probe powers with regard to decay rates for positive and negative delays, as well as changes in the amplitude of the peak. We started to build a theoretical model, combining the previously introduced two temperature model with a two pulse excitation scheme, but were not successful yet. The next step is to find an adequate function, that mirrors the emission process of linear and nonlinear luminescence. A key to determine this unknown function are excitation power dependent measurements, that are spectrally resolved in addition. We performed first experiments, involving larger delay steps and longer integration times, but ultimately one has to revert to a Lock-In based, spectrally resolved detection scheme, for smaller delay steps with a reasonable signal-to-noise ratio. Additionally, we introduced a new technique to obtain combined pulse lengths in multi color pump-probe experiments in this chapter. By using difference-frequency generation, we were able to measure cross-correlation frequency resolved optical gating traces in micro crystals made of lithium niobate. The two pulses, involved in the experiment, sample each other in the sample plane of the experiment and beside of the combined pulse

length, we were able to resolve a slight chirp in the traces. Moreover, we were also able to conduct this measurement on an isolated gold nanowire. To our knowledge, this is the first time this experiment has been demonstrated in an isolated plasmonic nanostructure and poses a big advantage for the future. The pulse characterization can be done in the exact same structure that will be used for the later experiment.

In conclusion, we laid the foundation for future experiments to reveal the role of the bandstructure and its occupation in nonlinear processes on the nanoscale. We introduced a new technique to gather information about the used pulses, observed first experimental hints on the topic and worked towards a theoretical model. With future experiments in the right direction, this fundamental physical question might be answered.

APPENDIX

A.1 LINEAR AND NONLINEAR ABSORPTION PROCESSES

In order to calculate absorption, we consider the time averaged rate of work done on a charge distribution. Poynting's theorem states this rate as

$$\langle \text{rate of work done} \rangle = \langle \mathbf{j} \cdot \mathbf{E} \rangle . \quad (139)$$

For the current \mathbf{j} we use

$$\mathbf{j} = \mathbf{j}_{\text{ext}} + \nabla \times \mathbf{M} + \frac{\partial \mathbf{P}}{\partial t} , \quad (140)$$

which simplifies for vanishing free currents and a non-magnetic material

$$\mathbf{j} = \frac{\partial \mathbf{P}}{\partial t} . \quad (141)$$

For simplicity, we only consider scalar fields and use the representation

$$E(t) = \sum_n E(\omega_n) e^{-i\omega_n t} , \quad (142)$$

$$P^{(k)}(t) = \sum_n P^{(k)}(\omega_n) e^{-i\omega_n t} , \quad (143)$$

where $P^{(k)}(t)$ is the k -th order nonlinear polarization and the index n sums over positive and negative frequencies. Since $E(t)$ and $P^{(k)}(t)$ are real quantities, we demand

$$E(-\omega_n) = E(\omega_n)^* , \quad (144)$$

$$P^{(k)}(-\omega_n) = P^{(k)}(\omega_n)^* , \quad (145)$$

$$\chi^{(k)}(-\omega_n; -\omega_1 \dots -\omega_k) = \chi^{(k)}(\omega_n; \omega_1 \dots \omega_k)^* , \quad (146)$$

$$\text{with } \omega_n = \sum_{i=1}^n \omega_i .$$

linear absorption

For linear absorption, we perform a detailed calculation. The monochromatic electric field is

$$E(t) = E(\omega) e^{-i\omega t} + E(-\omega) e^{i\omega t} . \quad (147)$$

This leads to a linear polarization in the medium

$$\begin{aligned}
P^{(1)}(t) &= \epsilon_0 \chi^{(1)} E(t) , \\
&= \underbrace{\epsilon_0 \chi^{(1)}(\omega; \omega) E(\omega)}_{P(\omega)} e^{-i\omega t} + \underbrace{\epsilon_0 \chi^{(1)}(-\omega; -\omega) E(-\omega)}_{P(-\omega)} e^{i\omega t} , \\
&= \underbrace{\epsilon_0 \chi^{(1)}(\omega; \omega) E(\omega)}_{P(\omega)} e^{-i\omega t} + \underbrace{\epsilon_0 \chi^{(1)}(\omega; \omega)^* E(\omega)^*}_{P(\omega)^*} e^{i\omega t} , \quad (148)
\end{aligned}$$

For the time averaged rate of work we find

$$\begin{aligned}
\left\langle \frac{\partial P^{(1)}(t)}{\partial t} E(t) \right\rangle &= \langle (-i\omega P(\omega) e^{-i\omega t} + i\omega P(\omega)^* e^{i\omega t})(E(\omega) e^{-i\omega t} + E(\omega)^* e^{i\omega t}) \rangle , \\
&= \underbrace{\langle -i\omega P(\omega) E(\omega) e^{-i2\omega t} \rangle}_{\langle \dots \rangle = 0} - i\omega P(\omega) E(\omega)^* + i\omega P(\omega)^* E(\omega) + \underbrace{\langle i\omega P(\omega)^* E(\omega)^* e^{-i2\omega t} \rangle}_{\langle \dots \rangle = 0} , \\
&= \langle -i\omega \epsilon_0 \chi^{(1)}(\omega; \omega) |E(\omega)|^2 + i\omega \epsilon_0 \chi^{(1)}(\omega; \omega)^* |E(\omega)|^2 \rangle , \\
&= \langle \omega \epsilon_0 |E(\omega)|^2 i(\chi^{(1)}(\omega; \omega)^* - \chi^{(1)}(\omega; \omega)) \rangle , \\
&= 2\omega \epsilon_0 |E(\omega)|^2 \text{Im}\{\chi^{(1)}(\omega; \omega)\} . \quad (149)
\end{aligned}$$

second order nonlinear absorption

Equivalent to linear absorption, the calculation can be done for a second order nonlinear polarization

$$\begin{aligned}
P^{(2)}(t) &= \epsilon_0 \chi^{(2)} E^2(t) , \\
&= \epsilon_0 \chi^{(2)}(2\omega; \omega, \omega) E^2(\omega) e^{-i2\omega t} + 2\epsilon_0 \chi^{(2)}(0; \omega, -\omega) |E(\omega)|^2 \\
&\quad + \epsilon_0 \chi^{(2)}(-2\omega; -\omega, -\omega) E^2(-\omega) e^{i2\omega t} , \\
&= \epsilon_0 \chi^{(2)}(2\omega) E^2(\omega) e^{-i2\omega t} + 2\epsilon_0 \chi^{(2)}(0) |E(\omega)|^2 + \epsilon_0 \chi^{(2)}(2\omega)^* E^2(\omega)^* e^{i2\omega t} , \\
&= P^{(2)}(2\omega) e^{-i2\omega t} + P(0) + P^{(2)}(2\omega)^* e^{i2\omega t} , \quad (150)
\end{aligned}$$

leading to a time averaged work of

$$\begin{aligned}
\left\langle \frac{\partial P^{(2)}(t)}{\partial t} E(t) \right\rangle &= \langle (-2i\omega P^{(2)}(2\omega) e^{-i2\omega t} + 2i\omega P^{(2)}(2\omega)^* e^{i2\omega t}) E(t) \rangle , \\
&= 0 . \quad (151)
\end{aligned}$$

Every element of the rate of work has a time harmonic part. Using the time average leads to an overall zero. Consequently, no energy can be deposited in a $\chi^{(2)}$ medium - within the assumptions made during the calculations.

third order nonlinear absorption

The third order nonlinear polarization is given as

$$\begin{aligned}
P^{(3)}(t) &= \epsilon_0 \chi^{(3)} E^3(t) , \\
&= \epsilon_0 \chi^{(3)}(3\omega; \omega, \omega, \omega) E^3(\omega) e^{-i3\omega t} + \epsilon_0 \chi^{(3)}(-3\omega; -\omega, -\omega, -\omega) E^3(-\omega) e^{i3\omega t} \\
&\quad + 3\epsilon_0 \chi^{(3)}(\omega; \omega, \omega, -\omega) |E(\omega)|^2 E(\omega) e^{-i\omega t} \\
&\quad + 3\epsilon_0 \chi^{(3)}(-\omega; \omega, -\omega, -\omega) |E(\omega)|^2 E(-\omega) e^{i\omega t} \\
&= P^{(3)}(3\omega) e^{-i3\omega t} + P^{(3)}(3\omega)^* e^{i3\omega t} + P^{(3)}(\omega) e^{-i\omega t} + P^{(3)}(\omega)^* e^{i\omega t} . \quad (152)
\end{aligned}$$

The time averaged work results in

$$\begin{aligned}
\left\langle \frac{\partial P^{(3)}(t)}{\partial t} E(t) \right\rangle &= \dots = \langle -i\omega P^{(3)}(\omega) E(\omega)^* + i\omega P^{(3)}(\omega)^* E(\omega) \rangle \quad , \\
&= \langle 3\omega\epsilon_0 |E(\omega)|^4 i(\chi^{(3)}(\omega)^* - \chi^{(3)}(\omega)) \rangle \quad , \\
&= 6\omega\epsilon_0 |E(\omega)|^4 \text{Im}\{\chi^{(3)}(\omega)\} \quad .
\end{aligned} \tag{153}$$

In contrast to a second order nonlinear medium, a $\chi^{(3)}$ medium can absorb. The process is called two-photon absorption.

A.2 MODE PROFILES OF A TWO WIRE TRANSMISSION LINE

In this section, the mode profiles of a TWTL are presented in detail. In figure 48 all electric field components of the anti-symmetric mode are shown and in figure 49 the equivalent is done for the symmetric mode. By black lines the chosen geometry is indicated. Both figures consist of two columns, where the left ones show a TWTL in a homogeneous surrounding ($n_{\text{air}} = 1.0002$) and in the right ones a substrate is added beneath the TWTL. In the later case, the substrate was given a purely real refractive index of ($n_{\text{substrate}} = 1.5$), while the upper part of the model was chosen as lossless air. Based on the shapes of the electric fields, charges are drawn in both wires of the TWTL. We only show the real parts of the electric fields and normalized the field strengths to the maximum absolute value of each individual panel.

In the anti-symmetric mode (figure 48, left panels) we clearly observe, that each vector component of the electric field possesses the highest strength in the gap of the waveguide. Moreover, the indicated charges in the wires perfectly match the surrounding fields. If we move to the right panels of the figure, where a substrate beneath the TWTL is added, the field components still have strong similarities to the homogeneous case. The basic axial symmetry to the vertical center of the structure hasn't changed. The main difference, caused by the introduced substrate, is visible in the x - and y -component of the field. Obviously, the symmetry in the fields, with respect to the horizontal center axis, has changed. Although the direction of the fields, and therefore the overall fundamental symmetry, remains the same, the symmetry in strength is now broken. The places of high field localization are in the gap, but stronger attracted to the substrate. Of course one reason for that is the smaller radius of curvature of the lower edges, combined with the material tripple point. In the edges, three materials come together in an infinitely sharp transition. Consequently, we observe stronger field localizations there. In the case of the symmetric mode (figure 49), the same observations hold. The fundamental symmetries of the modes haven't changes, but the localization of the fields is stronger attracted to the substrate. Overall we want to point out, that the consideration of a substrate does not alter the modal symmetry with respect to the central vertical symmetry axis. This is the symmetry, we are refering to in the main text and that is important for our argumentation and modelling.

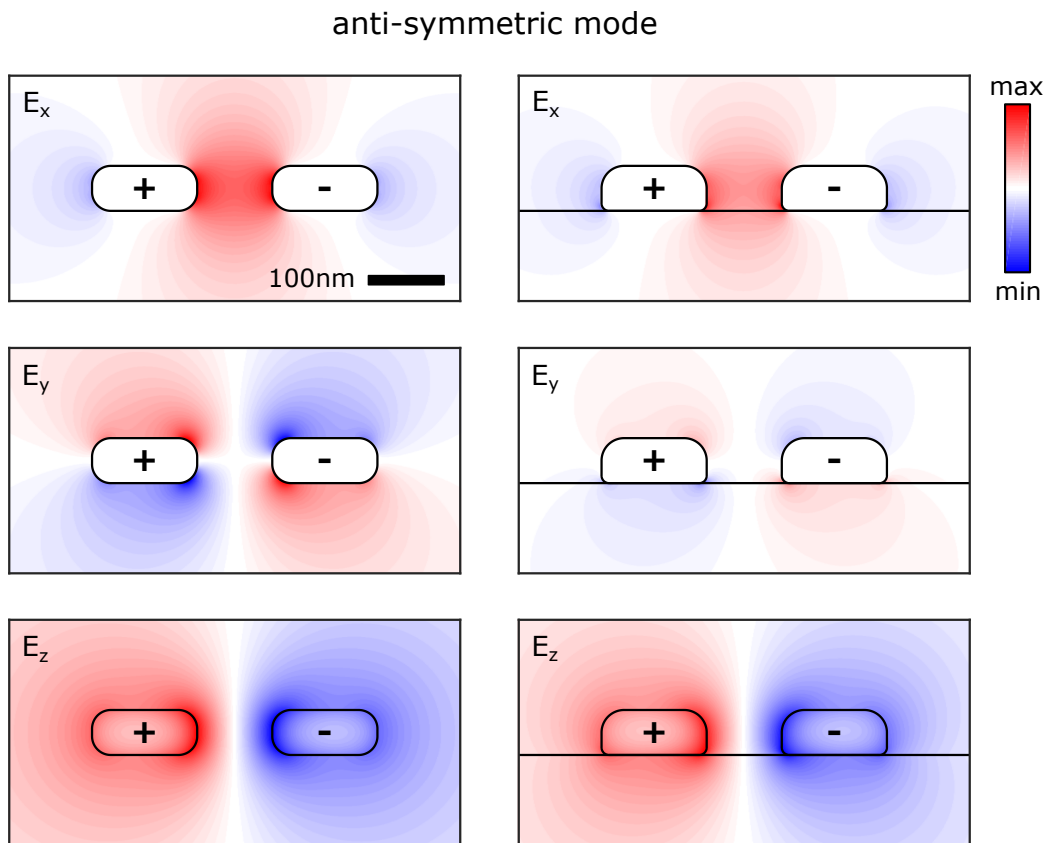


Figure 48: All electric field components of the anti-symmetric mode in a TWTL. The left column shows a TWTL in the case of a homogeneous environment. As comparison the right column shows a TWTL with underlying glass substrate. In every panel the electric field strengths were normalized highest absolute value and plotted in the interval $[-1; 1]$.

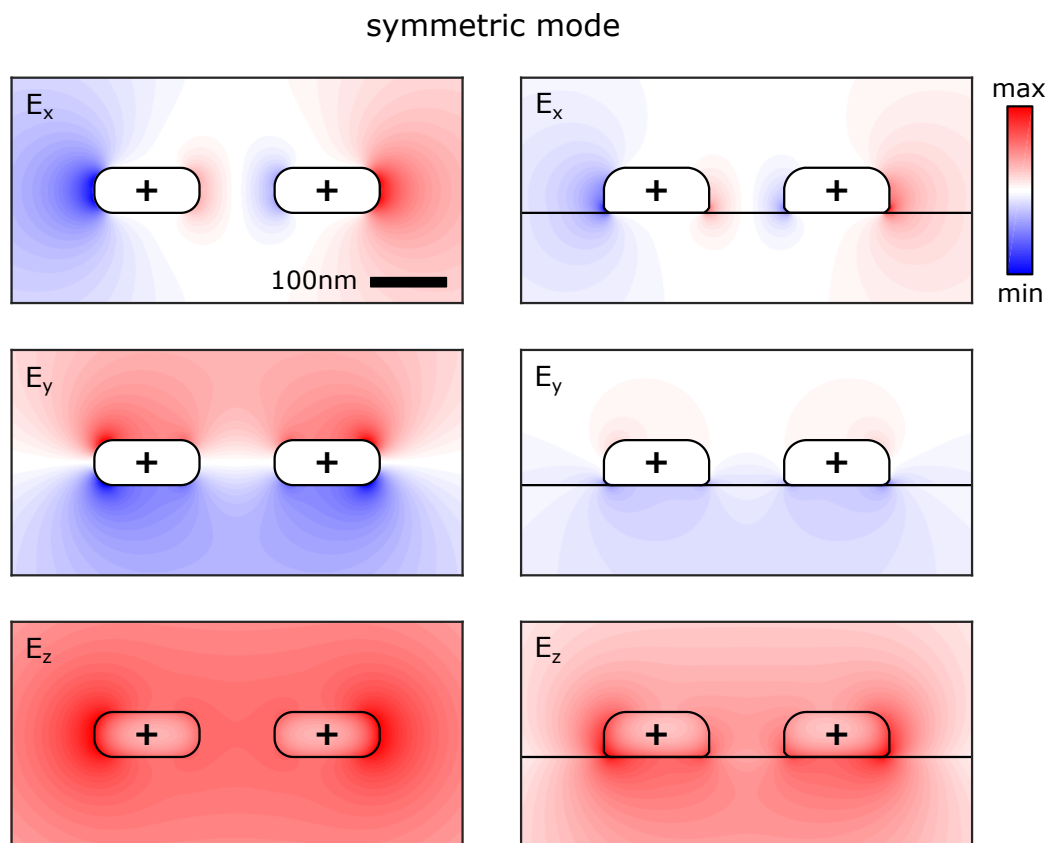


Figure 49: All electric field components of the symmetric mode in a TWTL. The left column shows a TWTL in the case of a homogeneous environment. As comparison the right column shows a TWTL with underlying glass substrate. In every panel the electric field strengths were normalized highest absolute value and plotted in the interval $[-1; 1]$.

A.3 MODULATION OF OPTICAL SIGNALS

Besides using AOMs for amplitude modulation of optical signals also mechanical choppers are widely used. On one hand, they offer two key advantages. First, the chopped beam maintains its full optical power while AOMs only allow up to 50% theoretical modulation efficiency - the power is split between the 0-th and the 1-st diffraction order. Second, no wavelength dependent beam displacements are induced as in the 1-st diffraction order of the AOM. On the other hand, choppers also give certain disadvantages. For example, the modulation frequencies are much lower (up to several tens of kHz) which leads to longer measurement times as well as an increased $1/f$ -noise. Moreover, mechanical imperfections and oscillations can limit the resolution of this measurement technique. A test setup for degenerate pump probe experiments, using an optical chopper, is shown in figure 50 (a). The chopper is a Thorlabs MC2000B equipped with a MC2F47 dual frequency blade. A fast photo diode (PicoQuant Trigger Diode) is used to record the chopped signals. The spectral analysis of the signals is performed using the spectral analyzer of Moku:Lab. The key idea is, to use double modulation and detection at the sum frequency in order to keep the pump-probe signal clean of any offset. The pump and probe modulation frequencies are given as

$$\nu_{\text{pump}} = \nu_{\text{motor}} n_{\text{inner}} \quad , \quad (154)$$

$$\nu_{\text{probe}} = \nu_{\text{motor}} n_{\text{outer}} \quad , \quad (155)$$

where ν_{motor} denotes the motor frequency of the chopper and $n_{\text{inner/outer}}$ the number of slots in the inner and outer ring of the chopper blade. In the test measurement, a blade with 4 respectively 7 slots was used with a motor frequency of $\nu_{\text{motor}} = 100$ Hz. The power spectra of the pump and probe signals are shown in figure 50 (b). The fundamental modulation frequencies at 400 and 700 Hz are clearly visible. The other strongest peaks are at odd multiples of the fundamental frequencies, which is a result of the rectangular modulation of the signals. A fourier decomposition of a rectangular pulse train only features odd multiples of the fundamental frequency. Nevertheless, also even multiples appear in the power spectra. They arise from an asymmetry in the flanks of the rectangular pulse. If the rise and fall times differ in time or shape, even frequency multiples become visible in the power spectrum.

We can also observe small peaks between the even and odd multiples of the fundamental frequency. The distance between those peaks is exactly the motor frequency ν_{motor} . This can be verified by using different modulation frequencies. The power spectra for four different pump frequencies are shown in figure 50 (c). The x-axis is normalized to the actual pump modulation frequency. As the side peaks do not change their location or disappear, we can rule out any measurement technique based origin like, e.g., sampling issues. Consequently, we observe a parasitic signal at multiples of the motor frequency, which therefore also affects the sum-frequency that should be used for detection

$$\nu_{\text{parasitic}} = n \nu_{\text{motor}} \quad \text{with } n \in \mathbb{N} \quad , \quad (156)$$

$$\nu_{\text{sum}} = (n_{\text{inner}} + n_{\text{outer}}) \nu_{\text{motor}} \quad . \quad (157)$$

This leads to the conclusion, that we will always have an offset at the sum-frequency that originates from both the pump and the probe signal alone. This limits the resolution of

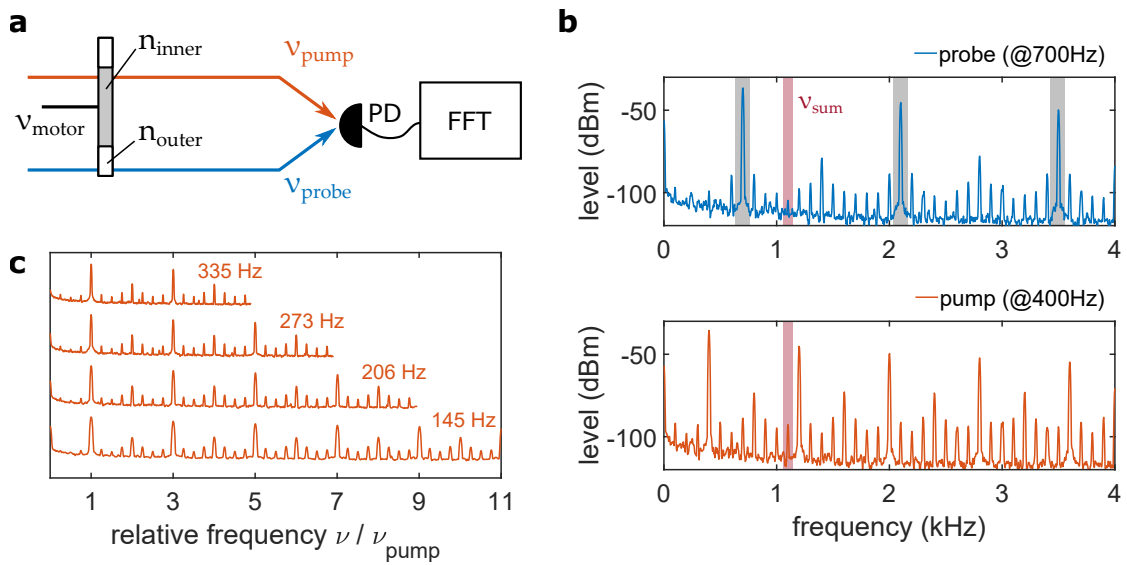


Figure 50: Double modulation setup with one dual-frequency chopper blade. (a) The setup is shown as a simplified scetch. The chopper motor is spinning with the motor frequency and thus generating pump and probe modulations based on the number of slots in the corresponding position of the chopper blade. For detection a fast photo diode (PD) is used together with subsequent FFT. (b) The power spectra of both isolated beams show odd multiples of the modulation frequency (gray shaded area, the upper panel). Even multiples are also visible. Additionally, We observe peaks at multiples of the motor frequency and also occur at the desired detection frequency (red shaded area). (c) Measurements with different motor frequencies prove, that the small peaks can be attributed to the driver motor.

the setup. The only way to prevent this offset, is to use two different choppers and use modulation frequencies that ensure that no multiples of the two motor frequencies $\nu_{\text{motor } 1/2}$ generate parasitic signal at the sum-frequency.

BIBLIOGRAPHY

- [1] Moore, G. E. "Cramming more components onto integrated circuits, Reprinted from Electronics, volume 38, number 8, April 19, 1965, pp.114 ff." In: *IEEE Solid-State Circuits Society Newsletter* 11.3 (2006), pp. 33–35.
- [2] Moore, S. K. "EUV lithography finally ready for fabs." In: *IEEE Spectrum* 55.1 (2018), pp. 46–48.
- [3] Tallents, G., Wagenaars, E., & Pert, G. "Lithography at EUV wavelengths." In: *Nature Photonics* 4.12 (2010), pp. 809–811. ISSN: 1749-4893.
- [4] Pirati, A. et al. "The future of EUV lithography: enabling Moore's Law in the next decade." In: *Extreme Ultraviolet (EUV) Lithography VIII*. Ed. by Panning, E. M. Vol. 10143. International Society for Optics and Photonics. SPIE, 2017, pp. 57–72.
- [5] Wagner, C. & Harned, N. "Lithography gets extreme." In: *Nature Photonics* 4.1 (2010), pp. 24–26. ISSN: 1749-4893.
- [6] MacQuarrie, E. R., Simon, C., Simmons, S., & Maine, E. "The emerging commercial landscape of quantum computing." In: *Nature Reviews Physics* 2.11 (2020), pp. 596–598. ISSN: 2522-5820.
- [7] "40 years of quantum computing." In: *Nature Reviews Physics* 4.1 (2022), pp. 1–1. ISSN: 2522-5820.
- [8] Ladd, T. D., Jelezko, F., Laflamme, R., Nakamura, Y., Monroe, C., & O'Brien, J. L. "Quantum computers." In: *Nature* 464.7285 (2010), pp. 45–53. ISSN: 1476-4687.
- [9] Paesani, S., Ding, Y., Santagati, R., Chakhmakhchyan, L., Vigliar, C., Rottwitt, K., Oxenløwe, L. K., Wang, J., Thompson, M. G., & Laing, A. "Generation and sampling of quantum states of light in a silicon chip." In: *Nature Physics* 15.9 (2019), pp. 925–929. ISSN: 1745-2481.
- [10] Bromley, T. R., Arrazola, J. M., Jahangiri, S., Izaac, J., Quesada, N., Gran, A. D., Schuld, M., Swinarton, J., Zabaneh, Z., & Killoran, N. "Applications of near-term photonic quantum computers: software and algorithms." In: *Quantum Science and Technology* 5.3 (2020), p. 034010.
- [11] Menicucci, N. C., Loock, P. van, Gu, M., Weedbrook, C., Ralph, T. C., & Nielsen, M. A. "Universal Quantum Computation with Continuous-Variable Cluster States." In: *Phys. Rev. Lett.* 97 (11 2006), p. 110501.
- [12] Arrazola, J. M. et al. "Quantum circuits with many photons on a programmable nanophotonic chip." In: *Nature* 591.7848 (2021), pp. 54–60. ISSN: 1476-4687.
- [13] "The rise of integrated quantum photonics." In: *Nature Photonics* 14.5 (2020), pp. 265–265. ISSN: 1749-4893.
- [14] Nordlander, P., Oubre, C., Prodan, E., Li, K., & Stockman, M. I. "Plasmon Hybridization in Nanoparticle Dimers." In: *Nano Letters* 4.5 (2004), pp. 899–903. ISSN: 1530-6984.

- [15] Prodan, E., Radloff, C., Halas, N. J., & Nordlander, P. "A Hybridization Model for the Plasmon Response of Complex Nanostructures." In: *Science* 302.5644 (2003), pp. 419–422.
- [16] Najer, D., Söllner, I., Sekatski, P., Dolique, V., Löbl, M. C., Riedel, D., Schott, R., Starosielec, S., Valentin, S. R., Wieck, A. D., Sangouard, N., Ludwig, A., & Warburton, R. J. "A gated quantum dot strongly coupled to an optical microcavity." In: *Nature* 575.7784 (2019), pp. 622–627. ISSN: 1476-4687.
- [17] Karrai, K., Warburton, R. J., Schulhauser, C., Högele, A., Urbaszek, B., McGhee, E. J., Govorov, A. O., Garcia, J. M., Gerardot, B. D., & Petroff, P. M. "Hybridization of electronic states in quantum dots through photon emission." In: *Nature* 427.6970 (2004), pp. 135–138. ISSN: 1476-4687.
- [18] Reithmaier, J. P., Sek, G., Löffler, A., Hofmann, C., Kuhn, S., Reitzenstein, S., Keldysh, L. V., Kulakovskii, V. D., Reinecke, T. L., & Forchel, A. "Strong coupling in a single quantum dot–semiconductor microcavity system." In: *Nature* 432.7014 (2004), pp. 197–200. ISSN: 1476-4687.
- [19] Gross, H., Hamm, J. M., Tufarelli, T., Hess, O., & Hecht, B. "Near-field strong coupling of single quantum dots." In: *Science Advances* 4.3 (2018), eaar4906.
- [20] Rossi, T. P., Shegai, T., Erhart, P., & Antosiewicz, T. J. "Strong plasmon-molecule coupling at the nanoscale revealed by first-principles modeling." In: *Nature Communications* 10.1 (2019), p. 3336. ISSN: 2041-1723.
- [21] Aharonovich, I., Englund, D., & Toth, M. "Solid-state single-photon emitters." In: *Nature Photonics* 10.10 (2016), pp. 631–641. ISSN: 1749-4893.
- [22] Verhagen, E. *Subwavelength light confinement with surface plasmon polaritons*. Utrecht University, 2009.
- [23] Baida, F. I. & Belkhir, A. "Superfocusing and Light Confinement by Surface Plasmon Excitation Through Radially Polarized Beam." In: *Plasmonics* 4.1 (2009), pp. 51–59. ISSN: 1557-1963.
- [24] Schuller, J. A., Barnard, E. S., Cai, W., Jun, Y. C., White, J. S., & Brongersma, M. L. "Plasmonics for extreme light concentration and manipulation." In: *Nature Materials* 9.3 (2010), pp. 193–204. ISSN: 1476-4660.
- [25] Giannini, V., Fernández-Domínguez, A. I., Heck, S. C., & Maier, S. A. "Plasmonic Nanoantennas: Fundamentals and Their Use in Controlling the Radiative Properties of Nanoemitters." In: *Chemical Reviews* 111.6 (2011), pp. 3888–3912. ISSN: 0009-2665.
- [26] Schumacher, T., Kratzer, K., Molnar, D., Hentschel, M., Giessen, H., & Lippitz, M. "Nanoantenna-enhanced ultrafast nonlinear spectroscopy of a single gold nanoparticle." In: *Nature Communications* 2.1 (2011), p. 333. ISSN: 2041-1723.
- [27] Xin, H., Namgung, B., & Lee, L. P. "Nanoplasmonic optical antennas for life sciences and medicine." In: *Nature Reviews Materials* 3.8 (2018), pp. 228–243. ISSN: 2058-8437.
- [28] Yao, K. & Liu, Y. "Plasmonic metamaterials." In: *Nanotechnology Reviews* 3.2 (2014), pp. 177–210.

- [29] High, A. A., Devlin, R. C., Dibos, A., Polking, M., Wild, D. S., Perczel, J., Leon, N. P. de, Lukin, M. D., & Park, H. "Visible-frequency hyperbolic metasurface." In: *Nature* 522.7555 (2015), pp. 192–196. ISSN: 1476-4687.
- [30] Zhang, S., Fan, W., Panoiu, N. C., Malloy, K. J., Osgood, R. M., & Brueck, S. R. J. "Experimental Demonstration of Near-Infrared Negative-Index Metamaterials." In: *Phys. Rev. Lett.* 95 (13 2005), p. 137404.
- [31] Schimpf, C., Reindl, M., Huber, D., Lehner, B., Silva, S. F. C. D., Manna, S., Vyvlecka, M., Walther, P., & Rastelli, A. "Quantum cryptography with highly entangled photons from semiconductor quantum dots." In: *Science Advances* 7.16 (2021), eabe8905.
- [32] Amendola, V., Pilot, R., Frasconi, M., Maragò, O. M., & Iatì, M. A. "Surface plasmon resonance in gold nanoparticles: a review." In: *Journal of Physics: Condensed Matter* 29.20 (2017), p. 203002.
- [33] Chen, T.-Y., Obermeier, J., Schumacher, T., Lin, F.-C., Huang, J.-S., Lippitz, M., & Huang, C.-B. "Modal Symmetry Controlled Second-Harmonic Generation by Propagating Plasmons." In: *Nano Letters* 19.9 (2019), pp. 6424–6428. ISSN: 1530-6984.
- [34] Jackson, J. D. *Klassische Elektrodynamik*. 5th. Berlin, Boston: De Gruyter, 2014.
- [35] Ashcroft, N. W. & Mermin, D. N. *Solid State Physics*. Saunders College, 1976.
- [36] Hunklinger, S. *Festkörperphysik*. De Gruyter Studium. De Gruyter, 2017. ISBN: 9783110567755.
- [37] Johnson, P. B. & Christy, R. W. "Optical Constants of the Noble Metals." In: *Physical Review B* 6.12 (1972), pp. 4730–4739.
- [38] Zeman, E. J. & Schatz, G. C. "An Accurate Electromagnetic Theory Study of Surface Enhancement Factors for Ag, Au, Cu, Li, Na, Al, Ga, In, Zn, and Cd." In: *J. Phys. Chem.* 91.3 (1987), pp. 634–643.
- [39] Guerrisi, M., Rosei, R., & Winsemius, P. "Splitting of the interband absorption edge in Au." In: *Phys. Rev. B* 12 (2 1975), pp. 557–563.
- [40] Christensen, N. E. & Seraphin, B. O. "Relativistic Band Calculation and the Optical Properties of Gold." In: *Phys. Rev. B* 4 (10 1971), pp. 3321–3344.
- [41] Etchegoin, P. G., Le Ru, E. C., & Meyer, M. "An analytic model for the optical properties of gold." In: *J. Chem. Phys.* 125 (2006).
- [42] Rangel, T., Keçik, D., Trevisanutto, P., Rignanese, G.-M., swygenhoven, H. van, & Olevano, V. "Band structure of gold from many-body perturbation theory." In: *Phys. Rev. B* 86 (Mar. 2012).
- [43] Otto, A. "Excitation of nonradiative surface plasma waves in silver by the method of frustrated total reflection." In: *Zeitschrift für Physik A Hadrons and nuclei* 216.4 (1968), pp. 398–410. ISSN: 0939-7922.
- [44] Kretschmann, E. & Raether, H. "Notizen: Radiative Decay of Non Radiative Surface Plasmons Excited by Light." In: *Zeitschrift für Naturforschung A* 23.12 (1968), pp. 2135–2136.

- [45] Devaux, E., Ebbesen, T., Weeber, J.-C., & Dereux, A. "Launching and decoupling surface plasmons via micro-gratings." In: *Applied Physics Letters* 83 (Dec. 2003), pp. 4936–4938.
- [46] Zia, R., Schuller, J., & Brongersma, M. "Near-field characterization of guided polariton propagation and cutoff in surface plasmon waveguides." In: *Physical Review B* 72 (Oct. 2006), p. 165415.
- [47] Zenin, V. A., Andryieuski, A., Malureanu, R., Radko, I. P., Volkov, V. S., Gramotnev, D. K., Lavrinenko, A. V., & Bozhevolnyi, S. I. "Boosting Local Field Enhancement by on-Chip Nanofocusing and Impedance-Matched Plasmonic Antennas." In: *Nano Letters* 15.12 (2015), pp. 8148–8154. ISSN: 1530-6984.
- [48] Khurgin, J. B. "How to deal with the loss in plasmonics and metamaterials." In: *Nature Nanotechnology* 10.1 (2015), pp. 2–6. ISSN: 1748-3395.
- [49] Berini, P. "Plasmon-polariton waves guided by thin lossy metal films of finite width: Bound modes of symmetric structures." In: *Phys. Rev. B* 61 (15 2000), pp. 10484–10503.
- [50] Berini, P. "Plasmon-polariton waves guided by thin lossy metal films of finite width: Bound modes of asymmetric structures." In: *Phys. Rev. B* 63 (12 2001), p. 125417.
- [51] Halperin, W. P. "Quantum size effects in metal particles." In: *Rev. Mod. Phys.* 58 (3 1986), pp. 533–606.
- [52] Mock, J. J., Barbic, M., Smith, D. R., Schultz, D. A., & Schultz, S. "Shape effects in plasmon resonance of individual colloidal silver nanoparticles." In: *The Journal of Chemical Physics* 116.15 (2002), pp. 6755–6759.
- [53] Fan, X., Zheng, W., & Singh, D. J. "Light scattering and surface plasmons on small spherical particles." In: *Light: Science & Applications* 3.6 (2014), e179–e179. ISSN: 2047-7538.
- [54] Bloembergen, N. *Nonlinear Optics*. 4th. WORLD SCIENTIFIC, 1996.
- [55] Boyd, R. W. *Nonlinear Optics*. 3rd. Academics Press, 2008.
- [56] Coso, R. del & Solis, J. "Relation between nonlinear refractive index and third-order susceptibility in absorbing media." In: *J. Opt. Soc. Am. B* 21.3 (2004), pp. 640–644.
- [57] Göppert-Mayer, M. "Über Elementarakte mit zwei Quantensprüngen." In: *Annalen der Physik* 401.3 (1931), pp. 273–294.
- [58] Sutherland, R. L. *Handbook of Nonlinear Optics*. 2nd. CRC Press, 2003.
- [59] Fiebig, M., Fröhlich, D., Krichevstov, B. B., & Pisarev, R. V. "Second Harmonic Generation and Magnetic-Dipole-Electric-Dipole Interference in Antiferromagnetic Cr₂O₃." In: *Phys. Rev. Lett.* 73 (15 1994), pp. 2127–2130.
- [60] Wegener, M. *Extreme Nonlinear Optics*. 1st. Springer-Verlag Berlin Heidelberg, 2005.
- [61] Hobden, M. V. "Phase-Matched Second-Harmonic Generation in Biaxial Crystals." In: *Journal of Applied Physics* 38.11 (1967), pp. 4365–4372.

- [62] Hum, D. S. & Fejer, M. M. "Quasi-phases matching." In: *Comptes Rendus Physique* 8.2 (2007). Recent advances in crystal optics, pp. 180–198. ISSN: 1631-0705.
- [63] Meschede, D. *Optik, Licht und Laser*. 3rd. Vieweg+Teubner, 2008.
- [64] Sumithra, P & Thiripurasundari, D. "Review on computational electromagnetics." In: *Advanced Electromagnetics* 6.1 (2017), pp. 42–55.
- [65] Jin, J.-M. *The Finite Element Method in Electromagnetics*. 3rd. Wiley-IEEE Press, 2014.
- [66] Ritz, W. "Über eine neue Methode zur Lösung gewisser Variationsprobleme der mathematischen Physik." In: 1909.135 (1909), pp. 1–61.
- [67] Galerkin, B. G. "On Electrical Circuits for the Approximate Solution of the Laplace Equation." In: *Vestnik Inzh.* 19 (1915). in russian, pp. 897–908.
- [68] Heinhold, J. "Variationsmethoden der mathematischen Physik." In: *ZAMM - Journal of Applied Mathematics and Mechanics / Zeitschrift für Angewandte Mathematik und Mechanik* 43.9 (1963), pp. 434–434.
- [69] Berenger, J. P. "A perfectly matched layer for the absorption of electromagnetic waves." In: *J. Computational Phys.* 114 (1994), pp. 185–200.
- [70] Sacks, Z., Kingsland, D., Lee, R., & Lee, J.-F. "A perfectly matched anisotropic absorber for use as an absorbing boundary condition." In: *IEEE Transactions on Antennas and Propagation* 43.12 (1995), pp. 1460–1463.
- [71] Crut, A., Maioli, P., Del Fatti, N., & Vallée, F. "Optical absorption and scattering spectroscopies of single nano-objects." In: *Chem. Soc. Rev.* 43 (11 2014), pp. 3921–3956.
- [72] Novotny, L. "Allowed and forbidden light in near-field optics. I. A single dipolar light source." In: *J. Opt. Soc. Am. A* 14.1 (1997), pp. 91–104.
- [73] Novotny, L. "Allowed and forbidden light in near-field optics. II. Interacting dipolar particles." In: *J. Opt. Soc. Am. A* 14.1 (1997), pp. 105–113.
- [74] Dodson, S., Haggui, M., Bachelot, R., Plain, J., Li, S., & Xiong, Q. "Optimizing Electromagnetic Hotspots in Plasmonic Bowtie Nanoantennae." In: *The Journal of Physical Chemistry Letters* 4.3 (2013), pp. 496–501.
- [75] Metzger, B., Hentschel, M., Schumacher, T., Lippitz, M., Ye, X., Murray, C. B., Knabe, B., Buse, K., & Giessen, H. "Doubling the Efficiency of Third Harmonic Generation by Positioning ITO Nanocrystals into the Hot-Spot of Plasmonic Gap-Antennas." In: *Nano Letters* 14 (2014), pp. 2867–2872.
- [76] Oh, Y.-J., Kang, M., Park, M., & Jeong, K.-H. "Engineering hot spots on plasmonic nanopillar arrays for SERS: A review." In: *BioChip Journal* 10.4 (2016), pp. 297–309. ISSN: 2092-7843.
- [77] Schörner, C. & Lippitz, M. "Single Molecule Nonlinearity in a Plasmonic Waveguide." In: *Nano Letters* 20.3 (2020), pp. 2152–2156. ISSN: 1530-6984.
- [78] Schörner, C., Adhikari, S., & Lippitz, M. "A Single-Crystalline Silver Plasmonic Circuit for Visible Quantum Emitters." In: *Nano Letters* 19.5 (2019), pp. 3238–3243. ISSN: 1530-6984.

- [79] Wu, X., Jiang, P., Razinskas, G., Huo, Y., Zhang, H., Kamp, M., Rastelli, A., Schmidt, O. G., Hecht, B., Lindfors, K., & Lippitz, M. "On-Chip Single-Plasmon Nanocircuit Driven by a Self-Assembled Quantum Dot." In: *Nano Letters* 17.7 (2017), pp. 4291–4296. ISSN: 1530-6984.
- [80] Schnepf, M. J., Brasse, Y., Goßler, F. R., Steiner, A. M., Obermeier, J., Lippitz, M., Fery, A., & König, T. A. "Single Particle Spectroscopy of Radiative Processes in Colloid-to-Film-Coupled Nanoantennas." In: *Zeitschrift für Physikalische Chemie* 232.9-11 (2018), pp. 1593–1606.
- [81] Smith, D. R., Padilla, W. J., Vier, D. C., Nemat-Nasser, S. C., & Schultz, S. "Composite Medium with Simultaneously Negative Permeability and Permittivity." In: *Phys. Rev. Lett.* 84 (18 2000), pp. 4184–4187.
- [82] Liu, Y. & Zhang, X. "Metamaterials: a new frontier of science and technology." In: *Chem. Soc. Rev.* 40 (5 2011), pp. 2494–2507.
- [83] Linden, S., Enkrich, C., Wegener, M., Zhou, J., Koschny, T., & Soukoulis, C. M. "Magnetic Response of Metamaterials at 100 Terahertz." In: *Science* 306.5700 (2004), pp. 1351–1353. ISSN: 0036-8075.
- [84] Hein, S. M. & Giessen, H. "Tailoring Magnetic Dipole Emission with Plasmonic Split-Ring Resonators." In: *Phys. Rev. Lett.* 111 (2 2013), p. 026803.
- [85] Kauranen, M. & Zayats, A. V. "Nonlinear Plasmonics." In: *Nature Photonics* 6 (2012), pp. 737–748.
- [86] Rockstuhl, C., Lederer, F., Etrich, C., Zentgraf, T., Kuhl, J., & Giessen, H. "On the reinterpretation of resonances in split-ring-resonators at normal incidence." In: *Opt. Express* 14.19 (2006), pp. 8827–8836.
- [87] Shen, Q., Hou, B., Chen, Z., & Wang, Z.-L. "Effect of gap width on enhanced magnetic optical fields in metallic split ring resonators." In: *AIP Advances* 2 (Dec. 2012).
- [88] Gramotnev, D. K. & Bozhevolnyi, S. I. "Nanofocusing of electromagnetic radiation." In: *Nature Photonics* 8.1 (2014), pp. 13–22. ISSN: 1749-4893.
- [89] Veronis, G. & Fan, S. "Guided subwavelength plasmonic mode supported by a slot in a thin metal film." In: *Opt. Lett.* 30.24 (2005), pp. 3359–3361.
- [90] Dionne, J. A., Sweatlock, L. A., Atwater, H. A., & Polman, A. "Plasmon slot waveguides: Towards chip-scale propagation with subwavelength-scale localization." In: *Phys. Rev. B* 73 (3 2006), p. 035407.
- [91] Zhang, Z. & Wang, J. "Long-range hybrid wedge plasmonic waveguide." In: *Scientific Reports* 4.1 (2014), p. 6870. ISSN: 2045-2322.
- [92] Moreno, E., Rodrigo, S. G., Bozhevolnyi, S. I., Martín-Moreno, L., & García-Vidal, F. J. "Guiding and Focusing of Electromagnetic Fields with Wedge Plasmon Polaritons." In: *Phys. Rev. Lett.* 100 (2 2008), p. 023901.
- [93] Holmgaard, T., Chen, Z., Bozhevolnyi, S. I., Markey, L., & Dereux, A. "Dielectric-loaded plasmonic waveguide-ring resonators." In: *Opt. Express* 17.4 (2009), pp. 2968–2975.

- [94] Geisler, P., Razinskas, G., Krauss, E., Wu, X.-F., Rewitz, C., Tuchscherer, P., Goetz, S., Huang, C.-B., Brixner, T., & Hecht, B. "Multimode Plasmon Excitation and In Situ Analysis in Top-Down Fabricated Nanocircuits." In: *Phys. Rev. Lett.* 111 (18 2013), p. 183901.
- [95] Brown, F., Parks, R. E., & Sleeper, A. M. "Nonlinear Optical Reflection from a Metallic Boundary." In: *Phys. Rev. Lett.* 14 (25 1965), pp. 1029–1031.
- [96] Lee, C. H., Chang, R. K., & Bloembergen, N. "Nonlinear Electroreflectance in Silicon and Silver." In: *Phys. Rev. Lett.* 18 (5 1967), pp. 167–170.
- [97] Sonnenberg, H. & Heffner, H. "Experimental Study of Optical Second-Harmonic Generation in Silver*." In: *J. Opt. Soc. Am.* 58.2 (1968), pp. 209–212.
- [98] Bloembergen, N., Chang, R. K., Jha, S. S., & Lee, C. H. "Optical Second-Harmonic Generation in Reflection from Media with Inversion Symmetry." In: *Phys. Rev.* 174 (3 1968), pp. 813–822.
- [99] Sipe, J. E., So, V. C. Y., Fukui, M., & Stegeman, G. I. "Analysis of second-harmonic generation at metal surfaces." In: *Phys. Rev. B* 21 (10 1980), pp. 4389–4402.
- [100] Guyot-Sionnest, P., Chen, W., & Shen, Y. R. "General considerations on optical second-harmonic generation from surfaces and interfaces." In: *Phys. Rev. B* 33 (12 1986), pp. 8254–8263.
- [101] Timbrell, D., You, J. W., Kivshar, Y. S., & Panoiu, N. C. "A comparative analysis of surface and bulk contributions to second-harmonic generation in centrosymmetric nanoparticles." In: *Scientific Reports* 8.1 (2018), p. 3586. ISSN: 2045-2322.
- [102] Wang, F. X., Rodriguez, F. J., Albers, W. M., Ahorinta, R., Sipe, J. E., & Kauranen, M. "Surface and bulk contributions to the second-order nonlinear optical response of a gold film." In: *Physical Review B* 80 (2009), p. 233402.
- [103] Mäkitalo, J., Suuriniemi, S., & Kauranen, M. "Boundary element method for surface nonlinear optics of nanoparticles." In: *Opt. Express* 19.23 (2011), pp. 23386–23399.
- [104] Roke, S., Bonn, M., & Petukhov, A. V. "Nonlinear optical scattering: The concept of effective susceptibility." In: *Phys. Rev. B* 70 (11 2004), p. 115106.
- [105] Beer, A. G. F. de & Roke, S. "Nonlinear Mie theory for second-harmonic and sum-frequency scattering." In: *Phys. Rev. B* 79 (15 2009), p. 155420.
- [106] O'Brien, K., Suchowski, H., Rho, J., Salandrino, A., Kante, B., Yin, X., & Zhang, X. "Predicting nonlinear properties of metamaterials from the linear response." In: *Nature Materials* 14.4 (2015), pp. 379–383. ISSN: 1476-4660.
- [107] Butet, J., Brevet, P.-F., & Martin, O. J. F. "Optical Second Harmonic Generation in Plasmonic Nanostructures: From Fundamental Principles to Advanced Applications." In: *ACS Nano* 9.11 (2015), pp. 10545–10562. ISSN: 1936-0851.
- [108] Wang, Q., He, S., & Chen, F. "An effective and accurate method for the design of directional couplers." In: *Selected Topics in Quantum Electronics, IEEE Journal of* 8 (Dec. 2002), pp. 1233 –1238.
- [109] Chen, T.-Y., Tyagi, D., Chang, Y.-C., & Huang, C.-B. "A Polarization-Actuated Plasmonic Circulator." In: *Nano Letters* 20.10 (2020), pp. 7543–7549. ISSN: 1530-6984.

- [110] Dai, W.-H., Lin, F.-C., Huang, C.-B., & Huang, J.-S. "Mode Conversion in High-Definition Plasmonic Optical Nanocircuits." In: *Nano Letters* 14.7 (2014), pp. 3881–3886. ISSN: 1530-6984.
- [111] Oh, D. K., Jeong, H., Kim, J., Kim, Y., Kim, I., Ok, J. G., & Rho, J. "Top-down nanofabrication approaches toward single-digit-nanometer scale structures." In: *Journal of Mechanical Science and Technology* 35.3 (2021), pp. 837–859. ISSN: 1976-3824.
- [112] Huang, J.-S., Callegari, V., Geisler, P., Brüning, C., Kern, J., Prangma, J. C., Wu, X., Feichtner, T., Ziegler, J., Weinmann, P., Kamp, M., Forchel, A., Biagioni, P., Sennhauser, U., & Hecht, B. "Atomically flat single-crystalline gold nanostructures for plasmonic nanocircuitry." In: *Nature Communications* 1.1 (2010), p. 150. ISSN: 2041-1723.
- [113] Stokes, D., Vystavel, T., & Morrissey, F. "Focused ion beam (FIB) milling of electrically insulating specimens using simultaneous primary electron and ion beam irradiation." In: *Journal of Physics D: Applied Physics* 40 (Jan. 2007), p. 874.
- [114] König, T. A. F., Ledin, P. A., Kerszulis, J., Mahmoud, M. A., El-Sayed, M. A., Reynolds, J. R., & Tsukruk, V. V. "Electrically Tunable Plasmonic Behavior of Nanocube–Polymer Nanomaterials Induced by a Redox-Active Electrochromic Polymer." In: *ACS Nano* 8.6 (2014), pp. 6182–6192.
- [115] Ma, Z., Li, Z., Liu, K., Ye, C., & Sorger, V. "Indium-Tin-Oxide for High-performance Electro-optic Modulation." In: *Nanophotonics* 4 (June 2015), pp. 198–213.
- [116] Moerland, R. J. & Hoogenboom, J. P. "Subnanometer-accuracy optical distance ruler based on fluorescence quenching by transparent conductors." In: *Optica* 3.2 (2016), pp. 112–117.
- [117] Kondilis, A., Aperathitis, E., & Modreanu, M. "Derivation of the complex refractive index of ITO and ITON films in the infrared region of the spectrum by the analysis of optical measurements." In: *Thin Solid Films* 516.22 (2008). Proceedings of the EMRS 2007 Fall Meeting Symposium H: Current trends in optical and x-ray metrology of advanced materials and devices II Warsaw, Poland, pp. 8073–8076. ISSN: 0040-6090.
- [118] Ghebremichael, F., Poga, C., & Kuzyk, M. G. "Optical second harmonic characterization of spontaneous symmetry-breaking at polymer/transparent conductor interfaces." In: *Applied Physics Letters* 66.2 (1995), pp. 139–141.
- [119] Wang, W., Xu, J., Liu, X., Jiang, Y., Wang, G., & Lu, X. "Second harmonic generation investigation of indium tin oxide thin films." In: *Thin Solid Films* 365.1 (2000), pp. 116–118. ISSN: 0040-6090.
- [120] Che, F., Grabtchak, S., Whelan, W. M., Ponomarenko, S. A., & Cada, M. "Relative SHG measurements of metal thin films: Gold, silver, aluminum, cobalt, chromium, germanium, nickel, antimony, titanium, titanium nitride, tungsten, zinc, silicon and indium tin oxide." In: *Results in Physics* 7 (2017), pp. 593–595. ISSN: 2211-3797.

- [121] Rodríguez-Suné, L., Scalora, M., Johnson, A. S., Cojocar, C., Akozbek, N., Coppen, Z. J., Perez-Salinas, D., Wall, S., & Trull, J. "Study of second and third harmonic generation from an indium tin oxide nanolayer: Influence of nonlocal effects and hot electrons." In: *APL Photonics* 5.1 (2020), p. 010801.
- [122] Capretti, A., Wang, Y., Engheta, N., & Negro, L. "Comparative Study of Second-Harmonic Generation from Epsilon-Near-Zero Indium Tin Oxide and Titanium Nitride Nanolayers Excited in the Near-Infrared Spectral Range." In: *ACS Photonics* 2 (Oct. 2015).
- [123] Reshef, O., De Leon, I., Alam, M. Z., & Boyd, R. W. "Nonlinear optical effects in epsilon-near-zero media." In: *Nature Reviews Materials* 4.8 (2019), pp. 535–551. ISSN: 2058-8437.
- [124] Sivis, M., Pazos-Perez, N., Yu, R., Alvarez-Puebla, R., Abajo, F. J. García de, & Ropers, C. "Continuous-wave multiphoton photoemission from plasmonic nanostars." In: *Communications Physics* 1.1 (2018), p. 13. ISSN: 2399-3650.
- [125] McClung, F. J. & Hellwarth, R. W. "Giant Optical Pulsations from Ruby." In: *Journal of Applied Physics* 33.3 (1962), pp. 828–829.
- [126] Spence, D. E., Kean, P. N., & Sibbett, W. "60-fsec pulse generation from a self-mode-locked Ti:sapphire laser." In: *Opt. Lett.* 16.1 (1991), pp. 42–44.
- [127] Keller, U., Weingarten, K., Kartner, F., Kopf, D., Braun, B., Jung, I., Fluck, R., Honninger, C., Matuschek, N., & Au, J. Aus der. "Semiconductor saturable absorber mirrors (SESAM's) for femtosecond to nanosecond pulse generation in solid-state lasers." In: *IEEE Journal of Selected Topics in Quantum Electronics* 2.3 (1996), pp. 435–453.
- [128] Guina, M., Rantamäki, A., & Härkönen, A. "Optically pumped VECSELS: review of technology and progress." In: *Journal of Physics D: Applied Physics* 50.38 (2017), p. 383001.
- [129] Jung, I. D., Kärtner, F. X., Matuschek, N., Sutter, D. H., Morier-Genoud, F., Shi, Z., Scheuer, V., Tilsch, M., Tschudi, T., & Keller, U. "Semiconductor saturable absorber mirrors supporting sub-10-fs pulses." In: *Applied Physics B* 65.2 (1997), pp. 137–150. ISSN: 1432-0649.
- [130] Bek, R., Kersteen, G., Kahle, H., Schwarzbäck, T., Jetter, M., & Michler, P. "Quantum dot based mode-locked AlGaInP-VECSEL." In: 9349 (2015). Ed. by Guina, M., pp. 96–100.
- [131] Bek, R., Daghestani, N., Kahle, H., Schwarzbäck, T., Jetter, M., Cataluna, M., & Michler, P. "Femtosecond mode-locked red AlGaInP-VECSEL." In: vol. 8966. Mar. 2014, 89660P.
- [132] Bek, R., Kahle, H., Schwarzbäck, T., Jetter, M., & Michler, P. "Mode-locked red-emitting semiconductor disk laser with sub-250 fs pulses." In: *Applied Physics Letters* 103.24 (2013), p. 242101.
- [133] Matt, S. "Synthese und Charakterisierung von flachen Gold-Einkristallen für die Plasmonik." Bachelor Thesis. University of Bayreuth, 2021.
- [134] Smowton, P., Lutti, J., Lewis, G., Krysa, A., Roberts, J., & Houston, P. "InP-GaInP quantum-dot lasers emitting between 690-750 nm." In: *IEEE Journal of Selected Topics in Quantum Electronics* 11.5 (2005), pp. 1035–1040.

- [135] Roßbach, R., Schulz, W., Reischle, M., Beirne, G., Jetter, M., & Michler, P. "Red to green photoluminescence of InP-quantum dots in Al_xGa_{1-x}InP." In: *Journal of Crystal Growth* 298 (2007). Thirteenth International Conference on Metal Organic Vapor Phase Epitaxy (ICMOVPE XIII), pp. 595–598. ISSN: 0022-0248.
- [136] Bek, R. "Gepulste Halbleiterscheibenlaser im roten Spektralbereich: Sättigbare Halbleiterabsorberspiegel, Frequenzverdopplung und absorberfreie Modenkopplung." Dissertationsschrift. Universität Stuttgart, 2018.
- [137] Spühler, G. J., Weingarten, K. J., Grange, R., Krainer, L., Haiml, M., Liverini, V., Golling, M., Schön, S., & Keller, U. "Semiconductor saturable absorber mirror structures with low saturation fluence." In: *Applied Physics B* 81.1 (2005), pp. 27–32. ISSN: 1432-0649.
- [138] Huang, Z., Zimmer, M., Hepp, S., Jetter, M., & Michler, P. "Optical Gain and Lasing Properties of InP/AlGaInP Quantum-Dot Laser Diode Emitting at 660 nm." In: *IEEE Journal of Quantum Electronics* 55.2 (2019), pp. 1–7.
- [139] Zhang, Z. Y., Oehler, A. E. H., Resan, B., Kurmulis, S., Zhou, K. J., Wang, Q., Mangold, M., Süedmeyer, T., Keller, U., Weingarten, K. J., & Hogg, R. A. "1.55 μm InAs/GaAs Quantum Dots and High Repetition Rate Quantum Dot SESAM Mode-locked Laser." In: *Scientific Reports* 2.1 (2012), p. 477. ISSN: 2045-2322.
- [140] Wilcox, K. G., Butkus, M., Farrer, I., Ritchie, D. A., Tropper, A., & Rafailov, E. U. "Subpicosecond quantum dot saturable absorber mode-locked semiconductor disk laser." In: *Applied Physics Letters* 94.25 (2009), p. 251105.
- [141] Wang, X., Zhu, Y. J., Jiang, C., Guo, Y. X., Ge, X. T., Chen, H. M., Ning, J. Q., Zheng, C. C., Peng, Y., Li, X. H., & Zhang, Z. Y. "InAs/GaAs quantum dot semiconductor saturable absorber for controllable dual-wavelength passively Q-switched fiber laser." In: *Opt. Express* 27.15 (2019), pp. 20649–20658.
- [142] Grange, R., Haiml, M., Paschotta, R., Spühler, G. J., Krainer, L., Golling, M., Ostinelli, O., & Keller, U. "New regime of inverse saturable absorption for self-stabilizing passively mode-locked lasers." In: *Applied Physics B* 80.2 (2005), pp. 151–158. ISSN: 1432-0649.
- [143] Haiml, M., Grange, R., & Keller, U. "Optical characterization of semiconductor saturable absorbers." In: *Applied Physics B* 79.3 (2004), pp. 331–339. ISSN: 1432-0649.
- [144] Thoen, E. R., Koontz, E. M., Joschko, M., Langlois, P., Schibli, T. R., Kärtner, F. X., Ippen, E. P., & Kolodziejski, L. A. "Two-photon absorption in semiconductor saturable absorber mirrors." In: *Applied Physics Letters* 74.26 (1999), pp. 3927–3929.
- [145] Langlois, P., Joschko, M., Thoen, E. R., Koontz, E. M., Kärtner, F. X., Ippen, E. P., & Kolodziejski, L. A. "High fluence ultrafast dynamics of semiconductor saturable absorber mirrors." In: *Applied Physics Letters* 75.24 (1999), pp. 3841–3843.
- [146] Schwarzbäck, T., Bek, R., Hargart, F., Kessler, C. A., Kahle, H., Koroknay, E., Jetter, M., & Michler, P. "High-power InP quantum dot based semiconductor disk laser exceeding 1.3W." In: *Applied Physics Letters* 102.9 (2013), p. 092101.

- [147] Rafailov, E., White, S., Lagatsky, A., Miller, A., Sibbett, W., Livshits, D., Zhukov, A., & Ustinov, V. "Fast quantum-dot saturable absorber for passive mode-locking of solid-State lasers." In: *IEEE Photonics Technology Letters* 16.11 (2004), pp. 2439–2441.
- [148] Hoffmann, M., Sieber, O. D., Wittwer, V. J., Krestnikov, I. L., Livshits, D. A., Barbarin, Y., Südmeyer, T., & Keller, U. "Femtosecond high-power quantum dot vertical external cavity surface emitting laser." In: *Opt. Express* 19.9 (2011), pp. 8108–8116.
- [149] Alfieri, C. G., Waldburger, D., Golling, M., & Keller, U. "High-Power Sub-300-Femtosecond Quantum Dot Semiconductor Disk Lasers." In: *IEEE Photonics Technology Letters* 30.6 (2018), pp. 525–528.
- [150] Meiser, N., Marcinkevicius, S., & Pasiskevicius, V. "Transient behaviour of quantum-dot saturable absorber mirrors at varying excitation fluence." In: *Applied Physics B* 116.4 (2014), pp. 919–927. ISSN: 1432-0649.
- [151] Aichele, T., Zwiller, V., & Benson, O. "Visible single-photon generation from semiconductor quantum dots." In: *New Journal of Physics* 6 (2004), pp. 90–90.
- [152] Yang, W., Lowe-Webb, R. R., Lee, H., & Sercel, P. C. "Effect of carrier emission and retrapping on luminescence time decays in InAs/GaAs quantum dots." In: *Phys. Rev. B* 56 (20 1997), pp. 13314–13320.
- [153] Klimov, V. I. & McBranch, D. W. "Auger-process-induced charge separation in semiconductor nanocrystals." In: *Phys. Rev. B* 55 (19 1997), pp. 13173–13179.
- [154] Klimov, V. I. & McBranch, D. W. "Femtosecond 1P-to- 1S Electron Relaxation in Strongly Confined Semiconductor Nanocrystals." In: *Phys. Rev. Lett.* 80 (18 1998), pp. 4028–4031.
- [155] Paschotta, R., Häring, R., Garnache, A., Hoogland, S., Tropper, A. C., & Keller, U. "Soliton-like pulse-shaping mechanism in passively mode-locked surface-emitting semiconductor lasers." In: *Applied Physics B* 75.4 (2002), pp. 445–451. ISSN: 1432-0649.
- [156] Luo, C. W., Wang, Y. T., Chen, F. W., Shih, H. C., & Kobayashi, T. "Eliminate coherence spike in reflection-type pump-probe measurements." In: *Opt. Express* 17.14 (2009), pp. 11321–11327.
- [157] Moser, M., Winterhoff, R., Geng, C., Queisser, I., Scholz, F., & Dörnen, A. "Refractive index of $(\text{Al}_x\text{Ga}_{1-x})_{0.5}\text{In}_{0.5}\text{P}$ grown by metalorganic vapor phase epitaxy." In: *Applied Physics Letters* 64.2 (1994), pp. 235–237.
- [158] Adachi, S. *GaAs and Related Materials*. WORLD SCIENTIFIC, 1994.
- [159] YU, P. & Cardona, M. *Fundamentals of Semiconductors: Physics and Materials Properties*. Advanced texts in physics Bd. 3. Springer Berlin Heidelberg, 2005. ISBN: 9783540254706.
- [160] Metzger, B., Hentschel, M., Nesterov, M., Schumacher, T., Lippitz, M., & Giessen, H. "Nonlinear optics of complex plasmonic structures: linear and third-order optical response of orthogonally coupled metallic nanoantennas." In: *Appl. Phys. B* 122.4 (2016), p. 77.

- [161] Kravtsov, V., Ulbricht, R., Atkin, J. M., & Raschke, M. B. "Plasmonic nanofocused four-wave mixing for femtosecond near-field imaging." In: *Nature Nanotechnology* 11.5 (2016), pp. 459–464. ISSN: 1748-3395.
- [162] Metzger, B., Schumacher, T., Hentschel, M., Lippitz, M., & Giessen, H. "Third Harmonic Mechanism in Complex Plasmonic Fano Structures." In: *ACS Photonics* 1 (2014), pp. 471–476.
- [163] Lippitz, M., van Dijk, M. A., & Orrit, M. "Third-Harmonic Generation from Single Gold Nanoparticles." In: *Nano Letters* 5.4 (2005), pp. 799–802.
- [164] Shibamura, T., Grinblat, G., Albella, P., & Maier, S. A. "Efficient Third Harmonic Generation from Metal–Dielectric Hybrid Nanoantennas." In: *Nano Letters* 17.4 (2017), pp. 2647–2651. ISSN: 1530-6984.
- [165] Hoogh, A. de, Opheij, A., Wulf, M., Rotenberg, N., & Kuipers, L. "Harmonics Generation by Surface Plasmon Polaritons on Single Nanowires." In: *ACS Photonics* 3.8 (2016), pp. 1446–1452.
- [166] Cotter, D., Manning, R. J., Blow, K. J., Ellis, A. D., Kelly, A. E., Nisset, D., Phillips, I. D., Poustie, A. J., & Rogers, D. C. "Nonlinear Optics for High-Speed Digital Information Processing." In: *Science* 286.5444 (1999), pp. 1523–1528. ISSN: 0036-8075.
- [167] Wolf, D., Schumacher, T., & Lippitz, M. "Shaping the nonlinear near field." In: *Nature Communications* 7 (2016), p. 10361.
- [168] Krauth, J., Giessen, H., & Hentschel, M. "Wavelength-Dependent Third-Harmonic Generation in Plasmonic Gold Nanoantennas: Quantitative Determination of the d-Band Influence." In: *ACS Photonics* 5.5 (2018), pp. 1863–1870.
- [169] Cheng, Y., Hong, H., Zhao, H., Wu, C., Pan, Y., Liu, C., Zuo, Y., Zhang, Z., Xie, J., Wang, J., Yu, D., Ye, Y., Meng, S., & Liu, K. "Ultrafast Optical Modulation of Harmonic Generation in Two-Dimensional Materials." In: *Nano Letters* 20.11 (2020), pp. 8053–8058.
- [170] Beversluis, M. R., Bouhelier, A., & Novotny, L. "Continuum generation from single gold nanostructures through near-field mediated intraband transitions." In: *Physical Review B* 68.115433 (2003).
- [171] Shahbazyan, T. & Stockman, M. *Plasmonics: Theory and Applications*. Challenges and Advances in Computational Chemistry and Physics. Springer Netherlands, 2014. ISBN: 9789400778054.
- [172] Ngoc, L. L. T., Wiedemair, J., Berg, A. van den, & Carlen, E. T. "Plasmon-modulated photoluminescence from gold nanostructures and its dependence on plasmon resonance, excitation energy, and band structure." In: *Opt. Express* 23.5 (2015), pp. 5547–5564.
- [173] Ladstädter, F., Hohenester, U., Puschnig, P., & Ambrosch-Draxl, C. "First-principles calculation of hot-electron scattering in metals." In: *Phys. Rev. B* 70 (23 2004), p. 235125.
- [174] Roaf, D. J. & Shoenberg, D. "The Fermi surfaces of copper, silver and gold. II. Calculation of the Fermi surfaces." In: *Philosophical Transactions of the Royal Society of London. Series A, Mathematical and Physical Sciences* 255.1052 (1962), pp. 135–152.

- [175] Mooradian, A. "Photoluminescence of Metals." In: *Phys. Rev. Lett.* 22 (5 1969), pp. 185–187.
- [176] Boyd, G. T., Yu, Z. H., & Shen, Y. R. "Photoinduced luminescence from the noble metals and its enhancement on roughened surfaces." In: *Phys. Rev. B* 33 (12 1986), pp. 7923–7936.
- [177] Fang, Y., Chang, W.-S., Willingham, B., Swanglap, P., Dominguez-Medina, S., & Link, S. "Plasmon Emission Quantum Yield of Single Gold Nanorods as a Function of Aspect Ratio." In: *ACS Nano* 6.8 (2012), pp. 7177–7184. ISSN: 1936-0851.
- [178] Mohamed, M., Volkov, V., Link, S., & El-Sayed, M. "The 'lightning' gold nanorods: Fluorescence enhancement of over a million compared to the gold metal." In: *Chemical Physics Letters* 317 (Feb. 2000), pp. 517–523.
- [179] Cai, Y.-Y., Liu, J. G., Tauzin, L. J., Huang, D., Sung, E., Zhang, H., Joplin, A., Chang, W.-S., Nordlander, P., & Link, S. "Photoluminescence of Gold Nanorods: Purcell Effect Enhanced Emission from Hot Carriers." In: *ACS Nano* 12.2 (2018), pp. 976–985. ISSN: 1936-0851.
- [180] Mertens, J., Kleemann, M.-E., Chikkaraddy, R., Narang, P., & Baumberg, J. J. "How Light Is Emitted by Plasmonic Metals." In: *Nano Letters* 17.4 (2017), pp. 2568–2574. ISSN: 1530-6984.
- [181] Hugall, J. T. & Baumberg, J. J. "Demonstrating Photoluminescence from Au is Electronic Inelastic Light Scattering of a Plasmonic Metal: The Origin of SERS Backgrounds." In: *Nano Letters* 15.4 (2015), pp. 2600–2604. ISSN: 1530-6984.
- [182] Knittel, V., Fischer, M. P., Roo, T. de, Mecking, S., Leitenstorfer, A., & Brida, D. "Nonlinear Photoluminescence Spectrum of Single Gold Nanostructures." In: *ACS Nano* 9.1 (2015), pp. 894–900. ISSN: 1936-0851.
- [183] Kittel, C. *Introduction to solid state physics*. 8th ed. Wiley, 2005. ISBN: 9780471415268.
- [184] Saavedra, J. R. M., Asenjo-Garcia, A., & Abajo, F. J. García de. "Hot-Electron Dynamics and Thermalization in Small Metallic Nanoparticles." In: *ACS Photonics* 3.9 (2016), pp. 1637–1646.
- [185] Crut, A., Maioli, P., Del Fatti, N., & Vallée, F. "Optical absorption and scattering spectroscopies of single nano-objects." In: *Chem. Soc. Rev.* 43 (11 2014), pp. 3921–3956.
- [186] Crut, A., Maioli, P., Vallée, F., & Fatti, N. D. "Linear and ultrafast nonlinear plasmonics of single nano-objects." In: *Journal of Physics: Condensed Matter* 29.12 (Feb. 2017), p. 123002.
- [187] Stoll, T., Maioli, P., Crut, A., Del Fatti, N., & Vallée, F. "Advances in femto-nano-optics: ultrafast nonlinearity of metal nanoparticles." In: *The European Physical Journal B* 87.11 (2014), p. 260. ISSN: 1434-6036.
- [188] Del Fatti, N. & Vallée, F. "Ultrafast electron interactions in metal clusters." In: *Comptes Rendus Physique* 3.3 (2002), pp. 365–380. ISSN: 1631-0705.
- [189] Hartland, G. V. "Optical Studies of Dynamics in Noble Metal Nanostructures." In: *Chemical Reviews* 111.6 (2011), pp. 3858–3887. ISSN: 0009-2665.

- [190] Block, A., Liebel, M., Yu, R., Spector, M., Sivan, Y., Abajo, F. J. García de, & Hulst, N. F. van. "Tracking ultrafast hot-electron diffusion in space and time by ultrafast thermomodulation microscopy." In: *Science Advances* 5.5 (2019).
- [191] Bin Lee, J., Kang, K., & Hyuk Lee, S. "Comparison of Theoretical Models of Electron-Phonon Coupling in Thin Gold Films Irradiated by Femtosecond Pulse Lasers." In: *materials transactions* 52.3 (2011), pp. 547–553.
- [192] Bonn, M., Denzler, D. N., Funk, S., Wolf, M., Wellershoff, S.-S., & Hohlfeld, J. "Ultrafast electron dynamics at metal surfaces: Competition between electron-phonon coupling and hot-electron transport." In: *Phys. Rev. B* 61 (2 2000), pp. 1101–1105.
- [193] Trebino, R. *Frequency-Resolved Optical Gating: The Measurement of Ultrashort Laser Pulses*. Springer US, 2012. ISBN: 9781461511816.
- [194] Träger, F. *Springer Handbook of Lasers and Optics*. Springer Handbooks. Springer Berlin Heidelberg, 2012. ISBN: 9783642194092.
- [195] Linden, S., Kuhl, J., & Giessen, H. "Amplitude and phase characterization of weak blue ultrashort pulses by downconversion." In: *Opt. Lett.* 24.8 (1999), pp. 569–571.
- [196] Linden, S., Giessen, H., & Kuhl, J. "XFROG — A New Method for Amplitude and Phase Characterization of Weak Ultrashort Pulses." In: *physica status solidi (b)* 206.1 (1998), pp. 119–124.
- [197] Dmitriev, V., Gurzadyan, G., & Nikogosyan, D. *Handbook of Nonlinear Optical Crystals*. Springer Series in Optical Sciences. Springer Berlin Heidelberg, 2013. ISBN: 9783662138304.
- [198] Bronstein, I. N., Semendjajew, K. A., Musiol, G., & Mühlig, H. *Taschenbuch der Mathematik*. 5. Thun, Frankfurt am Main: Verlag Harri Deutsch, 2001.

EIDESSTATTLICHE ERKLÄRUNG

Hiermit versichere ich an Eides statt, dass ich die vorliegende Arbeit selbstständig verfasst und keine anderen als die von mir angegebenen Quellen und Hilfsmittel verwendet habe.

Weiterhin erkläre ich, dass ich die Hilfe von gewerblichen Promotionsberatern bzw. Promotionsvermittlern oder ähnlichen Dienstleistern weder bisher in Anspruch genommen habe, noch künftig in Anspruch nehmen werde.

Zusätzlich erkläre ich hiermit, dass ich keinerlei frühere Promotionsversuche unternommen habe.

Ort, Datum

Julian Obermeier

COLOPHON

This document was typeset using the typographical look-and-feel classicthesis developed by André Miede. The style was inspired by Robert Bringhurst's seminal book on typography "*The Elements of Typographic Style*". classicthesis is available via CTAN.